The University of Maine
DigitalCommons@UMaine

Electronic Theses and Dissertations | Fogler Library

Summer 8-2021

Deciphering the Perpetual Fight Between Virus and Host: Utilizing Bioinformatics to Elucidate the Host's Genetic Mechanisms that Influence JC Polyomavirus Infection

Michael P. Wilczek
University of Maine, michael.wilczek@maine.edu

Follow this and additional works at: https://digitalcommons.library.umaine.edu/etd

 Part of the Bioinformatics Commons, Cell Biology Commons, Genetics Commons, Immunology of Infectious Disease Commons, Molecular Biology Commons, Nervous System Diseases Commons, Virology Commons, and the Virus Diseases Commons

Recommended Citation

Wilczek, Michael P., "Deciphering the Perpetual Fight Between Virus and Host: Utilizing Bioinformatics to Elucidate the Host's Genetic Mechanisms that Influence JC Polyomavirus Infection" (2021). *Electronic Theses and Dissertations*. 3430.
https://digitalcommons.library.umaine.edu/etd/3430

This Open-Access Thesis is brought to you for free and open access by DigitalCommons@UMaine. It has been accepted for inclusion in Electronic Theses and Dissertations by an authorized administrator of DigitalCommons@UMaine. For more information, please contact um.library.technical.services@maine.edu.

DECIPHERING THE PERPETUAL FIGHT BETWEEN VIRUS AND HOST:

UTILIZING BIOINFORMATICS TO ELUCIDATE THE HOST'S GENETIC MECHANISMS THAT INFLUENCE JC POLYOMAVIRUS INFECTION

By

Michael P. Wilczek

B.S. The University at Albany, State University of New York, 2013

A DISSERTATION

Submitted in Partial Fulfillment of the

Requirements for the Degree of

Doctor of Philosophy

(in Microbiology)

The Graduate School

The University of Maine

August 2021

Advisory Committee:

Melissa Maginnis, Associate Professor of Microbiology, Advisor

Benjamin King, Assistant Professor of Bioinformatics

Melody Neely, Associate Professor of Molecular and Biomedical Sciences

Con Sullivan, Assistant Professor of Biology, University of Maine at Augusta

Kristy Townsend, Associate Professor, The Ohio State University, Adjunct Faculty, The University of Maine

© 2021 Michael Wilczek

All Rights Reserved

DECIPHERING THE PERPETUAL FIGHT BETWEEN VIRUS AND HOST:

UTILIZING BIOINFORMATICS TO ELUCIDATE THE HOST'S GENETIC MECHANISMS THAT INFLUENCE JC POLYOMAVIRUS INFECTION

By Michael Wilczek

Dissertation Advisor: Dr. Melissa Maginnis

An Abstract of the Dissertation Presented
in Partial Fulfillment of the Requirements for the
Degree of Doctor of Philosophy
(in Microbiology)
August 2021

JC polyomavirus (JCPyV) is a human-specific pathogen that infects 50-80% of the population, and can cause a deadly, demyelinating disease, known as progressive multifocal leukoencephalopathy (PML). In most of the population, JCPyV persistently infects the kidneys but during immunosuppression, it can reactivate and spread to the central nervous system (CNS), causing PML. In the CNS, JCPyV targets two cell types, astrocytes, and oligodendrocytes. Due to the hallmark pathology of oligodendrocyte lysis observed in disease, oligodendrocytes were thought to be the main cell type involved during JCPyV infection. However, recent evidence suggests that astrocytes are targeted by the virus and act as a reservoir for JCPyV. From these findings and lack of a tractable model to study JCPyV infection, the infectious cycle was characterized in primary human astrocytes (NHAs) compared to a well-studied but immortalized glial cell line, SVGA cells (SVGAs). It was discovered that the JCPyV infectious cycle was delayed in NHAs compared to SVGAs, contributed in part by the transformed properties of SVGAs.

To further define the mechanisms of JCPyV infection in NHAs, RNA sequencing (RNA-seq) analysis was performed in both cell types at time points established to be important during the infectious cycle. RNA-seq revealed a temporal difference in differential gene expression between primary and immortalized cells. Through complementary cell-based assays, the involvement of the

mitogen-activated protein kinases/extracellular signal-regulated kinases (MAPK/ERK) pathway was validated, and the phosphoinositide 3-kinase (PI3K)/AKT/mechanistic target of rapamycin (mTOR) pathway was discovered to be involved in JCPyV infection in NHAs. Altogether, RNA-seq revealed and confirmed pathways important for JCPyV in NHAs, yet infection and PML pathogenesis is a complex composition of variation in viral genomic sequences, contributing to a quasispecies that can impact infection and disease pathogenesis. A bioinformatic approach characterizing 181 sequences of a hypervariable region of the JCPyV genome validated and further characterized how this region is diverse from various locations in individuals and among patients with disease. Overall, this dissertation addresses how astrocytes are involved during JCPyV infection and how the virus mutates, highlighting the interplay of viral and host cell factors that contribute to pathogenesis of this deadly disease.

DEDICATION

Thank you to my family, especially my parents, for supporting me throughout my life.

Thank you to my partner, where none of this would be possible if it were not for you.

ACKNOWLEDGEMENTS

Thank you to everyone at the University of Maine who supported me throughout my graduate career these past years. Especially to everyone in the Maginnis Lab, including Colleen Mayberry, Kashif Mehmood, Jeanne DuShane, Avery Bond, and Mason Crocker. As well as Francesca Armstrong, Remi Geohegan, Laura Horowitz, Lauren Cusson, and Aiden Pike, in which I had the opportunity to mentor each one. I was fortunate enough to be surrounded by a team that facilitated my growth and made the laboratory environment an enjoyable place to be in.

Thank you to Dr. Sally Molloy and Dr. Melody Neely, who were my unofficial mentors, helping me build my skillset in teaching and allowing me to be part of numerous meetings. I would not have been able to facilitate an active learning environment or even make it through my first semester in teaching a course if it were not for the guidance of either of them, especially during the few months of the COVID-19 pandemic!

Thank you to all the professors in the Molecular and Biomedical Department, including Patricia Singer- who saved me more than a few times with last-minute experiments, Tammy (Gosselin) Randall, and Doreen Sanborn- who supported this Department. Also, thank you to the Graduate School, the Graduate Student Government, and especially Scott Delcourt, who has facilitated my professional development more than ever imagined.

Lastly, thank you to my mentor, Dr. Melissa Maginnis. You have helped me grow as a researcher, teacher, and person. None of the accomplishments I had the opportunity to earn would have been achieved if not for you. Knowing this from firsthand experience, every person has the potential to succeed. Yet, the environment they are placed in makes all the difference.

TABLE OF CONTENTS

LIST OF TABLES

LIST OF EQUATIONS

LIST OF FIGURES

CHAPTER 1

INTRODUCTION

Viruses and the Balance of Life and Knowledge

Viruses are the most significant biological group globally, offering incredible genetic diversity and exceedingly unexplored potential (1). These characteristics, though exciting, strengthen the driving force of viral evolution through ecological pressures and mechanistically by horizontal gene transfer (2). Continued research is critical to remain knowledgeable in one of the largest and most dynamic biological groups that we coinhabit within this world. The large number of viruses on Earth, known as the virosphere (2, 3), as well as the study of viruses, can be thought of as a teetering "balance of life and knowledge," educating us in the fundamentals of DNA replication (4–6), protecting and aiding us in the response of our immune system (7), but also having the potential to cause global catastrophes, displacing our way of life (8, 9).

Recent bodies of evidence suggest that before we are born, viruses contribute to our health, especially to the biology of the placenta (10). Specifically, exogenous retroviruses promote the placental biology by facilitating the formation of the multinuclear barrier, protect the fetus from other viruses, suppress maternal immunity, and may even play a role in controlling gene expression during pregnancy (10–13). Additionally, the human virome, (i.e., a large diversity of viruses colonized in healthy humans), can also benefit our health. Studies have demonstrated the protective effect to infants contributed to breast milk, inhibiting viral infection and illuminating the diversity of viruses affected (14), as well as having antiviral properties to a range of viruses (15–18), including severe acute respiratory syndrome coronavirus (SARS-CoV) (19). Unfortunately, viruses can also become pathogenic, demonstrated in the 1918 H1N1 pandemic (9) and recently, the World Health Organization (WHO) declaring the outbreak of COVID-19, caused by SARS-CoV-2 virus, a global pandemic on March 11th, 2020 (8).

A virus becoming pathogenic is dictated by several variables (20). The most important, is viral persistence in the host/population and how it contributes to the overall ecosystem (20). This includes viral transmission or spread through a given population (20), which was directly observed during the COVID-19 pandemic where transmission occurred at a higher frequency in more dense populations. For another example, measles virus requires a relatively large naïve human population to exist, of approximately 250,000 to 500,000 individuals, requiring a human host quickly for it to remain infectious (21, 22). Yet, the virus has contributed to ~110,000 deaths annually according to 2017 estimates (23, 24). Due to the aggressive nature of measles, massive human efforts were undertaken, developing a vaccine, which reduced the number of cases from 145 cases per million in 2000 to 19 cases per million in 2016 (24). Interestingly, 2019 saw the highest reported cases in 23 years (25), however in 2020 a significant decrease in the number of measles cases occurred, most likely contributed to the public health interventions in place during the COVID-19 pandemic (26). These measles outbreak dynamics, highlights the vulnerability of the virus as well as its limitations in viral spread throughout a population. This contrasts with, herpes simplex viruses, which, persist in their host for a lifetime and unlike measles, require a smaller group of people to persist in the population as it has many more opportunities to establish infection (20). As a result of this numerical trade off, in 2016, an estimated 491.5 million people, ~13.2% of the population aged 15 – 49 years, were infected with herpes simplex virus 2 (HSV2), and 3,752 million people or ~66.6% of the global population from 0 – 49 years of age was infected with HSV1 (27). Additionally, zoonotic diseases, viruses transmitted from animals to humans, are pathogens that can infect humans, for which they expand their ecological niche, and in the case of SARS-CoV-2, can cause a global pandemic. Overall, numerous variables are available to measure the extent of virus pathogenicity, including the mortality rate, the morbidity rate within a community, and the range of host tropism; however, the most successful virus is transmitted from one host to the next, accomplishing a persistent infection, and is almost undetectable to the host.

Epidemiology of JC Polyomavirus

JC polyomavirus (JCPyV) persistently infects up to 80% of the adult population (28–30). Viral infection commonly occurs in childhood via horizontal transmission (31) and spreads from one person to the next through peroral transmission acquired from contact of contaminated surfaces, food, and water (32, 33). This virus has successfully created an ecological niche with humans through 100,000 to 200,000 years of coevolution with the population (34–37). Interestingly, given the low mutational rate of JCPyV compared to other viruses, subtypes of JCPyV have been used to map population movement across the world (37–40). In total, there are approximately 19 subtypes of JCPyV, defined by specific mutations of the late portion of the viral genome (discussed later) (41). Briefly, these subtypes are unique upon geographical area, type 1 and type 4 are associated with Europeans and European-Americans (37), type 2A found in Asian and Native American populations (42), and type 3 and 6 are associated with Africans and African Americans (43).

JCPyV is characterized as a persistent, asymptomatic infection in the kidneys of healthy individuals, where the virus is periodically shed in the urine (28, 30, 44–47). As the virus is transmitted through the peroral route, primary infection is thought to occur in the tonsillar tissue (44, 48). Upon initial infection however, the virus establishes further secondary infections in circulating B cells, bone marrow, and the kidneys (44). These sites of secondary infections are referred to as latent, yet true latency is not observed (47), as the virus does not express latency genes or latency transcripts (LATs) (49, 50). Viral DNA is quantified by highly sensitive polymerase chain reaction (PCR) (51–53) and it is thought that the virus may sporadically or intermittently replicate within these secondary locations, specifically in the kidneys, characterized as a persistent state of viral infection (47). It has also been reported that JCPyV can be present in the brain among healthy individuals as an additional secondary location in the body, however this site harboring latent virus is still inconclusive (54–57). A few reports demonstrated that viral DNA was present in the brain yet there was no presence of the viral proteins (54, 56). These

include areas such as the frontal cortex, hippocampus, and cerebellum but only fragments of viral DNA were detected (56). The authors concluded that this could have been due to circulating JCPyV-infected B cells that traversed the blood brain barrier, and fragments of viral DNA were possibly able to integrate as free episomal DNA molecules and persist in specific brain cells (56). Overall, JCPyV is an accomplished virus because it has adapted well to the human host, demonstrating the characteristic of viral persistence in the human population. Unfortunately, JCPyV is capable of a more serious and fatal infection, causing disease. During a state of immunosuppression, JCPyV can reactivate and spread to the central nervous system (CNS) (45, 58, 59) causing the fatal, demyelinating disease, progressive multifocal leukoencephalopathy (60–63).

Progressive Multifocal Leukoencephalopathy

As discussed, JCPyV subtypes can be defined by the geographical location, creating a global perspective of viral spread and mapping human population movement (37–40). Moreover, these subtypes are also associated with varying levels of virulence. Specifically, the JCPyV subtype 2B, often isolated from Asians and Eurasians, has demonstrated a higher incidence of PML (64, 65), in contrast to type 4, being associated with a lower risk of disease (66). PML is caused by the cytolytic destruction of astrocytes and oligodendrocytes within the CNS as illustrated in Figure 1.1 (58, 59, 67). Clinical patient samples have indicated that the destruction of oligodendrocytes, the cells that produce myelin, lead to demyelination of the CNS and onset of PML. Yet, recent research has demonstrated astrocytes are the main target during JCPyV infection (68), highlighting the complexity of PML.

JCPyV reactivation from sites of secondary infection are poorly understand and the direct mechanism of reactivation lacks definitive evidence (69). However, it is conclusive that PML occurs in immunosuppressed hosts, observed in patients with deficiencies in $CD4^+$ T cells (70). For this reason, individuals who are positive for human immunodeficiency virus (HIV) were historically, at most risk for

disease, representing up to 5% of all PML cases (60, 71). Fortunately, the use of highly active antiretroviral therapy (HAART) has significantly reduced the rate of PML among HIV-positive individuals (72, 73). Due to the opportunistic nature of the disease, recent risk groups for the development of PML have emerged, specifically among individuals who take immunomodulatory therapies for immune-mediated diseases. This includes patients who take natalizumab and rituximab for multiple sclerosis (MS), rheumatoid arthritis, or systemic lupus erythematosus (SLE) (71, 74–76). This is especially true for patients who take natalizumab with prolong treatment and seropositivity, with an overall risk of developing PML of 1 in 1,000 (77).

PML treatments are significantly limited, and their success is relatively limited as PML is typically

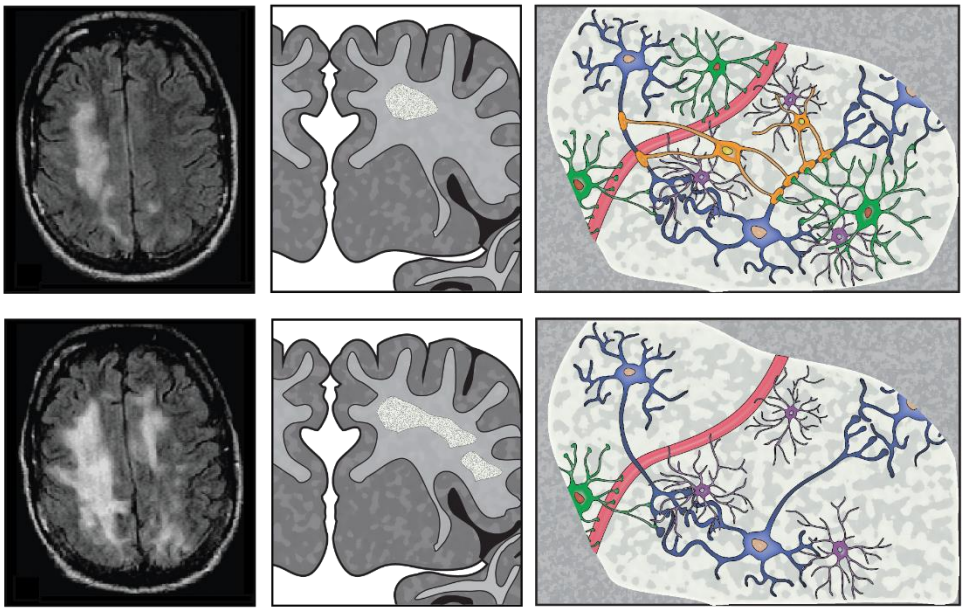

Figure 1.1. Progression PML development and the cell types involved. MRI displaying PML lesion development in white matter of the brain. MRI adapted with permission from (67). Bottom MRI is of the same individual, 4 months apart. Demyelination is caused by the cytosolic destruction (left and center panels) of oligodendrocytes (orange) and astrocytes (green) (right panels). Other cell types displayed, neurons (blue) and microglial (purple) are not considered to be the main cell types involved in PML.

diagnosed late, when neurological deficits are manifested (74). A proactive approach, especially for individuals who are at heightened risk for disease is recommended, through risk stratification of treatment regimens and monitoring both JCPyV antibodies and frequent brain MRIs (78). Treatments most often address the underlying immunosuppression, either treating HIV with HAART or discontinuing

immunosuppressive therapies (71, 79–81). Recently, there has been studies demonstrating the possible benefits of T cell therapy, however these treatments can result in severe morbidity (71, 82, 83). This includes an increased risk of immune reconstitution inflammatory syndrome (IRIS), a condition in which extensive inflammation can lead to immune-mediated injury and death (84, 85). Overall, contrary to the persistent nature of JCPyV infection among healthy individuals, PML in immunosuppressed patients is characterized by uncontrolled JCPyV replication, partly due to the individual's health but can also be attributed to the JCPyV genome driving the infectious cycle of the virus.

JCPyV Infectious Cycle

JCPyV is a nonenveloped double-stranded DNA virus with a circular genome of approximately 5,100 base pairs in size (86, 87). JCPyV infection begins with attachment to α2,6-linked sialic acid on lactoseries tetrasccharide (LSTc), through a major viral protein (VP) that contributes to the viral capsid (88–90). For viral entry into the cell, JCPyV requires the 5-hydroxytryptamine 2 family of serotonin receptors (5-HT_2Rs) and clathrin-mediated endocytosis (91, 92). Following entry, the virus traffics to the endoplasmic reticulum (ER), through the endocytic compartment (93–95). In the ER, JCPyV undergoes partial disassembly (93) before it arrives at the nucleus. Here, the remaining events of the JCPyV infectious cycle is accomplished by genes expressed in three regions of the genome, that make up its entirety: the noncoding control region (NCCR), and two bidirectional coding regions that encode for the early genes and late genes (Figure 1.2) (47). The NCCR orchestrates the transformation of the cell to create a supportive environment for viral DNA replication.

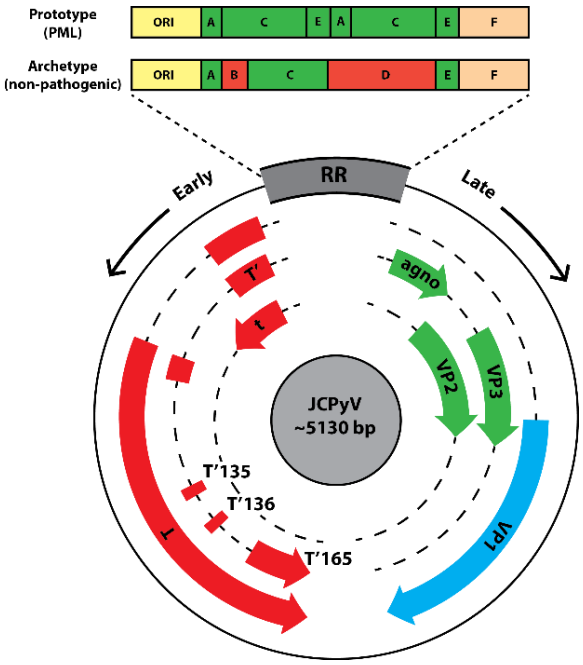

Figure 1.2. Schematic of JCPyV genome. The viral genome is temporally regulated. Host factors bind to the regulatory region (RR), also called the noncoding control region (NCCR), initiating transcription of the early genes, T Antigens (red). Following production of the early proteins, the late genes are transcribed, translated into the viral structural proteins (VP1, VP2 and VP3) and agnoprotein, which assists in virus regulation and release. The RR is hypervariable. The archetype consists of 6 blocks (A-F) however the PML-like strains commonly have deletions of B and D (repressors) and duplications of A, C, and E (enhancers). (Adapted from (41)).

NCCR

The NCCR is approximately 145 base pairs in length and this region is critical not only in establishing infection but correlates with PML risk (96, 97). Numerous host factors, including nuclear factor kappa-light-chain-enhancer of activated B cells (NF-κB) (98, 99), Spi-B transcription factor (SpiB) (100), and in glial cells, nuclear factor of activated T-cells 4 (NFAT4) (101) and subtypes of the nuclear factor-1 (NF-1) family (102, 103) bind to the NCCR to initiate early gene transcription. These host transcription factors are important for viral transcription and play a role in the cellular tropism of the virus. For example, JCPyV can infect circulating B cells, whereas when B cells mature, transcription factors such as NFIX and SpiB are upregulated (100, 104), influencing viral replication. Additionally, individuals who receive natalizumab treatment have induced B cell differentiation, possibly facilitating the development of PML (105).

Yet, the NCCR is a hypervariable region of the JCPyV genome; subject to homologous recombination that leads to large deletions and tandem duplications in this region (Figure 1.2) (74). This approximately 145-base pair region is organized into six DNA sequence blocks, denoted as lowercase

letters “a”, “b”, “c”, “d”, “e” and “f” which can undergo rearrangements (106–108). The strain not associated with disease is called the archetype or CY, and these blocks are arranged “a” through “f”, found predominantly in the kidneys of healthy individuals (74, 109). However, the PML-type strains, most commonly contain a 98-base pair tandem repeat, known as an enhancer element, composed of blocks, “a,” “c,” and “e.” These duplicated sequences allow for duplicate TATA boxes and additional transcription factor binding sites (TFBS) (69, 110, 111). These additional TFBS allow for the recruitment of transcription factors, such as NFIX, to bind to the NCCR and enhance viral transcription of both the early and late genes (112, 113), including JCPyV Large T Antigen (T Ag), needed to transform the cell to support viral DNA replication.

JCPyV T Antigen and SV40 T Antigen

The prefix of polyoma in JCPyV means “many” and “tumor” given the name due to the production of the viral oncoprotein T Ag. T Ag can transform and induce immortalization properties into the host cells and animals (114). Located in the early genes of the JCPyV genome, T Ag is a multifunctional protein. These functions include driving the cell into S phase, during which viral DNA is replicated, by binding to phosphorylated retinoblastoma (pRB) causing the release of the transcription factor, E2F-1 (114, 115). It also sequesters p53 in the cytoplasm to prevent the activation of apoptotic pathways (116), and it acts as a helicase to unwind the viral DNA for replication by binding to the origin of replication located on the NCCR (41, 116).

There is high nucleotide similarity across the *Polyomaviridae* family with JCPyV and BK polyomavirus (BKPyV) (117). BKPyV also establishes an asymptomatic infection, yet during immunosuppression BKPyV can cause nephropathy and hemorrhagic cystitis (118). JCPyV and BKPyV share 80% homology in their early coding regions, like anther polyomavirus, simian virus 40 (SV40) ((96, 117). Even though there is a high degree of nucleotide similarity observed between JCPyV and SV40

early genes, including within T Ag, the T Ag of SV40 can enhance JCPyV replication, through binding more efficiently to the JCPyV genome (119–121). SV40 T Ag can also dysregulate the cell cycle and activate cellular pathways that can support JCPyV infection (122, 123). Consequently, numerous studies understanding JCPyV infection have utilized SVG-A cells (herein as SVGAs), a glial cell line, immortalized with SV40 T Ag to support robust levels of JCPyV infection (120, 121, 124). SV40 T Ag can support higher levels of JCPyV infection because it can bind more efficiently to the JCPyV viral genome than the JCPyV T Ag, consequently creating a more conducive environment for JCPyV infection and driving JCPyV DNA replication forward (120).

Cell Cycle Regulation

Polyomavirus (PyV) T Ag, including SV40 T Ag can also induce expression of cyclins A, B1, and E but not of cyclin D (125, 126). Cyclins are often used as cell cycle markers (68, 127–129) and have been implemented to understand how JCPyV influences the cellular environment (68, 130, 131). Among the cyclins, the expression of cyclin E and cyclin B are the most useful to characterize JCPyV infection. Cyclin E is activated towards the end of the G1 phase and accumulates in the cell during S phase; this event is perhaps facilitated by T Ag binding to Rb and releasing the transcription factor E2F-1 (114, 115, 132–134), as illustrated in Figure 2.4. It has been previously demonstrated that cyclin E expression is upregulated during JCPyV infection in cells immortalized and not immortalized SV40 T Ag (130, 131). On the other hand, cyclin B1 accumulates in the cell during late stages of the G2 phase and activating in the nucleus during the initiation of the M phase. Cyclin B1 is expressed during JCPyV infection (131), and during later stages of infection, it is expressed in the cytoplasm, demonstrating G2/M phase arrest (130) (Figure 2.4). This arrest phase is critical for a successful viral infection, giving an opportunity for the viral proteins that were previously created, encapsidate the viral DNA (68).

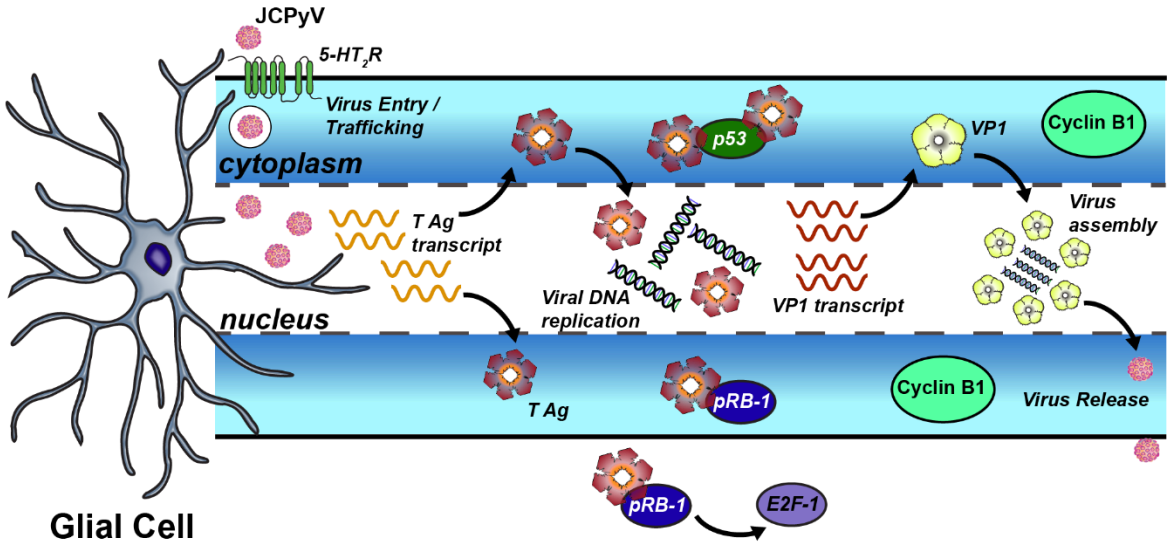

Figure 1.3. JCPyV infectious cycle in a glial cell type. Upon virus entry through clathrin-mediated endocytosis and trafficking to the nucleus, the virus transcribes and translates the early genes, T Ags. By binding to pRB-1 and p53 the cell is transformed to support viral DNA replication. This drives the infectious cycle forward, to transcribe and translate the late viral genes, including the capsid protein VP1. VP1 encapsidates the newly formed viral DNA with VP2 and VP3 before release to infect other surrounding cells.

Late Gene Expression

Following viral DNA replication, the late viral genes are transcribed, producing the structural proteins: VP1, VP2, and VP3, as well as a multifunctional protein, agnoprotein (96). The viral capsid is made up of 72 VP1 pentamers, along with VP2 and VP3, where VP1 is the major component of the capsid (135). Research has demonstrated that VP1 production is delayed in cells not immortalized with SV40 T Ag, solely relying on the efficiency of JCPyV T Ag (130). Additionally, the main cell types impacted by PML, astrocytes and oligodendrocytes, express varying levels of JCPyV infection quantified by early and late viral protein expression. Astrocytes were more readily targeted in the CNS, expressing higher levels of the late viral gene product, compared to only a few oligodendroglia expressing VP1 (68). Lastly, agnoprotein is produced during the later stages of infection. This viral protein has been demonstrated to interact with T Ag, suppressing viral DNA replication and helping transition the cell into G2/M phase

(136). Research has also demonstrated that agnoprotein can act as a viroporin, facilitating viral release from the cell (137).

Astrocytes and JCPyV Infection

Recent research has demonstrated that when JCPyV invades the CNS, astrocytes may be the main target during JCPyV infection (68). This evidence reevaluated the need to study astrocytes in PML pathogenesis and help elucidate mechanisms of astrocyte biology and their role in viral defense. Furthermore, research on astrocyte biology and their role in the CNS related to CNS disorders has dramatically increased over the past 25 years (138), especially true concerning neuroinvasive viruses and neurodegenerative disorders from a viral infection like SARS-CoV-2 (139). For example, more than 35% of patients with COVID-19 develop neurological symptoms (140). Current research suggests that this is not from direct virus infection but rather systemic inflammation, where astrocytes play a crucial role (139).

Astrocytes and the Host Defense

Astrocytes are the most abundant glial cell type in the brain with many important roles in the CNS, including the support of myelination (141–143). Historically, the role in astrocytes regarding neurodegenerative diseases and how they were involved was limited, considering they were only significant in supporting neural tissue and were used as a marker for diseased tissue (144). However, research in recent years, have greatly expanded how essential astrocytes are in the healthy CNS, the primary role in disease processes, including the role in the pathology of a disease, and how they respond to viral infection (144–149).

There are two main astrocyte morphologies found in the CNS, protoplasmic and fibrous astrocytes. Protoplasmic astrocytes are in the gray matter and display many major branches from the

astrocyte soma, with numerous branchlets (150), while fibrous astrocytes are found throughout white matter and have straight, long processes which contain less branches (141). Glial fibrillary acid protein (GFAP) has been a well-used marker to determine the population of protoplasmic astrocytes, however GFAP does have limitations, like not being able to determine non-reactive astrocytes (144). Additional markers, such as Aldehyde dehydrogenase 1 family, member L1 (ALDH1L1) is another astrocyte marker, and unlike GFAP, has a broader pattern of expression in astrocytes (151). Reactive astrocytes are a state in which these cells induce a range of significant molecular, cellular, and functional changes from inter- and intra-cellular signals (144, 152). These changes can result in both gain and loss of functions which can result in either beneficial or detrimental impacts to surrounding neural and non-neural cells (144, 152). An example of this, are reactive astrocytes that play essential roles in regulating CNS inflammation (152). Recent research has demonstrated that reactive astrocytes can exert both pro-inflammatory and anti-inflammatory signals (153, 154). Interestingly, the dynamics between these conflicting responses in the CNS can be unraveled by temporal and spatial regulation; reactive astrocytes may exert pro-inflammatory roles early during response, directly within the lesion, and anti-inflammatory roles later, between lesions and healthy tissue (148, 152).

Astrocytes are also prominent cells in the CNS during viral infection. These viruses include flaviviruses, such as West Nile Virus (WNV) and Zika Virus (ZIKV), and other viruses, like human herpes virus 6, human T-lymphotropic virus type-1, and HIV-1 (155–159). In HIV-1 infection, astrocytes are not the primary cell type infected by the virus; however, they contribute to neurotoxicity and disease pathogenesis from the crosstalk of astrocytes with microglia (155, 160). When astrocytic coinfection is observed, such as HIV-1 and JCPyV, severe disease pathogenesis ensues (161).

Astrocytes in JCPyV infection

PML is the result of demyelination caused by the lytic destruction of oligodendrocytes, but in addition to this, neuroimaging findings also consistently illustrate, giant, bizarre astrocytes in PML pathology (162). As previously mentioned, astrocytes are thought to be a main target of JC polyomavirus, acting as reservoirs, during infection (68). Interestingly, this transformation of astrocytes during viral infection may be a novel mechanism, in which this change in morphology is from the response to T cell attack from immunological synapses (163) potentially clearing infected cells (163, 164). However, more research is needed to determine if this mechanism is occurring in JCPyV infection of astrocytes.

Overall, research on JCPyV infection in astrocytes is limited, yet there are a few notable studies. One of the first studies using progenitor cell-derived astrocytes determined that cell death from JCPyV, was caused by necrosis and not by apoptotic pathways (165). Another study illustrated numerous genes involved including NFIX, during the differentiation of brain-derived multipotential CNS progenitor cells (NPCs) into progenitor-derived astrocytes (PDAs) (166). Interestingly, the authors also examined GFAP expression, and observed that expression of GFAP could serve as a marker for productive JCPyV infection, induced by the changing transcriptional environment (166). An alternative hypothesis could be that astrocytes may be inducing a reactive state from JCPyV infection, as GFAP is also a well-known marker for reactive astrocytes (144). Recently, JCPyV DNA replication was observed in astrocytes, demonstrating that host DNA damage occurred at sites of replication, and there was an observed delay or cessation in viral DNA replication in infected astrocytes (167). In summary, research on astrocytes, and specifically reactive astrocytes, has become more robust in recent years. However, there are many challenges to extrapolating that to JCPyV infection, mainly due to a lack of a tractable animal model to study astrocytic infection and how it contributes to PML pathology.

Animal Models and Primary Cell Models to Study PML

Over the decades, there have been numerous experimental animal models to study JCPyV pathogenesis, but none were able to recapitulate the clinical symptoms of PML. One of the largest contributors to this, was that nonhuman cells lacked the appropriate host factors to bind to the NCCR to initiate transcription of the late genes to complete the infectious cycle (168). Most notably, in recent animal models, including Syrian golden hamsters (169, 170), owl monkeys, or squirrel monkeys, JCPyV infection resulted in tumorigenesis, contributed to the JCPyV protein, T Ag (171–174). The greatest success was demonstrated by developing animal models that included engrafted human cells and humanized or weakened immune systems (68, 175). For example, a model has been generated with neonatal mice engrafted with human glial progenitor cells that became humanized with age and immunodeficient mice, reconstituted with positive human fetal live $CD34^+$ cells (68, 175). These humanized models highlighted the importance of astrocytes during JCPyV infection, and in contrast oligodendrocytes were infected in a delayed manner and are not required for viral propagation and spread (68).

Due to these challenges, our understanding of JCPyV infection has been limited to *in vitro* approaches. SVGAs have been an important model cell line, being implemented in numerous studies and significantly advancing JCPyV research, but due to their transformed characteristics, it is difficult to make direct comparisons to JCPyV infection in primary cell types. Primary normal human astrocytes (NHAs) have been used to compare JCPyV infection to SVGAs, where a delayed infectious cycle was observed in NHAs (130). The expression of SV40 T Ag enhanced JCPyV infection, as NHAs expressing SV40 T Ag (NHA-Ts) demonstrated comparable levels of the late viral protein observed in SVGAs (130). Unfortunately, SV40 T Ag can impact many aspects of the normal cellular functions and confound what is happening during JCPyV infection. To broadly understand the cellular impacts of viral infection and

compare it to an immortalized cell line, bioinformatics, specifically RNA sequencing, can be employed to determine the host transcriptome profile.

NGS and other Bioinformatic Tools to Study Virus Infection

Next-generation sequencing (NGS) has completely revolutionized the way we approach biomedical science, even emerging as promising strategies for detection of novel viruses (176, 177). This includes even many more PyVs, a diverse group of viruses, of which 14 PyVs are of human origin and in recent years, NGS contributed to the discovery of Merkel cell polyomavirus (MCPyV), MW polyomavirus (MWPyV), MX polyomavirus (MXPyV), Human polyomavirus 9 (HPyV9) and Human polyomavirus 10 (HPyV10) (178–182). One method for NGS is using Illumina sequencing. Illumina sequencing works in a few steps. First input DNA (or cDNA) is randomly fragmented, size-fractionated and ligated to adapters. Next, these modified DNA fragments are annealed onto a glass plate that is precoated with oligos, which are complementary to adapters, and allow the template DNA to bind to these oligos and is the basis for amplification (183). Amplification occurs through a process called “bridge amplification,” in which the adapters on both ends of the template DNA bind to the oligo primers on the slide (183). Through successive rounds of PCR, clusters of these amplified molecules appear and serve as clones for sequencing using chain terminators. Unique with Illumina sequencing, these terminators are fluorescently labelled and reversible, so each single nucleotide base incorporated, temporarily terminates the reaction. During this time, a high-resolution digital imager captures the nucleotide being incorporated in each DNA clonal cluster. Finally, once the image is taken, the terminator is removed, allowing the DNA template to be extended again in the next round of PCR, until this occurs to almost all the molecules (176).

Other than genome sequencing, that was used to discover PyVs, we can also use NGS to determine the transcriptomic profile, or measuring mRNA, to determine host gene expression during

viral infection. This method called RNA-sequencing (RNA-seq) (184, 185) determines the host transcriptomic profile by isolating RNA and removing rRNA by selecting for polyadenylated RNA or removing rRNA with antisense oligos. cDNA is synthesized and methods such as Illumina sequencing can be used to determine the nucleotide base pairs. Analysis of RNA-seq data begins with mapping the newly sequenced reads to a reference genome, using programs like HTSeq (186). Statistical analyses determining the read counts per gene as well as quantifying relative levels of expression can be performed using R, specifically using the statistical package edgeR (187, 188). This technique has been used to study many virus-host interactions, including Epstein-Barr virus (EBV) (189), human cytomegalovirus (HCMV) (190), and polyomaviruses JCPyV and BKPyV (191). Specifically, with JCPyV and BKPyV, RNA-seq was performed to determine host gene expression in a primary kidney cell line. BKPyV is like JCPyV except in immunosuppressed hosts, specifically individuals who received kidney transplants, BKPyV causes disease in the kidneys (118). RNA-seq elucidated that JCPyV does not cause disease in the kidneys, rather a persistent infection in the kidneys, mainly due to the host immune system inducing an IFN-β response, not observed in BKPyV infection (191). Overall, RNA-seq can determine viral-host interaction, but paired with other bioinformatics techniques and databases, we can also determine the cellular signaling pathways involved during JCPyV infection.

Cellular Pathways Targeted by JCPyV

DNA viruses need to hijack cellular pathways to be transported to the nucleus and to accomplish viral DNA replication. These pathways are essential in cell proliferation, differentiation, and survival; however, the virus uses these cellular functions to drive the viral infectious cycle to completion. Two pathways that JCPyV takes advantage of are the mitogen-activated protein kinase, extracellular signal-regulated kinase (MAPK/ERK) pathway, and the phosphoinositide 3-kinase (PI3K)/AKT/ mechanistic target of rapamycin (mTOR) signaling pathway as illustrated in Figure 1.4 (94, 192–196).

The MAPK/ERK Pathway

The MAPK/ERK pathway is a tightly controlled pathway that, through a series of phosphorylation events involving four major protein kinases Ras, Raf, MEK and ERK, can influence cell proliferation, differentiation, and survival (197). Upon extracellular signaling, the GTPase Ras binds to Raf, which phosphorylates MEK1 and MEK2 (192, 198–200), which in turn, phosphorylates ERK1 and ERK2 (201–203). Phosphorylated ERK1/2 is then translocated into the nucleus to regulate transcription factors important in cellular functions and involved in JCPyV infection, including NFAT4, SMADs 2 and 4, and cMyc (101, 202, 204, 205). Many viruses hijack this pathway to reprogram the cell and support viral infection (193, 206–208). However, given the importance of this pathway in cellular fate, it is also tightly controlled. A family of protein tyrosine phosphatases, dual specificity phosphatases (DUSPs), strongly regulate and deactivate MAPK signaling (209–212), specifically, DUSP1 and DUSP6. DUSP6 is a cytoplasmic phosphatase that inhibits ERK1/2 phosphorylation (213) while DUSP1 is found in the nucleus and binds to JNK, p38, and ERK1/2, leading to the dephosphorylation and inactivation of these kinases (212). Moreover, ERK phosphorylation can be sustained in the cell following DUSP1 degradation via the ubiquitin/proteasome pathway (214–216). These mechanisms are crucial for cellular homeostasis, however, are also susceptible during virus infection.

Numerous viruses use the MAPK/ERK pathway to establish infection including EBV, vaccinia virus (VACV), hepatitis B virus (HBV) and PyVs, like JCPyV and BKPyV (217). Research has demonstrated that JCPyV uses the MAPK/ERK pathway in both SVGAs and a primary kidney cell line, highlighting the importance of this pathway across cell types (193). Additionally, ERK and MEK were both phosphorylated as little as 15 minutes post infection in SVGAs (94, 193, 205). Along with the MAPK/ERK pathway, DUSPs have also been implicated in viral infection. DUSP1 is important in regulating the MAPK pathway but is also involved in the inflammatory response (218). Research has demonstrated that knockdown of the protein can reduce hepatitis C virus (HCV) infection, as it promoted the induction of

interferon stimulated genes (ISGs) (219). As previously mentioned, astrocytes play a key role in the inflammatory response, producing chemokines and cytokines upon cellular stress (145, 220) and research has already demonstrated that JCPyV persists in the kidneys due to IFN response (191). Thus, the MAPK/ERK pathway and the expression of DUSP1 during JCPyV infection of astrocytes is an attractive mechanism for viral infection and astrocytic host defenses.

The PI3K/AKT/mTor Pathway

Comparable to the MAPK/ERK pathway, the PI3K/AKT/mTor signaling pathway is important in cell growth and survival (221–227). The regulation of the PI3K/AKT/mTor signaling pathway is slightly more complex compared to the MAPK/ERK pathway, divided into the PI3K pathway and the downstream impacts AKT and mTor (228, 229). PI3Ks are divided into three classes, (class I, class II, and class III) where the most well studied are class I. Class I can be further divided into class IA and class IB, based on how they are activated at the cellular surface. Class IA PI3Ks are activated by receptor tyrosine kinases (RTKs), G protein-coupled receptors (GPCRs), and Ras. While Class IB PI3Ks are only activated by GPCRs, consisting of the subunit PI3Kγ (230). Following uptake of extracellular signals and the utilization of a GPCR, the PI3K subunits couples with the receptor, activating the catalytic subunit, and PIP2 is converted to PIP3, which recruits downstream targets, such as AKT (231). Subsequently, AKT has numerous downstream targets, including the Forkhead family (FOX) of transcription factors, important in cell proliferation, apoptosis, and differentiation (232, 233), glycogen synthase kinase-3 (GSK-3), and mTOR, critical in regulating cell growth and proliferation (234). mTOR includes both mTOR complex 1 (mTORC1) and mTORC2. The functions of mTORC1 include cell growth and energy metabolism, while mTORC2 is involved in cytoskeleton formation and cell survival (235, 236). mTORC1 activation occurs directly through AKT, while mTORC2 is activated upon the phosphorylation of subunit SIN1 by AKT,

activating mTORC2 through a positive feedback loop (237). Additionally, mTORC2 can also activate AKT to regulate cell survival, migration, and cytoskeletal organization (238).

Like the MAPK/ERK pathway, research has also demonstrated that the PI3K/AKT/mTOR signaling pathway is involved during JCPyV infection (194–196); however, the research is conflicting, most likely due to the immortalization characteristics of the cell (194, 195, 239, 240). mTor inhibitors, such as rapamycin, increased expression of JCPyV T Ag in an immortalized kidney cell line, human embryonic kidney (HEK) 293 cells (195), while an AKT inhibitor, MK2206, reduced JCPyV DNA replication in an oligodendrocyte cell line (194). Additionally, PI3Kγ has also been implicated during JCPyV infection in SVGAs (196). Targeting PI3γ reduced JCPyV infection however this kinase is activated by GPCRs and GPCRs, specifically serotonin 5-hydroxytryptamine (5-HT) receptors are required for JCPyV internalization (91, 92, 241), thus additional studies are warranted to determine if the other PI3Ks are involved as they are activated by RTKs and Ras.

Consequences of Immortalization on Signaling Pathways and JCPyV infection

Immortalization of cells can be accomplished through recombinant DNA, such as a plasmid or viral vectors expressing transforming proteins, like SV40 T Ag or adenovirus E1 A (242). Overexpression of these oncogenes promote DNA replication through interfering with the cell cycle, enabling a continuous cell line to be established (242). Although cells expressing SV40 T Ag allows us to study JCPyV infection *in vitro* more proficiently as it supports higher levels of JCPyV production, SV40 T Ag is also known to dysregulate the cell cycle which can activate cellular pathways that can potentially confound mechanisms of JCPyV infection (122, 123). Research has demonstrated that SV40 T Ag can activate the AKT signaling pathway in *ts*13 cells, inhibiting apoptosis, and directly activating AKT in U2OS cells (243, 244). Due to these potential confounding measures and initial observations that illustrated differences in the cell cycle progression between primary and transformed cells (130), it is important to validate and

elucidate the involvement of cellular pathways during JCPyV infection using primary cell lines, as transformation alters metabolic pathways and signal transduction within those pathways (245, 246).

Crosstalk between MAPK/ERK and PI3K/AKT/mTOR Signaling Pathways

In addition to viruses hijacking cellular pathways to establish infection and activating numerous kinases, these kinases can also exhibit crosstalk between signaling pathways. This can be demonstrated during inhibition of one pathway and a secondary pathway compensating for the loss. For example, treatment of cells with MEK inhibitors, such as U0126, results in increased AKT activity in various cell types (247–249). The MAPK/ERK pathway can interact with the AKT signaling pathway (250) to induce cellular transformation and survival (221, 251). Furthermore, the most prominent kinase in these pathways is Ras, which can activate the PI3K complex (252) and can positively impact the ERK1/2 cascade (253, 254). AKT can also directly phosphorylate B-Raf and C-Raf, inhibiting the scaffolding protein 14-3-3 and directly activating the ERK1/2 cascade (255–260). Recent evidence has also suggested a direct interaction of MEK1 and MEK2 with AKT, leading to the phosphorylation of the transcription factor FOXO1 (261). These interactions were important in cell migration and adhesion (261). Overall cellular pathways are complex, interacting with each other to provide synergistic effects or impacting the strength and duration of downstream signals, which provides further difficulty when studying how cellular pathways are involved to establish infection in the cell.

Summary

JCPyV has successfully co-evolved with the human species, establishing infection in up to 80% of the population. Unfortunately, the virus can reactivate and spread to the CNS when individuals are immunosuppressed, causing the fatal disease PML. Essential questions, like how reactivation occurs and how the virus can establish infection in the CNS, specifically in astrocytes, remain unanswered. One of

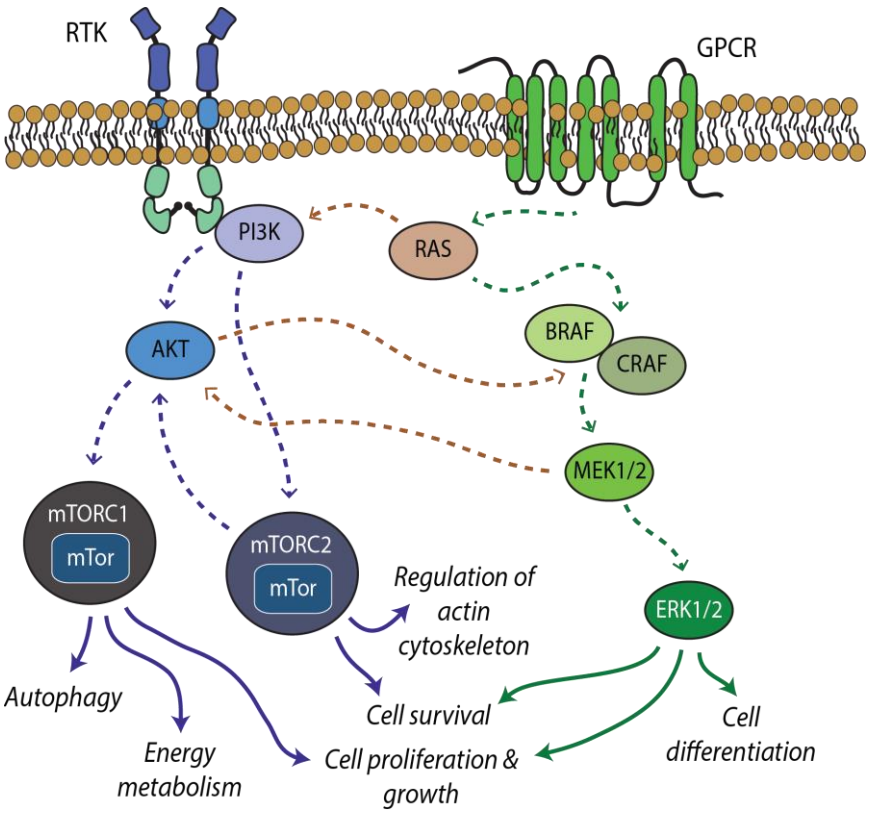

Figure 1.4. Schematic of the PI3K/AKT/mTor and MAPK/ERK signaling pathways. A simplified version of the proteins involved in the MAPK/ERK (green) and PI3K/AKT/mTor signaling pathway (blue) and the interactions between the two pathways (orange), and the downstream cellular functions. RTK, receptor tyrosine kinase; GPCR, G protein-coupled receptor; PI3K, phosphoinositide 3-kinase; mTor, mechanistic target of rapamycin; Ras, Rat sarcoma; BARF, B Rapidly Accelerated Fibrosarcoma; CRAF, C Rapidly Accelerated Fibrosarcoma; MEK1/2, Mitogen-activated protein kinase kinase 1/2; ERK1/2, extracellular signal-regulated kinase 1/2.

the most significant challenges is a tractable animal model to study JCPyV infection. Thus, primary cell models are an accurate method to understand JCPyV infection. Using RNA-seq and additional bioinformatics techniques, my research compared JCPyV infection in primary astrocytes to a more well-studied but immortalized cell model of infection. Overall, this approach was used to validate and elucidate cellular pathways and additional mechanisms that JCPyV uses to successfully establish astrocytic infection and can facilitate future research to address therapeutics for this deadly disease.

CHAPTER 2

JC POLYOMAVIRUS INFECTION REVEALS DELAYED PROGRESSION OF THE INFECTIOUS CYCLE IN NORMAL HUMAN ASTROCYTES

This chapter represents a modified form of the published work from: Wilczek MP, DuShane JK, Armstrong FJ, Maginnis MS. 2019. JC polyomavirus infection reveals delayed progression of the infectious cycle in normal human astrocytes. J Virol https://doi.org/10.1128/jvi.01331-19.

Introduction

Progressive multifocal leukoencephalopathy (PML) is a fatal, demyelinating disease caused by the neuroinvasive pathogen, JC polyomavirus (JCPyV) (60, 262). JCPyV resides in the kidneys in 50 to 80% of the healthy adult population, causing an asymptomatic infection (28, 30, 46, 263, 264). During immunosuppression, JCPyV can reactivate and lead to the development of PML in the central nervous system (CNS) (59, 264, 265). Although rare, individuals who are HIV-1 positive (60, 71) and those using immunomodulatory therapies for immune-mediated diseases (75, 266, 267), such as natalizumab for multiple sclerosis, are at an increased risk for PML development (75, 76). While experimental treatments in development have led to some clinical improvements in patients, the current standard is treatment of the underlying immunosuppression and supportive care (268–270). Successful treatment of the immunosuppression has improved the one-year PML survival rates, which range from ~20% in natalizumab-associated PML to 50-80% in HIV-associated PML (268, 270). Although there is no cure for PML, patients can survive up to 15 years with the disease, albeit with significant morbidity including neurological symptoms that range from mild to severe dysfunction (268, 271).

In the CNS, the virus primarily targets two types of glial cells, astrocytes and oligodendrocytes (63, 272, 273). Clinical patient samples have indicated that myelin-producing oligodendrocytes are

targeted by the virus, leading to demyelination of the CNS and onset of PML. However, the role of astrocytes in JCPyV infection and PML remains unclear (63, 272, 273). Questions underlying astrocytic infection, including whether astrocytes provide protection during PML pathogenesis or whether astrocytes support a favorable environment for viral replication, are not clearly understood (274). While cell culture models have provided significant advances to the field, limitations include differences in primary versus immortalized cell types that could confound comparisons to disease pathogenesis in vivo. Thus, understanding the JCPyV-host cell interactions and the viral infectious cycle in biologically relevant primary astrocytes is critical to better understand JCPyV pathogenesis and to develop therapies for PML.

JCPyV pathogenesis is the result of the virus hijacking host cell machinery, and the temporal regulation of the infectious cycle in the nucleus is carefully orchestrated by numerous host cell transcription factors; this, in part, significantly contributes to the unique host and cellular tropism of the virus. JCPyV is a small, non-enveloped double stranded DNA virus, that is ~5100 base pairs in length (86, 87). The genome is organized into three regions: the regulatory region, or noncoding control region (NCCR) containing the origin of replication, TATA box, and enhancer elements, and two bidirectional coding regions that encode for the early genes and late genes (47). Isolates of JCPyV from PML patients include naturally occurring variants, like Mad-1 and Mad-4, that all have this general genome composition, with most of the differences displayed in the NCCR. For example, the NCCR of the Mad-4 variant contains a 19-bp deletion and only one late-proximal TATA box compared to the Mad-1 variant, which contains duplicate TATA boxes and an enhancer element (41). There are modified variants as well, including the Mad-1/SVEΔ, a laboratory-derived variant, with improved infectivity in cell culture due to insertion of the SV40 enhancer (275).

For productive viral replication to occur in the nucleus, many host transcription factors, including nuclear factor kappa-light-chain-enhancer of activated B cells (NF-κB) (98, 99), Spi-B transcription factor (SpiB) (100), and in glial cells, nuclear factor of activated T-cells 4 (NFAT4) (276) and subtypes of the nuclear factor-1 (NF-1) family (277, 278) bind to the regulatory region to initiate early gene transcription. This results in the production of the virus-origin binding protein, large Tumor antigen (T Ag) and other proteins needed to transform the cell into a "virus factory." These early gene products orchestrate this transformation by binding to retinoblastoma (Rb) (279), consequently driving the cell into S phase, sequestering p53, and thus blocking apoptotic pathways (280). T Ag also functions as a DNA helicase to unwind the viral DNA for replication (281). With increasing viral early gene transcript concentration within the nucleus, the infectious cycle undergoes a "switch" towards viral DNA replication and late gene transcription, producing agnoprotein and viral protein 1 (VP1), VP2, and VP3 (282). These viral proteins encapsidate the newly replicated, viral DNA. Understanding the infectious cycle in human cells that contribute to PML pathogenesis is necessary to design therapeutics and prevent disease, but unfortunately there are not many biologically representative cell culture models or *in vivo* models that outline JCPyV infection in astrocytes or oligodendrocytes.

While experimental animal models to study JCPyV pathogenesis have been attempted, the most tractable model systems have not been able to recapitulate the clinical symptoms of PML. Early animal models, including Syrian golden hamsters (170, 283), owl monkeys, or squirrel monkeys resulted in tumorigenesis upon JCPyV infection due to the oncogenic potential of the JCPyV protein, T Ag (171, 284–286). These studies reinforced the fact that nonhuman cells lacked the appropriate host factors for the virus to initiate transcription of the late genes in order to complete the infectious cycle (287), thus resulting in tumor formation. To overcome this challenge, recently developed animal models have included engrafted human cells and humanized or weakened immune systems (175, 273). In the most-recently reported animal model for PML pathogenesis, Kondo et al. (273) developed a humanized

mouse model with engrafted glial progenitor cells (GPCs). Their results, unlike other models, highlighted that the primary cells targeted by JCPyV were GPCs and astrocytes, demonstrating that astrocytes are the main target in PML pathogenesis (273). In contrast, oligodendrocytes were infected in a delayed manner and are not required for viral propagation and spread (273), which represents a significant paradigm shift in the understanding of PML development within the field. This research illuminated the importance of astrocytic infection in PML, which is currently understudied in the field.

There are a few reports of JCPyV infection of primary astrocytes in the literature. In 2004, progenitor cell-derived astrocytes were used to understand their capacity to support JCPyV infection, concluding that cell death was the result of necrosis and not by inducing apoptotic pathways (288). Further research validated their susceptibility to JCPyV infection, in contrast to progenitor cells in which infection was lower (289). A 2003 microarray study revealed 355 genes upregulated and 130 downregulated during infection of primary human astrocytes, leading to further examination of specific proteins such as Grb-2, cyclin A, cyclin E, PAK2, and TGFβ-R1 in JCPyV infection (274). Another microarray analysis in 2013, examined the genes influenced by JCPyV infection during the differentiation of brain-derived multipotential CNS progenitor cells (NPCs) into progenitor-derived astrocytes (PDAs). Their findings highlighted transcription factors including Nuclear Factor I (NFI) -X, NFI-A, c-jun, and c-fos that promoted JCPyV infection during the differentiation to PDAs (290). A recent study examined JCPyV DNA replication in primary astrocytes, SVGAs, and primary human choroid plexus cells (167). Erickson and Garcea (167) demonstrated that replication in the nucleus of primary astrocytes was like that of other polyomaviruses, recruiting similar host DNA damage response proteins to sites of replication. The authors concluded that there was either a delay or cessation in viral DNA replication in infected astrocytes (167).

The purpose of this study was to extend from previously published research to improve our understanding of JCPyV infectivity in primary human astrocytes, while comparing infection to SVGAs, a mixed glial cell model widely used to study JCPyV. SVGAs, which constitutively express simian virus 40 (SV40) T Ag, were developed to study JCPyV infection *in vitro* (291). Due to the challenges of generating an animal model, SVGAs have been an important model cell line in the field, being implemented in numerous studies and significantly advancing JCPyV research, but due to their transformed characteristics, it is difficult to make direct comparisons to JCPyV infection in primary cell types. This study establishes a foundation for future JCPyV research by using primary human astrocytes, which may reflect a more accurate approach to *in vitro* infection studies. We demonstrate that normal human astrocytes (NHAs) can be readily infected with JCPyV and serve as an effective model to study JCPyV infection. NHAs demonstrate a delayed infectious cycle in comparison to the progression of the infectious cycle in SVGAs, suggesting that infection may proceed in a delayed manner in primary cells. Overexpression of SV40 T Ag in NHAs revealed that T Ag can drive the infectious cycle and induce expression of cyclins, which serve as a marker of cell cycle progression. Lastly, with advancements in culturing primary cells, the experiments and methodologies used in this study can be extrapolated to other models used to understand viral infections. By performing single cell analyses, examining multiple proteins in one cell, and performing statistical procedures like dimensionality reduction, one can strengthen *in vitro* studies, especially where animal models are lacking or are difficult to understand and develop.

Materials and Methods

Cells, plasmids, and viruses

Normal Human Astrocytes (NHAs) (passage 1 [P1]) were obtained from Lonza (product no. CC-2565) and maintained in the Astrocyte Growth Medium (AGM) supplemented with the AGM

SingleQuots Supplements (product no. CC-3186) and 1% penicillin-streptomycin (P/S) (Mediatech, Inc.). NHAs were provided with Lonza's Certificate of Analysis. Donor was a 19-week gestation female who had no detected levels of HIV, hepatitis B virus (HBV) and hepatitis C virus (HCV). Cells were most likely isolated from the cerebrum and associated structures to the cerebrum, and thus most likely represent primarily Type I astrocytes. NHAs were used at low passages (P3 to P8) and subcultured according to Lonza instructions. SVGAs and HEKs, generously provided by the Atwood Laboratory (Brown University) (291) were cultured in complete minimum essential medium (MEM) (Corning) and complete Dulbecco's modified Eagle medium (DMEM) (Corning), respectively, with 10% fetal bovine serum (FBS), 1% P/S and 0.2% Plasmocin prophylactic (InvivoGen).

NHAs were transformed with SV40 large T Ag (NHA-Ts) by transfecting them with the origin-defective mutant of SV40 inserted in the pMK16 vector (pMK16) (provided by the Atwood Laboratory, Brown University). NHAs (P8) were seeded at 5,000 cells/cm^2 in a 25-cm^2 flask and transfected with 1 μg of pMK16 containing the SV40 ori^- mutant using Fugene (Roche) at a 1.5:1 ratio (Fugene/DNA) and incubated at 37^{o}C. The medium was replaced with fresh AGM supplemented with the SingleQuots Supplements every two days, and after 2 weeks proliferation of cells in areas of the flask was clear. The cells were passaged, and the AGM media was replaced with MEM with 1% P/S and 16% FBS. To validate that NHA-Ts express SV40 Large T Ag, cells were fixed and stained by indirect immunofluorescence using the SV40 T Ag specific antibody, AB2 (Calbiochem; 1:50). 100% of the cells displayed nuclear staining for SV40 T Ag, which was validated before and after experiments were performed. NHAs, SVGAs, and NHA-Ts were grown in a humidified incubator at 37^{o}C with 5% CO_2.

The generation and production of purified JCPyV strain Mad-1, Mad-4, and Mad-1/SVEΔ was described previously (93), and were kindly provided by the Atwood laboratory (Brown University) or purchased through the ATCC (Mad-4).

JCPyV infection

NHAs, NHA-Ts, and SVGAs were seeded into 96-well plates with 10,400 cells/well (~70% confluence). Cells were infected (multiplicity of infection [MOI] as indicated in figure legends) with 42 µl/well of the respective cell media at 37^{o}C for 1 h. After infection, the cells were fed with 100 µl/well and incubated at 37^{o}C for the duration of the infection. At the indicated time points, cells were fixed and stained for both viral proteins, T Ag and VP1. Additionally, for long-term experiments (Fig. 4) supernatant was collected from each well to be subsequently used to inoculate naive SVGAs with 42 µl of supernatant at 37^{o}C for 1 h. After infection with supernatants, cells were incubated at 37^{o}C for 72 h and then fixed and stained by indirect immunofluorescence using VP1-specific antibodies.

Indirect immunofluorescence staining and quantitation of JCPyV infection

Following infection, cells were stained for both viral proteins and host cell proteins at RT. NHAs, NHA-Ts, and SVGAs were washed with 1X PBS then fixed in 4% paraformaldehyde (PFA) for 15 mins and washed with PBS-0.01% Tween, three times. Cells were permeabilized for 15 mins using PBS-0.5% Triton X-100. Following permeabilization, NHAs, NHA-Ts, and SVGAs were blocked in PBS-10% goat serum for 45 mins. Cells were then stained using antibodies specific for viral proteins and host cell proteins for one hour at RT except for antibodies specific for GFAP and ALDH1L1, which were incubated for ~16 hours at 4^{o}C. Cells were subsequently washed three times in PBS- 0.01% Tween (PBS-T) and counterstained with the appropriate secondary antibodies, indicated in Table 2.1. Following primary and secondary incubations, cells were counterstained using 4’,6-diamidino-2-phenylindole (DAPI) at RT for 5 mins and washed with 1X PBS.

To visualize the cells expressing nuclear VP1 or T Ag, a Nikon Eclipse Ti epifluorescence microscope (Micro Video Instruments, Inc.) equipped with a 20x objective was utilized. The percentage of cells infected was determined by counting the number of T Ag- or VP1-positive nuclei divided by the

number of DAPI-positive nuclei for 5 fields of view/ well. DAPI-positive nuclei were determined by using the Nikon NIS-Elements Basic Research software (version 4.50.00, 64 bit). A binary algorithm was generated using the software that separates cells based on intensity, diameter, and circularity in each field of view. At least 3 images/well using a 20x objective, with 1 sec exposure, and 2.2x gain were taken to quantify the relative intensity values of viral protein expression in the nucleus.

TABLE 2.1 Antibodies used in immunofluorescence (IF) and ICW assays.

Protein	1^o antibody (dilution, manufacturer)	2^o antibody (dilution, manufacturer)
JCPyV T Ag	PAB962 (1:5, hybridoma)	anti-mouse Alexa Fluor 594 or anti-mouse Alexa Fluor 588 (1:1000, Thermo Fisher Scientific)
JCPyV VP1	ab34756 (1:1000, abcam)	
SV40 T Ag	AB2 (1:50, Calbiochem)	anti-mouse Alexa Fluor 594 (1:1000, Thermo Fisher Scientific)
Cyclin B1	4138 (1:300; Cell Signaling Technology)	anti-rabbit Alexa Fluor 488 (1:1000, Thermo Fisher Scientific)
Cyclin E	50-9714-80 (2.5 µg/ml, Invitrogen)	--*
GFAP	ab4674 (1:2000, abcam)	Anti-chicken Alexa Fluor 488 (1:1000, Abcam) (IF) or anti-chicken LI-COR 800 (1:12,000) (ICW)
ALDH1L1	19H14L20 (1:100, Invitrogen)	anti-rabbit Alexa Fluor 594 (1:1000, Thermo Fisher Scientific) (IF) or anti-rabbit LI-COR 800 (1:12,000) (ICW)

*, Cyclin E antibody is conjugated to eFluor® 660

In-Cell Western assay and host protein quantification

Cells were seeded in 96-well plates and following fixation, NHAs (P2-P8), SVGAs (P78-P84) and HEKs (P66) were permeabilized with 1X PBS-1% Triton X-100 at RT for 15 min. Cells were incubated with TBS Odyssey Blocking Buffer (Li-Cor) at RT for 1 h. Cells were stained with either antibodies detecting GFAP or ALDH1L1 (Table 2.1) in TBS Odyssey Blocking Buffer at 4^oC for ~16 h while rocking. After primary incubation, cells were washed with PBS-T and incubated with an anti-chicken or anti-rabbit LI-COR 800 secondary antibody (Table 2.1) and CellTag 700 at RT for 1 h. Cells were washed again with PBS-T and aspirated prior to scanning. Plates were imaged using the LI-COR Odyssey CLx Infrared

Imaging system to detect both the 700 and 800 nm intensities. Plates were read at 42 µm resolution, at medium quality, and a 3.0 mm focus offset. After scanning, the 700 and 800 nm channels were aligned using the Image Studio software (version 5.2) and In-Cell Western (ICW) analysis was performed in Image Studio. Subsequently, the ratio of the 800 nm channel (GFAP or ALDH1L1) to the 700 nm channel (CellTag) was determined (292).

Host-cell and viral protein expression by confocal microscopy

Cells were seeded in 96-well, 1.5 glass-bottom plates (CellVis) to 40 to 50% confluence. NHAs were plated in AGM media supplemented with the AGM SingleQuots Supplements, NHA-Ts were plated in MEM, 1% P/S and 16% FBS, and SVGAs were plated in MEM, 1% P/S, and 2% FBS. Following infection (MOI = 1 FFU/cell), cells were incubated for 48, 72, and 96 h. Cells were fixed stained for host cell proteins, cyclin B1 and cyclin E, and viral proteins, T Ag and VP1, as described above. Approximately 30 cells per cell type and time point were imaged expressing no viral protein (mock), T Ag or VP1 (JCPyV-infected), co-expressing cyclin B1 and cyclin E. Images were collected using an Olympus laser scanning confocal microscope (model IX81; Olympus America) with an 60x objective (oil immersion) with Z-stacks for each image and 0.32 µm slice spacing. Fluorescence images were collected using the 488-, 568-, and 647-nm multiline argon lasers.

Image J quantification of host-cell and virus protein

Images were analyzed using ImageJ. For confocal microscopy experiments, Supplemental Figure 1 indicates the workflow performed using ImageJ. Briefly, a z projection taking the average intensity of each z slice (~30 slices) was generated for each image. Each channel of the image was split, and a binary was generated, referred to as a mask, representing the nucleus of the cell (shown below, A). The nucleus was dilated 10 times to encompass the cytoplasm (shown below, B). This region of the cell is an accurate

representation of the cytoplasm because cyclin B1 and cyclin E expression is diffuse and is not localized to one specific region (Figure 2.8A) (293). The image of the dilated mask was subtracted by the nucleus to create a ring-shaped structure (shown below, C). To eliminate non-cell background, a second mask was generated from both cyclin E and cyclin B expression and subtracted by the previous mask, resulting in cytoplasmic regions of interest (ROIs), considering cellular boundaries (shown below, D-F). The mask created for both cyclin E and cyclin B1 expression was not used to quantify cytoplasmic intensity because there was no method to distinctly separate cells and would not result in an accurate representation of the cells being selected. These ROIs were overlaid on the 488 channel (cyclin B1) and the 660 channels (cyclin E) to measure the relative intensity values of cyclin expression in the cytoplasm (shown below, G and H). Equation 2.1 exhibits the derivation of the relative intensity values of the cytoplasm. ROIs were also created from the mask indicating the nucleus (shown below, A) to measure

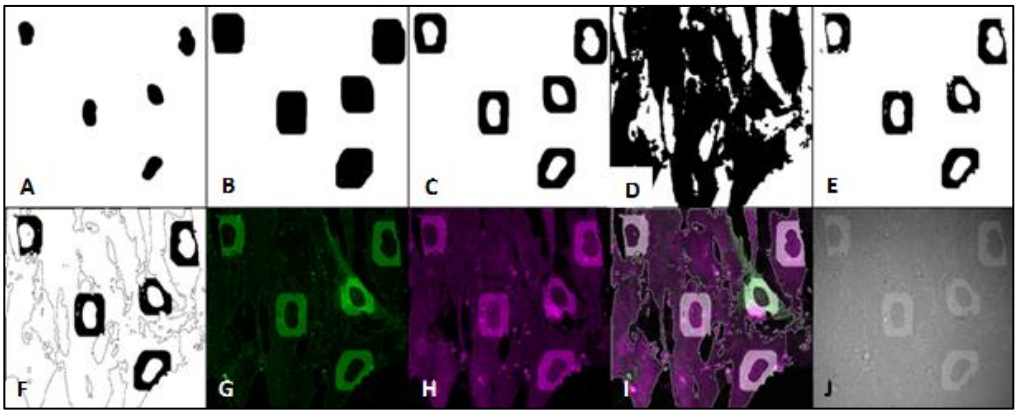

Figure 2.1. Workflow in ImageJ to quantify host cell and virus protein expression. Images from confocal microscopy experiments were imported into ImageJ and intensities determined by this general workflow. First, a binary mask representing the nucleus was generated (A). The nucleus was dilated 10 times to encompass the cytoplasm (B) and the image illustrated in panel A subtracted to generate an outline of the cytoplasm without the nucleus (C). A second mask was generated from both cyclin E and cyclin B expression (D). The mask illustrated in panel D was subtracted from the image illustrated in panel B to create cytoplasmic regions of interest (ROIs), considering cellular boundaries (E and F). These ROIs were overlaid on the 488-nm channel (cyclin B1) and the 660-nm channel (cyclin E) to measure the relative intensities of cyclin expression in the cytoplasm (G and H). Nuclear ROIs were generated from the mask illustrated in panel A, and the nuclear-to-cytoplasmic (N/C) ratio was determined. The image illustrated in panel I represents the merged channels of 488 and 660 nm, and the image illustrated in panel J represents the phase channel (not measured).

relative intensity values of cyclin expression and viral protein expression in infected cells. Finally, the nuclear to cytoplasm (N/C) ratio was determined for each selected cell (Equation 2.2).

$$\text{Cytoplasmic relative intensity} = \frac{[(\text{Dilated nucleus} \times \text{Area of dilated nucleus}) - (\text{nucleus} \times \text{Area of nucleus})]}{\text{whole cell area-nucleus area}} \quad (2.1)$$

$$\text{N:C ratio} = \frac{\text{Nuclear Intensity}}{\text{Cytoplasm relative intensity}} \quad (2.2)$$

Absolute quantification of T Ag and VP1 transcript levels by qPCR

NHAs, NHA-Ts, and SVGAs were plated to 70% confluence in 96 well plates. Media was removed, and cells were infected with JCPyV at a MOI = 0.5 fluorescence forming units (FFU) /cell in 42 µl with the respected cell media and incubated at 37^{o}C for 1 h. After 1 h, cells were fed with 100 µl of the appropriate media and incubated at 37^{o}C for 24, 48, 72, and 96 h. At each time point, cells were washed with 1X PBS then fixed with 4% paraformaldehyde and subsequently stained for JCPyV T Ag, SV40 T Ag, or JCPyV VP1, or separate wells were treated with 50 µl of TRIzol Reagent (Invitrogen) and stored in the -20^{o}C. After validating similar levels of infectivity by immunofluorescence at 48 hpi, cells suspended in TRIzol Reagent were removed from the -20^{o}C and RNA was extracted from each sample with the Direct-zol RNA kits per manufacturers protocol (Zymo Research). All 72 samples (3 cell types, mock and JCPyV infected, in triplicate for three time points) were randomized and prepped for RNA extraction in two separate isolation procedures, ensuring that each group had an even representation of cell type, treatment, and time point (36 samples/ group). RNA was immediately converted to cDNA with the iScript cDNA synthesis kit (Bio-Rad) using 1 µg of RNA. The two groups generated from the RNA extraction were randomly divided into two further groups (ensuring that each group was represented equally) for qPCR analysis of viral transcripts using T Ag and VP1 primers (294) and GAPDH was used for

a housekeeping gene yet was not used in quantification (16 samples/T Ag, VP1, and GAPDH primer set). Briefly, using Hard-Shell 96-well PCR plates (Bio-Rad), each sample contained 150 nM of both forward and reverse primers, 100 ng of cDNA, 5 µl of iQ SYBR Green Supermix (Bio-Rad) and nuclease-free water to a total volume of 10 µl per well. Plates were sealed with Microseal 'B' seal Seals (Bio-Rad) and analysis was performed on a Bio-Rad CFX96 Real-Time System, using Bio-Rad CFX Manager software 3.1. qPCR results for T Ag and VP1 transcript was calculated using absolute quantification. In brief, a standard curve was developed using the JCPyV-pUC19 plasmid, performing 10-fold dilutions to generate 1 to 10^9 copies/µl of the plasmid. Cq values for both T Ag and VP1 was determined at each dilution creating a linear equation from the standard curve. This equation was used to extrapolate the copies/µl of T Ag and VP1 transcript in infected NHAs, NHA-Ts, and SVGAs at each time point, determined from the raw Cq values in each sample. Absolute quantification of viral transcript levels of T Ag and VP1 were determined in triplicate samples from three independent experiments. Statistical significance of the number of copies/µl of viral transcript was determined between cell types at 24, 48, 72, and 96 hpi.

Statistical analysis and graphing in RStudio

A two-sample, student's *t*-test assuming unequal variances was used to compare the means for at least triplicate samples that were normally distributed; a *P* value of <0.05 or <0.01 was considered statistically significant. A one-way analysis of variance (ANOVA) was used to compare two or more samples when the data was normally distributed. The Kruskal-Wallis test was used when comparing the median of more than two samples. Lastly, the Wilcoxon signed rank test was used when comparing two populations that were not normally distributed. All statistical analyses were performed in RStudio (Version 1.2.1335) except the student's *t*-test, which was determined in Microsoft Excel. The Shapiro-Wilk's test and a Q-Q plot was used to determine if populations were normally distributed in RStudio. Principal component analyses (PCA) of the correlation of either T Ag or VP1 expression and both cyclin

B1 and cyclin E expression was determined from z sectioned confocal micrograph images of ~30 cells. Analyses were performed in RStudio using the library "ggfortify" (295) and the library "ggplot2" (296) to interpret the PCA objects. Other plots were also generated using "ggplot2", importing the raw values from excel into RStudio using the library "XLConnect" (297).

Scripts for PCA and ImageJ

Macros for creating masks and quantifying protein expression by relative fluorescence units (RFU) in ImageJ and code for PCA performed in RStudio are supplied upon request.

Results

NHAs display established characteristics of astrocytes

Astrocytes, one of the most abundant glial cells in the brain with many key roles in the CNS including support of myelination (141–143), have been implicated in PML (273), yet are challenging to study due to limited markers. The most commonly used astrocyte marker, glial fibrillary acid protein (GFAP) is a reliable marker for reactive astrocytes yet has limitations (144) as much as 40% of astrocytes can be found negative (298). Aldehyde dehydrogenase 1 family, member L1 (ALDH1L1) is another astrocyte marker, and unlike GFAP, has a broader pattern of expression in astrocytes (151). To characterize NHAs before JCPyV infection, cells were subcultured to determine variability in expression of both astrocyte markers GFAP and ALDH1L1 over time. NHAs (P2 - P8), SVGAs (P78 - P84), and human embryonic kidney 293A cells (HEKs) (P66), a non-glial cell control that expresses low levels of GFAP (299), were plated and fixed and analyzed by indirect immunofluorescence using antibodies targeting both astrocyte markers (Figure 2.2A). NHA morphology is characterized as protoplasmic because they were isolated from gray matter (300). At early passages (P2 to P4) NHAs displayed many major branches from the astrocyte soma, and thousands of branchlets (Figure 2.2A) similar to the findings in other

published research (150). As subculturing continued however, these protoplasmic traits diminished (Figure 2.2A). This is in comparison to ALDH1L1, however, of which expression remained diffuse through continued passages, corroborating the findings in other research (151). In-Cell Western assay (ICW)™ was used to quantify GFAP and ALDH1L1 expression in all three cell types (Figure 2.2B and 1C). GFAP expression decreased in NHAs from P2 to P3 but then remained consistent throughout P8. Levels of GFAP expression was higher in NHAs and SVGAs in comparison to HEKs (Figure 2.2B and 1C). ALDH1L1 expression in NHAs also decreased from P2 to P3 however at less appreciable levels. Both glial cell types however, expressed higher levels of ALDH1L1 compared to the non-glial cell type (Figure 2.2C). These data corroborate a previous report, that GFAP expression in NHAs decreases over time (301) but ALDH1L1 expression remains present (151).

Multiple variants of JCPyV infect NHAs

To determine whether NHAs are permissive to multiple variants of JCPyV, NHAs and SVGAs were infected with Mad-1, Mad-4 and Mad-1/SVEΔ, fixed at 48 and 72 hpi, and stained with antibodies specific for the early viral gene product, T Ag and the late viral gene product, VP1 (Fig. 2). Timepoints correspond to T Ag and VP1 production in SVGAs, respectively, and served as a starting point to understand JCPyV infection in NHAs. Mad-1 and Mad-1/SVEΔ demonstrated an equivalent percentage of cells expressing T Ag in NHAs and SVGAs at 48 hpi (Figure 2.3A and 2B). However, the expression of VP1 in NHAs was significantly lower compared to SVGAs at both 48 and 72 hpi. Infectivity of Mad-4 was lower, but a similar trend was observed with the percentage of NHAs expressing VP1 (Figure 2.3C). This suggests that JCPyV, regardless of variant, can establish infection in NHAs, but the production of late viral proteins is delayed, suggesting a delay in the infectious cycle. Based on similarities with multiple JCPyV variants, Mad-1/SVEΔ was utilized for subsequent experiments due to enhanced infectivity and ease of production.

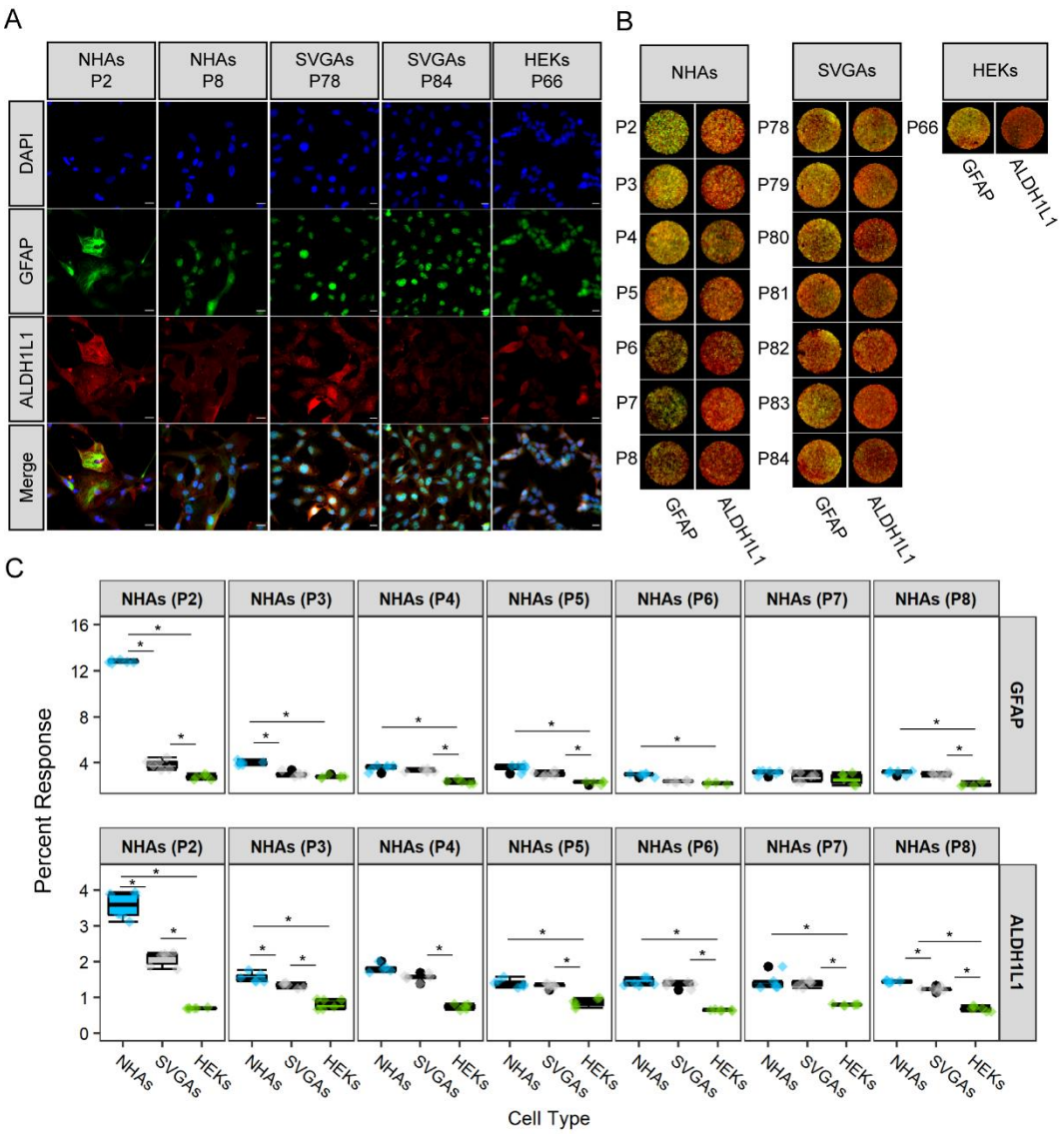

Figure 2.2. NHAs display established characteristics of astrocytes. NHAs and SVGAs (at indicated passages) were plated and fixed for staining using antibodies targeting glial fibrillary acidic protein (GFAP) and aldehyde dehydrogenase family 1, member L1 (ALDH1L1). HEK293A cells (HEKs) were used as a non-glial cell-type control. (A) Representative images of NHAs, SVGAs, and HEKs stained with antibodies specific for GFAP (green) and ALDH1L1 (red); nuclei were counterstained with DAPI (blue). Cells were analyzed by indirect immunofluorescence using an epifluorescence microscope at x40 magnification. Bars = 20 ^{o}m. (B) Cells were plated in 96-well plates, stained using antibodies specific for GFAP or ALDH1L1 (green) or CellTag (red), and analyzed by ICW. (C) Percentage of GFAP orALDH1L1 for each passage was quantitated by ICW signal intensities (GFAP or ALDH1L1/CellTag x 100 = % response) for NHAs (P2to P8), SVGAs (P78 to P84), and HEKs (P66). Box and whisker plots represent the distribution of data from 6 samples, with median values denoted by the black lines and whiskers representing values 1.5 times the distance between the first and third quartiles (interquartile range). Colored diamonds represent individual points for NHAs and SVGAs (6 replicates), and HEKs represent the experimental control, comprising box-and-whisker plots. Outliers are represented by black points. The Kruskal-Wallis test was used to compare all three cell types within each passage analysis. * , $P < 0.01$. Data are representative of three independent experiments.

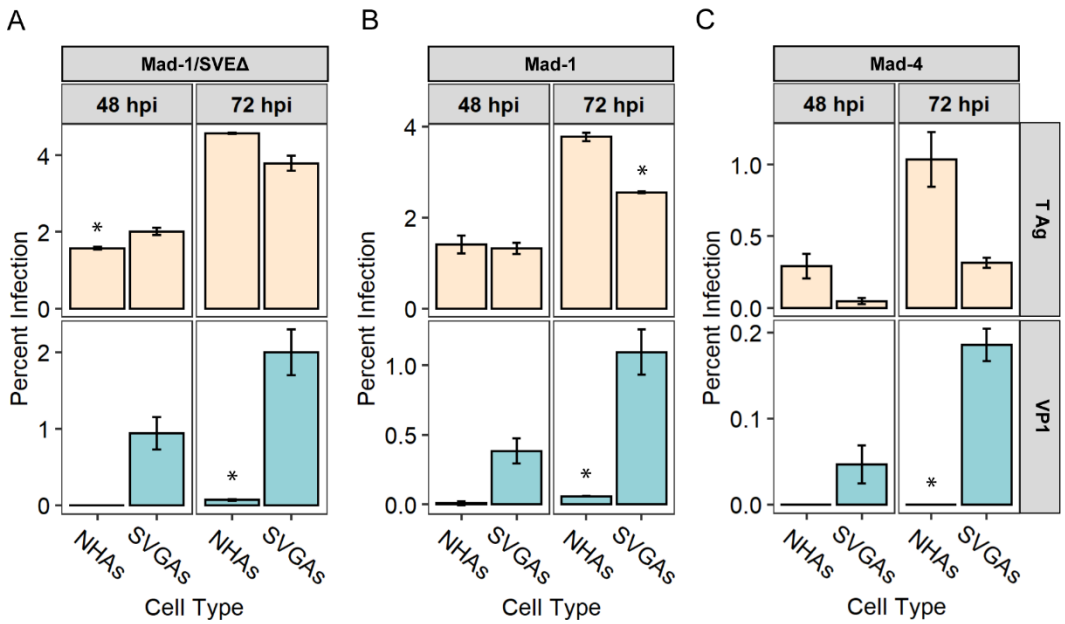

Figure 2.3. Multiple JCPyV strains demonstrate robust T Ag production but delayed production of VP1 in NHAs. NHAs and SVGAs were infected with the Mad-1/SVEΔ (A), Mad-1 (B), and Mad-4 (C) strains of JCPyV at MOIs of 0.5, 0.5, and 0.05 FFU/cell, respectively, and fixed at 48 or 72 hpi. Cells were stained with antibodies specific for the early gene product T Ag and the late gene product VP1 and analyzed by indirect immunofluorescence. Percent infection was determined by counting the number of T Ag- orVP1-positive nuclei divided by the number of DAPI-positive nuclei for five x 20 fields of view for triplicate samples. Data are representative of three individual experiments. Error bars indicate standard deviations (SD). Student's t test was used to determine statistical significance comparing data for NHAs and SVGAs within each time point and viral protein. *, $P < 0.01$.

JCPyV infection of NHAs occurs in a delayed manner independent of MOI

To determine if the delay in infection in NHAs occurs when they are inoculated with increased virus concentrations, NHAs and SVGAs were infected at varying MOIs, fixed at 48 and 72 hpi, and stained with antibodies specific for JCPyV T Ag and VP1 (Figure 2.4A and 3B). At 48 hpi, the percentages of JCPyV-infected NHAs expressing T Ag were comparable to the results for SVGAs, regardless of the MOI utilized. In contrast, VP1 expression was not detectable in NHAs at 48 hpi (Figure 2.4B). At 72 hpi, the percentage of NHAs expressing T Ag continued to increase (Figure 2.4B) yet the number of VP1-positive cells was significantly reduced in comparison to SVGAs (Figure 2.4B). Infecting the NHAs with a MOI ~6, resulted in ~50% of the cells expressing T Ag at 72 hpi, yet this still resulted in less than 3% of cells

expressing VP1 (data not shown). This suggests that JCPyV can establish infection in NHAs, but the production of late viral proteins is prolonged, suggesting a delay in the infectious cycle.

To determine the extent of the delay in VP1 production in infected NHAs, both cell types were infected and analyzed for the production of viral proteins T Ag and VP1 over a long-term time course (12 days) (Figure 2.5A). VP1 expression in NHAs was significantly lower than in SVGAs (Figure 2.5B), despite the increased expression of T Ag in NHAs. However, appreciable amounts of VP1 were detected in NHAs at 12 days postinfection (dpi), suggesting that VP1 production is delayed rather than absent (Figure 2.5A). In SVGAs, at 3 and 7 dpi, 42 to 53% of infected cells expressed VP1, and at 12 dpi, 63% of cells expressed VP1. In NHAs, however, only 4 to 15% of infected cells were expressing VP1at 3 and 7 dpi, and only 40% expressed VP1 at 12 dpi (Figure 2.5B). Finally, to determine the efficiency of viral assembly and release, supernatant was collected at each time point from the infected cells and was then used to inoculate naive SVGAs. Cells were fixed at 3 dpi and stained using a VP1-specific antibody to determine whether the viral particles released into the supernatant were infectious. The results shown in Figure 2.5C illustrate that supernatant collected from SVGAs resulted in a significantly higher percentage of infected cells than supernatant collected from NHAs. By 12 dpi, however, the infectious virus in the supernatant collected from NHAs increased noticeably, resembling the trend observed in the infectivity analysis (Fig. 3). These data suggest that VP1 production in NHAs is significantly delayed before 7 dpi compared to the VP1 production in SVGAs; however, after 7 dpi, levels of VP1 increase, releasing infectious virus particles from the cell.

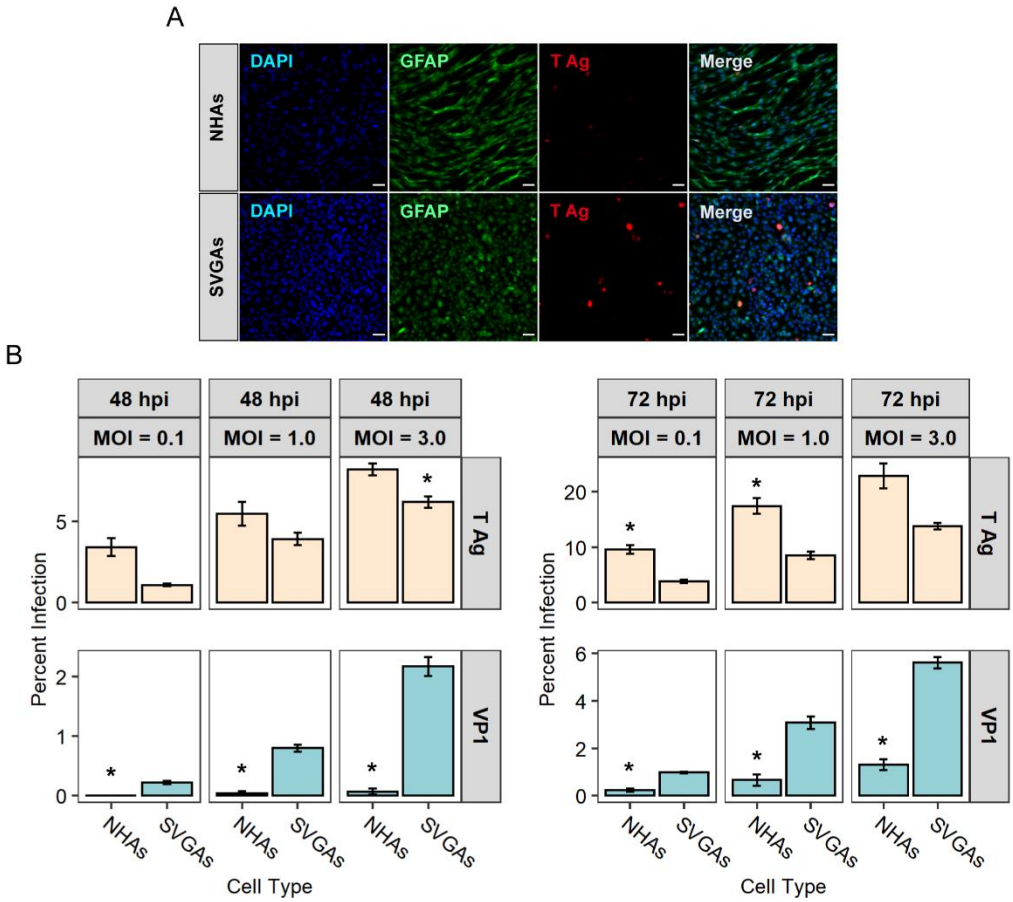

Figure 2.4. Late JCPyV gene products are delayed across a range of MOIs. (A) Representative images of NHAs and SVGAs infected with JCPyV (MOI = 0.1 FFU/cell), fixed at 48 hpi, and stained with antibodies specific for JCPyV T Ag (red)or glial fibrillary acidic protein (GFAP) (green); nuclei were counterstained with DAPI (blue). Cells were analyzed by indirect immunofluorescence using an epifluorescence microscope at x 20 magnification. Bars = 50 µm. (B) NHAs and SVGAs were infected with JCPyV at the indicated MOIs (FFU/cell) and fixed at 48 or 72 hpi. Cells were stained with antibodies specific for the early gene product T Ag and the late gene product VP1. Percent infection was determined by counting the number of T Ag- or VP1-positive nuclei divided by the number of DAPI-positive nuclei for 5 x 20 fields of view for triplicate samples. Data are representative of three individual experiments. Error bars indicate SD. Student's t test was used to determine statistical significance comparing data for NHAs and SVGAs at each respective MOI, within each time point and viral protein. *, $P < 0.01$.

SV40 Large T Ag restores VP1 production in NHAs

SVGAs were developed specifically to support JCPyV infection, through the utilization of the origin-defective mutant of SV40 (291). Constitutive expression of the SV40 Large T Ag in the nucleus allows for efficient transcription and replication of the JCPyV genome during JCPyV infection (119). It is thought that the enhanced efficiency is due to SV40 Large T Ag binding more effectively to the JCPyV

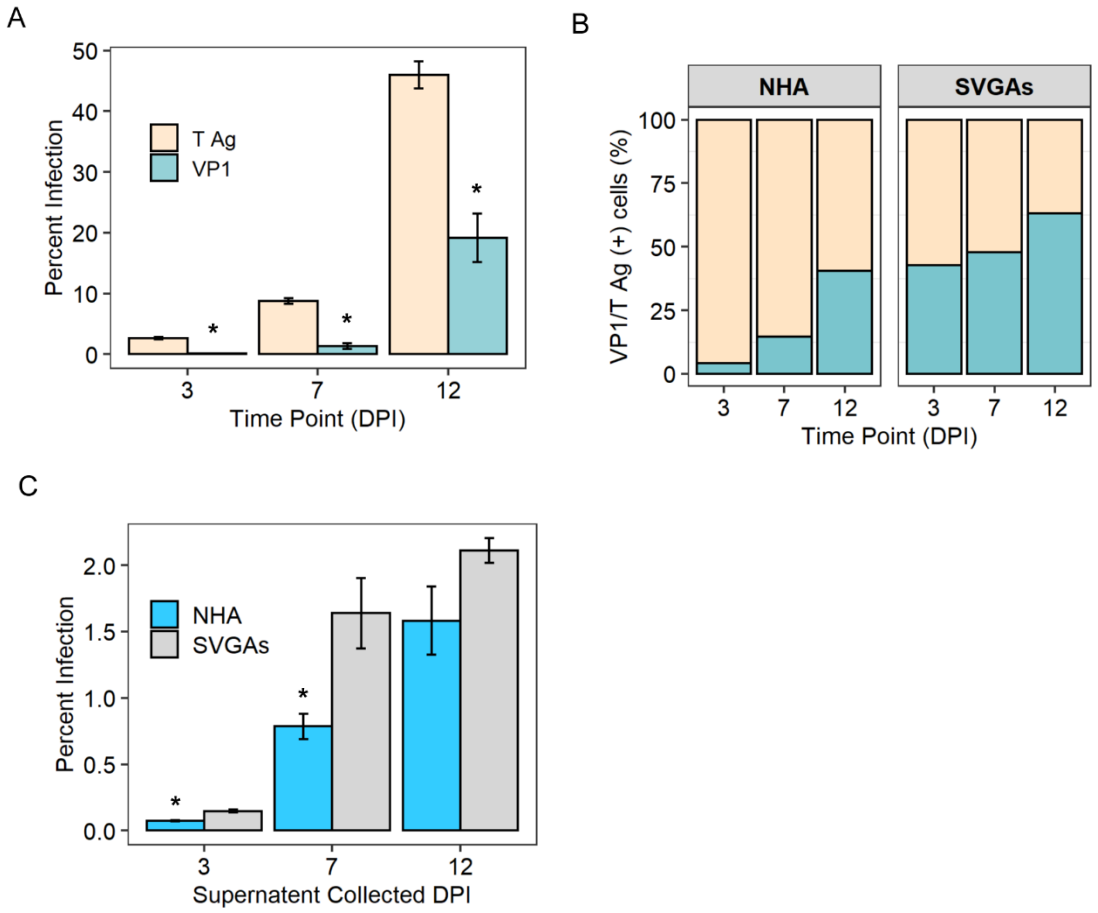

Figure 2.5. The JCPyV infectious cycle is significantly prolonged in primary astrocytes. (A) NHAs were infected with JCPyV (MOI = 0.1 FFU/cell) and fixed at 3, 7, and 12 dpi. Cells were stained with antibodies specific for T Ag and VP1, and percent infection was quantified by indirect immunofluorescence, counting the number of T Ag- or VP1-positive nuclei and dividing by the number of DAPI-positive nuclei for 5 fields of view at x 20 magnification for triplicate samples. (B) The ratios of VP1- to T Ag-positive cells from NHAs in the experiment (results are shown in panel A) and from SVGAs were measured. (C) Naive SVGAs were inoculated with viral supernatant collected from the specific cell types on the days indicated, incubated for 72 h, and then fixed and stained for VP1. Data represent percentages of JCPyV-infected cells for five x 20 fields of view for triplicate samples. All data are representative of at least 3 independent experiments. Error bars indicate SD. Student's t test was used to determine statistical significance. *, $P < 0.05$.

origin of replication, ultimately leading to enhanced transcription of the JCPyV early gene products, including JCPyV T Ag (121, 302). Expression of T Ag drives the infectious cycle forward, leading to the "switch" from producing T Ag to replication then production of the late gene products, including VP1. To determine if the delay in the JCPyV infectious cycle in NHAs could be overcome by the constitutive expression of SV40 Large T Ag, NHAs stably expressing the origin-defective mutant of SV40 were

generated, referred to as NHA-Ts (Figure 2.6A). NHAs, SVGAs, and NHA-Ts were infected with JCPyV and fixed at 48, 72, and 96 hpi, and JCPyV T Ag and VP1 protein production was measured using indirect immunofluorescence. T Ag production was similar across the three cell types at 48 hpi, yet there was a significant difference in VP1 production (Figure 2.6B). VP1 expression was significantly higher in NHA-Ts compared to NHAs, and the level of VP1 production was comparable to SVGAs at 48 (Figure 2.6B). At 96 hpi, NHAs demonstrated a significantly higher level of T Ag expression but significantly lower levels of VP1 in comparison to NHA-Ts and SVGAs. In contrast, NHA-Ts continued to express higher percentages of both T Ag and VP1 (Figure 2.6B). These data suggest that SV40 Large T Ag enhances JCPyV infection in NHAs and allows for efficient production of VP1.

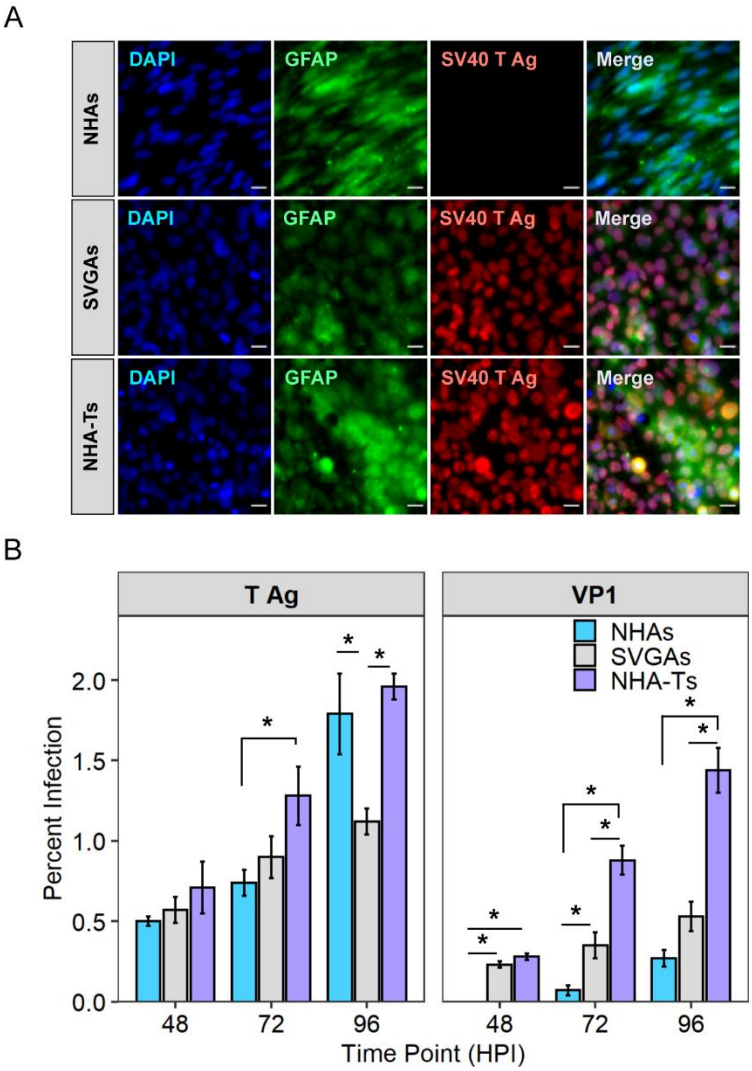

Figure 2.6. SV40 T Ag reestablishes VP1 production in NHAs. (A) Representative epifluorescence images of NHAs, SVGAs, and NHAs stably expressing SV40 T Ag (NHA-Ts) as determined by staining cells with antibodies specific for SV40 T Ag (red) and astrocyte marker GFAP (green); nuclei were counterstained with DAPI (blue). Bars = 20 µm. (B) NHAs, SVGAs, and NHA-Ts were infected with JCPyV (MOI = 0.1FFU/cell), incubated at 37°C, fixed at 48, 72, and 96 hpi, stained with antibodies specific for JCPyV T Ag and VP1, and analyzed by indirect immunofluorescence. Data represent percentages of JCPyV-infected cells for five x 20 fields of view for triplicate samples. Error bars indicate SD. One-way ANOVA was used to determine statistical significance comparing NHAs and NHA-Ts to SVGAs for each time point and viral protein. *, $P < 0.01$.

Production of VP1 transcript is delayed in NHAs

To further understand the delay in JCPyV infection in NHAs and define whether there are cell-type dependent differences in viral transcription, viral transcripts were quantified at 24 to 96 hpi by quantitative PCR (qPCR) in NHAs, SVGAs, and NHA-Ts. The 24-hpi timepoint was included to serve as an initial measure of viral transcript in each cell type, which demonstrated no significant difference in T Ag transcript levels between NHAs and SVGAs (Figure 2.7A). At 48 hpi, both SVGAs and NHA-Ts had significantly more T Ag transcripts compared to NHAs (Figure 2.7A), and this trend was retained over the course of analyzed timepoints. Not surprisingly, there was a significant difference in VP1 transcript levels from 48 to 96 hpi in NHAs in comparison to SVGAs but transcript levels in NHA-Ts were restored to levels comparable to SVGAs (Figure 2.7B). Interestingly, VP1 transcript levels increased in NHAs to almost comparable levels to SVGAs and NHA-Ts at 72 and 96 hpi. These data correspond with the long-term infection results (Fig. 4), as after 7 dpi, there was a significant increase in VP1-expressing cells in NHAs, further corroborated by qPCR analyses. Additionally, as T Ag accumulates in the infected cell, viral DNA replication is occurring and the switch to transcription of the late viral genes ensues, including the production of VP1. Thus, it is hypothesized, that without the presence of SV40 Large T Ag, effective late gene transcription in NHAs does not occur until 48 h after SVGAs and NHA-Ts.

To further define the transcriptional and translational productivity of JCPyV infection, the relative intensity values of T Ag and VP1 protein expression in infected cells was quantified using ImageJ (293). Approximately 70 T Ag- and ~30 VP1- expressing cells were quantified from 48 to 96 hpi (Figure 2.7B). There was a significant difference in T Ag expression in infected-NHAs compared to SVGAs and NHA-Ts at all time points (Figure 2.7B). As T Ag expression is needed to drive the transcriptional and translational productivity of VP1, these data help to explain the low levels of VP1-positive cells in NHAs compared to SVGAs. Additionally, NHA-Ts serve as a suitable positive control for this experiment, as there was no significance difference in T Ag expression in comparison to SVGAs (Figure 2.7B), confirming

that cell type-dependent differences did not affect the relative intensity values. Lastly, when the infectious cycle was able to progress to produce VP1 in infected NHAs, there was no difference in the relative intensity values compared to SVGAs and NHA-Ts (Figure 2.7C). These data suggest that after adequate production of JCPyV T Ag, the infectious cycle is driven forward, ultimately producing VP1 transcript so that the virus can translate into VP1 protein. These data reinforce that the delay in the infectious cycle in NHAs is caused by ineffective levels of JCPyV T Ag protein being produced in the cell.

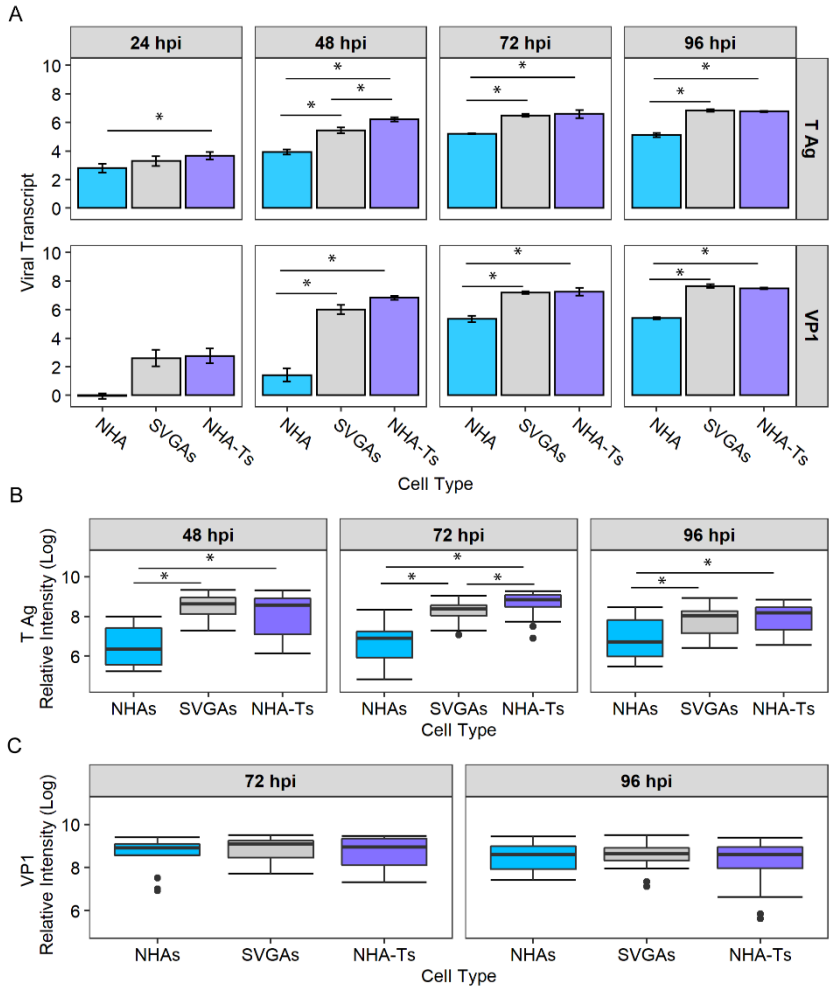

Figure 2.7. Reduced production of T Ag protein delays transcription of VP1 in NHAs. (A) NHAs, SVGAs, and NHA-Ts were infected with JCPyV (MOI = 0.1 FFU/cell) and incubated for 24, 48, 72, and 96 h. At each time point, RNA was extracted, and viral transcript levels were determined by qPCR. Data represent the absolute quantification of viral transcripts for triplicate samples. Error bars indicate SD. Data are representative of 3 independent experiments. One-way ANOVA was used to determine statistical significance comparing data for NHAs and NHA-Ts to data for SVGAs for each time point and viral protein. *, $P < 0.01$. (B, C) Cells infected in parallel were also fixed and counterstained for viral proteins, and the relative fluorescence intensity units (RFUs) for T Ag (70 cells) (B) and VP1 (~30 cells) (C) were quantified by indirect immunofluorescence for five x 20 fields of view. (B) The Kruskal-Wallis test was used to compare the relative intensities of T Ag and VP1, comparing all cell types within each time point. *, $P < 0.01$.

Polyomavirus proteins dysregulate the cell cycle in primary and immortalized cells

All polyomaviruses produce T Ag during the infectious cycle to transform the cell into a viral factory allowing for the effective replication of viral DNA and ultimately, virus production (279). Viral T Ag is a multifunctional protein, serving as a DNA helicase (281), binding to p53 and blocking apoptosis, and inducing the infected cell into S phase (280). To observe the broad view of cell cycle progression during JCPyV infection of NHAs, cells were stained for cell cycle markers, cyclin E and cyclin B1. Cyclin E accumulates in the cell during S phase and cyclin B1 accumulates during the progression to G2/M phase (303–305). Cyclin B1 has been used to investigate the cell cycle status of JCPyV-infected cells as well as other viruses (127–129, 273). Thus, analyzing the expression of cyclin E and with viral proteins T Ag and VP1 provides a better understanding of the infectious cycle over time in NHAs and SVGAs with relation to the cell cycle status. Using confocal microscopy, fields of view were analyzed for nuclear (N) and cytoplasmic (C) cyclin B1 and cyclin E and nuclear T Ag or VP1 expression for 30 cells for NHAs, SVGAs, and NHA-Ts at 48 to 96 hpi (representative images are presented in Figure 2.8A).

Nuclear cyclin E expression was significantly higher in NHAs expressing JCPyV T Ag at all time points measured as compared to mock-infected cells (Figure 2.8). In comparison, JCPyV infected cells had higher levels of cyclin E in the nucleus compared to mock-infected cells at 48 and 96 hpi, and this comparison was only seen in NHA-Ts at 48 hpi (Figure 2.8). Conversely, cyclin B1 expression was significantly higher in the cytoplasm of NHAs compared to mock-infected cells and higher in the nucleus of SVGAs at 96 hpi compared to mock-infected cells (Figure 2.8C). A principal-component analysis (PCA) was performed examining the relationship of T Ag expression and the nuclear and cytoplasmic expression of cyclin B1 and cyclin E within each cell population. A loading plot of the first two, most explained principal components illustrating the relationship of each of the 5 variables was established (Figure 2.9A). The first component (*x* axis) separates cyclin B (nuclear and cytoplasmic) and T Ag expression (positive) and cyclin E expression (negative). The second component (*y* axis) is influenced by

all vectors (positive) (Figure 2.9A). Applying the same loading plot to each cell type and time point, NHAs were defined as having low expression of T Ag and cyclin B1 expression, distinctly different than SVGAs and NHA-Ts at 24 hpi (Figure 2.9B). However, at later time points, the NHA population began to resemble the SVGA and NHA-T populations (Figure 2.9B).

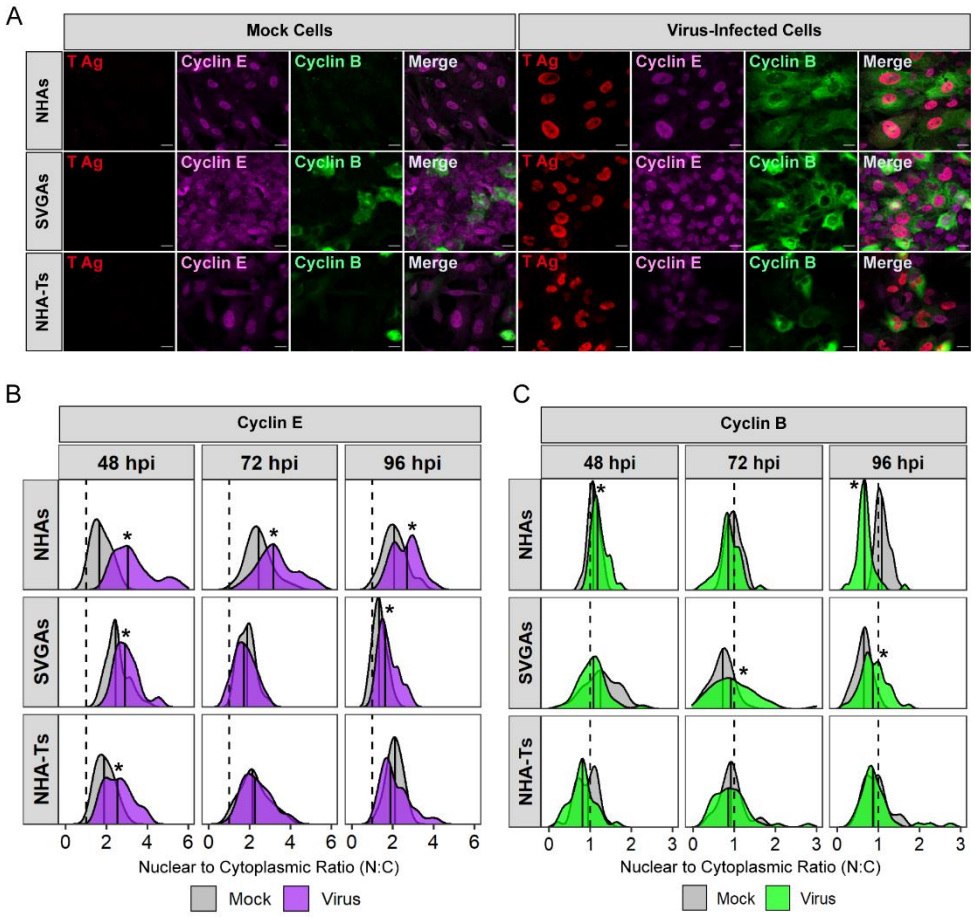

Figure 2.8. JCPyV T Ag drives nuclear expression of cyclin E in all cell types, while cyclin B1 expression is variable. (A to C) NHAs, SVGAs, and NHA-Ts were infected with JCPyV (MOI = 5 FFU/cell), incubated for 48, 72, and 96 h, and then fixed and stained with antibodies specific for T Ag (red), cyclin E (magenta), and cyclin B1 (green) and complementary secondary antibodies. Bars = 20 µm. (A) Representative confocal micrograph images (60 x objective) of samples at 96 hpi. (B) Image analysis was performed for mock-infected and infected cells (~30 cells per time point and sample), quantifying the RFUs for nuclear and cytoplasmic expression (N/C) of cyclin E (B) and cyclin B1 (C) using ImageJ. One outlier was removed from the cyclin E analysis(B), and two outliers were removed from the cyclin B1 analysis (C). The dashed lines represent an N/C ratio of 1. Solid lines represent the median values. The Kruskal-Wallis test was used to compare the relative intensities of T Ag, comparing all cell types within each time point. *, $P < 0.01$.

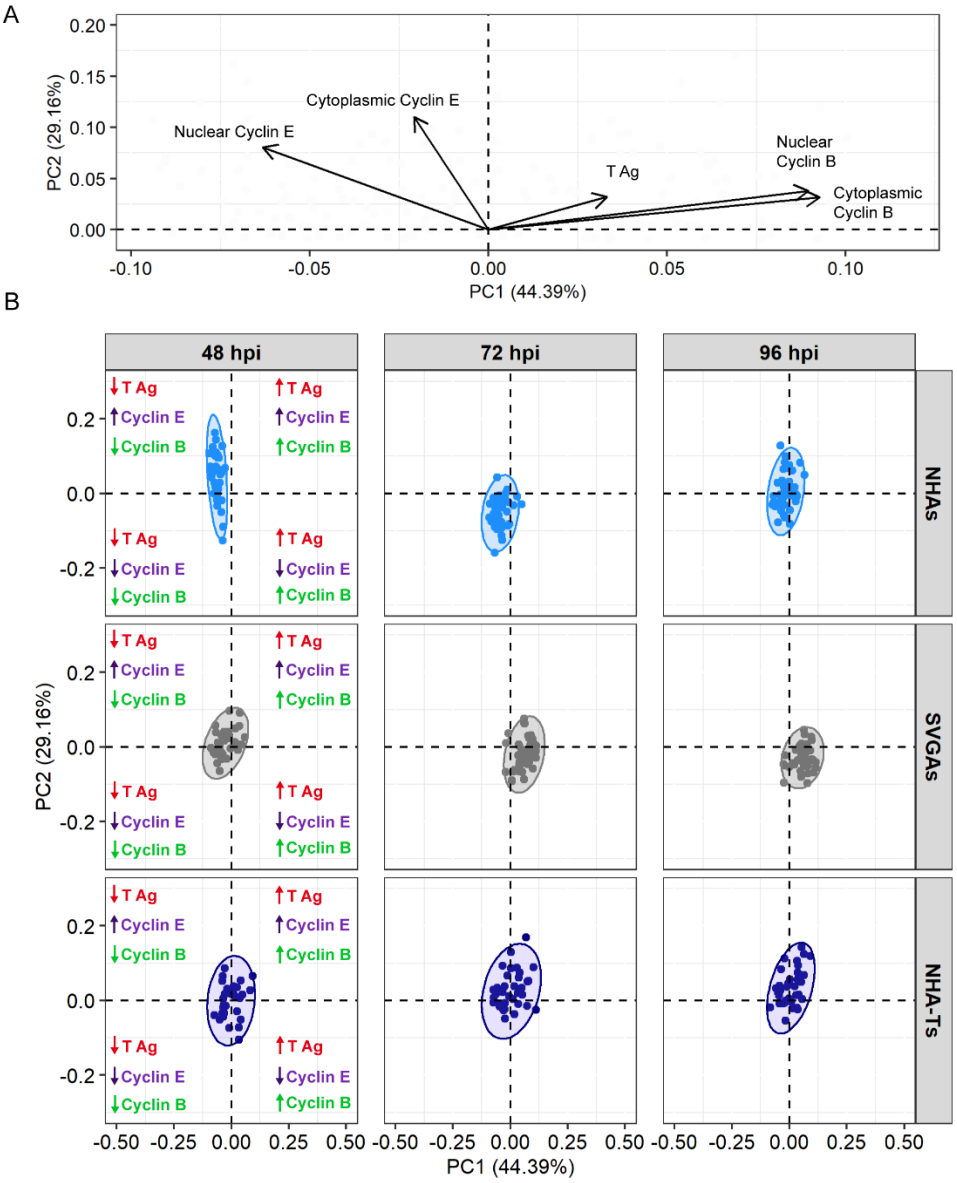

Figure 2.9. PCA separates the NHA population early during JCPyV infection. (A) A loading plot of the first two components. The first component (x axis) separates cyclin B1 and T Ag expression (positive) and cyclin E expression (negative). The second component (y axis) is influenced by all vectors (positive). (B) Principal-component analysis was performed on samples from the experiment whose results are shown in Fig. 7, using the loading plot to demonstrate correlations between nuclear and cytoplasmic expression of cyclin E and cyclin B and nuclear T Ag expression, separated by cell type and faceted by time point.

Cyclin E and cyclin B1 expression was also examined in VP1-positive cells for each cell type at 96 hpi (Figure 2.10A). Only the 96-hour time point was quantified for NHAs as the number of VP1-positive cells for this cell type at the earlier time points was insufficient for analysis. As in Figure 2.8B and 7C, NHAs expressed higher amounts of cyclin E but lower amounts of cyclin B1 in the nucleus compared to mock-infected cells (Figure 2.10B). In SVGAs, cyclin E and cyclin B1 levels were slightly higher in the nucleus and there was no difference in cyclin expression in NHA-Ts compared to the mock-infected populations (Figure 2.10B). A PCA was also performed on VP1-positive cells, and a loading plot illustrates the principal components used to define each of the five variables (Figure 2.11A). First component (*x*

axis) is influenced by all vectors (positive). The second component (*y* axis) separates cyclin E expression and VP1 (negative) with cyclin B expression (positive) at 96 hpi (Figure 2.11A). Applying the loading plot to each cell type, expression levels of cyclins in VP1-positive NHAs more closely resemble those of SVGAs and NHA-Ts, in comparison to the distinct populations observed in T Ag-positive cells at earlier time points. However, VP1-positive NHAs still express lower levels of cyclin B1 (Figure 2.11B). These data, along with the previous PCA, illustrate that at earlier times during infection, NHAs are uniquely defined by the level of viral protein expression and cyclin expression, but as infection progress, infected NHAs become more variable and the population begins to resemble those of SVGAs and NHA-Ts.

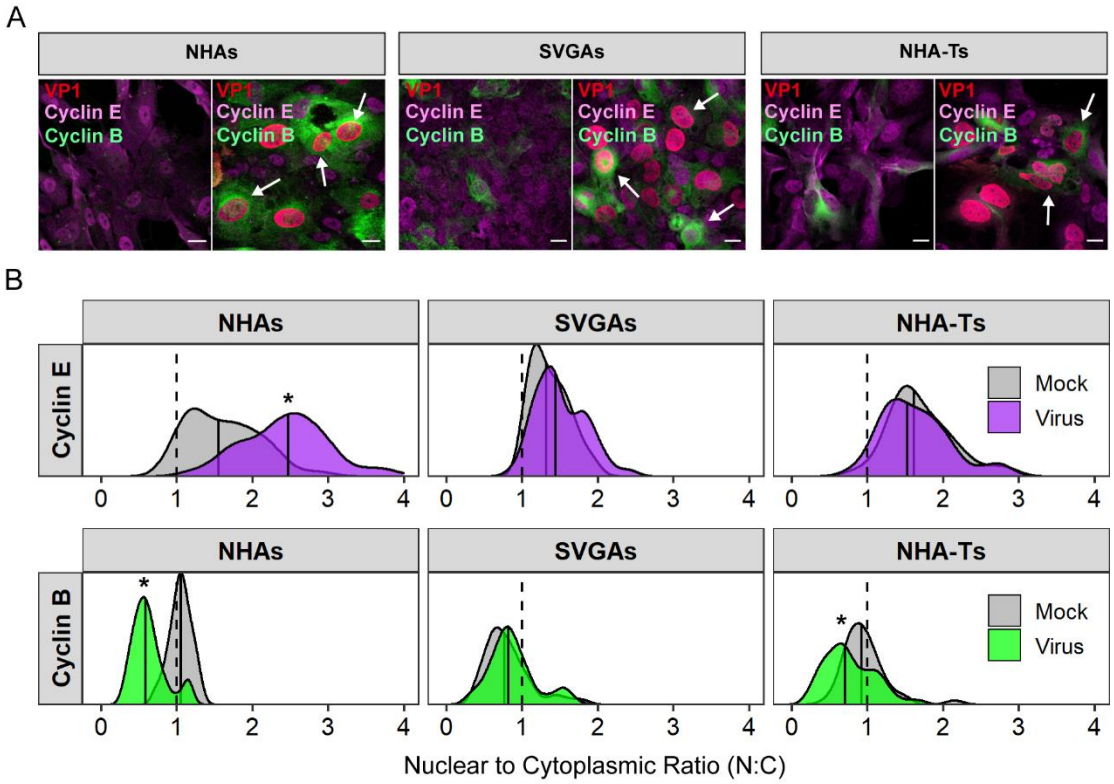

Figure 2.10. Nuclear cyclin E expression is enhanced in NHAs expressing VP1. NHAs, SVGAs, and NHA-Ts were infected with JCPyV (MOI = 5 FFU/cell), incubated for 96 h, and then fixed and stained with antibodies specific for VP1 (red), cyclin E (magenta), and cyclin B1 (green) and with complementary secondary antibodies. Bars = 20 µm. (A)Representative confocal micrograph images (60 x objective) of samples at 96 hpi. (B) Image analysis was performed for mock-infected and infected cells (~30 cells per time point and sample), quantifying the RFUs for nuclear and cytoplasmic expression (N/C) of cyclin E (B) and cyclin B1 (C) using ImageJ. One outlier was removed from the cyclinB1 analysis (C). The dashed lines represent an N/C ratio of 1. Solid lines represent the median values. The Kruskal-Wallis test was used to compare the relative intensities of VP1, comparing all cell types within each timepoint. *, $P < 0.01$.

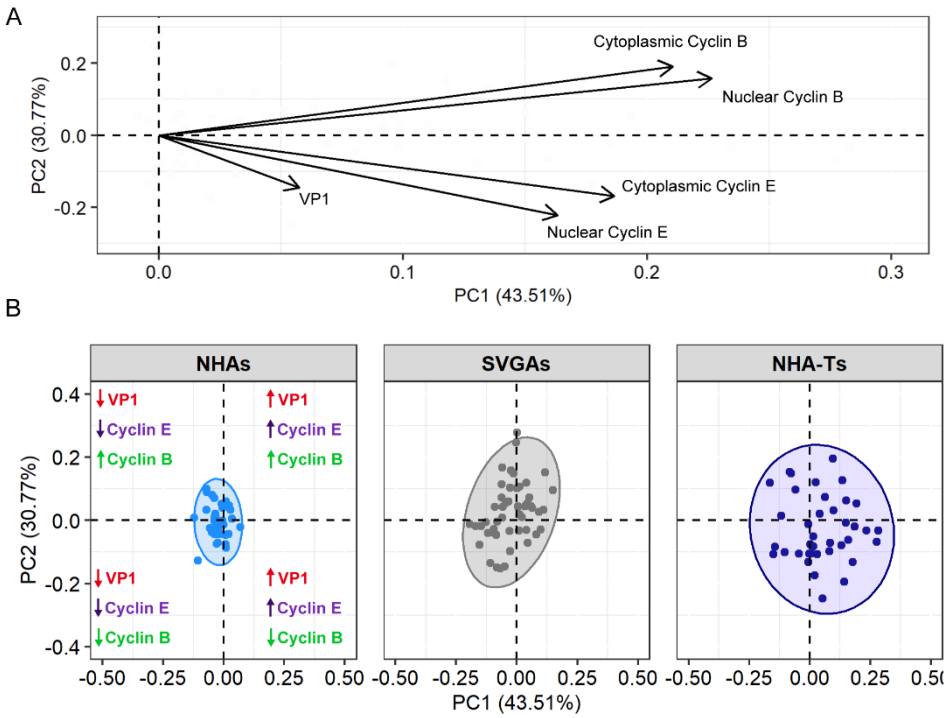

Figure 2.11. VP1 expression correlates with cyclin expression in JCPyV-infected cells. (A) A loading plot of the first two components in PCA. The first component (x axis) is influenced by all vectors (positive). The second component (y axis) separates cyclin E and VP1 expression (negative) and cyclin E expression (positive) at 96 hpi. (B) Principal component analysis was performed on samples from the experiment whose results are shown in Fig. 9, using the loading plot to demonstrate correlations between nuclear and cytoplasmic expression of cyclin E and cyclin B1 and nuclear VP1 expression, separated by cell type.

Discussion

SVGAs transformed with SV40 T Ag, serve as a robust model to study JCPyV infection and have been especially important due to the challenges of growing the virus in commonly used cell culture models. Studies in SVGAs have significantly improved our understanding of JCPyV infection, being cost effective and easy to maintain and utilize in the laboratory. Unfortunately, the immortalized characteristics of these cells present challenges when comparing to viral infection that results in disease in human hosts and may not reflect the progression of infection in a natural host cell (306). First, SVGAs are a heterogenous population of cells and are thus difficult to generate conclusions from a single cell type. Furthermore, cells transformed with SV40 T Ag, like SVGAs, are susceptible to chromosomal

changes through repeated passages, demonstrating alterations in both karyotype and phenotype in SVGAs (307). As a result of these challenges, we further characterized JCPyV infection in primary astrocytes, specifically analyzing the temporal regulation of the virus. We have demonstrated herein that NHAs exhibited established characteristics of protoplasmic astrocytes based on expression of astrocytic markers GFAP and ALDH1L1 (Figure 2.2A). The expression of astrocytic markers decreases in initial passaging but remains constant thereafter and, thus, independent of the initial events of the infectious cycle (Fig 1A). The infectious cycle in NHAs is comparable to SVGAs, yet subsequent steps are delayed resulting in a significant reduction of the late viral gene product VP1. As it is well understood that SV40 T Ag can bind more effectively than JCPyV T Ag to the early region of JCPyV to initiate JCPyV replication (121, 302), we sought to characterize the differences in JCPyV infectivity in primary cells compared to cells transformed with SV40 T Ag, NHA-Ts. The expression of SV40 T Ag conferred an enhanced capacity of NHAs to support JCPyV infection to the level of SVGAs. These findings illustrate that primary astrocytes support JCPyV infection yet have a delayed infectious cycle, and expression of SV40 T Ag alters the course of infection in NHAs through cellular reprogramming that is not attributable to JCPyV infection.

Other cell culture models have been used to study JCPyV infection *in vitro*. This includes other immortalized cells such as COS-7 cells (CV-1 cells transformed with SV40 T Ag) (308) and 293TT cells (human embryonic kidney [HEK] cells expressing high levels of SV40 T Ag) (119) and primary cells, like RPTECs (renal proximal tubule epithelial cells) (309), neural progenitor cells (NPCs) (290), choroid plexus epithelial cells (167, 310), and human embryonic stem cells (hESC)-derived oligodendrocytes (311). RPTECs, represent a potential primary model for studying the low-level persistent infection in the kidney. NPCs and hESC-derived oligodendrocytes are useful models to study glial-specific infection yet are challenging to differentiate and maintain in cell culture (312). On the other hand, primary astrocytes are easy to culture and maintain, and most recently, were discovered to play a critical role in PML

development in a human chimeric glial mouse model (273). Previously, PML development has been defined by the lytic infection of oligodendrocytes, which were thought to be the main target of PML (60, 313). Kondo et al. suggested that astrocytes are readily targeted by the virus and produce higher levels of JCPyV infection in comparison to oligodendrocytes, and interestingly, astrocytes may act as a reservoir for JCPyV infection (273). The delayed characteristics noted in that study align with our results demonstrating that JCPyV can infect NHAs producing significantly more JCPyV T Ag-positive cells and fewer infected cells expressing VP1 (Fig. 2-4). Infecting NHAs with multiple JCPyV variants, resulting in the same trends in T Ag and VP1 production, demonstrates that the NCCR region may not influence the temporal regulation of the virus in primary cells (Fig. 2); however, future studies would be necessary to further validate this finding.

Previous research has also demonstrated that the overexpression of SV40 T Ag enhances replication of JCPyV that naturally replicates poorly in cell culture. 293TTs for example, HEK cells with an SV40 T Ag expression plasmid and an integrated SV40 genome, can support infection because of their capacity to produce high levels of SV40 T Ag (119). Similarly, results reported herein illustrate that JCPyV infection is enhanced in NHAs that express SV40 T Ag in *trans* (Figure 2.6B). Although viral DNA replication was not directly measured, previous research has shown that SV40 T Ag enhances JCPyV replication (119). In line with previous results, NHA-Ts had equivalent levels of both early and late JCPyV transcript and protein levels, like those of SVGAs (Fig. 6). A possible explanation lies in the flanking sequences around the core origin of JCPyV T Ag not being able to stimulate DNA replication as well as SV40 T Ag (121). This dependency results in JCPyV T Ag binding less efficiently to the viral genome (302), leading to less virus replication and ultimately less expression of the late gene products, including VP1.

Polyomavirus T Ag proteins can impact the cell cycle, allowing the forced entrance of quiescent cells into S phase and binding to p53 and Rb (280, 314), which is necessary for viral replication. SV40 T

Ag can also induce expression of cyclins A, B1, and E but not cyclin D (315, 316). Cyclins are commonly used as markers for the cell cycle (127–129, 273) and have been previously used as cell cycle markers during JCPyV infection (273, 274). Cyclin E is activated during the end of G1 and accumulates in the cell during S phase and it has been previously demonstrated to be upregulated during JCPyV infection around 5 dpi but later decreased (274). Cyclin B1 on the other hand, accumulates in the cell during late stages of the G2 phase and becomes activated in the nucleus during the initiation of the M phase. Further, previous research has demonstrated that cyclin B1 expression increased in infected astrocytes from initial infection up to 15 dpi (274). Unfortunately, previous immunofluorescence analyses were subject to a qualitative approach which could lead to inherent biases of defining a cell expressing a given protein and not quantitatively illustrating the range of expression in infected cells. Secondly, cyclins are dynamic proteins within the cell, translocating to the cytoplasm and nucleus and thus, other techniques used may not be able to accurately quantitate this translocation event (293).

Quantitative fluorescence microscopy methods allow for single cell analyses to determine the amount of protein within a cell, information that could be lost by biochemical fractionation from an analysis such as western blot (293). Examining the nuclear (N) to cytoplasmic (C) ratios (N:C), it was determined that cyclin E expression was higher in the nucleus of infected cells compared to mock-infected cells in both NHAs and SVGAs, which was shown previously in cells infected with JCPyV (274). When examining cyclin B expression however, infected NHAs had a lower N to C ratio compared to mock-infected cells which contrasted with SVGAs, especially at 96 hpi (Figure 2.8). These findings illustrate the advantages of using this technique and highlight the differences of JCPyV infection in NHAs. As JCPyV infection continues, the cell progresses into the G2 phase and is arrested at G2/M, shown by the increase in cyclin B1 expression in the cytoplasm, which allows for virus assembly and subsequent virus release (Figure 2.12). In NHAs, cyclin B1 is activated but is sequestered in the cytoplasm, while in SVGAs, cyclin B1 expression is greater in the nucleus of infected cells compared to

mock-infected cells (Figure 2.8A and 7B). This difference is most likely due to expression of SV40 T Ag as both the mock and infected cells of the newly transformed NHA-T population resembles that of SVGAs (Figure 2.8 and Figure 2.9B), resulting in the infected cell not being able to progress to later stages of the cell cycle.

Image analysis also allows for the generation of a unique data set, defining selected cells by the expression of multiple proteins. In this study, the nuclear and cytoplasmic expression of host proteins was analyzed as well as nuclear viral protein levels by performing a principal component analysis across various timepoints, revealing interesting trends developed by the correlation among the variables chosen. Compared to SVGAs and NHA-Ts, NHAs, were defined as a small, unified population of cells expressing low levels of cyclin B and T Ag. As infection progressed however, the NHA population began to overlap with SVGAs and NHA-Ts, most likely the result of continued JCPyV T Ag production, further inducing expression of cyclin E and potentially driving the cells into S phase (Figure 2.9B and Figure 2.11B).

This research further characterizes primary astrocytes as a useful model to study early events in JCPyV infection as NHAs support the production of abundant levels of JCPyV T Ag. Furthermore, techniques and methodological approaches explained here can be extrapolated to other primary cells, including oligodendrocyte progenitor cells and mature oligodendrocytes to determine the temporal regulation of JCPyV infection in this other critical cell type in the pathogenesis of PML. The differences between infection in primary astrocytes in comparison to the transformed model SVGA cell line provides insights into the mechanism by which SV40 T Ag enhances JCPyV infection. Taken together, these analyses illustrate a timeline of the progression of JCPyV infection in a primary cell type, NHAs. Initially delayed (compared to cells expressing SV40 T Ag), the infectious cycle is prolonged due to the low levels of JCPyV T Ag (Figure 2.12). However, the prolonged expression of JCPyV T Ag may lead to T Ag binding

to the viral DNA as well as p53 and Rb, inducing the cell into S phase and ultimately driving the transcription of the late genes, such as VP1. In a field where the development of an animal model is hampered due to the narrow host range of JCPyV, this research may serve to establish a foundation for future studies to examine and discover molecular mechanisms of astrocytic viral infection that ultimately lead to human disease.

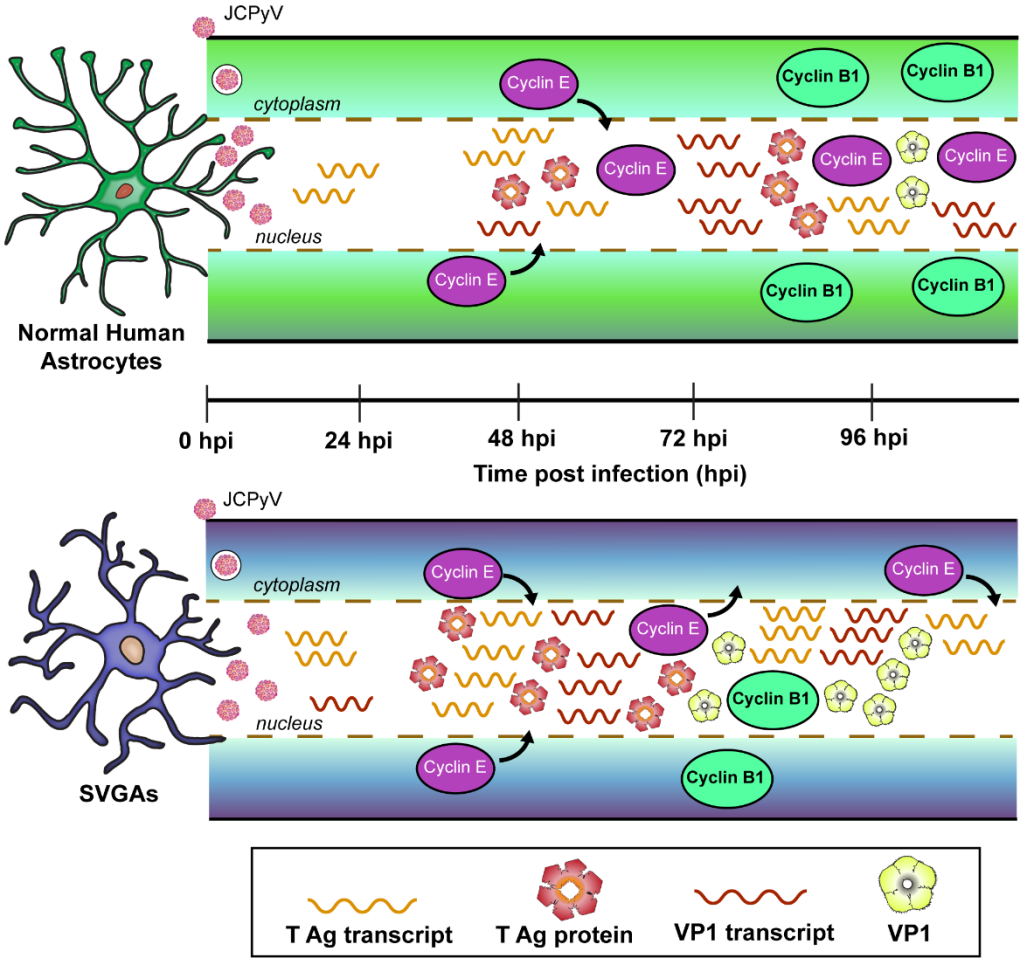

Figure 2.12. Model of the temporal regulation of JCPyV infection and cell cycle progression, comparing NHAs to SVGAs. JCPyV translocate to the nucleus after arrival in the endoplasmic reticulum (ER) (~6to12h); comparable levels of T Ag transcript are produced at 24 hpi in NHAs and SVGAs. T Ag transcript is translated to T antigen protein, but at decreased levels in NHAs compared to the levels in SVGAs. Subsequently, less VP1 transcript is produced, delaying the translation of VP1 protein. Cyclin E continues to accumulate in the nucleus of NHAs from 48 to 96 hpi as T Ag transforms the cell to support viral replication. VP1 transcript begins to accumulate in the nucleus at 72 hpi and cyclin B accumulates in the cytoplasm, and at 96 hpi, VP1 is produced. In comparison, JCPyV infection in SVGAs occurs in a more rapid fashion, where T Ag transcript is translated to T Ag protein and cyclin E accumulates in the nucleus at 48 hpi. VP1 transcripts drastically increase at 48 hpi as well, and at 72 hpi, nucleus expression of cyclin E is reduced, and VP1 production occurs soon after.

CHAPTER 3

THE MAPK/ERK PATHWAY AND ROLE OF DUSP1 IN JCPYV INFECTION OF PRIMARY ASTROCYTES

The work presented in this chapter is in preparation for resubmission.

Introduction

JC polyomavirus (JCPyV) is a human-specific virus that infects astrocytes and oligodendrocytes leading to the fatal, demyelinating disease, progressive multifocal leukoencephalopathy (PML) (60–63, 68). JCPyV infects most of the population, residing in the kidneys of healthy individuals (28, 30, 44–46). However, during immunosuppressive events, the virus can escape the kidneys and enter the central nervous system (CNS), infecting glial cell types (45, 58, 59). If left untreated, PML can be fatal within a few months (317). Individuals most at risk for this disease include those who undergoing immunomodulatory therapies, such as natalizumab for multiple sclerosis (MS) or people who are HIV positive (60, 71, 75, 76). While there have been advancements in treatment, which address the underlining immunosuppression aligned with supportive care, resulting in improved survival rates, a sufficient cure for the disease is still lacking (71, 79–81).

Limited approaches to studying JCPyV *in vivo*, pose challenges in understanding PML pathogenesis. When non-human cells are infected, the JCPyV infectious cycle cannot be completed due to the lack of appropriate host cell factors, ultimately resulting in tumorigenesis (168, 171–173, 318). Recent progress has been accomplished however, by using humanized, chimeric mouse models. In 2014, Kongo et. al generated a chimeric humanized mouse model to study JCPyV pathogenesis and demonstrated that astrocytes were the main target of glial infection, may act as a reservoir during infection, and supported viral replication to a greater extent compared to oligodendrocytes (68). This discovery greatly impacted our understanding of PML progression and suggested that exploration of

astrocytic infection in greater detail was warranted. Our laboratory recently characterized JCPyV infection in primary normal human astrocytes (NHAs) as a tool to understand the infectious cycle (130, 167).

To date, many advancements of the mechanistic understanding of JCPyV infection has been attributed to *in vitro* work, specifically using immortalized human fetal glial cells, constitutively expressing SV40 Large T antigen (T Ag), termed SVG-A cells (referred herein as SVGAs) (124). Initially, the virus replicated poorly in cell cultures that lacked SV40 Large T Ag expression, but in cells immortalized with SV40 Large T Ag, replication of the JCPyV genome was increasingly efficient (120, 121). The JCPyV genome is ~5,100 bp in size and accomplishes viral infection through two bidirectional coding areas, orchestrated by the noncoding control region or NCCR (47, 86). Host factors bind to the NCCR of the viral genome in the nucleus of the host cell and initiate transcription and translation of the viral early genes. The early genes of JCPyV, specifically Large T Ag, facilitates replication by inducing the cell into S phase and acts as a helicase to unwind the viral DNA (116, 122). Research has demonstrated that SV40 Large T Ag may better support JCPyV replication by binding more efficiently to the viral genome and thus, SVGAs, have more robust levels of infection comparative to other cell lines (120, 121). Following JCPyV replication, late gene expression induces production of the viral proteins (VP) 1, 2, and 3, which encapsidate the viral DNA before virions are released to subsequently infect surrounding cells (41).

Due to the discovery of astrocytes as the main targets in the CNS for JCPyV infection, and the accumulation of research performed using SVGAs, the infectious cycle was characterized in primary human astrocytes in comparison to infection in SVGAs (130). It was discovered that JCPyV infection was delayed in primary astrocytes mostly due to the inadequate production of JCPyV Large T Ag compared to levels of this viral protein in cells immortalized with SV40 Large T Ag (130). This research corroborated the observations of Kondo et. al. in the chimeric mouse model; astrocytes were readily infected but

expressed low levels of the late viral gene product VP1 (68, 166, 167, 319). Further research suggested that the immortalization of NHAs with SV40 Large T Ag, termed NHA-Ts, restored levels of VP1 expression comparable to JCPyV infection in SVGAs (130). Unfortunately, expression of SV40 Large T Ag may impact cells in other ways in addition to supporting JCPyV replication, including dysregulating the cell cycle and activating cellular pathways (122, 123).

Previous research established that JCPyV uses the cellular, mitogen-activated protein kinase, extracellular signal-regulated kinase (MAPK/ERK) pathway to reprogram the cell and support viral infection (94, 193). It was determined that both SVGAs and a primary kidney cell line, renal proximal tubule epithelial cells (RPTECs) required ERK phosphorylation as using the MEK inhibitor, U0126, a kinase upstream of ERK, reduced infection in both cell types (193). It was further validated that, kinases in this pathway, BRAF, CRAF, MEK1, and MEK2 were all critical for infection in SVGAs (205).

The MAPK/ERK pathway is important in determining cell fate in proliferation, differentiation, and survival (192). Other viruses hijack this pathway to reprogram the cell and support viral infection (193, 206–208). However, there has been little research implicating the negative regulatory role of the MAPK/ERK pathway may play in viral infection, including the function of dual specificity phosphatases (DUSPs). DUSPs are made up of a family of protein tyrosine phosphatases that strongly regulate and deactivate MAPK signaling (209–212). Typical DUSPs, or phosphatases that contain a MAP kinase-binding (MKB) motif or the kinase-interacting motif (KIM), are dynamic proteins further classified by their subcellular cytoplasmic and/or nuclear localization (213, 320). The most studied DUSPs in glial cells are DUSP1 and DUSP6 (209). DUSP6 is a cytoplasmic phosphatase that inhibits ERK1/2 phosphorylation (213). Recent evidence has elucidated the involvement of DUSP6 with MEK1/2-ERK1/2 signaling and the infectious bronchitis virus (IBV), a strain of *Gammacoronaviruses* (321). The authors discovered that overexpression of DUSP6 led to inhibition of ERK1/2 signaling and diminished IBV infection, while

suppression of DUSP6 led to phosphorylation of ERK1/2 and increased levels of IBV replication (321). Converse to DUSP6, DUSP1 is found in the nucleus and binds to JNK, p38, and ERK1/2, leading to the dephosphorylation and inactivation of these kinases (212). Interestingly, cellular levels of ERK can be sustained by targeting DUSP1 for degradation via the ubiquitin/proteasome pathway (214–216), further highlighting the complexity of the regulatory processes of the MAPK/ERK pathway. DUSPs, specifically DUSP1, have been implicated in other viral infections as well, including hepatitis C virus (HCV), vaccinia virus (VACV), human respiratory syncytial virus (RSV), and Sendai virus (SeV) (219, 322, 323). Through ERK phosphorylation, DUSP1 is upregulated and stabilized, further promoting viral replication and release during VACV infection (322). Moreover, DUSP1 may also be differentially expressed during coronavirus infection (324), highlighting the importance of this protein during infection across many viral families. Lastly, DUSP1 is also known to be involved in the inflammatory response (218) as research has demonstrated that knockdown of the protein can reduce HCV infection, as it promoted the induction of interferon stimulated genes (ISGs) (219).

The purpose of this study was to elucidate and define the cellular pathways involved in JCPyV infection in primary astrocytes. This was established through a comparative approach, using RNA sequencing (RNA-seq), bioinformatics analysis, and complementary cell-based assays to compare the host transcriptome profile in primary astrocytes versus SVGAs during JCPyV infection. These data further validate the importance of ERK in JCPyV infection, reveals novel regulatory roles of the MAPK/ERK pathway, and highlights the importance of DUSP1 expression during JCPyV infection in primary astrocytes.

Materials and Methods

Cells and viruses

The maintenance and description of normal human astrocytes (NHAs) (passage 1 [P1]) were previously described (130). Briefly, NHAs were cultured in astrocyte growth medium and supplemented with SingleQuots supplements and 1% penicillin-streptomycin (P-S). The donor was a 19-week-gestation female with no detected levels of HIV, hepatitis B virus (HBV), or hepatitis C virus (HCV). All experiments were performed at low passages (P2 to P10). SVGAs were generously provided by the Atwood Laboratory (Brown University) and cultured in complete minimum essential medium (MEM) (Corning), with 10% fetal bovine serum (FBS), 1% P-S and 0.1% Plasmocin prophylactic (InvivoGen). The generation and maintenance of NHA-Ts are previously described (130). All cell types were grown in a humidified incubator at 37°C with 5% CO_2.

The generation and production of either lysate or purified JCPyV strains of Mad-1/SVEΔ were described previously (275, 325), and the strain was kindly provided by the Atwood laboratory (Brown University).

siRNA treatment

NHAs and NHA-Ts were plated for ~70% confluency while SVGAs were plated to ~50% confluency in 96 well plates and transfected with siRNAs specific for MEK1/2, ERK1/2, epidermal growth factor receptor (EGFR) control (Cell Signaling Technology) or DUSP1 (Santa Cruz Biotechnology). A final concentration of 1pmol of siRNA/well for MEK1/2 and ERK1/2, and a final concentration of 4 pmol of DUSP1 siRNA/well was used with RNAiMax transfection reagent (Invitrogen) by mixing transfection complexes in Opti-MEM, reduced serum medium (Gibco) at RT for 7 min. Complexes were added to the cells (10 µl/well) and incubated at 37^{o}C for 72 h for the MEK1/2 and ERK/12 siRNA and 24 h for the

DUSP1 siRNA. Protein reduction was measured by ICW assay (205, 292) or cells were infected with JCPyV following treatment of siRNA.

JCPyV infection

NHAs, SVGAs and NHA-Ts were seeded into 96-well plates with approximately 10,400 cells/well to achieve ~70% confluency at the time of infection. Cells were infected (multiplicities of infection [MOIs] as indicated in the figure legend) with 42 µl/well of MEM containing 10% FBS, 1% P-S and 0.1% Plasmocin prophylactic, at 37°C for 1 h. After the initial 1 h, cells were fed with the respective medium at 100 µl/well and incubated at 37°C for the duration of the infection. Experiments in which the % infection was quantified following treatment, cells were fixed at 48 h and stained by indirect immunofluorescence for the viral protein, T Ag; except for Fig. 6 as both viral proteins, T Ag and VP1 were quantified and fixed at 72 h, following treatment.

Chemical inhibitors, BCI treatment

The allosteric inhibitor of DUSP1, BCI (*(E)*-2-Benzylidene-3-(cyclohexylamino)-2,3-dihydro-1H-inden-1-one), (Calbiochem) was reconstituted in DMSO and used at 1 µM. All cell types were pretreated with the inhibitor for 1 h, in MEM containing 10% FBS, 1% P-S and 0.1% Plasmocin prophylactic, prior to JCPyV infection. Following JCPyV infection, all cell types were fed with 100 µl/well of media containing 1 µM BCI or the DMSO control for 72 h. This concentration did not affect cell viability as measured by 4,5-dimethylthiazol-2-yl)-5-(3A- carboxymethoxyphenyl)-2-(4-sulfophenyl)-2H-tetrazolium (MTS) assay (data not shown).

Indirect immunofluorescence staining and quantitation of JCPyV infection

Following infection, all cell types were stained for T Ag or both T Ag and VP1 (Fig. 3.7) at room temperature (RT). NHAs, SVGAs, and NHA-Ts were fixed with 4% paraformaldehyde (PFA) for 11 min and washed with 1 X phosphate-buffered saline (PBS) with 0.01% Tween (PBS-T). Cells were permeabilized for 15 min using PBS-0.5% Triton X-100 and then blocked with PBS with 0.01% Tween and 10% goat serum for 45 min. Cells were then stained using antibodies specific for viral proteins at RT for 1 h (Table 3.1). Following 1° antibody incubation, cells were washed three times in PBS-T and counterstained with a 2° antibody, specifically an anti-mouse Alexa Fluor 594 (Table 3.1) for 1 h. Cells were subsequently washed with PBS-T and counterstained using DAPI (4',6-diamidino-2-phenylindole) at RT for 5 min. Cells were washed with PBS-T two more times and stored in PBS-T.

TABLE 3.1. Antibodies used in immunofluorescence and ICW assays.

Protein	1^o antibody (dilution, manufacturer)	2^o antibody (dilution, manufacturer)
JCPyV T Ag	PAB962 (1:5, hybridoma)	anti-mouse Alexa Fluor 594 (1:1000, Thermo Fisher Scientific)
JCPyV VP1	#ab34756 (1:1000, Abcam)	
Total ERK (p44/42 MAPK)	#4695S (1:500, CST)	anti-rabbit IRDye 800CW (1:10,000, LI-COR)
pERK (P-p44/42 MAPK at T202/Y204)	#9101S (1:750, CST)	
pMEK (at S222/S226)	#44-454G (1:750, Invitrogen)	
pDUSP1 (at S359)	#2857S (1:750, CST)	
Total DUSP1	#sc-373841 (1:75, Santa Cruz Biotechnology)	anti-mouse IRDye 800CW (1:10,000, LI-COR)
Total MEK1/2	#4694S (1:300, CST)	

CST, Cell Signaling Technology; ICW, In-Cell Western

To visualize the cells expressing the nuclear, viral protein T Ag or VP1, a Nikon Eclipse Ti epifluorescence microscope (Micro Video Instruments, Inc.) equipped with a 20 X objective was used. Percent infection of each well was quantified by counting the T Ag- or VP1-positive cells over the total number of DAPI-positive cells in five fields of view/well. The DAPI-positive cells were determined by using a binary algorithm in the Nikon NIS-Elements Basic Research software (version 4.50.00, 64 bit). The

algorithm created an accurate number of cells in each field by separating them based on intensity, diameter, and circularity (92, 130, 193, 205, 241).

ICW assay and LI-COR quantification

Protein expression measuring total or phosphorylated ERK, total or phosphorylated MEK, and total or phosphorylated DUSP1 were performed using an ICW assay (205, 292). Following infection or siRNA treatment cells were fixed in 4% PFA, washed with PBS-T and permeabilized with 1 X PBS-0.5% Triton X-100 at RT for 15 min. Cells were blocked with Tris-buffered saline (TBS) Odyssey buffer (LI-COR) at RT for 1 h. Cells were stained with the appropriate antibody, dilutions indicated in Table 3.1, in TBS Odyssey blocking buffer at 4°C for ~16 h while rocking. The next day, cells were washed with PBS-0.01% Tween three times and incubated with the corresponding secondary antibody in Table 3.1 and CellTag (1:500, LI-COR) for 1 h. Cells were washed with PBS-T, aspirated and the bottom of the plate was cleaned with 70% ethanol prior to scanning. Plates were weighted down using a silicone mat (LI-COR) and the lid was removed before imaging, using the LI-COR Odyssey CLx infrared imaging system to detect both the 700- and 800-nm intensities. Plates were read at medium quality, at 42-µm resolution, with a 3.0mm focus offset. Once scanning was complete, the 700- and 800-nm channels were aligned and ICW analysis was performed in Image Studio software (version 5.2). Quantification was determined by subtracting the background from the 800-nm channel (secondary antibody alone) from each well, in which the protein of interest was being measured. Next, the ratio of the 800-nm channel (protein of interest) signal to the 700-nm channel (CellTag) in each well was determined.

Absolute quantification of DUSP1 transcript levels by qPCR

NHAs, SVGAs, and NHA-Ts were plated to 70% confluence in 96-well plates. Medium was removed and cells were infected with JCPyV (MOI = 0.1 FFU/cell [same virus prep used in the RNA-seq

infection]) in 42 µl of the respective cell medium and incubated at 37°C for 0, 24, 48, and 96 h. RNA was extracted as outlined previously and was converted to cDNA using the iScript cDNA synthesis kit (Bio-Rad) using 1 µg of RNA. Primers for DUSP1 (F: GGATACGAAGCGTTTTCGGC, R: AGAGGTCGTAATGGGGCTCT)(326) and glyceraldehyde-3-phosphate dehydrogenase (GAPDH) was used as a housekeeping gene (327). After creating the master mix of qPCR reagents with the iQ SYBR green supermix (Bio-Rad), 150 nM of each primer set, 100 ng of cDNA, along with the master mix was added to each well of a 96-well PCR plate, to a total volume of 10 µl. The qPCR reaction settings are as follows: 95°C for 5 min followed by a 40-cycle setting at 95°C for 30 s, 55°C for 1 min, and 72°C for 1 min, followed by 95°C for 30 s, 55°C for 30 s, and lastly 95°C for 5 min. A melting curve was added at the end to determine primer specificity for each sample.

Preparation of samples for RNA-seq and RNA-seq analysis

NHAs and SVGAs were plated to 70% confluence in a 24-well plate. Medium was removed and cells were infected with JCPyV (MOI = 0.1 FFU/cell) in 200 µl or mock-infected with an empty cell preparation control. Cells were incubated at 37°C for 1 h in the respective medium and following infection the cells were fed with 1 ml of media and incubated at 37°C for 24, 48, and 96 h. At each time point, cells were either fixed and stained for T Ag or 200 µl of TRIzol reagent (Invitrogen) was added to each well and stored in the -20°C. After validating similar levels of infection in NHAs and SVGAs at each timepoint by indirect immunofluorescence assay, cells in TRIzol reagent were removed from the -20°C storage and total RNA was extracted from each sample with the Direct-zol RNA kits according to the manufacturer's protocol (Zymo Research). RNA quantification was determined by using the NanoDrop One, both mRNA libraries were prepared, and samples were sequenced at Beckman Coulter Genomics (Genewiz). Remaining RNA was converted to cDNA and both T Ag and VP1 transcript was measured by qPCR as previously reported (130) to validate transcript levels at each time point.

Strand-specific RNA-seq was prepared, and the paired-end reads were sequenced on an Illumina HiSeq with 20 to 30 million reads per sample with polyA selection, using next generation sequencing technology. Quality control was performed on the sequenced reads using FastQC (Version 0.11.8) (http://www.bioinformatics.babraham.ac.uk/projects/fastqc/) and reads were trimmed using Trimmomatic (Version 0.39) (328). Trimmed reads were then aligned to the human genome assembly (Version GRCh38) using HISAT2 (329) and read counts per gene generated using the Ensembl GTF file (Ensembl version 103) and HTSeq (Version 0.13.5) (186). The read counts per gene were analyzed using RStudio (version 1.2.1335) and R/edgeR (version 3.30.3) (187).

STRING Interaction database, GO Enrichment Analysis, and PANTHER pathway analysis

Interaction of genes, including genes in the MAPK/ERK cascade were visualized using STRING (http://string-db.org). STRING is a database that illustrates the direct and indirect, or the physical and functional association, respectively, of two or more proteins (330). Interactions of genes were defined as indicated in the figure legends. Gene networks were imported into Cytoscape (Version 3.8.2) to merge information from the R/EdgeR analysis. Furthermore, for Figure 8, the list of genes from the STRING database were used for a Gene Ontology enrichment analysis using PANTHER (331). The PANTHER pathway terms corresponding to the gene list were visualized using the R package, GOplot (332).

Statistical analysis and graphing in RStudio

For data that was normally distributed, the two-sample Student's *t* test assuming unequal variances was used to compare the mean values for at least triplicate samples. However, for data that was not normally distributed, the Wilcoxon signed rank test was used to compare the median values for two populations. For comparing more than two samples the One-way analysis of variance (ANOVA) or the Kruskal-Wallis test was used depending on the distribution of the data. If the Kruskal-Wallis test

determined a significant difference between groups, the pairwise Wilcoxon rank sum test, along with the Bonferroni adjustment was used to determine the pair of groups that were different. Distribution of the data was determined by the Shapiro-Wilk's test and a quantile-quantile plot (Q-Q plot), a plot to illustrate normality of the data, in RStudio (version 1.2.1335). All statistical analyses were performed in RStudio, other than the Student's *t* test, which was determined in Microsoft Excel. All statistical analyses referring to the RNA-seq data was performed using the R/edgeR (version 3.30.3) (187), including the MA plots. All graphs, including heatmaps were creating using ggplot2 (version 3.3.3) (296).

Data Availability

The RNA-seq data were deposited in the National Center for Biotechnology Information (NCBI) Gene Expression Omnibus (GEO) database, under accession number GSEXXXX (in progress).

Results

RNA-seq reveals unique differential gene expression in JCPyV-infected primary astrocytes versus SVGAs

RNA-seq was performed to measure gene expression in NHAs and SVGAs that were either mock- or JCPyV-infected at 24, 48, and 96 hpi, as illustrated in Figure 3.1A. Time points selected were previously identified as critically different in the JCPyV infectious cycle in NHAs compared to SVGAs (130). Differential gene expression was determined for NHAs and SVGAs at each time point. To compare the magnitude of genes that were differentially expressed from JCPyV infection in NHAs versus SVGAs, a statistical and expression criterion was established, represented as red points in Figure 1B (unadjusted $P < 0.05$ and $\log_2FC > 1$ or $\log_2FC < 1$). At 24 hpi, 95 genes were upregulated, and 21 genes downregulated in NHAs versus only 51 genes upregulated and 1,123 genes downregulated in SVGAs (Fig. 1B). At 48 hpi,

the relationship between genes having a $\log_2$ fold change above or below one with an unadjusted *P value* less than 0.05 were reversed for each cell type: 72 genes were downregulated in NHAs opposed to only 28 genes upregulated, and in SVGAs, 25 genes were upregulated, and 17 genes downregulated. Finally, the 96 hpi time point mirrored the relationship found at 24 hpi for both cell types. More genes were upregulated (301 genes) and only 33 genes were downregulated in NHAs, versus SVGAs where 286 genes were downregulated and only 34 genes were upregulated at 96 hpi (Fig. 3.1B). Taken together, these data reveal a pattern of differential gene expression over the course of JCPyV infection that is uniquely different in primary human astrocytes versus an immortalized glial cell line.

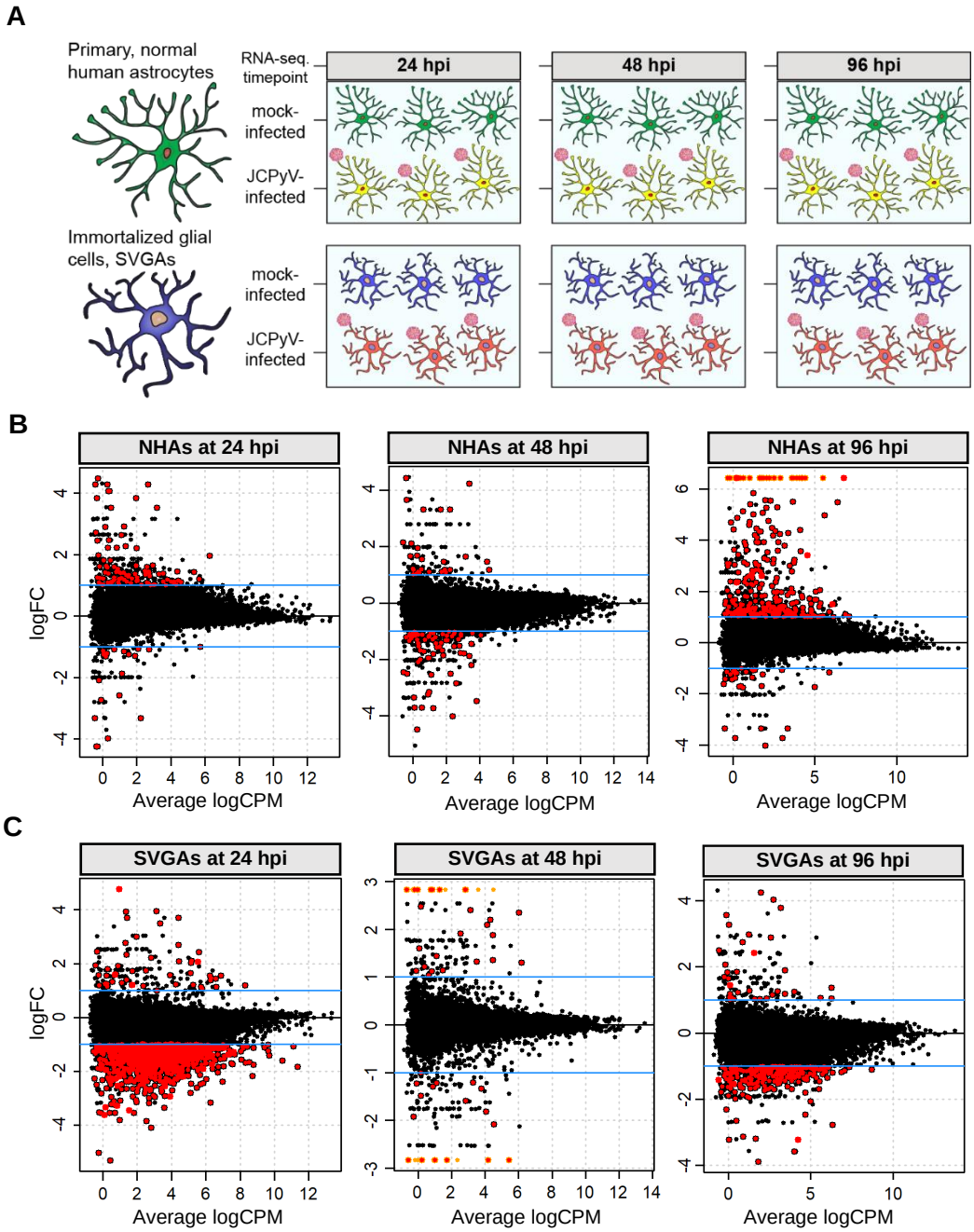

Figure 3.1. Whole transcriptome RNA-seq profiles of JCPyV infected primary astrocytes and SVGAs during course of infection reveals differential gene expression between primary and immortalized cells. (A) Primary, normal human astrocytes (NHAs) and immortalized glial cells (SVGAs) were either infected with JCPyV (MOI = 0.1 FFU/cell) or mock-infected with a vehicle control and the transcriptomic profile was determined at 24, 48, and 96 hpi. (B) RNA-seq data were normalized with the read CPM method and MA plots were generated from DEseq2 analysis at each timepoint representing the $\log_2$ fold changes of JCPyV-infected versus mock-infected NHAs or JCPyV-infected versus mock-infected SVGAs. Black points are genes from the R/EdgeR analysis. Orange points represent genes that have a slightly greater logFC than the y axis displays. Red points represent genes with a logFC greater or less than 1 and an unadjusted *P value* < 0.05. The blue lines in each plot represent the logFC = 1 and logFC = -1; *FC*: Fold-change, CPM: Counts per million.

The MAPK/ERK pathway is differentially expressed in NHAs during JCPyV infection

The MAPK/ERK pathway has been previously established to regulate JCPyV infection in both SVGAs and primary RPTECs (94, 193, 205). This regulatory network is influenced by numerous genes upstream and downstream of the pathway; to further elucidate the differential gene expression observed in Figure 1B, genes within the network of the MAPK/ERK pathway were analyzed (Fig. 3.2). *NRAS, KRAS, HRAS, BRAF, RAF1, MAP2K1* (MEK1)*, MAP2K2* (MEK2), *MAPK1* (ERK2), and *MAPK3* (ERK1) were entered into the STRING interaction database. The network was expanded to further reveal only the known interactions determined experimentally or from curated databases, having a minimum interaction score of 0.9 and having no more than 10 interactors in the 1st and 2nd shell. The list of genes was then examined in the RNA-seq data to determine the cell-specific expression patterns, examining both the $\log_2$ fold change and unadjusted *P value* for each gene in NHAs and SVGAs at 24 hpi. The interactions of 29 genes were examined, however 4 genes were not included (gray) as they were lowly expressed and were filtered out during the R/edgeR analysis (Fig. 3.2A). In NHAs, there were 19 genes that had a negative $\log_2$ fold change and two of them, *PIK3R1* and *SOS1* had an unadjusted *P value* threshold of less than 0.05 (Fig. 2A, right). In the MAPK/ERK cascade specifically, *HRAS, MAP2K2* (MEK2), and *MAPK3* (ERK1) had a positive $\log_2$ fold change, however only *HRAS* and *MAP2K2* (MEK2) had an unadjusted *P value* less than 0.1. This contrasts with SVGAs, where *HRAS, MAP2K2* (MEK2)*,* and *MAPK3* (ERK1) had a negative fold change and a *P value* less than 0.05 for *HRAS* and *MAP2K2* (MEK2) (Fig. 3.2A). To understand how the MAPK/ERK cascade changes over the course of JCPyV infection, the $\log_2$ fold change of the genes within the cascade for each time point in both NHAs and SVGAs was determined and illustrated as a heatmap in Figure 2B. The differing gene expression seen at 24 hpi between NHAs versus SVGAs was also apparent at 48 and 96 hpi. This pattern was most pronounced with the following genes: *HRAS, MAP2K2* (MEK2), and *MAPK3* (ERK1). At 48 hpi these genes had a negative $\log_2$ fold change in NHAs whereas in SVGAs, these genes had a positive $\log_2$ fold change (Fig. 3.2B). Collectively, these

data illustrate that the temporal patterns of the genes in the MAPK/ERK pathway during JCPyV infection in NHAs is distinct and contrary from the MAPK/ERK gene expression pattern in SVGAs, and this distinction can be expanded to surrounding genes of the MAPK/ERK cascade, specifically at 24 hpi.

Knockdown of MEK and ERK in primary astrocytes influences JCPyV infection

To better compare the differences observed in the MAPK/ERK pathway in NHAs and SVGAs, NHA-Ts, NHAs immortalized with SV40 T Ag were used in parallel with the other two cell types (130). All cell types were treated with siRNAs targeting MEK and ERK and subsequently infected 72 h post siRNA transfection. Protein knockdown was analyzed by In-Cell Western (ICW) (Fig. 3.3A) and quantified using LI-COR software (Fig. 3.3B). Greater than 60% reduction of MEK and ERK was achieved in all cell types at 3 days post transfection (Fig. 3.3B). Following siRNA treatment, all cell types were infected with JCPyV and infectivity was measured at 2 days post infection (dpi) for cells treated with the MEK siRNA (Fig. 3.3C) or ERK siRNA (Fig. 3.3D). Knockdown of MEK significantly increased JCPyV infection in NHAs compared to SVGAs and NHA-Ts (Fig. 3.3C). However, knockdown of ERK resulted in a decrease of JCPyV infection in all cell types although a more appreciable decrease was observed in NHAs (Fig. 3.3D). These notable outcomes of JCPyV infection in primary astrocytes highlight the complexity of the MAPK/ERK pathway, introduces the requirement of ERK in JCPyV infection in NHAs, and suggests unique regulatory mechanisms of the MAPK/ERK pathway observed in NHAs but not SVGAs and NHA-Ts.

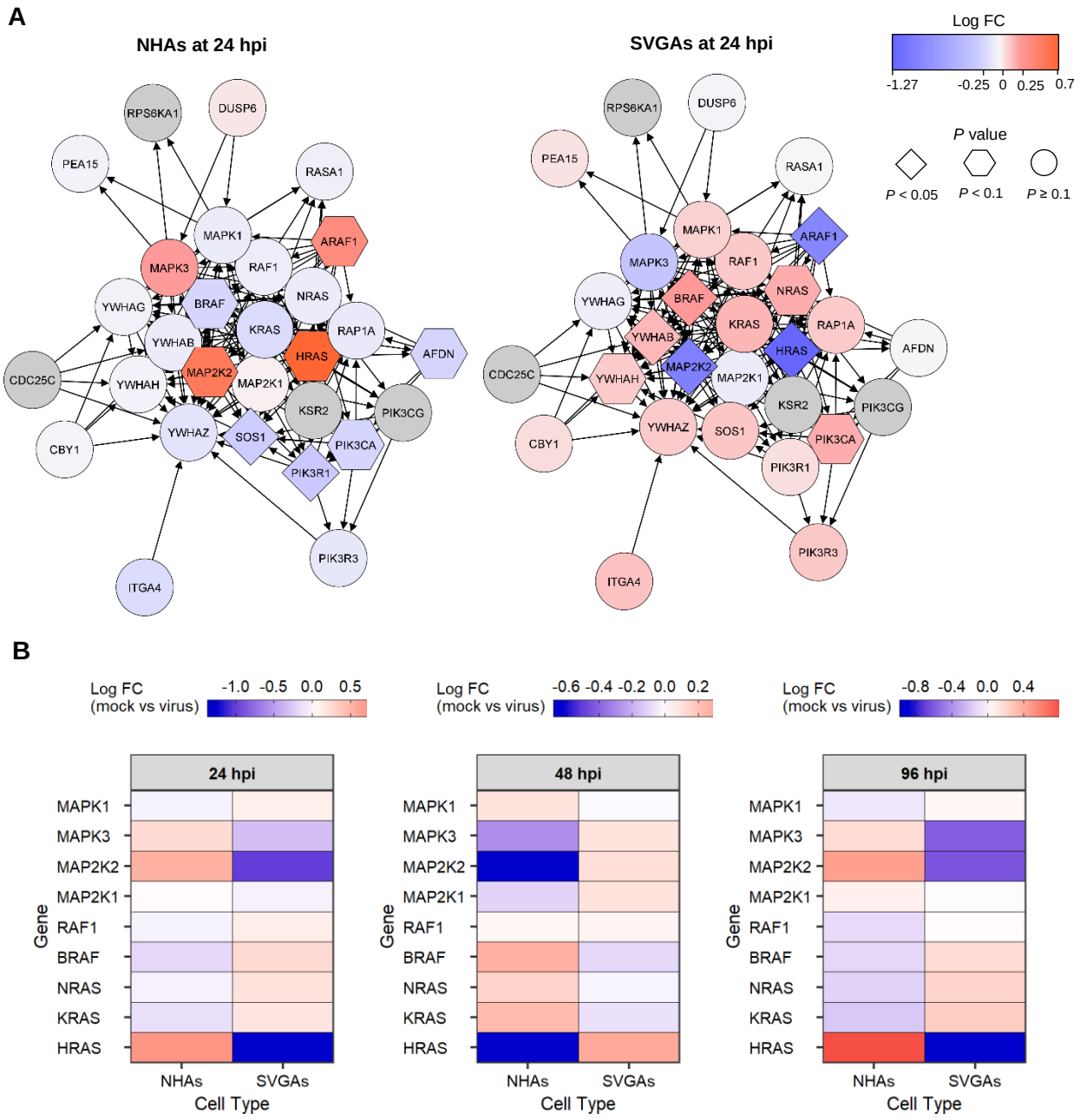

Figure 3.2. The MAPK-ERK1/2 cascade and associated gene networks are differentially expressed in NHAs compared to SVGAs during JCPyV infection. (A) Genes of the MAPK-ERK1/2 cascade were entered in the STRING interaction database to determine the protein-protein interactions determined experimentally or from curated databases of the immediate, surrounding genes within the MAPK-ERK1/2 cascade of NHAs (left) or SVGAs (right). These interactions were defined as having an interaction score of 0.9 with no more than 10 interactors in the 1st and 2nd shell. Each node (i.e. gene) was colored based on the Log_2 fold change of JCPyV-infected to mock-infected cells at 24 h, and the shape of the gene represents the significance. Arrows point from the source gene to the target gene. Genes colored gray were in the network but filtered out of the RNA-seq analysis. (B) Heat map indicates the Log_2 fold change of JCPyV-infected versus mock-infected cells of the genes within the MAPK-ERK1/2 cascade at 24, 48, and 96 hpi (B).

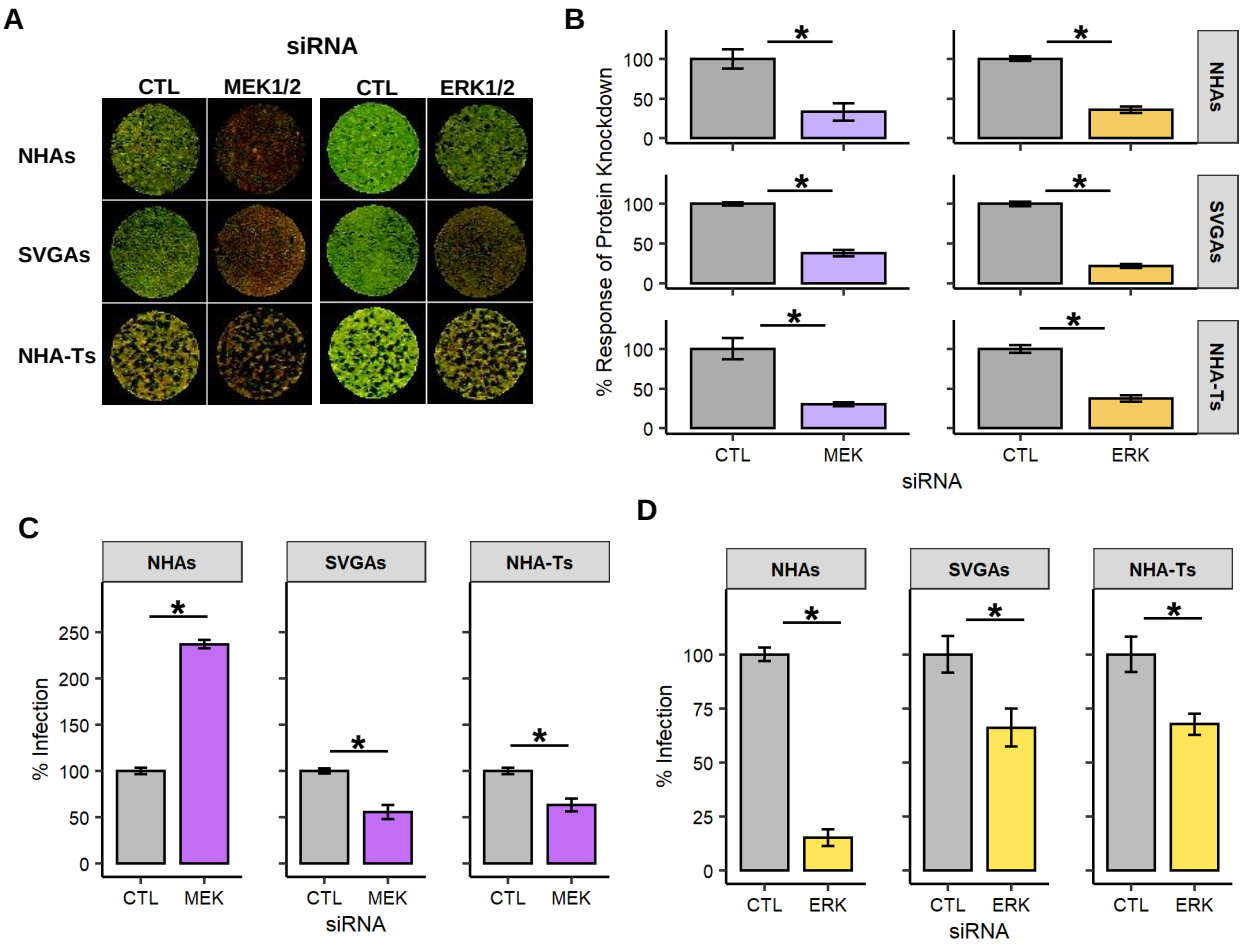

Figure 3.3. MEK and ERK knockdown in NHAs ensue remarkable differences in the outcome of JCPyV infection. NHAs, SVGAs, and NHA-Ts were transfected with MEK1/2, ERK1/2, or EGFR (CTL) siRNA. At 72 h post-transfection, cells were fixed for analysis of MEK or ERK protein expression (A and B) or infected (C and D). (A) MEK1/2 or ERK1/2 protein expression was determined by In-Cell Western (ICW), counterstained for Total MEK1/2 or Total ERK1/2 (green) or CellTag (red). (B) Percentage of protein knockdown was measured by ICW signal intensity values per [(MEK1/2 or ERK1/2)/Cell Tag x 100% = % response] within each ICW analysis using LI-COR software. Error bars indicate SD. Student's *t test* was used to determine statistical significance comparing EGFR (CTL) treated cells to either MEK1/2 or ERK1/2 treated cells, for each cell type. *, $P < 0.01$. (C and D) Following 3 d post-transfection, cells were infected with JCPyV (MOI = 1.0 FFU/cell) at 37^{o}C for 1 h. Cells were incubated in complete media at 37^{o}C for 48 h and then fixed and stained by indirect immunofluorescence. Infectivity following MEK1/2 knockdown (C) or ERK1/2 knockdown (D) was determined by counting the number of JCPyV T Ag-positive nuclei divided by the number of DAPI-positive nuclei for five ×20 fields of view for triplicate samples. Error bars indicate SD. Student's *t test* was used to determine statistical significance comparing EGFR (CTL)-treated cells to either MEK1/2- (C) or ERK1/2- (D) treated cells, for each cell type. *, $P < 0.01$.

DUSP1 transcript decreases during JCPyV infection in NHAs and is essential in regulating the MAPK/ERK pathway compared to immortalized cells

DUSPs are key regulators in the MAPK/ERK pathway, important for the magnitude, duration, and spatiotemporal expression patterns of MAPKs (210–212). Due to the significant differences in JCPyV infection observed from siRNA knockdown of MEK and ERK among cell types, and the implication of DUSPs in viral infection, the role of these phosphatases was investigated to determine whether they play a role in JCPyV infection and regulation of the MAPK/ERK pathway in NHAs. RNA-seq data revealed that the majority of typical DUSPs (i.e. DUSPs that have either the MAP kinase-binding (MKB) motif or the kinase-interacting motif (KIM)) (320) were upregulated at 24 hpi in NHAs compared to SVGAs, including DUSP1, DUSP6, DUSP7, and DUSP8 (Fig. 3.4A). However, only the expression of DUSP1 declined in NHAs at 48 hpi and remained low at 96 hpi, as JCPyV infection progressed (Fig. 3.4A). These findings suggest that the downregulation of DUSP1 is required for JCPyV to establish infection in NHAs. To validate these findings, both DUSP1 transcript levels and expression were further evaluated. During the progression of JCPyV infection, DUSP1 mRNA transcript levels significantly declined in NHAs compared to SVGAs at 48 hpi and this reduction continued at 96 hpi, corresponding to trends observed in the RNA-seq data (Fig. 3.4A and Fig. 3.4B).

Cellular stability of DUSP1 can be influenced by the MAPK/ERK pathway through direct phosphorylation, preventing protein degradation (215). To further understand the biology of DUSP1 following MEK and ERK knockdown, the total and phosphorylated levels of both kinases as well as DUSP1 phosphorylation were measured by ICW following three days post-transfection of MEK and ERK siRNA treatment (Fig. 3.4C and Fig. 3.4D). A specific antibody that recognizes ERK-mediated phosphorylation of DUSP1 at residues Ser-359 and Ser-364 was used to understand if MEK or ERK knockdown resulted in DUSP1 stability (215). There was no significant difference in levels of total MEK, pMEK, total ERK, or pERK in NHAs compared to SVGAs following treatment of MEK siRNA (Fig. 3.4C);

however, it is important to note, that ERK phosphorylation was significantly increased in NHAs treated with MEK siRNA compared to the control siRNA (data not shown). These results are surprising, as MEK1/2 are the only kinases known to activate ERK1/2 (333, 334). Additionally, there were no significant differences in total ERK, pERK, total MEK, or pMEK across cell types following treatment of ERK siRNA (Fig. 3.4C). However, there were significant differences in DUSP1 phosphorylation following MEK or ERK knockdown (Fig. 3.4D). Treating cells with MEK siRNA resulted in increased levels of pDUSP1 in NHAs compared to SVGAs and NHA-Ts, while having similar levels of protein knockdown (Fig. 3.4D). Conversely, treating cells with ERK siRNA resulted in decreased levels of pDUSP1 in NHAs compared to SVGAs and NHA-Ts at 3 days post-transfection, with similar levels of ERK knockdown (Fig. 3.4D). Altogether, these data suggest that JCPyV infection in NHAs is dependent upon DUSP1 expression, more so, than in immortalized cells. Additionally, when the MAPK/ERK pathway is disrupted in primary astrocytes, either from MEK or ERK knockdown, regulatory proteins like DUSP1 are activated or suppressed, respectively. MEK knockdown resulted in increased levels of ERK phosphorylation in NHAs, subsequent increased levels of DUSP1 phosphorylation and thus DUSP1 stability (215), while ERK knockdown resulted in a decrease of DUSP1 phosphorylation. These regulatory mechanisms were distinct to primary astrocytes and not seen in immortalized cells, which may result in the differences in outcomes of viral infection following either MEK or ERK knockdown in NHAs (Fig. 3.3).

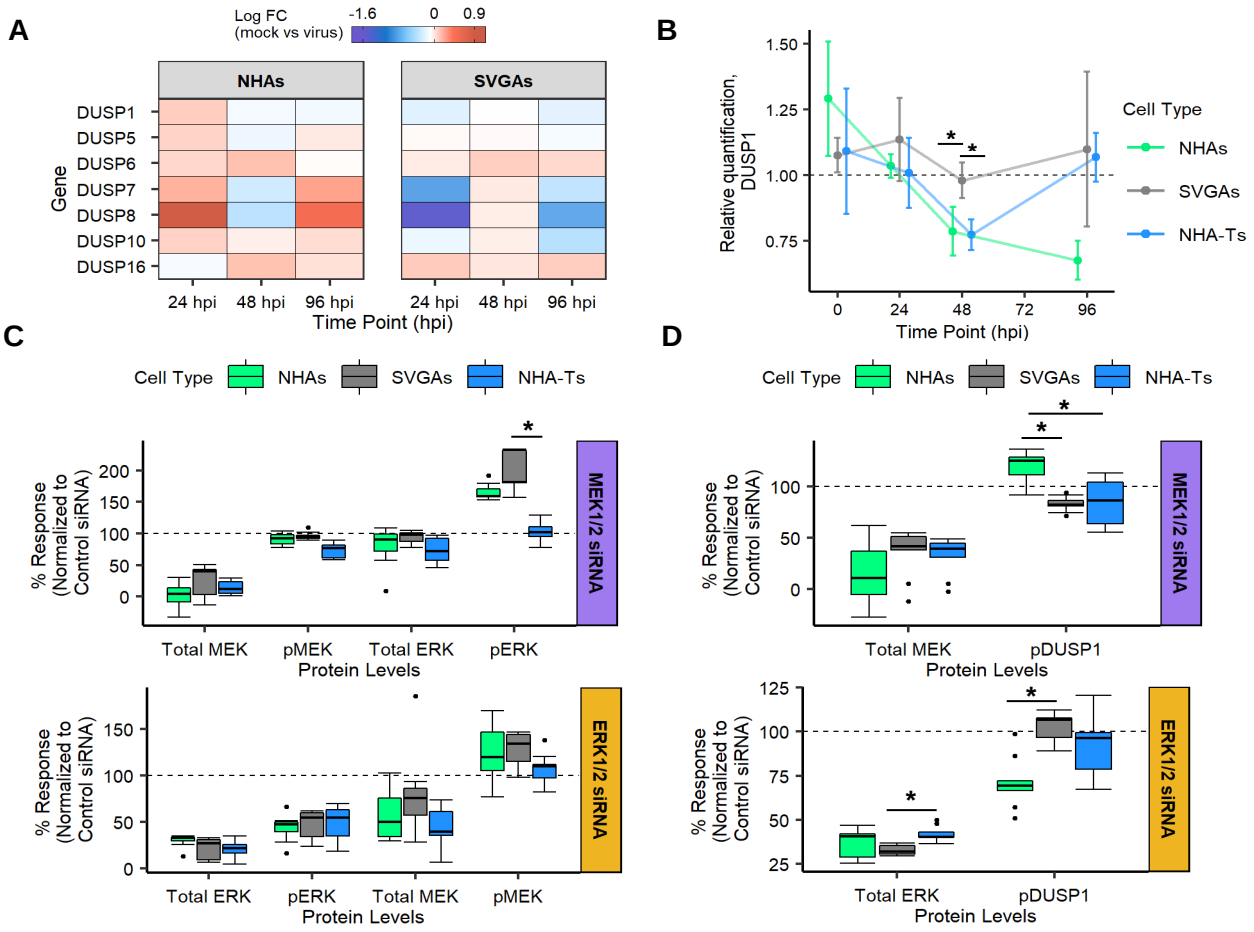

Figure 3.4. Dual-specificity phosphatases (DUSPs) are differentially expressed early during infection and when either expression of MEK1/2 and ERK1/2 are reduced in primary astrocytes. (A) Heat map indicates the Log_2 fold change of typical DUSPs differentially expressed in NHAs and SVGAs at 24, 48, and 96 hpi derived from the RNA-Seq data. (B) NHAs, SVGAs, and NHA-Ts were infected with JCPyV (MOI = 0.1 FFU/cell) or the mock-infected vehicle control at 37°C for 1 h and incubated in complete media for 0, 24, 48, and 96 h. At each time point, RNA was extracted, and host transcript levels were determined by qPCR. Data represent the relative quantification of DUSP1 transcript in infected cells compared to uninfected cells, first normalized to the Ct values of GAPDH for each treatment ($2^{-\Delta\Delta CT}$). Error bars indicate SD. Data are representative of the average fold change calculated from triplicate samples from three independent experiments. One-way analysis of variance (ANOVA) was used to determine statistical significance comparing the relative quantification of DUSP1 in NHAs, NHA-Ts, and SVGAs at each timepoint. *, $P < 0.05$. (C and D) NHAs, SVGAs, and NHA-Ts were transfected with MEK1/2, ERK1/2, or EGFR (CTL) siRNA. At 72 h post-transfection, cells were fixed for analysis of protein expression. Total MEK, pMEK, Total ERK, and pERK levels were measured following MEK1/2 siRNA (C, top) or ERK1/2 siRNA (C, bottom) treatment. DUSP1 phosphorylation was also measured following MEK1/2 siRNA (D, top) or ERK1/2 siRNA (D, bottom). Percentage of protein expression was measured by ICW signal intensity values per [(protein of interest)/Cell Tag x 100% = % response] within each ICW analysis using LI-COR software. Cells treated with MEK1/2 or ERK1/2 siRNAs were normalized to the respected EGFR (CTL) control (dashed line). Box and Whisker plots represent the distribution of 9 samples, with the median denoted by the black line and whiskers representing values 1.5 times the distance of the inter-quartile range. Outliers are represented by black dots. A pairwise Wilcoxon rank sum test, along with the Bonferroni adjustment was used to compare mock and infected cells at each time point across each cell type. *, $P < 0.01$. Data represent three independent experiments performed in triplicate.

ERK phosphorylation and subsequently DUSP1 phosphorylation was significantly inhibited in primary astrocytes early during JCPyV infection

Considering the significant disparity of differential gene expression in NHAs versus SVGAs at 24 hpi (Fig. 3.1B), decreased DUSP1 transcript levels 24 hpi in NHAs (Fig. 3.4A and Fig. 3.4B), and significantly altered DUSP1 phosphorylation in NHAs following either MEK or ERK siRNA, the expression of both ERK and DUSP1 was measured 24 hpi. As reported in Robitaille et. al, DUSP1 is induced as early as 6 hpi by SeV and RSV (323). To understand if DUSP1 is activated early during JCPyV infection in NHAs, DUSP1 phosphorylation and ERK phosphorylation was measured at 0, 6, and 24 hpi in all three cell types. At 6 hpi, both ERK and DUSP1 phosphorylation was significantly lower in NHAs compared to immortalized cells, and at 24 hpi, this distinction was more discernible (Fig. 3.5). NHA-Ts expressed the highest levels of ERK and DUSP1 phosphorylation followed by SVGAs, while NHAs expressed the lowest (Fig. 3.5). Total levels of DUSP1 remained unchanged at 0, 6, and 24 hpi compared across all three cell types, suggesting the protein was not targeted for degradation (data not shown). Together, these data indicate that ERK phosphorylation and subsequent DUSP1 phosphorylation is inhibited early during JCPyV infection, reducing DUSP1 stability by ERK-mediated phosphorylation in primary astrocytes, but is not targeted for protein degradation.

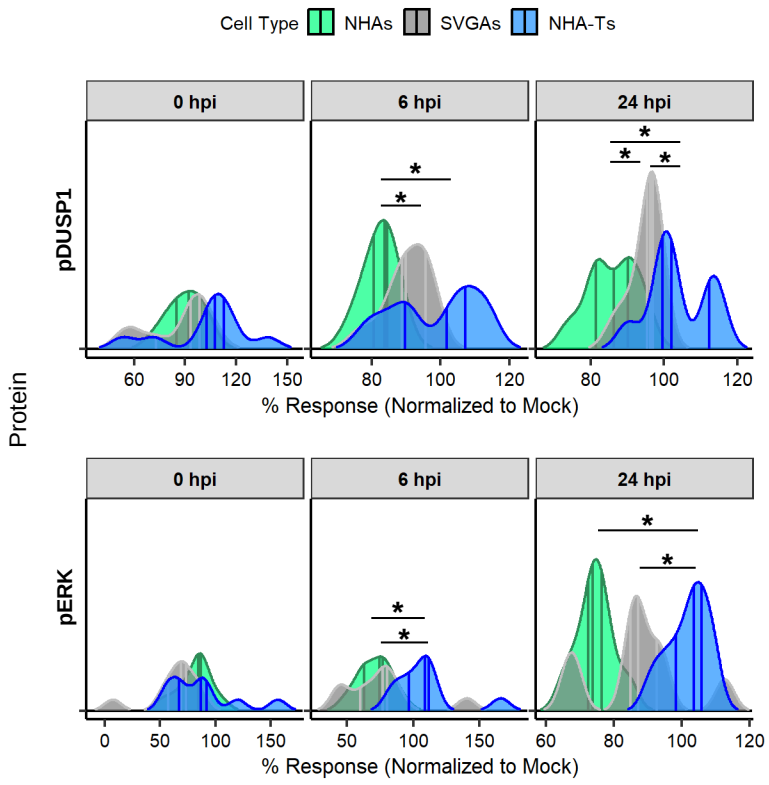

Figure 3.5. DUSP1 and ERK phosphorylation is reduced in NHAs compared to immortalized cells during JCPyV infection. NHAs, SVGAs, and NHA-Ts were infected with JCPyV (MOI = 1 FFU/cell) or mock-infected with a vehicle control, incubated at 37°C for 0, 6, or 24 h, fixed and counterstained for pDUSP1 (top) or pERK (bottom). Protein expression was measured by ICW and quantitation was performed using LI-COR software. Wells infected with JCPyV were normalized to the wells that were treated with the mock-infected vehicle control. Density ridgeline plots represent the distribution of samples with the lower quartile, median and upper quartile denoted as colored lines in each distribution. A pairwise Wilcoxon rank sum test, along with the Bonferroni adjustment was used to compare the median distribution in each cell type. *, $P < 0.05$. Data represent three independent experiments performed in triplicate.

Hyperactivation of ERK through DUSP inhibition increases JCPyV infection in primary astrocytes

As increasing ERK phosphorylation significantly increased infection in NHAs (Fig. 3.4C and Fig. 3.3C), we hypothesized that activation of ERK in NHAs, through inhibition of DUSP1, would increase JCPyV infection. To inhibit the enzymatic activity of DUSP1 on ERK, all cell types were treated with BCI, an allosteric inhibitor of DUSP1 and DUSP6 that has been shown to result in the activation of ERK (335–337), were subsequently infected with JCPyV, and infection was scored by quantitation of both the early gene product, T Ag and late gene product, VP1 by indirect immunofluorescence (Fig. 3.6A). BCI

significantly increased JCPyV infection in NHAs while no difference in infection was observed in immortalized cells (Fig. 3.6A). Despite the significant increase in VP1 expression in NHAs however, the overall level of VP1 expression in NHAs remained lower compared to SVGAs and NHA-Ts (data not shown). To validate that BCI treatment results in increased ERK phosphorylation in NHAs during JCPyV infection, cells were pre-treated with BCl and infected with JCPyV in the presence of either DMSO or BCI for 24 h, and cellular ERK and DUSP1 phosphorylation, as well as total DUSP1 levels, were measured by ICW (Fig. 3.6B). BCI treatment increased the levels of pERK in NHAs similar to that in immortalized cells, while decreasing the levels of pDUSP1 and total DUSP1, although this difference was not significant among cell types (Fig. 3.6B). Collectively, these data suggest that ERK is phosphorylated upon blocking the interaction of DUSP1 with ERK, leading to increased JCPyV infection in NHAs. These data substantiate the significant increase of JCPyV infection following MEK siRNA as well (Fig. 3.3C), therein treatment of MEK siRNA resulted in a significant increase of phosphorylated ERK (Fig. 3.4C).

DUSP1 is required for JCPyV infection in NHAs

It has been previously reported that DUSP1 knockdown reduced viral infection by HSV (219, 322). To further unfold the importance of DUSP1 during JCPyV infection, the protein was knocked down using siRNA followed by infection with JCPyV (Fig. 3.7). Protein knockdown was analyzed by ICW (Fig. 3.7A) and quantified using LI-COR software (Fig. 3.7B). Reduction of DUSP1 protein levels was significantly lower compared to the control siRNA, in all cell types at 24 hours post siRNA treatment (Fig. 3.7B). Following protein knockdown, all cell types were infected with JCPyV and infection was scored at 48 hpi (Fig. 3.7C). DUSP1 knockdown significantly reduced JCPyV infection in NHAs yet had no impact on infection in SVGAs or NHA-Ts (Fig. 3.7C). These results demonstrate the requirement of DUSP1 during JCPyV infection of NHAs. Also, this further validates the importance of this protein during viral infection

that is confounded by the immortalized properties in SVGAs and NHA-Ts, as both inhibition by BCI (Fig. 3.6A) and siRNA reduction of DUSP1 (Fig. 3.7C) did not influence JCPyV infection in either cell type.

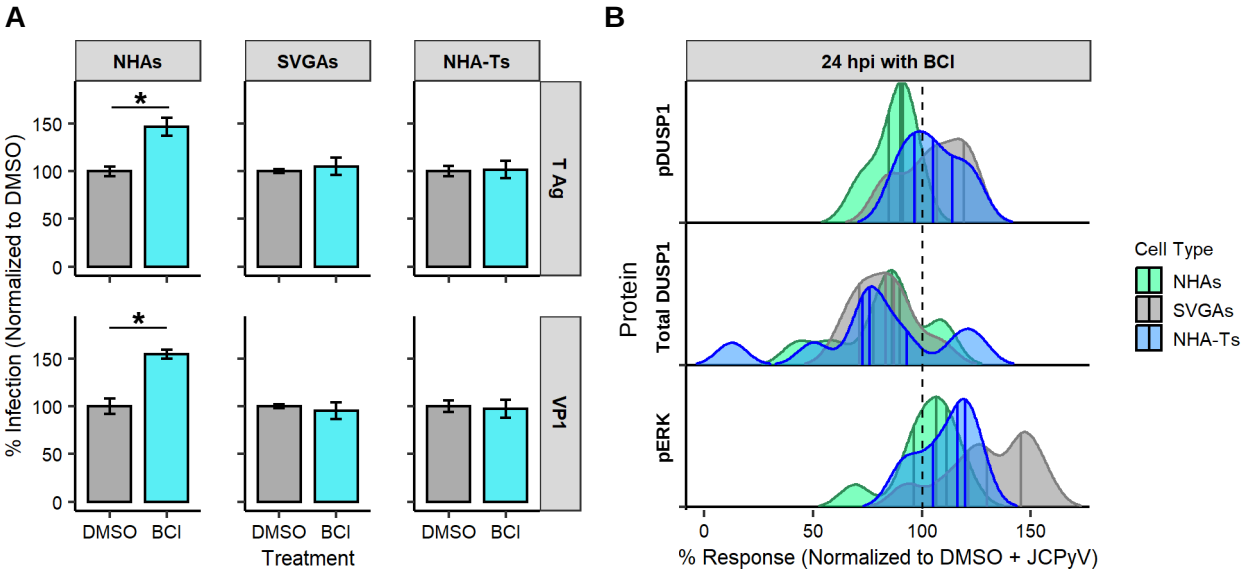

Figure 3.6. Activation of ERK through allosteric inhibition of DUSP1, increases infection in NHAs. (A) NHAs, SVGAs, and NHA-Ts were pretreated with the DUSP1/6 inhibitor, BCI at 1uM or DMSO at an equivalent volume and then infected with JCPyV (MOI = 2.0 FFU/cell) at 37°C for 1 h. Cells were incubated in media containing DMSO or BCI for 72 h then fixed and stained by indirect immunofluorescence for JCPyV T Ag and VP1, respectively. Percent infection was determined by quantifying the number of T Ag- (top) or VP1- (bottom) positive nuclei divided by the number of DAPI-positive nuclei for five ×20 fields of view for triplicate samples. Data is representative of three individual experiments. Error bars indicate SD. Student's *t test* was used to determine statistical significance comparing DMSO to BCI, within each cell type and viral protein. *, $P < 0.01$. (B) NHAs, SVGAs, and NHA-Ts were pretreated with the DUSP1/6 inhibitor, BCI at 1uM or DMSO at an equivalent volume control and then infected with JCPyV (MOI = 2.0 FFU/cell) at 37°C for 1 h. Cells were incubated in media containing DMSO or BCI for 24 h then fixed and counterstained for pDUSP1 (top), Total DUSP1 (middle), or pERK (bottom). Protein expression was measured by ICW and image analysis was performed in the LI-COR software. BCI-treated wells were normalized to the wells that were treated with DMSO + JCPyV (dashed line). Density ridgeline plots represent the distribution from three independent experiments performed in triplicate with the lower quartile, median and upper quartile denoted as colored lines in each distribution. A pairwise Wilcoxon rank sum test, along with the Bonferroni adjustment was used to compare the median distribution in each cell type. Protein levels were not significant with each cell type, $P < 0.01$.

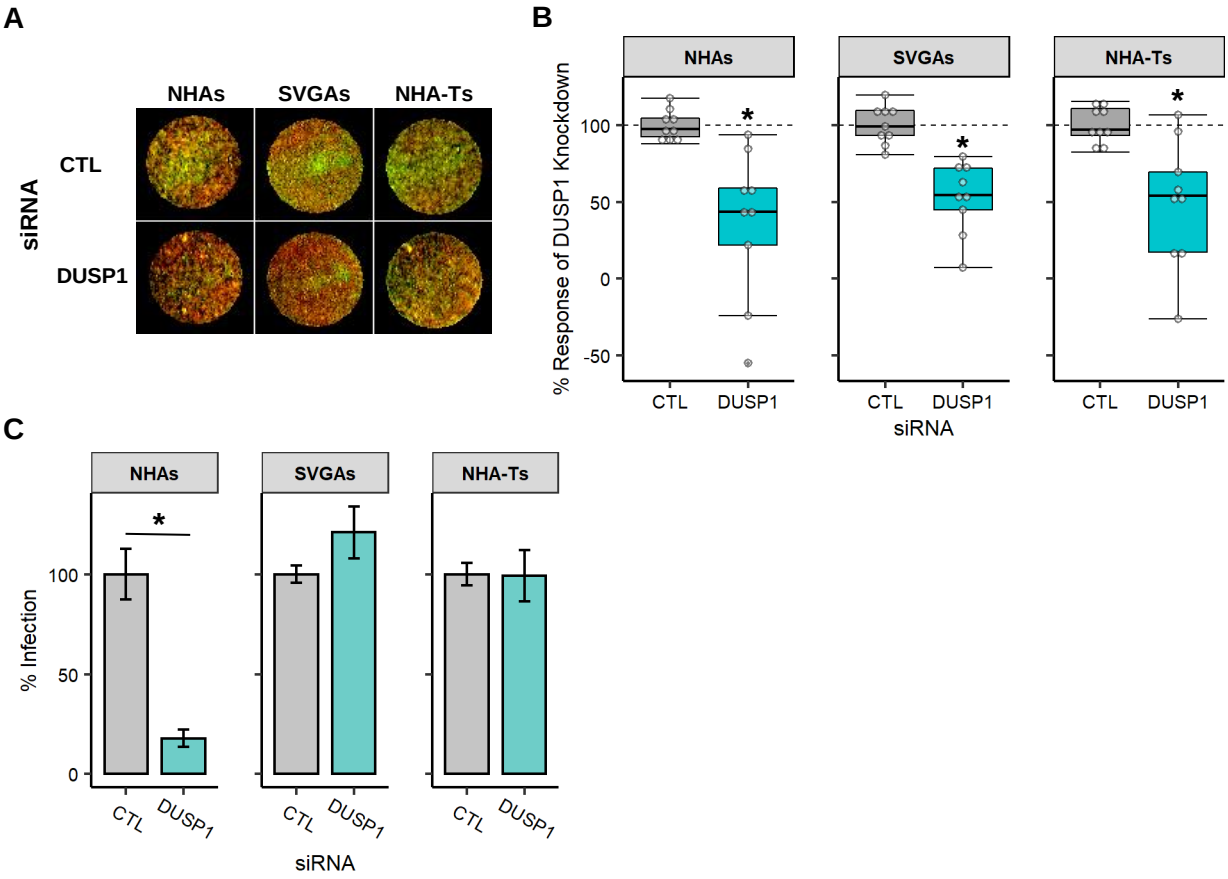

Figure 3.7. DUSP1 is required for JCPyV infection in NHAs. NHAs, SVGAs, and NHA-Ts were transfected with DUSP1 or EGFR (CTL) siRNA. At 24 h post-transfection, cells were fixed, imaged, and quantified for protein knockdown (A and B) or infected (C). (A) DUSP1 protein expression was determined by ICW, counterstained for total DUSP1 (green) or CellTag (red). (B) Quantification of DUSP1 protein expression was measured by ICW signal intensity values per [(DUSP1)/Cell Tag x 100% = % response] within each ICW analysis in LI-COR software. Cells treated with DUSP1 siRNA were normalized to the respected EGFR (CTL) siRNA (dashed line). Box and Whisker plots represents the distribution of 9 samples, with the median denoted by the black line and whiskers representing values 1.5 times the distance of the inter-quartile range. Outliers are represented by gray dots. A pairwise Wilcoxon rank sum test, along with the Bonferroni adjustment was used to compare mock and infected cells at each time point across each cell type. *, $P < 0.01$. Data are representative of three independent experiments performed in triplicate. (C) At 24 h post-transfection, cells were infected with JCPyV (MOI = 1.0 FFU/cell) at 37^{o}C for 1 h. Cells were incubated in complete media for 48 h and then fixed and stained by indirect immunofluorescence. Percent infection following DUSP1 knockdown was determined by quantifying the number of JCPyV T Ag-positive nuclei divided by the number of DAPI-positive nuclei for five ×20 fields of view for triplicate samples. Error bars indicate SD. Student's *t test* was used to determine statistical significance comparing EGFR (CTL) siRNA-treated cells to DUSP1 siRNA-treated cells, for each cell type. *, $P < 0.01$.

The network of genes related to the interactions of DUSP1 and ERK1/2 are involved in the pathways of the immune response, cell survival, and apoptosis

To understand the cellular pathways and the downstream impacts that may be influenced by the disruption of DUSP1 interactions with ERK1/2 through knockdown, the genes: *DUSP1, MAPK3* (ERK1), and *MAPK1* (ERK2) were entered in the STRING interaction database and an over-representation analysis was performed using the PANTHER (protein analysis through evolutionary relationships) pathway database (Fig. 3.8). The network was expanded three times to elucidate the genes in the immediate proximity of *DUSP1, MAPK3* (ERK1), and *MAPK1* (ERK2) having known and predicted interactions with other genes and a medium confidence interaction score, with no more than 10 interactors in the 1st and 2nd shell (Fig. 3.8A). These genes were then analyzed in the RNA-seq data to determine the $\log_2$ fold change in NHAs and SVGAs at 24 h and are summarized as a heatmap (Fig. 3.8B). These data illustrate that largely, genes within the DUSP1 and ERK1/2 network, have a negative fold change in SVGAs during JCPyV infection, however, *MAPK3* (ERK1), *ATF3, JUNB*, and *MAPK8IP1* were differentially expressed in NHAs during viral infection (Fig. 3.8B). To further understand the biological function of the network of genes from the interactions of DUSP1 and ERK1/2, the list was entered in the Gene Ontology website and an over-representation analysis was performed, using the PANTHER pathway database (Fig. 3.8C). The GoChord plot summarizes the 17 genes (*MAPK8IP1* was not included as it is not in the PANTHER database) and are connected with ribbons to the respected cellular pathway. The legend defines the difference from the $\log_2$ fold change of NHAs to the $\log_2$ fold change of SVGAs to simplify the output. Genes that are orange/yellow have a large positive difference between NHAs and SVGAs, and genes colored blue have a small or negative change between cell types during JCPyV infection. Genes that had a greater positive change (i.e. *JUNB, IRS1, MAPK3* (ERK1)*, FOS, JUN*, and *ATF3*) were associated with pathways of inflammation mediated by chemokine and cytokine signaling pathways, including TGF-β signaling, apoptotic, and cholecystokinin receptors (CCKR) signaling pathways

(Fig. 3.8C). These data suggest that in primary astrocytes, the network of genes associated with *DUSP1, MAPK3* (ERK1), and *MAPK1* (ERK2) are important during JCPyV infection for both the host and the virus. Primary astrocytes may induce an immune response by releasing cytokines and chemokines early during infection, not seen in SVGAs, but in turn, the virus is slowly activating transcription factors, like Smad4 from the TGF-β signaling pathway to support viral replication in the nucleus of NHAs (205). The differences in signaling pathway outcomes can help postulate why DUSP1 inhibition either through knockdown (Fig. 3.7) or hyperactivation of ERK through allosteric inhibition of DUSP1 (Fig. 3.6) can lead to different outcomes of JCPyV infection in primary astrocytes (Fig. 3.9).

Discussion

JCPyV specifically targets glial cells in the CNS, including astrocytes, which have been implicated as a potential reservoir for infection, eventually leading to the pathogenesis of PML (68). However, due to limited *in vivo* approaches, our knowledge of JCPyV infection in astrocytes is incomplete. Thus, RNA-seq analysis was performed using primary human astrocytes infected with JCPyV at time points previously established to be important in the production of viral T Ag and VP1 (Fig. 3.1A) (130). A comparative approach of JCPyV infection in primary human astrocytes to the more-commonly studied immortalized glial cell line, SVGAs, provides a thorough understanding of the host transcriptomic profile during infection in primary vs. immortalized cells. RNA-seq revealed a significant, distinct transcriptomic profile in NHAs during JCPyV infection when compared to SVGAs. This is illustrated by the temporal difference in gene expression of the MAPK/ERK pathway during infection and illuminated a critical role for DUSPs, specifically DUSP1, during JCPyV infection in NHAs. The role of ERK1/2 and DUSP1 were further validated using protein expression assays and protein inhibition or activation by either chemical treatment or siRNA, revealing the notable role these proteins have during JCPyV infection in NHAs (Fig.

3.9). Utilizing additional bioinformatics techniques, we have elucidated novel pathways that are activated during JCPyV infection in NHAs.

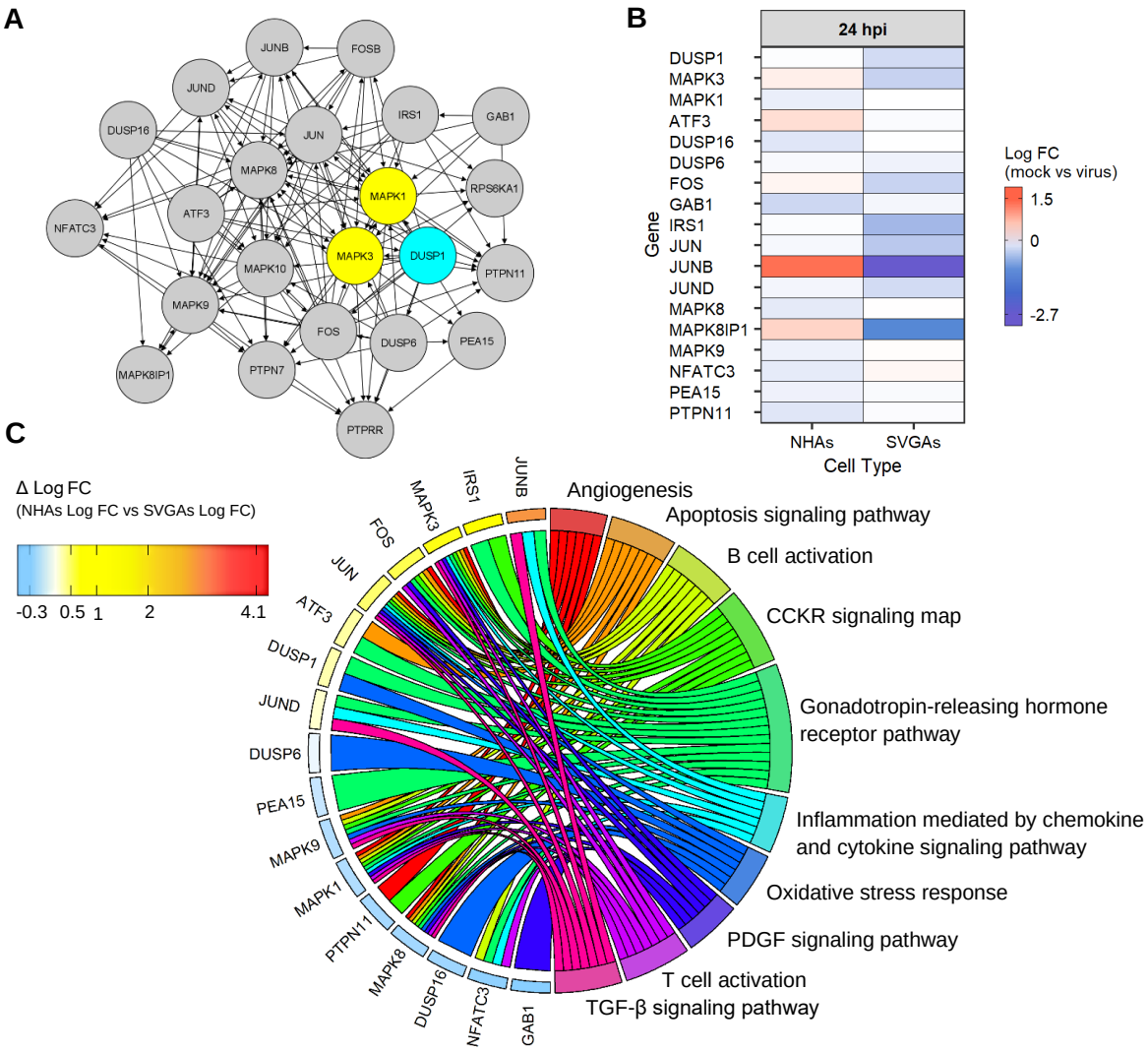

Figure 3.8. PANTHER pathway analysis of the genes within the DUSP1-ERK1/2 network demonstrate a response to immune activation and downstream activation of the receptor tyrosine kinase pathways. (A) Genes, ERK1/2 and DUSP1 were analyzed in the STRING interaction database and the network was expanded three times to determine the protein-protein interactions of both known and predicted interactions of the surrounding genes. These interactions were defined as having an interaction score of 0.4 with no more than 10 interactors in the 1st and 2nd shell. Arrows point from the source gene to the target gene. (B) The heat map illustrates the Log_2 fold change of JCPyV-infected versus mock-infected NHAs and SVGAs for all genes in the previous network that were differentially expressed at 24 h. (C) PANTHER pathway analysis was used to identify the pathways from the genes in the ERK1/2 and DUSP1 network. A GOChord plot represents the top ten pathways, representing at least 35% of the 17 genes in the network. Each gene is linked via ribbons to their assigned PANTHER pathway term and the colored bars next to each gene represent the difference of the Log_2 fold change in JCPyV-infected versus mock-infected NHAs and JCPyV-infected versus mock-infected SVGAs. The gene, *MAPK8IP1* was not included in the PANTHER pathway analysis as there was no hit in the PANTHER pathway database.

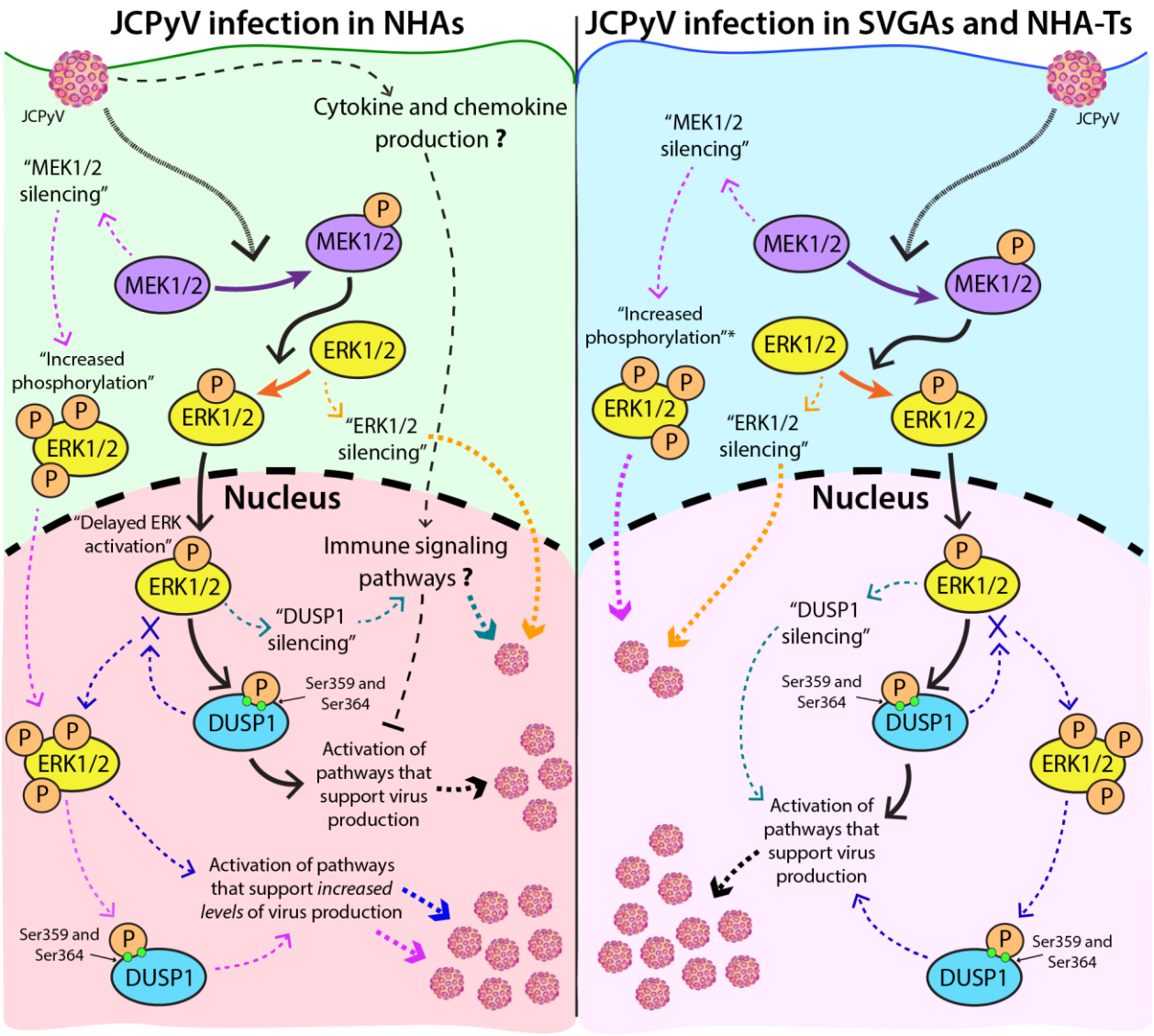

Figure 3.9. **MAPK/ERK pathway during JCPyV infection and summary of the various outcomes following treatment of siRNAs or inhibitors.** In NHAs (left) JCPyV activates the MAPK/ERK pathway resulting in the phosphorylation of kinases and DUSP1 to subsequently activate additional pathways supporting virus production (black, solid arrows). Dashed, black arrows represent possible pathways activated in NHAs, modulating an immune response during JCPyV infection, not seen in SVGAs. Treatment of MEK1/2 siRNA (purple, dashed arrows), increased ERK phosphorylation which led to an increase in JCPyV infection in NHAs while treatment of ERK1/2 (orange, dashed arrows) and DUSP1 (turquoise, dashed arrows) siRNA decreased viral infection. Using an allosteric inhibitor of DUSP1 (blue, dashed arrows) led to an increase in ERK phosphorylation and subsequently increased JCPyV infection in NHAs (left). In comparison, infection of SVGAs and NHA-Ts also requires hijacking the MAPK/ERK pathway, however there are notable differences (right). Treatment of MEK1/2 (purple, dashed arrows) and ERK1/2 (orange, dashed arrows) siRNA significantly reduced infection in SVGAs and NHA-Ts, (right), while DUSP1 siRNA (turquoise, dashed arrows) or allosteric inhibition (blue, dashed arrows) did not alter JCPyV infection in either cell type, regardless of ERK activation. (*, Increased ERK phosphorylation was observed in SVGAs following MEK1/2 siRNA not in NHA-Ts).

Our laboratory recently determined that the JCPyV infectious cycle in NHAs was delayed compared to the infectious cycle in SVGAs (130). RNA-seq analysis revealed that at 24 hpi, a significant number of genes that were differentially expressed in SVGAs were downregulated during JCPyV infection; comparatively, more genes were upregulated in NHAs (Fig. 3.1B). At 48 hpi, most genes differentially expressed in NHAs were downregulated, resembling the 24-hour time point in SVGAs (Fig. 3.1B). These data suggest that the delay of JCPyV infection in NHAs previously described, may be regulated in part by the virus establishing infection more efficiently in SVGAs as numerous genes may already be downregulated due to the immortalized characteristics of the cell type (122, 123), however, SVGAs are also a heterogeneous population of cells (124). The results illustrated in Figure 3.1 may accurately portray the differential gene expression of JCPyV infection in astrocytes, further elucidating their role during JCPyV infection and pathogenesis of the CNS.

To further define astrocytic infection, the MAPK/ERK pathway was explored as it has been demonstrated to be a critical regulator of JCPyV infection in SVGAs and other cell types (94, 193). The MAPK/ERK pathway activates various genes and transcription factors through a cascade of kinases that organize events for cellular proliferation, differentiation, and survival (192). Given this evidence, the MAPK/ERK pathway and genes with protein-protein interactions were identified in the RNA-seq data (Fig. 3.2). Several kinases within the pathway were differentially expressed, most notably, *HRAS,* and *MAP2K2* (MEK2) at 24 and 96 hpi in NHAs (Fig. 3.2B). Expanding this analysis to genes that interact with the MAPK/ERK pathway also revealed differentially expressed genes. For example, at 24 hpi, *SOS1* was significantly downregulated in NHAs. *SOS1,* is a critical linker between tyrosine kinase receptors, and activation of *KRAS* in the MAPK/ERK pathway, as it interacts with *KRAS* to potentially influence the duration and magnitude of ERK activation (338–340). The significant downregulation of this gene at 24 hpi in NHAs provides additional rationale for the decreased phosphorylation of ERK and DUSP1 observed during infection (Fig. 3.5). ERK activation is delayed in NHAs compared to infection in immortalized cells

(Fig. 3.5), pronounced more so with upstream kinases (i.e. *KRAS, NRAS, RAF1,* and *BRAF*). Further, genes determined to have protein-protein interactions, like *SOS1*, of the MAPK/ERK pathway, were downregulated at 24 hpi (Fig. 3.2A). RNA-seq results also revealed temporal, differential gene expression over the course of infection in both cell types from 24 to 96 hpi. It has been previously reported that MEK and ERK phosphorylation is biphasic during JCPyV infection (193, 205) and these data substantiate the biphasic expression of not only ERK but the other kinases in the pathway. Interestingly, the gene expression of these kinases was temporally regulated in NHAs and SVGAs, yet the expression of them was non-concurrent at each timepoint (Fig. 3.2). These data establish the requirement of the MAPK/ERK pathway in NHAs; however, it reveals differential expression and activation dynamics between cell types for MAPK/ERK pathway utilization during viral infection.

To validate the RNA-seq results and further define the importance of the MAPK/ERK pathway in NHAs during JCPyV infection, MEK1/2 and ERK1/2 were targeted for knockdown using siRNA (Fig. 3.3). Knocking down ERK1/2 resulted in a significant decrease in JCPyV infection in NHAs, confirming previously-reported results (193). Conversely, when knocking down MEK1/2 in NHAs, infection significantly increased, yet in NHAs immortalized with SV40 T Ag (i.e. NHA-Ts), infection was reduced, comparable to infection in SVGAs (Fig 3.3C). Research demonstrated thereafter, characterized this outcome by examining both the regulatory role of DUSPs, specifically DUSP1, in the MAPK/ERK pathway and how ERK is involved in JCPyV infection of NHAs compared to infection in SVGAs and NHA-Ts.

DUSPs are key negative regulatory proteins of the MAPK/ERK pathway (209–212). RNA-seq analysis revealed that multiple DUSPs were differentially expressed during infection of NHAs at 24 hpi (Fig. 3.4A). However, only the expression of DUSP1 was downregulated at 48 and 96 hpi, as the JCPyV infectious cycle progressed in NHAs (Fig. 3.4A). To validate these findings, the relative quantification of DUSP1 was determined by qPCR. Although there were no significant differences at 24 hpi across cell types, there was a significant decrease of DUSP1 transcript at 48 hpi in NHAs compared to SVGAs and

the transcript levels of DUSP1 further decreased in NHAs at 96 hpi (Fig. 3.4B). Taken together, as viral infection ensues in NHAs, the MAPK/ERK pathway is activated, impeding the negative regulatory role of DUSP1, and ultimately, transforming the cell into a conducive environment to support viral replication.

Apart from DUSP1 expression during JCPyV infection, DUSP1 phosphorylation following MEK1/2 and ERK1/2 siRNA was only impacted in NHAs (Fig. 3.4C and Fig. 3.4D). These data revealed that compared to immortalized cells, the expression of DUSP1 in NHAs was sensitive to disruptions of the MAPK/ERK pathway. Furthermore, it introduced rationale for the significant differences observed from siRNA treatment. ERK phosphorylation induced DUSP1 phosphorylation (Fig. 3.4C, top and Fig. 3.4D, top) which led to a significant increase in JCPyV infection in NHAs (Fig. 3.3C). However, when ERK phosphorylation was inhibited, DUSP1 phosphorylation was reduced (Fig. 3.4C, bottom and Fig. 3.4D, bottom), and JCPyV infection decreased in NHAs (Fig. 3.4D). Noticeably, ERK was significantly phosphorylated in NHAs and SVGAs following MEK1/2 siRNA. Future studies are required to understand how ERK1/2 is being phosphorylated in these circumstances, as MEK1/2 are the only kinases that are known to phosphorylate ERK at the Thr and Tyr residues (333, 334).

To substantiate the results of ERK hyperactivation from MEK1/2 siRNA leading to an increase in JCPyV infection in NHAs, an allosteric inhibitor of DUSP1, that is known to activate ERK, was used to determine the impacts of JCPyV infection on each cell type. NHAs were treated with the inhibitor, BCI, resulting in a significant increase in viral infection (Fig. 3.6A), concurrently increasing levels of pERK comparable to that in SVGAs and NHA-Ts (Fig. 3.6B) and similarly following MEK1/2 siRNA. The percent of VP1 expression however, was proportionate to the increase observed from T Ag, suggesting that the delay in this late gene product during JCPyV infection observed in NHAs was not due to the hindered levels of pERK and pDUSP1 observed in the first 24 h of infection (Fig. 3.5). Additionally, BCI, is an allosteric inhibitor of both DUSP1 and DUSP6 and even though only DUSP1 was examined, this research

demonstrates that only JCPyV infection in primary astrocytes was impacted during treatment, outcomes that were not observed in cells immortalized with SV40 T Ag. Further research should examine however, the role of other DUSPs, including DUSP6, 7, 8, and 10, which demonstrated interesting patterns of differential regulation in NHAs compared to SVGAs across time points. This differential expression may represent contributions to the regulation of signaling pathways or gene expression that impact JCPyV infection in these cell types.

To further define the role of DUSP1 during JCPyV infection in all three cell types, siRNA was used to target the phosphatase and infectivity was scored at 48 hpi. DUSP1 siRNA treatment resulted in a significant decrease in JCPyV infection in NHAs, but there was no difference during infection of immortalized cells (Fig. 3.7). The unaltered viral infection in SVGAs and NHA-Ts validates the previous results that were observed when treating cells with BCI. This indicates that DUSP1 is dispensable during JCPyV infection in cells immortalized with SV40 T Ag, as reduction of this phosphatase did not alter viral infection. This was observed in RSV infection of A549 cells as well, in which silencing DUSP1 did not alter viral replication (323). Conversely, the decrease in infection observed in NHAs is comparable to the results found by Choi et. al (219). HCV infection was significantly reduced upon silencing DUSP1, in which authors demonstrated that this was due to STAT1 translocation to the nucleus, increasing expression of the ISGs and thus, suppressing HCV infection (219). Similarly, Assetta et. al. demonstrated that pSTAT1 was localized to nuclei in JCPyV-infected cells, leading to the activation of ISGs and this contributed to the persistent nature of JCPyV infection in a primary kidney cell model (191). These previous findings provide premise, that when DUSP1 is knocked down during JCPyV infection in NHAs, viral infection is reduced because STAT1 is translocated to the nucleus, activating ISGs and thus, inhibiting JCPyV infection, however more research is required to support this hypothesis.

Research has demonstrated that DUSP1 has a critical role in the inflammatory response against various pathogens (218, 219, 341–343) and plays an intricate role in regulating pro- and anti-inflammatory cytokines (218). Furthermore, astrocytes are important in maintaining many neuronal functions in the CNS through production of cytokines and chemokines (145, 220). This ultimately results in astrocytes having a neurotoxic or neuroprotective role in the brain of human neurological diseases (144). Due to the role of DUSP1 in the inflammatory response and the interaction of ERK1 and ERK2, an over-representation analysis using PANTHER (331) was performed on the list of genes that have known and predicted interactions with these proteins (Fig 3.8). *JUNB,* has both predicted and known interactions with *DUSP1, MAPK3,* (ERK1), and *MAPK1* (ERK2), determined by the STRING interaction database (330), and was significantly upregulated at 24 hpi in NHAs and significantly downregulated in SVGAs (Fig. 3.8B). Through the PANTHER analysis, *JUNB*, along with *MAPK3* (ERK1), *JUN,* and *JUND*, were associated with the inflammation mediated by chemokine and cytokine signaling pathway (PANTHER Accession: P00031) (Fig. 3.8C). Furthermore, determined by a gene set enrichment analysis, preliminary data suggests, that the interleukin 10 (IL-10) signaling pathway is expressed in NHAs at 24 hpi (data not shown). These data establish that early during JCPyV infection in NHAs, astrocytes may modulate an immune response which is not activated in SVGAs.

The TGF-β signaling pathway (PANTHER Accession: P00052) was also associated with genes that had a greater difference of differential gene expression in NHAs compared to SVGAs (Fig. 3.8C). SMAD4, is involved in the TGF-β signaling pathway, regulating transcription factors of target genes in the nucleus (344) and has also been implicated in JCPyV infection (204, 205). Previous research has demonstrated that JCPyV-infected cells, expressed higher levels of SMAD4 in the nucleus compared to uninfected cells (205). Furthermore, the gene, *ATF3* (activation transcription factor-3), demonstrated higher expression in infected NHAs compared to SVGAs and is known to interact with SMAD4 (345). These findings indicate that early during JCPyV infection, genes associated with *DUSP1, MAPK3* (ERK1), and *MAPK1* (ERK2) are

involved in activating pathways that both induce a host response, while simultaneously creating a conducive environment for viral replication. This evidence provides a foundation for future studies to define how JCPyV infection activates alternative pathways in primary cells not observed in immortalized cells and may provide insight into the delayed infection in NHAs compared to infection in SVGAs.

This research further characterizes JCPyV infection in primary human astrocytes and determines the transcriptomic profile compared to that in SVGAs. These differences were also seen in the timing of MAPK/ERK pathway expression, and even though ERK phosphorylation was delayed in NHAs during JCPyV infection, siRNA targeting of the protein, significantly reduced infection. Furthermore, this research highlights a role for DUSPs, specifically DUSP1, during JCPyV infection in NHAs, which is not observed in immortalized cells. Lastly, by analyzing pathways and gene networks we have further defined how the interactions of DUSP1, ERK1, and ERK2 may activate novel cellular pathways during JCPyV infection in primary human astrocytes. This research validates and establishes novel mechanisms of JCPyV infection in primary human astrocytes, in turn, further elucidating how viral infection can lead to a deadly human disease.

CHAPTER 4

PI3K/AKT/MTOR SIGNALING PATHWAY IS REQUIRED FOR JCPYV INFECTION IN PRIMARY ASTROCYTES

The work presented in this chapter is in preparation for submission.

Introduction

JC polyomavirus (JCPyV) is a human-specific pathogen and the causative agent of a fatal disease in the central nervous system (CNS), known as progressive multifocal leukoencephalopathy (PML) (60–63). The virus is present in ~60 to 80% of the adult population, where initial infection is thought to occur in tonsillar tissue (28, 30, 44, 48), allowing for secondary infections in circulating B cells, bone marrow, and kidneys (44). In nearly all infected individuals, JCPyV is characterized as a persistent, asymptomatic infection, and virus is periodically shed in the urine (28, 30, 44–47). However, during immunosuppression JCPyV can reactivate and spread to the CNS (45, 58, 59) causing the fatal, demyelinating disease, PML (60–63). Due to the immunosuppressive state associated with HIV infection, a large proportion of individuals diagnosed with PML are infected with HIV; however, due to more effective treatments related to HIV/AIDS, PML incidence is decreasing in this population (74, 317, 346). Unfortunately, new risk groups are emerging, with a higher proportion of PML cases diagnosed in patients with hematological malignancies and in patients taking immunomodulatory therapies for immune-mediated diseases (74). Specifically, individuals with multiple sclerosis (MS) and undergoing natalizumab treatment are significantly at risk for PML development (71, 74–76). Current treatment for PML is focused on removal of immunosuppressive therapies or treating the underlying immunosuppression (71, 79–81). Additional treatment options, including adoptive T cell transfer and checkpoint inhibitors, prolong life expectancy; however, these treatments are still relatively new, and only address the underlying immunosuppression and can result in severe morbidity (71, 79, 82, 83, 347).

In the CNS, astrocytes are thought to be the main target during JCPyV infection (68). The lytic destruction of these cells, along with JCPyV infection of oligodendrocytes, leads to PML (60–63). Once a cell becomes infected, JCPyV hijacks host cell machinery to produce viral proteins, including Large T Antigen (T Ag), to create a favorable environment for JCPyV DNA replication; this occurs through the binding of Large T Ag to retinoblastoma (Rb) and sequestering p53 (114, 122). As transformation ensues and viral DNA replication progresses, the late gene expression of JCPyV occurs (116, 122). Here, viral proteins (VP) 1, 2, and 3 are transcribed and translated to encapsidate the viral DNA (282), before subsequent release of the newly formed virions into the surrounding environment. Initial studies were performed to better understand JCPyV infection in astrocytes, and the infectious cycle was compared to infection in SVG-A cells (SVGAs) (130). SVGAs are a mixed population of glial cells, mostly comprised of astrocytes, immortalized with SV40 T Ag to support robust levels of JCPyV infection (120, 121, 124). Research demonstrated that the infectious cycle was delayed in primary normal human astrocytes (NHAs) (130). This delay was most likely the consequence of SV40 T Ag, as the immortalization of NHAs with this protein (referred to as NHA-Ts) resulted in levels of infection comparable to that observed in SVGAs (130). In addition, differences in JCPyV infection between cell types was associated to variation in cyclin expression (130). Cyclins are commonly used as markers for the cell cycle (68, 127–129), and it was demonstrated that JCPyV infection was able to drive the cell into S phase by the accumulation of cyclin E in nucleus of NHAs (130). The S phase is needed for successful DNA viral replication (122). However, as the infectious cycle ensued, cyclin B1, a marker of the G_2/M phase, accumulated in the cytoplasm of NHAs, allowing for productive viral infection, by assembling the VPs to encapsidate the viral DNA, not observed during infection of immortalized cells at the same time points (130).

SV40 T Ag is known to dysregulate the cell cycle and activate cellular pathways that can potentially confound mechanisms of JCPyV infection (122, 123). One of these pathways is the AKT signaling pathway, important in cell growth and survival (221–227). Research has demonstrated that

SV40 T Ag can inhibit apoptosis in *ts*13 cells by activating the AKT signaling pathway and can directly phosphorylate Akt in U2OS cells (243, 244). In relation to this, our understanding of the AKT signaling pathway during JCPyV infection is limited. Currently, it has been shown that components of the AKT pathway, specifically phosphoinositide 3-kinase γ (PI3Kγ), are involved in JCPyV infection in cells immortalized with SV40 T Ag, such as SVGAs; the authors hypothesize that this pathway was activated upon stimulation of G protein-coupled receptors (GPCRs) (196). However, PI3K signaling is complex, is activated by various mechanisms, including Ras, a component of the mitogen-activated protein kinase (MAPK) pathway, and has numerous isoforms defined by their catalytic and regulatory subunits (348). As a result of SV40 T Ag activating AKT, and being able to influence other pathways, it is unclear if the PI3K/AKT signaling pathway previously identified was due to the immortalization of cells by SV40 T Ag or by JCPyV infection, itself. Additionally, genes downstream of AKT, mechanistic target of rapamycin (mTor), has also been implicated in JCPyV infection (195). Yet, in both experiments, immortalized cells were used to demonstrate the importance of PI3Kγ and mTor (195, 196).

There have been many advances in understanding the PI3K/AKT/mTor signaling pathway, as this pathway is frequently altered in human cancer (349). As a result, there have been numerous chemical inhibitors developed, some of which are in phase clinical trials or are already FDA approved, targeting the PI3K/AKT/mTor signaling pathway (350). This includes MK2206, an AKT inhibitor (351), and rapamycin, also known clinically as sirolimus (the generic drug name), a mTor inhibitor, that has been FDA approved for decades, used to prevent organ transplant rejection and to protect coronary stents (352–354). Additionally, a human clinical study has demonstrated that mTor inhibitors, like rapamycin, can cross the blood-brain barrier (BBB), providing a premise for treatment of neurological disorders (355, 356).

Along with the diverse drugs targeting this pathway and their ability to traverse the BBB, they have also been implicated in JCPyV infection, contributing to a framework for future PML therapeutics. MK2206, has been demonstrated to reduce JCPyV DNA replication in an oligodendrocyte cell line (194), however, mTor inhibitors, such as rapamycin, increased expression of JCPyV T Ag in an immortalized kidney cell line, human embryonic kidney (HEK) 293 cells (195). Due to these recent findings, no effective treatment for PML, and observed differences in JCPyV infection in immortalized cells, action of components of the PI3K/AKT/mTor signaling pathway were analyzed through RNA Sequencing (RNA-seq) analysis and various chemical inhibitors that target this signaling pathway were examined for their capacity to reduce JCPyV infection. These studies were conducted in primary human astrocytes (i.e. NHAs) and compared to cell types immortalized with SV40 T Ag, SVGAs, and NHA-Ts, to determine whether transformation of cells with T Ag, yielding differing outcomes in activation of the PI3K/AKT/mTor pathway and the JCPyV infectious cycle. This study also further characterizes the mechanisms of JCPyV infection of NHAs and describes how additional cellular pathways are possibly intertwined to support viral infection, pathways that are required to transform the cell into a successful viral factory.

Materials and Methods

Cells and viruses

The maintenance of primary normal human astrocytes (i.e., NHAs) were previously described (130). In brief, NHAs were purchased from Lonza, where they were isolated from a 19-week-gestation female with no detected levels of HIV, hepatitis B virus (HBV), or hepatitis C virus (HCV). They were cultured according to manufacture guidelines, in astrocyte growth medium and supplemented with SingleQuots supplements and 1% penicillin-streptomycin (P-S). All experiments were performed at low passages (P2 to P10). SVGAs were graciously provided by the Atwood Laboratory (Brown University).

They were cultured in complete minimum essential medium (MEM) (Corning), with 10% fetal bovine serum (FBS), 1% P-S, and 0.1% Plasmocin prophylactic (InvivoGen). All cell types were grown in a humidified incubator at 37°C with 5% CO_2. The generation of NHA-Ts were previously described (130) and they were cultured similarly to SVGAs, however 16% FBS was used. All cell types were grown in a humidified incubator at 37°C with 5% CO_2.

JCPyV strains were provided by the Atwood Laboratory (Brown University). The generation and production of the lysate viral strains of Mad-1/SVEΔ were described previously (275).

JCPyV infection

All cell types were seeded into 96-well plates with ~10,400 cells/well, for 70% confluency at the time of infection. Cells were infected at 37°C for 1 h with 42 µl/well of MEM containing 10% FBS, 1% P-S, and 0.1% Plasmocin prophylactic, across all cell types. The multiplicities of infection [MOIs] are indicated in the figure legend. Following the 1 h incubation, cells were fed with 100 µl/well of medium and incubated at 37°C for the duration of the infection. Cells were fixed at timepoints indicated in the legends, and either stained for indirect immunofluorescence to determine % infection or stained for ICW to measure protein expression.

Chemical Inhibitors

All chemical inhibitors were reconstituted in DMSO. Inhibitors that targeted the PI3K/AKT/mTor signaling pathway were used to pretreat cells for 30 min, while U0126 pretreatment was 1 h. The concentrations of chemical inhibitors are indicated in the figure legends. All chemical inhibitors were in MEM containing 10% FBS, 1% P-S, and 0.1% Plasmocin prophylactic, prior to JCPyV infection. Following the 1 h viral incubation, all cell types were fed with 100 µl/well of media containing the chemical inhibitor or the DMSO control. For experiments that quantified protein expression, all chemical

inhibitors were diluted in incomplete MEM (0% FBS), and cells were treated for 24 h and then fix in 4% PFA for subsequent analysis. U0126 was purchased from Cell Signaling Technology (#9903S), wortmannin was purchased from Sigma (#W1628), rapamycin was purchased from Frontier Scientific (#JK948477), and MK2206 and PP242 was purchased from Selleckchem (#S1078 and #S2218). The concentrations of all the chemical inhibitors utilized did not affect cell viability as measured by 4,5-dimethylthiazol-2-yl)-5-(3A- carboxymethoxyphenyl)-2-(4-sulfophenyl)-2H-tetrazolium (MTS) assay (data not shown).

Indirect immunofluorescence staining and quantitation of JCPyV infection

Following JCPyV infection, all cell types were stained for T Ag or VP1 (Fig. 4.6A and Fig. 4.6B) at RT. When quantifying for T Ag, NHAs, SVGAs and NHA-Ts were fixed at 48 hpi and when quantifying for both viral proteins, cells were fixed at 72 hpi and stained for both T Ag and VP1. Cells were fixed with 4% PFA for 11 min and washed with 1 X phosphate-buffered saline (PBS) with 0.01% Tween. NHAs, SVGAs, and NHA-Ts were then permeabilized using PBS-0.5% Triton X-100 for 15 min and blocked with PBS with 0.01% Tween and 10% goat serum for 45 min. Cells were then stained for T Ag or both viral proteins using antibodies listed in Table 4.1, at RT for 1 h. Following the 1° antibody incubation, all cell types were washed three times in PBS-0.01% Tween and counterstained with an anti-mouse Alexa Fluor 594 2° antibody. Cells were then washed with PBS- 0.01% Tween and the nuclei were stained using DAPI (4',6-diamidino-2-phenylindole) at RT for 5 min. Finally, cells were washed with PBS-0.01% Tween and stored in PBS-0.01% Tween.

To quantify infectivity the nuclear expression of viral protein, T Ag or VP1 over the total number of DAPI-positive cells (percent infection), a Nikon Eclipse Ti epifluorescence microscope (Micro Video Instruments, Inc.) equipped with a 20 X objective was used. T Ag or VP1 expressing cells were counted manually, however the DAPI-positive cells were determined using a binary algorithm in the Nikon NIS-

Elements Basic Research software (version 4.50.00, 64 bit). This algorithm separated cells based on three variables: intensity, diameter, and circularity, resulting in an accurate measurement of the total number of cells, in each field of view (92, 130, 193, 205, 241).

TABLE 4.1. Primary and secondary antibodies used in immunofluorescence and ICW assays

Protein	1^o antibody (dilution, manufacturer)	2^o antibody (dilution, manufacturer)
JCPyV T Ag	PAB962 (1:5, hybridoma)	anti-mouse Alexa Fluor 594 (1:1000, Thermo Fisher Scientific)
JCPyV VP1	ab34756 (1:1000, abcam)	
pERK (P-p44/42 MAPK at T202/Y204)	9101S (1:750, CST)	anti-rabbit IRDye 800CW (1:10,000, LI-COR)
pAKT (S473)	4060S (1:400, CST)	
pmTor (S2448)	44-1125G (1:1000, Invitrogen)	

CST, Cell Signaling Technology; ICW, In-Cell Western

ICW assay to measure protein expression using LI-COR software

Protein expression measuring phosphorylated ERK, phosphorylated AKT, and phosphorylated mTor were performed at 24 h post treatment using an ICW assay (205, 292). Following treatment of the chemical inhibitors, cells were fixed in 4% PFA and washed with PBS-0.01% Tween. Cells were then permeabilized with 1 X PBS-0.5% Triton X-100 at RT for 15 min and blocked with Tris-buffered saline (TBS) Odyssey buffer (LI-COR) at RT for 1 h. All cell types were stained with the respected 1^o antibody (Table 4.1) in TBS Odyssey blocking buffer at 4°C for ~16 h while rocking. The following day, the 1^o antibody was removed and the cells were washed twice with PBS-0.01% Tween. NHAs, SVGAs, and NHA-Ts were then counterstained with 2^o antibody, as indicated in Table 4.1 and CellTag (1:500, LI-COR) for 1 h. Finally, cells were washed with PBS-0.01% Tween and the wells were aspirated. Prior to scanning, the bottom of the plate was cleaned with 70% ethanol and the lid was removed. Plates were weighted with a silicone mat (LI-COR) and imaged using the LI-COR Odyssey CLx infrared imaging system to detect both the 700- and 800-nm intensities. The imaging settings for the LI-COR were as followed: medium quality, 42-µm resolution, with a 3.0 mm focus offset; when the scan was complete, the 700- and 800-nm

channels were aligned and the ICW analysis was performed in Image Studio (version 5.2). Protein quantification was determined in two steps. First, background fluorescence from the 800-nm channel (wells that only received 2^{o} antibody) were subtracted to the 800-nm channel, in which the protein of interest was being quantified. Next, the ratio was determined using this new value (protein of interest), normalized to the 700-nm channel (CellTag) or the overall number of cells in each well.

RNA-seq and pathway analysis

RNA-seq data is available under accession number: GSEXXXX (Chapter 3). The read counts were generated as previously described (Chapter 3) and analyzed using RStudio (version 1.2.1335) and R/edgeR (version 3.30.3) (187). Genes expressed were mapped to the PI3K/AKT signaling pathway from KEGG (357–359) by obtaining the gene symbols and then converting them to Ensembl Gene IDs using BioMart (360). The Ensembl Gene IDs were matched to the RNA-seq data to acquire the genes expressed in the PI3K/AKT signaling pathway. The list of expressed PI3K/AKT genes was then merged with results of the R/EdgeR analysis (Add citation to RNA-Seq paper) and subdivided based on an unadjusted *P value* less than 0.10. Venn diagrams showing the overlap among the differentially expressed genes for each cell type and timepoint were created using the R package, eulerr (version 6.1.0) (361).

Statistical analysis and graphing in RStudio

A two-sample Student's *t* test assuming unequal variances was used to compare the mean values for at least triplicate samples, when the data was normally distributed. Data not normally distributed was determined by both the Shapiro-Wilk's test and a quantile-quantile (Q-Q plot) in R. Statistical analyses were performed using the Wilcoxon signed rank test, to compare the median values for two populations, or the Kruskal-Wallis test to compare the median values of more than two

populations. If the Kruskal-Wallis test determined a significant result with at least two groups, then the pairwise Wilcoxon rank sum test, along with the Bonferroni adjustment was used to determine the pair of groups that were statistically different. The Student's *t* test was determined in Microsoft Excel, and all other statistical tests were performed using R. Statistical analyses for the RNA-seq data (Fig. 3 and Fig. 4A) was performed using the R/edge R (version 3.30.3) (187).

Results

U0126, a common MEK inhibitor does not reduce JCPyV infection in primary astrocytes

In addition to the PI3K/AKT/mTor signaling pathway implicated in JCPyV infection (194–196), the mitogen-activated protein kinase, extracellular signal-regulated kinase (MAPK/ERK) pathway is also required for JCPyV infection (94, 192, 193). This pathway is temporally regulated, specifically being phosphorylated upon JCPyV infection, and upon ERK siRNA, infection is significantly reduced (Chapter 3)(94, 192, 193). The MAPK/ERK pathway overlaps with the PI3K/AKT/mTor pathway and both pathways have important roles in cell survival and differentiation (221, 251). To determine if inhibiting the phosphorylation of ERK decreases JCPyV in primary astrocytes, a well-known, MEK inhibitor, U0126 was tested for its effects on JCPyV infection. NHAs, SVGAs, and NHA-Ts were treated with U0126 at 10 µM or the DMSO vehicle control (vehicle control), and subsequently infected with JCPyV (Fig. 4.1A). U0126 did not decrease infection in NHAs at 48 hpi compared to SVGAs and NHA-Ts (Fig. 4.1A, top). As a negative control, all cell types were infected with SV40, which does not require MEK for infection (362, 363), and U0126 did not influence SV40 infection in any cell type (Fig. 4.1A, bottom). To confirm the inhibitory effect of U0126 in NHAs, SVGAs, and NHA-Ts, ERK phosphorylation following treatment of the MEK inhibitor for 1 h was evaluated by In-Cell Western (ICW) (Fig. 4.1B). U0126 nearly abolished ERK phosphorylation in all three cell types (Fig. 4.1C). PMA, an ERK activator, was used as a control to further determine the specificity of the MEK inhibitor. All cell types were treated with U0126 following PMA

treatment, and ERK phosphorylation was nearly reduced to comparable levels to cells treated with U0126 alone (Fig. 4.1C). Together, these data suggest that although elevated levels of ERK phosphorylation promote JCPyV infection (Chapter 3), inhibition of ERK phosphorylation does not decrease JCPyV infection in primary astrocytes when compared to cells immortalized with SV40 T Ag. Thus, additional experiments are needed to define the mechanisms of cell signaling activation utilized in JCPyV infection of NHAs that are not otherwise observed in SVGAs and NHA-Ts.

AKT phosphorylation was moderately increased in NHAs during U0126 treatment compared to SVGAs and NHA-Ts

The ERK signaling cascade can interact with the AKT signaling pathway (250) and work together to induce cellular transformation and survival (221, 251). Research has demonstrated that treatment of cells with MEK inhibitors, such as U0126, results in increased AKT activity in various cell types (247–249). To determine if U0126 influences AKT phosphorylation, NHAs, SVGAs, and NHA-Ts were treated with U0126 and AKT phosphorylation was measured (Fig. 4.2). Cells were serum starved and treated with U0126 (10 μM) or the vehicle control for 24 h and both ERK and AKT phosphorylation was measured by ICW (Fig. 4.2A). U0126 increased AKT phosphorylation in NHAs, albeit an ~20% increase, while AKT phosphorylation was not altered in SVGAs and NHA-Ts (Fig. 4.2B). This experiment demonstrated that the crosstalk between the AKT signaling pathway and the ERK signaling cascade is evident in primary astrocytes. Additionally, it provides a premise to explain why U0126 did not decrease JCPyV infection in NHAs (Fig. 4.1); U0126 inhibits ERK phosphorylation, however the virus may also hijack the AKT signaling pathway to support viral replication.

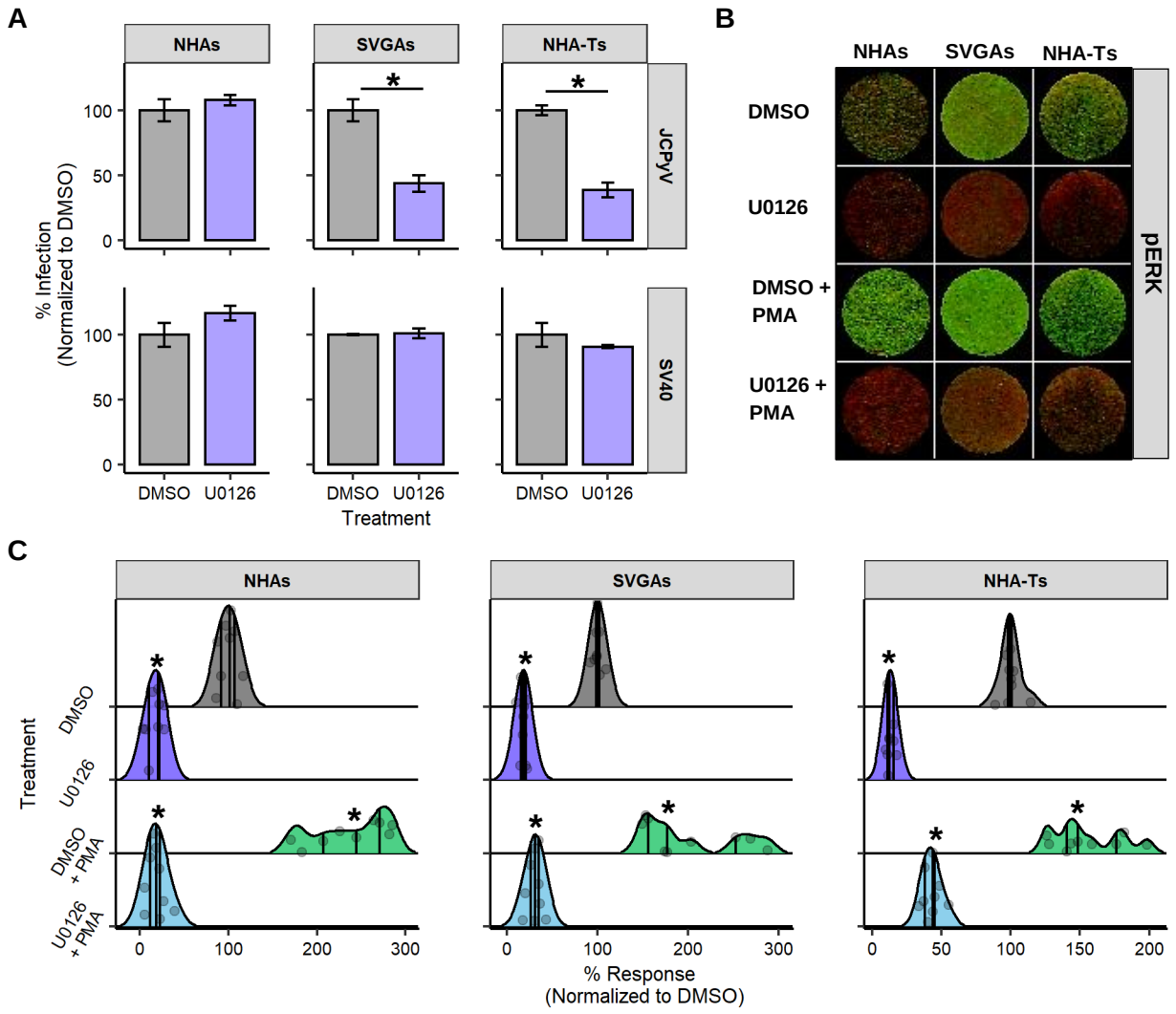

Figure 4.1. MEK inhibitor U0126 does not decrease JCPyV infection in NHAs. (A) NHAs, SVGAs, and NHA-Ts were pretreated with the MEK inhibitor U0126 at 10 µM or DMSO at an equivalent volume control and then infected with JCPyV (MOI = 2.0 FFU/cell) (A, top) or SV40 (MOI = 2.0 FFU/cell) (A, bottom) at 37°C for 1 h. Cells were incubated in media containing DMSO or U0126 for 48 h and then fixed and stained by indirect immunofluorescence. Percent infection was determined by counting the number of JCPyV T Ag- or SV40 VP1-positive nuclei divided by the number of DAPI-positive nuclei for five ×20 fields of view for triplicate samples. Data is representative of three individual experiments. Error bars indicate SD. Student's *t test* was used to determine statistical significance comparing DMSO to U0126, with each cell type and viral protein. *, $P < 0.01$. (B) NHAs, SVGAs, and NHA-Ts were pretreated with DMSO or U0126 for 1 h in addition to PMA (40 nM) treatment of the indicated wells for the final 5 min at 37°C. Cells were fixed and counterstained for pERK (green) or CellTag (red). (C) Percentage of pERK for each treatment was quantitated by In-Cell Western signal intensity values per [(pERK)/Cell Tag x 100% = % response] within each ICW analysis with LI-COR software. Density ridgeline plots represent the distribution of samples (individual points) with the lower quartile, median and upper quartile denoted as black lines in each distribution. A Kruskal-Wallis test, along with the Bonferroni adjustment, was used to compare treatments in each cell type, however only significance with the DMSO treatment versus other treatments are illustrated. *, $P < 0.01$. Data are representative of three independent experiments performed in triplicate.

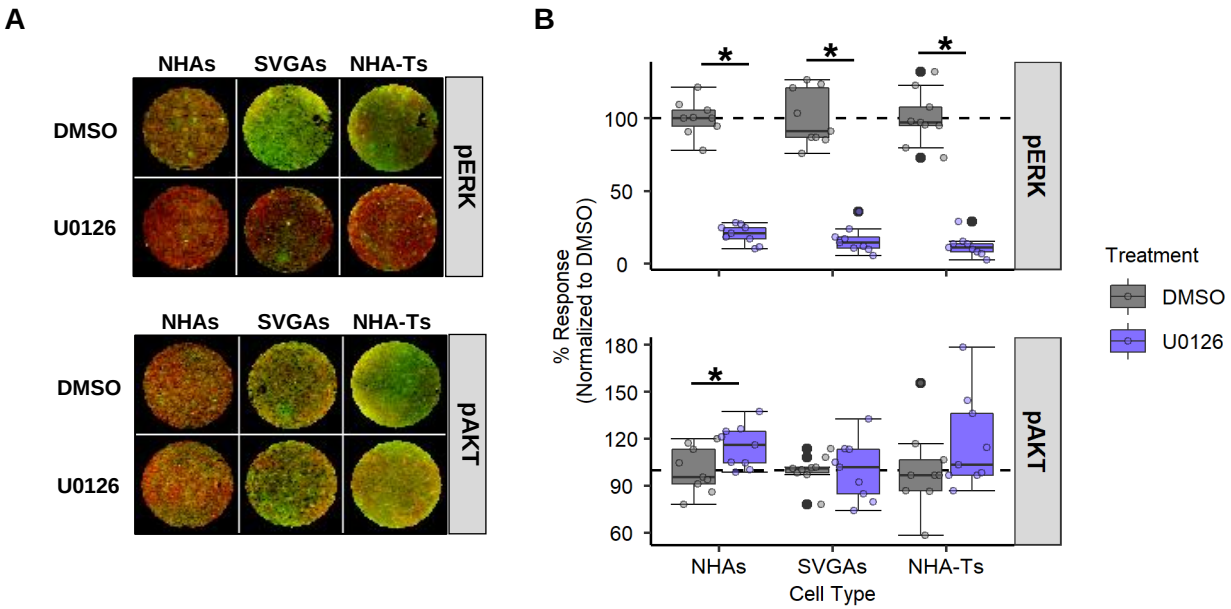

Figure 4.2. U0126 increases AKT phosphorylation in NHAs. (A) NHAs, SVGAs, and NHA-Ts were treated with DMSO or U0126 (10 µM) at 37°C for 24 h. Cells were fixed and counterstained for pERK or pAKT (green) or CellTag (red). (B) Percentage of pERK and pAKT for each cell type was quantitated by ICW signal intensity values per [(pERK or pAKT)/Cell Tag x 100% = % response] within each ICW analysis with LI-COR software. Box and whisker plots represent the distribution of samples (individual points) with the lower quartile, median and upper quartile denoted as black lines. The dashed line indicates the normalized DMSO % response of pERK and pAKT. A Wilcoxon rank sum exact test was used to compare treatments in each cell type. Data are representative of three independent experiments performed in triplicate. *, $P < 0.05$.

PI3K/AKT signaling pathway genes were upregulated during JCPyV infection in NHAs

Previous research has demonstrated that the PI3K/AKT signaling pathway, specifically AKT and PI3Kγ, are required for JCPyV infection (194, 196, 364). To determine if this pathway is implicated in NHAs, RNA-seq data was analyzed (Chapter 3) over the course of JCPyV infection in NHAs and SVGAs. Differentially expressed genes (unadjusted p-value < 0.10) were mapped to the PI3K/AKT signaling pathway from the Kyoto Encyclopedia of Genes and Genomes (KEGG) database (357–359). At 24 hpi, 25 genes that mapped to the pathway were downregulated in SVGAs but upregulated in NHAs (Fig. 4.3, top). At 48 hpi, only one gene was upregulated in SVGAs compared to 23 genes upregulated in NHAs (Fig. 4.3, middle). At 96 hpi, approximately 51% of the genes that mapped to the pathway were upregulated in NHAs versus ~38% in SVGAs (Fig. 4.3, bottom). These data illustrate that compared to

SVGAs, JCPyV infection in NHAs activated more genes in the PI3K-AKT signaling pathway providing additional evidence for the involvement of this pathway during infection in primary astrocytes.

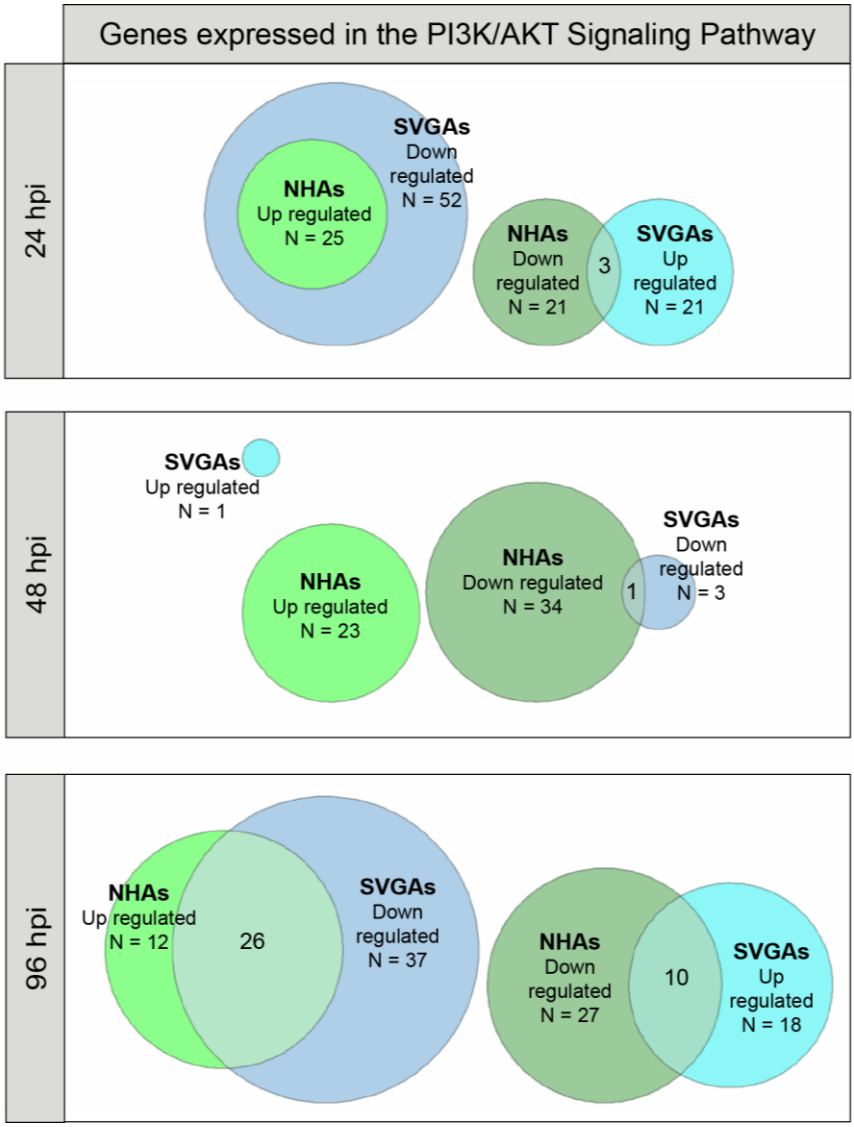

Figure 4.3. Genes in the PI3K/AKT pathway were differentially expressed during JCPyV infection in NHAs compared to viral infection in SVGAs. NHAs and SVGAs were either infected with JCPyV (MOI = 0.1 FFU/cell) or mock-infected with a vehicle control and the transcriptomic profile was determined at 24, 48, and 96 h using RNA-seq. Genes of the PI3K/AKT pathway were determined from the KEGG database with an unadjusted *p value* < 0.10. Upregulated genes (Log FC > 0) and downregulated genes (Log FC < 0) are represented as Venn diagrams for each time point and cell type. The size of each circle is proportionate to the number of genes that apply to the above criteria. The green colors are representative of NHAs, while the blue colors are representative of SVGAs. Brighter shades are upregulated genes and darker shades are downregulated genes. (FC, Fold Change).

AKT was differentially expressed and required for JCPyV infection in NHAs

To further validate the previous results, the expression of the three isoforms of AKT (AKT1, AKT2 and AKT3) were analyzed (Fig. 4.4A). Both ATK1 and ATK2 were significantly downregulated in SVGAs at 24 and 96 hpi (unadjusted *P value* < 0.05) and upregulated in NHAs (unadjusted *P value* < 0.1) (Fig. 4.4A). Due to the differential gene expression observed, NHAs, SVGAs, and NHA-Ts were pretreated with the

AKT inhibitor, MK2206, or the vehicle control at increasing concentrations, and subsequently infected with JCPyV (Fig. 4.4B). A dose-dependent decrease in viral infection was observed in NHAs, however, a dose-dependent increase was measured in SVGAs and NHA-Ts (Fig. 4.4B). Considering the significant differences in JCPyV infection among cell types, MK2206 was validated for its inhibitory effects of AKT phosphorylation by ICW (Fig. 4.4C). Cells were serum starved and treated with the highest concentration of MK2206 for 24 h. The chemical inhibitor significantly reduced AKT phosphorylation in all three cell types compared to the vehicle control demonstrating that the inhibitor is working effectively at the concentrations used (Fig. 4.4D). This data revealed that JCPyV requires AKT during infection in NHAs and the utilization of this pathway is perhaps, confounded by the immortalized properties of SVGAs and NHA-Ts.

PI3K was required for JCPyV infection in NHAs

Upstream of AKT, PI3K was targeted by chemical inhibitor to understand if additional proteins in the PI3K/AKT pathway are involved during JCPyV infection in NHAs. Cells were pretreated with the PI3K inhibitor, wortmannin, or the vehicle control at increasing concentrations, and subsequently infected with JCPyV (Fig. 4.5A). Comparable to AKT inhibition, wortmannin significantly reduced JCPyV infection by 50% in NHAs, while increasing infection in SVGAs and not influencing infection in NHA-Ts (Fig. 4.5A). The chemical inhibitor was validated for the inhibition of the PI3K/AKT signaling pathway by measuring AKT phosphorylation using ICW (Fig. 4.5B). Cells were serum starved and treated with the highest concentration of wortmannin. Across all three cell types, wortmannin significantly reduced AKT phosphorylation (Fig. 4.5C). Altogether, these data illustrate that treatment of cells with the PI3K inhibitor equivalently impaired the PI3K/AKT signaling pathway, and a decrease in JCPyV infection during PIK3K inhibition was only observed in NHAs, verifying the results demonstrated with MK2206 treatment (Fig. 4.4).

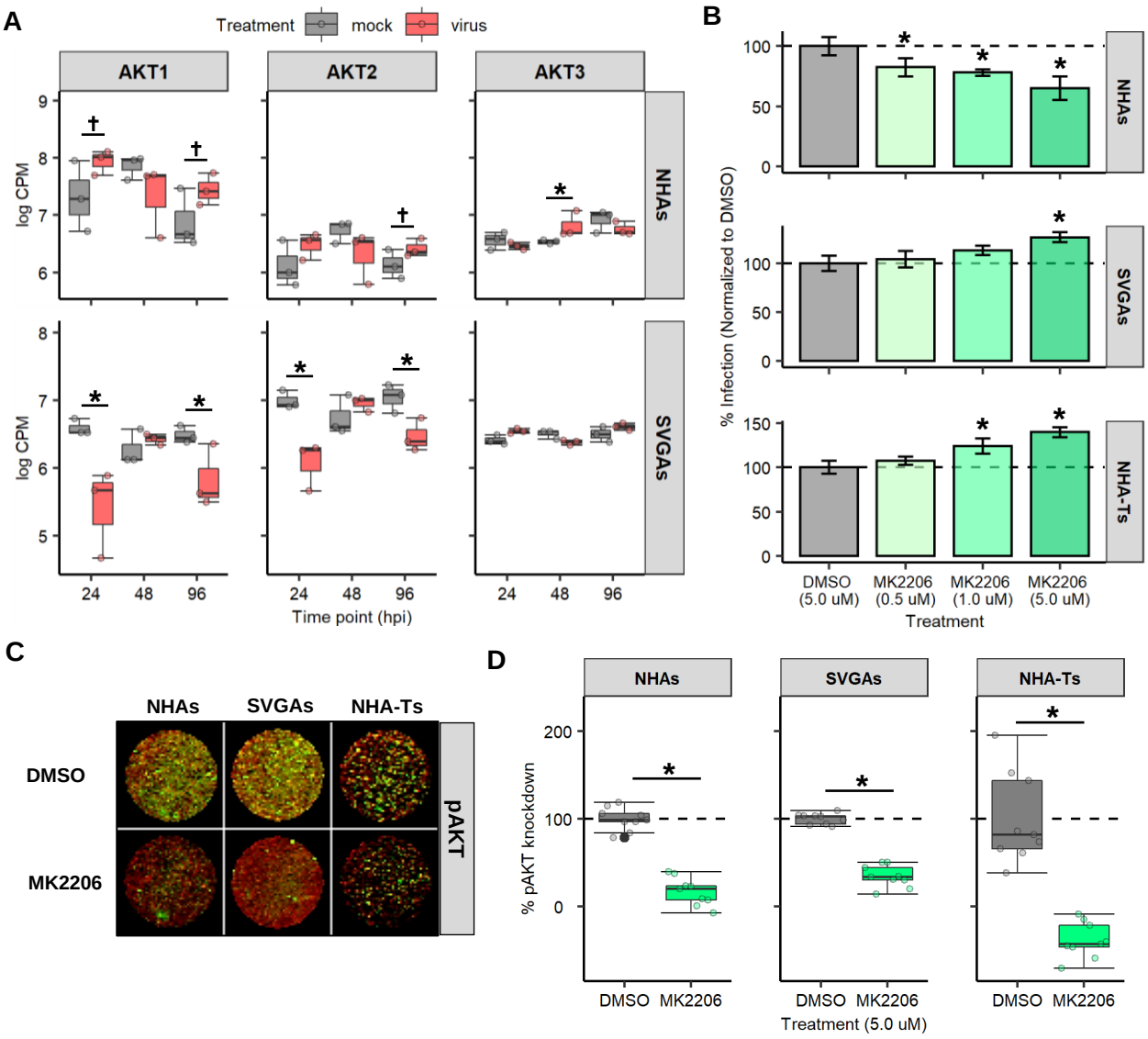

Figure 4.4. AKT is required for JCPyV infection in NHAs. (A) The log CPM was determined for the three isoforms of AKT (*AKT1*, *AKT2*, and *AKT3*) in mock-infected and JCPyV-infected cells at each time point from the RNA-seq data. †, $P < 0.10$; *, $P < 0.05$. (B) NHAs, SVGAs, and NHA-Ts were pretreated with indicated concentrations of an AKT inhibitor, MK2206, or DMSO at an equivalent volume control for 30 min and then infected with JCPyV (MOI = 1.0 FFU/cell) at 37°C for 1 h. Cells were incubated in media containing DMSO or MK2206 for 48 h and then fixed and stained by indirect immunofluorescence. Infectivity was determined by counting the number of JCPyV T Ag-positive nuclei divided by the number of DAPI-positive nuclei for five ×20 fields of view for triplicate samples (% Infection). Data is representative of three individual experiments. Error bars indicate SD. Student's *t test* was used to determine statistical significance comparing DMSO to MK2206 for each cell type. (C) NHAs, SVGAs, and NHA-Ts were treated with DMSO or MK2206 (5.0 µM) at 37°C for 24 h. Cells were fixed and counterstained for pAKT (green) or CellTag (red). (D) Percentage of pAKT for each cell type was quantitated by ICW signal intensity values per [(pAKT)/Cell Tag x 100% = % response] within each ICW analysis using LI-COR software. Box and whisker plots represent the distribution of samples (individual points) with the lower quartile, median, and upper quartile denoted as black lines. The dashed line indicates the normalized DMSO % response of pAKT. A Wilcoxon rank sum exact test was used to compare treatments in each cell type. Data are representative of three independent experiments performed in triplicate. *, $P < 0.05$.

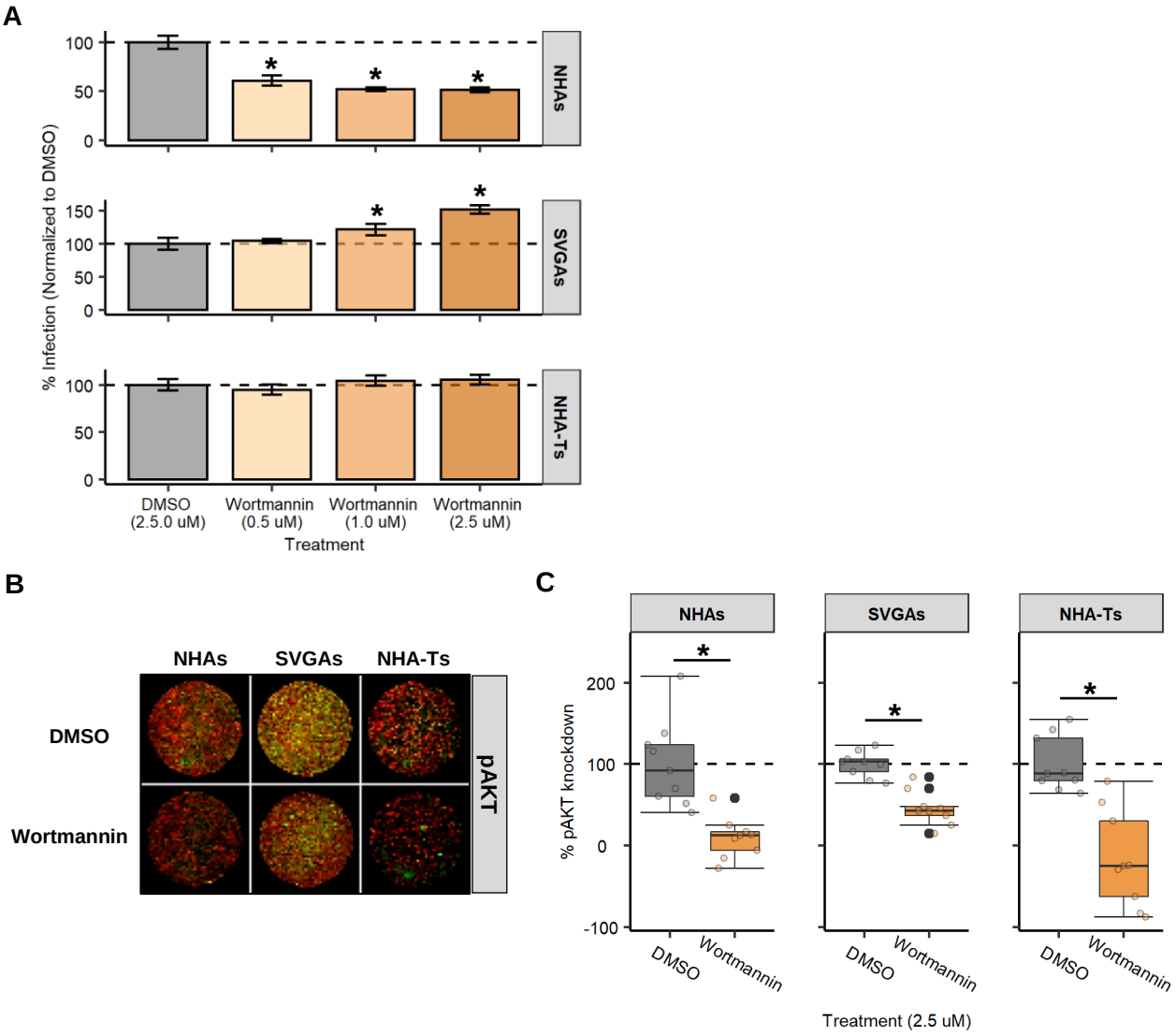

Figure 4.5. PI3K inhibitor wortmannin reduces JCPyV infection in NHAs. (A). NHAs, SVGAs, and NHA-Ts were pretreated with indicated concentrations of a PI3K inhibitor, wortmannin, or DMSO at an equivalent volume control and then infected with JCPyV (MOI = 1.0 FFU/cell) at 37°C for 1 h. Cells were incubated in media containing DMSO or wortmannin for 48 h and then fixed and stained by indirect immunofluorescence. Infectivity was determined by counting the number of JCPyV T Ag-positive nuclei divided by the number of DAPI-positive nuclei for five ×20 fields of view for triplicate samples (% infection). Data is representative of three individual experiments. Error bars indicate SD. Student's *t test* was used to determine statistical significance comparing DMSO to wortmannin for each cell type. (B) NHAs, SVGAs, and NHA-Ts were treated with DMSO or wortmannin (2.5 µM) at 37°C for 24 h. Cells were fixed and counterstained for pAKT (green) or CellTag (red). (C) Percentage of pAKT for each cell type was quantitated by ICW signal intensity values per [(pAKT)/Cell Tag x 100% = % response] within each ICW analysis using LI-COR software. Box and whisker plots represent the distribution of samples (individual points) with the lower quartile, median and upper quartile denoted as black lines. The dashed line indicates the normalized DMSO % response of pAKT. A Wilcoxon rank sum exact test was used to compare treatments in each cell type. Data are representative of three independent experiments performed in triplicate. *, $P < 0.05$.

mTor inhibition significantly reduces JCPyV infection in NHAs

A downstream target of the PI3K/AKT signaling pathway is mTor (230); previous research has determined that mTor inhibition led to an increase in JCPyV infection (195). Moreover, research has also demonstrated that JCPyV infection is delayed in NHAs, compared to SVGAs and NHA-Ts (130). To determine if mTor is required for JCPyV infection and if mTor inhibition increases late viral protein expression in NHAs, all cell types were treated with either rapamycin, mTor inhibitor PP242, or the vehicle control, were subsequently infected with JCPyV, and infectivity was measured by assessing both early (T Ag) and late (VP1) viral protein production (Fig. 4.6). Rapamycin and PP242 significantly reduced JCPyV infection in NHAs quantified by both T Ag and VP1 production (Fig. 4.6A and Fig. 4.6B). Rapamycin significantly increased JCPyV infection in SVGAs and NHA-Ts (Fig. 4.6A), however, PP242 did not influence viral infection in either cell type (Fig. 4.6B). To validate the effectiveness of the chemical inhibitors in NHAs, SVGAs, and NHA-Ts, mTor phosphorylation was measured by ICW, following serum starvation and treatment with each inhibitor for 24 h (Fig. 4.6C). Rapamycin and PP242 significantly reduced mTor phosphorylation, relatively, in each cell type, however PP242 reduced phosphorylation to more appreciable levels when compared to rapamycin (Fig. 4.6D). Overall, these findings demonstrate that mTor phosphorylation, a downstream target of the PI3K/AKT signaling pathway, is required for JCPyV infection in NHAs. Furthermore, it substantiates the previous findings that JCPyV uses alterative signaling pathways in primary astrocytes, viral mechanisms not observed in cell types that are immortalized with SV40 T Ag.

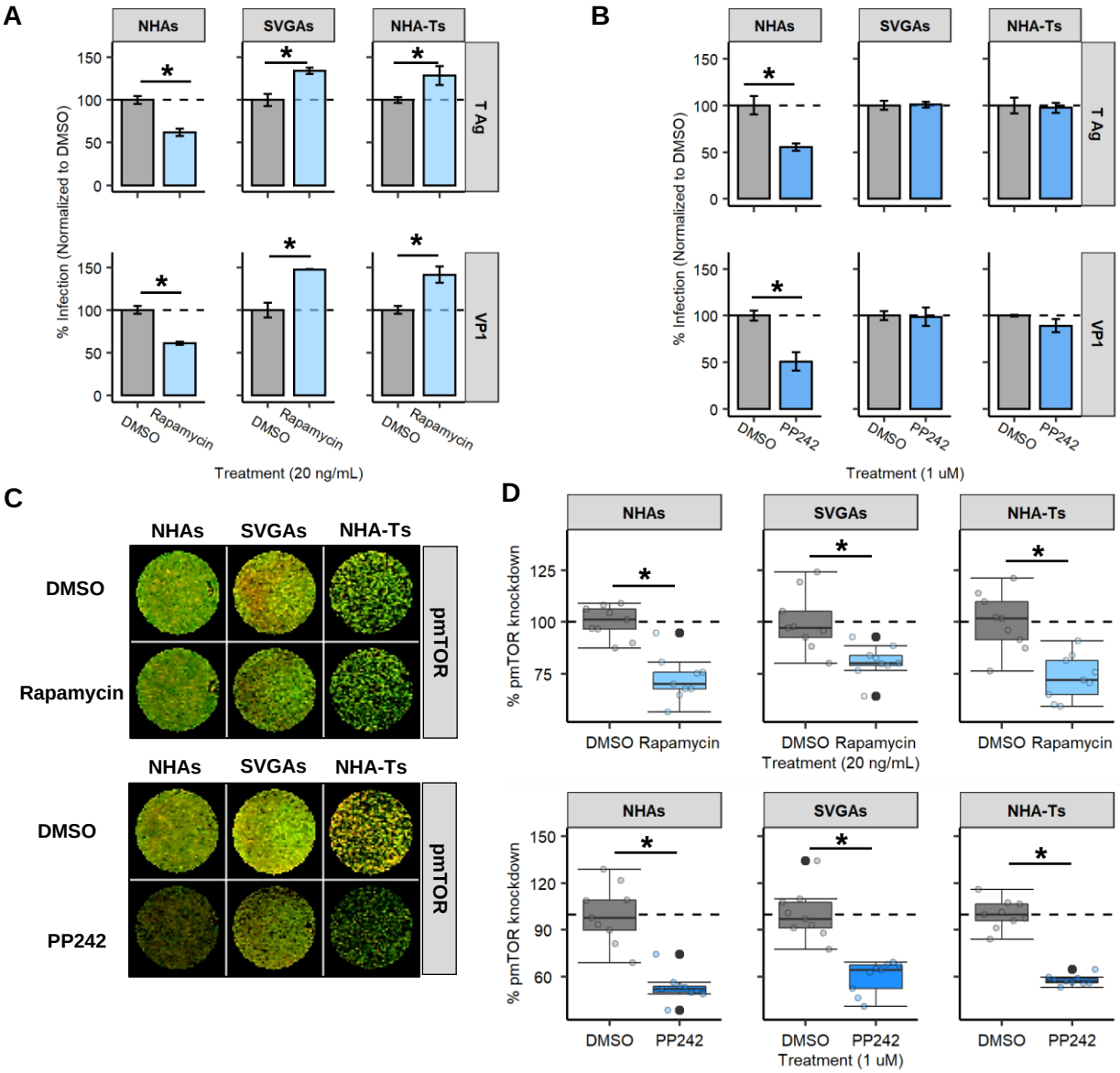

Figure 4.6. Inhibitors of mTOR, a target of the PI3K/AKT pathway, reduce JCPyV infection in NHAs. (A and B). NHAs, SVGAs and NHA-Ts were pretreated with (A) rapamycin at 20 ng/mL, (B) PP242 at 1 µM, or the DMSO control at an equivalent volume control and then infected with JCPyV (MOI = 1.0 FFU/cell) at 37°C for 1 h. Cells were incubated in media containing DMSO or mTOR inhibitors for 72 h and then fixed and stained by indirect immunofluorescence. Infectivity was determined by counting the number of JCPyV T Ag- or VP1- positive nuclei divided by the number of DAPI-positive nuclei for five ×20 fields of view for triplicate samples (% infection). Data is representative of three individual experiments performed in triplicate. Error bars indicate SD. Student's *t test* was used to determine statistical significance comparing DMSO to either mTOR inhibitor, with each cell type and viral protein. (C) All cell types were treated with DMSO or rapamycin at 20 ng/mL (top) or PP242 at 1 µM (bottom) at 37°C for 24 h. Cells were fixed and counterstained for pAKT (green) or CellTag (red). (C) Percentage of pmTOR for each cell type was quantitated by ICW signal intensity values per [(pmTOR)/Cell Tag x 100% = % response] within each ICW analysis with LI-COR software. Box and whisker plots represent the distribution of samples (individual points) with the lower quartile, median, and upper quartile denoted as black lines. The dashed line indicates the normalized DMSO % response of pmTOR. A Wilcoxon rank sum exact test was used to compare treatments in each cell type. Data are representative of three independent experiments performed in triplicate. *, $P < 0.05$.

Discussion

Astrocytes are main targets of JCPyV infection in the CNS, where the destruction of these cells, along with oligodendrocytes, leads to PML (60–63, 68). With no cure for this aggressive and ultimately fatal disease, more research is needed to reveal potential therapeutic targets. Cellular pathways, like the PI3K/AKT/mTor signaling pathway, is an attractive candidate because there are numerous, established drugs that inhibit this pathway for cancer treatment (349, 350). In this study, we investigated the role of various chemical inhibitors of the PI3K/AKT/mTor signaling pathway on JCPyV infection in primary astrocytes compared to immortalized cells. Our results demonstrate that viral infection is significantly reduced in primary astrocytes compared to cells transformed with SV40 T Ag, highlighting both the importance of this signaling pathway, and the need to use either *ex vivo* approaches or validate findings in primary cells to further understand how JCPyV infection may occur in the human host.

JCPyV requires the MAPK/ERK pathway to successfully infect the cell ((94, 192, 193), Chapter 3). However, when a well-studied MEK inhibitor, U0126, did not reduce JCPyV infection in primary astrocytes, only reducing JCPyV infection in cells immortalized with SV40 T Ag (Fig. 4.1A), additional studies were performed to identify alternative pathways that regulate JCPyV infection. Research has shown that the PI3K/AKT/mTor signaling pathway intersects with the MAPK/ERK pathway (247–249). Our findings also support this, as treatment of NHAs with U0126 led to an increase in phosphorylated AKT, while U0126 treatment did not exhibit any difference in AKT phosphorylation in SVGAs and NHA-Ts (Fig. 4.2).

The PI3K/AKT/mTor signaling pathway has been previously implemented in other polyomavirus infections as well (194–196, 239, 240, 365, 366). Earlier research has demonstrated that BK polyomavirus (BKPyV), murine polyomavirus, and JCPyV influence the PI3K/AKT signaling pathway by modulating the cellular phosphatase, protein phosphatase 2A (PP2A) (239, 365, 366). Comparable to

JCPyV, BKPyV also establishes an asymptomatic infection, yet during immunosuppression BKPyV can cause nephropathy and hemorrhagic cystitis (118). Treatment of cells with sirolimus (i.e., rapamycin) significantly reduced BKPyV infection, however the concentration of the chemical inhibitor used in these studies was significantly different between immortalized and primary cells (239, 240). Hirsch et al., used a primary kidney cell line to determine the outcome of BKPyV infection during rapamycin treatment. They confirmed that using rapamycin at least a magnitude lower in concentration significantly reduces BKPyV infection in this primary kidney cell line, specifically during the first 24 hours of infection (i.e. before Large T Ag viral genome replication) (240). The authors concluded that these differences in concentration of the drug were the result of the transformed phenotype of the other cell line to require significantly higher concentrations of the inhibitor to reduce BKPyV infection. Unfortunately, understanding viral infection is challenging when using transformed cell lines, as transformation alters metabolic pathways and signal transduction within those pathways (245, 246).

Our findings substantiate the consequences of immortalization in investigation of JCPyV infection with chemical inhibitors that target the PI3K/AKT/mTor signaling pathway. Wortmannin, MK2206, rapamycin, and PP242, chemical inhibitors that target different steps of this signaling pathway, resulted in a significant reduction of JCPyV infection in NHAs that was not observed in SVGAs or NHA-Ts. These results, specifically with MK2206, are consistent with other published research reporting the impacts of JCPyV infection in an oligodendrocyte cell line treated with inhibitors of this pathway. MK2206 treatment of a glioma-derived stem cell line with oligodendrocyte precursor phenotypes (G144 cells), reduced JCPyV DNA replication (194). It is important to note, that even though these cells are established through glioblastoma samples, G144 cells specifically display features that resemble normal fetal neural stem cells (367). Together, these data suggest the importance of MK2206 as a potential antiviral for PML, as oligodendrocytes and astrocytes are the main cell types impacted by disease (60–63, 68).

Our research also corresponds with findings demonstrated with BKPyV infection and mTor inhibition with respect to both polyomavirus infection and cell-type dependent differences. Rapamycin significantly reduced JCPyV infection in primary astrocytes (Fig. 4.6A), and similarly, BKPyV infection was reduced in a primary kidney cell line with rapamycin treatment (240). Likewise, using both rapamycin and PP242, a secondary mTor inhibitor, did not decrease JCPyV infection in immortalized cells, SVGAs and NHA-Ts (Fig. 4.6A and Fig. 4.6B). Similarly, rapamycin and other mTor inhibitors did not decrease but rather enhanced JCPyV replication in HEK293A cells (195). HEK293A cells are transformed with adenovirus type 5 DNA (368) and not SV40 T Ag, yet immortalization through adenovirus have been shown to the adenovirus oncogene interacts with Rb and p53, disrupting important checkpoints in cell cycle and growth, similar to SV40 T Ag transformation (369–373). Additionally, cells transformed with viral oncogenes can also influence PP2A, known to regulate numerous cellular pathways, such as the MAPK and PI3K signaling pathways, which is also important during JCPyV infection (366, 374, 375). Together, these findings demonstrate both the requirement of the PI3K/AKT/mTor signaling pathway and the importance of using primary cell lines to characterize polyomavirus infection.

Furthermore, rapamycin and PP242 are both mTor inhibitors, yet the mode of inhibition is slightly different between drugs. mTor forms two complexes in mammalian cells, mTor complex 1 (mTORC1) and mTORC2, and activation of these complexes results in different functions for the cell (238). The formation and activation of mTORC1 results in protein translation, cell growth, and autophagy, while mTORC2 results in survival, migration, and cytoskeletal organization (238). Rapamycin has been demonstrated to inhibit mTORC1 more so than mTORC2, particularly *in vitro* (376), while PP242 results in greater inhibition of both mTORC1 and mTORC2 (377). These modes of mTor inhibition may explain the differences observed in immortalized cells during JCPyV infection, however it does substantiate the importance of mTor during infection of primary astrocytes (Fig. 4.6). Additionally, if we increased the concentration of PP242, the results of JCPyV infection were similar, and in fact, higher

concentrations resulted in cytotoxic effects (data not shown). To conclude, each chemical inhibitor was tested for cellular viability compared to the vehicle control in each cell type and in all assays performed in this research. Additionally, the inhibitory effect measuring phosphorylation of AKT or mTor were similar across cell types, demonstrating that cell type differences were not from cytotoxic effects or from inequitable impacts of AKT or mTor phosphorylation from the chemical treatments.

Research has demonstrated that enhanced JCPyV infection from mTor inhibition is perhaps due to Skp-Cullin Fbox (SCF) E3 ligase, S-phase kinase-associated protein 2 (Skp2) (195, 378), and the expression of this protein is highly variable in immortalized versus primary cells (379). Skp2 is important in regulating the cell cycle, accumulates in the cell during the transition to the G1/S phase, remains highly expressed during S phase (380) and can also interact with polyomavirus Large T Ag (195, 378). Previous studies have concluded that the interaction of Skp2 and Large T Ag of numerous polyomaviruses (PyVs), including murine PyV, JCPyV, and BKPyV, declined with treatment of mTor inhibitors, which resulted in an increase of Large T Ag expression (195). Skp2 is highly expressed in glioma cell lines compared to normal astrocyte cell lines (379) and this could explain the differences observed between NHAs versus SVGAs and NHA-Ts. First, JCPyV Large T Ag expression is significantly less in NHAs compared to SVGAs and NHA-Ts (130) and as a result, Skp2 may not be involved to the same extent in JCPyV infection of NHAs, thus, this interaction between Skp2 and Large T Ag is not sensitive to mTor inhibition. However future research should elucidate the mechanisms of viral protein production and the PI3K/AKT/mTor signaling pathway.

Lastly, PI3K expression has been recently demonstrated to decrease JCPyV infection in SVGAs (196). A reason for the differences in JCPyV infection between the findings reported here and by Clark et. al could be the PI3K isoform that was targeted as well as the technique used. The authors determined PI3K, specifically PI3Kγ, facilitates JCPyV infection in SVGAs through genetic knockdown

approaches (196). It is known that JCPyV facilitates entry into the cell through the utilization of a GPCR, serotonin 5-hydroxytryptamine (5-HT) receptors (91, 92, 241) which upon activation, couples with PI3Kγ (196). The authors speculated that knockdown of PI3Kγ disrupted early events of GPCR signaling and as a result, disrupted possible virus capsid disassembly or trafficking to the endoplasmic reticulum or nucleus (196). Wortmannin is one of the most well-characterized PI3K inhibitors and has been shown to interact strongly *in vitro* with PI3K, thus inhibiting numerous isoforms in the PI3K family (381, 382). However, wortmannin has also been demonstrated to have off target effects, inhibiting other serine/threonine kinases of the PI3K family such as mTor (383). The differences that we have observed could be the consequence of wortmannin targeting other PI3Ks in the pathway and thus having similar results to the other inhibitors used in this research, specifically in SVGAs. Further, JCPyV entry in primary astrocytes has not been well studied and thus we do not yet know whether GPCRs are utilized during entry thereby activating PI3Kγ to the same extent as it does in viral entry of SVGAs. Additionally, recent work has suggested that JCPyV may use extracellular vesicles to gain entry in astrocytes because they do not express the sialic acid attachment receptor (384). Future studies should define the role of PI3Ks in viral infection of primary astrocytes, using more targeted approaches such as siRNA. Nonetheless, wortmannin, MK2206, rapamycin, and PP242 significantly reduced JCPyV infection in primary astrocytes, while also inhibiting the phosphorylation of AKT and mTor in all three cell types (Fig. 4.7). Furthermore RNA-seq analysis revealed numerous genes within the PI3K/AKT/mTor pathway that were upregulated during JCPyV infection of NHAs but downregulated in SVGAs, providing more evidence of the requirement of this pathway in primary astrocytes (Fig. 4.3).

In summary, this research has revealed and outlined the requirement of the PI3K/AKT/mTor signaling pathway in JCPyV infection of primary human astrocytes. Using various chemical inhibitors, we have characterized how JCPyV uses this pathway to support viral infection, and importantly, how immortalized characteristics may alter signaling events that, in turn, confound the requirement of this

pathway in JCPyV infection of transformed cell lines. Overall, these findings will aid in the discovery of therapeutics to treat or slow the progression of PML, as no effective treatments are available for this deadly disease.

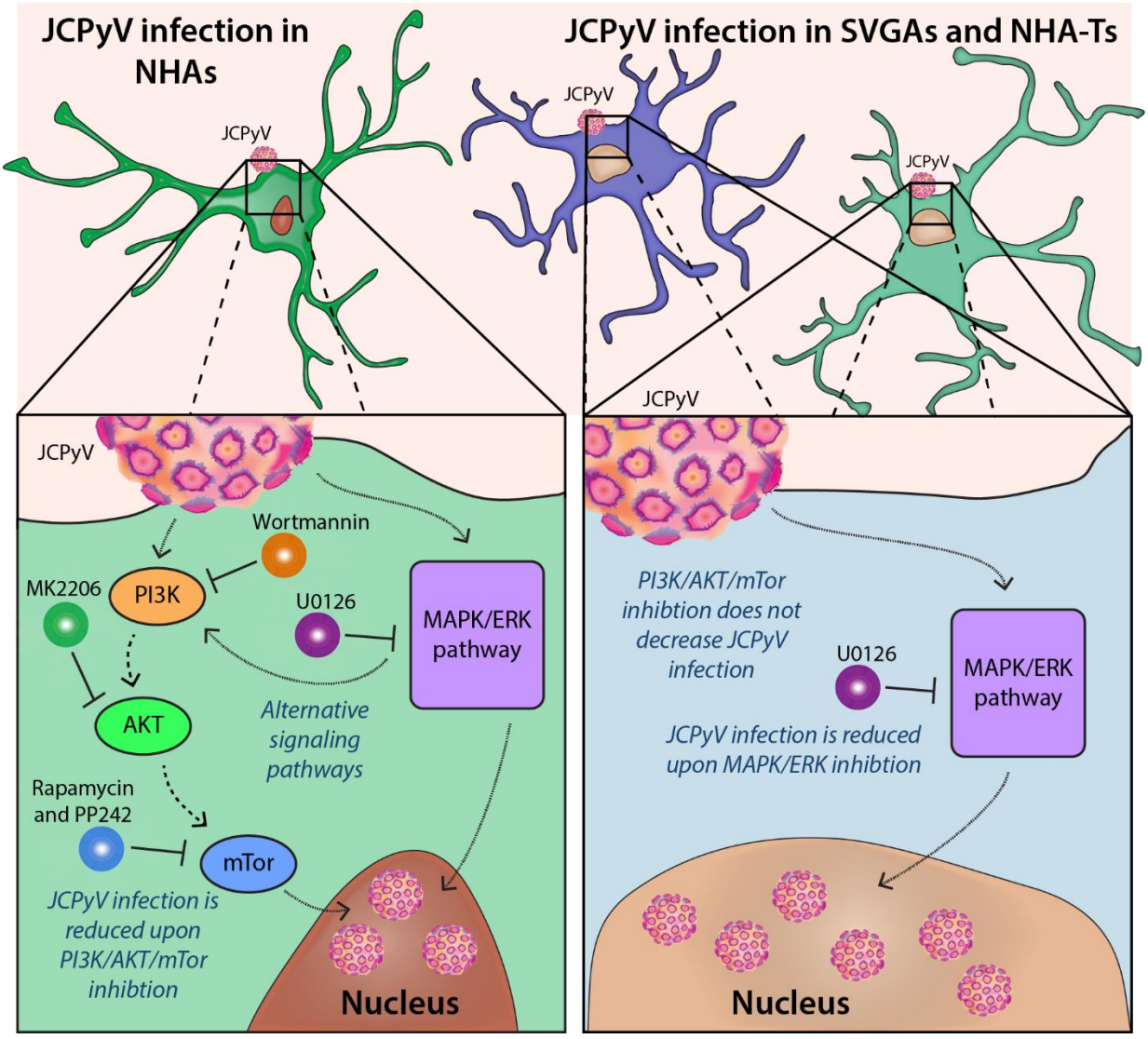

Figure 4.7. Chemical inhibitors that reduce JCPyV infection in NHAs, SVGAs, and NHA-Ts. Previous research has demonstrated the importance of the MAPK/ERK pathway in NHAs, however JCPyV can also use the PI3K/AKT/mTor signaling pathway for infection (left). Using chemical inhibitors targeting PI3K, AKT, and mTor, significantly reduced JCPyV infection in primary astrocytes (left). However, in immortalized cells, SVGAs and NHA-Ts, these chemical inhibitors did not reduce JCPyV infection and treatment of cells with U0126, a MEK inhibitor of the MAPK/ERK pathway, significantly reduced JCPyV infection (right). This demonstrates that during viral infection of immortalized cells, the virus is more dependent on the MAPK/ERK pathway and may not use other pathways, such as the PI3K/AKT/mTor signaling pathway, to establish successful infection, compared to JCPyV infection in primary astrocytes.

CHAPTER 5

REARRANGEMENT IN THE HYPERVARIABLE REGION OF JC POLYOMAVIRUS GENOMES ISOLATED FROM PATIENT SAMPLES AND IMPACT ON TRANSCRIPTION FACTOR-BINDING SITES AND DISEASE OUTCOMES

The work presented in this chapter is in preparation for submission.

Introduction

JC polyomavirus (JCPyV) is a virus that is known to only infect humans, wherefore it successfully infects most of the population (28, 30, 60). JCPyV persistently infects the kidneys of healthy individuals, however during immunosuppression, the virus can reactivate and spread to the central nervous system (CNS) causing the fatal disease, progressive multifocal leukoencephalopathy (PML) (30, 44–47). There are currently no approved cures for PML, and when left untreated, the disease can be fatal within a few months (71, 79). Historically, individuals most at risk for disease were positive for HIV, representing up to 5% of all PML cases (60, 71). The use of highly active antiretroviral therapy (HAART) has significantly reduced the rate of PML among HIV individuals (72, 73). Unfortunately, new risk groups are emerging that encompass patients receiving immunomodulatory therapies for immune-mediated diseases (74). This includes individuals with multiple sclerosis (MS) taking natalizumab and individuals receiving rituximab for treatment of systemic lupus erythematosus (SLE) (71, 74–76). As there are no approved therapies for PML, current treatments address treatment of the underlying immunosuppression by either treating HIV with HAART or discontinuing immunosuppressive therapies (71, 79–81). Recently, there has been treatments related to adoptive T cell transfer, and checkpoint inhibitors, such as pembrolizumab, however these treatments can also result in severe morbidity (71, 82, 83, 347).

The pathogenicity of JCPyV, infecting most of the population and causing disease in immunosuppressive hosts, is determined not only by the underlying health of the host but also by the

viral genome. JCPyV is a small, nonenveloped double-stranded DNA virus with a circular genome of approximately 5,100 bp in size (86, 87). Transcription and replication occur in the nucleus and are orchestrated by the noncoding control region (NCCR) (47, 96). The NCCR divides the viral genome into two regions, the early genes needed to transform the cell into a supportive environment and regulate downstream steps in the replication cycle, and late genes, needed for subsequent stages of infection, that include viral assembly and release (96).

Within the nucleus, host transcription factors bind to the NCCR to initiate transcription of the early genes, Large T Antigen (T Ag), small t antigen (t ag), and three alternatively spliced transcripts, T'135, T'136, and T'165 (41). T Ag is a multifunctional protein that is critical in establishing a conducive environment for viral replication. First, it binds to retinoblastoma (pRB), causing the release of the transcription factor, E2F-1, and inducing the cell into S phase (114, 115). Secondly, T Ag can also bind to p53, blocking the cell from activating apoptotic pathways, and lastly, it can act as a helicase, unwinding the viral DNA to continue the production of virus progeny (116, 122). t ag and the spliced variants facilitate T Ag in driving the cell cycle into S phase and assist the function of it by mediating the interactions with p107 and p130, related to the Rb family (385, 386). Once viral DNA is replicated in the nucleus, the late viral genes are transcribed, producing the structural proteins: viral protein 1 (VP1), VP2, and VP3, as well as a multifunctional protein, agnoprotein (96). VP1 is the major component of the capsid, and along with VP2 and VP3; the viral capsid consists of 72 VP1 pentamers (135). Like T Ag, agnoprotein is also considered to be a multifunctional protein. Research has demonstrated that agnoprotein can interact with T Ag, suppressing viral DNA replication and help transition the cell into G2/M phase, allowing the viral DNA to be encapsidated by the VPs (136). Additionally, agnoprotein can act as a viroporin, facilitating viral release from the cell (137).

DNA viruses, including JCPyV are completely dependent on host transcription factors to initiate and coordinate the viral infectious cycle. Host transcription factors bind to the NCCR in JCPyV, where

this small region of the viral genome, that is approximately 145 base pairs, is not only highly important in the infectious cycle but it is a strong indicator of viral disease (96, 97). Previous research has demonstrated that 100% of JCPyV isolates from patients that were diagnosed with PML had genetic mutations in the NCCR compared to the non-disease strain and to other regions of the viral genome, like VP1 (97). The NCCR is characterized as having an early and late proximal region. The early region contains the origin of replication, binding sites for transcription of early genes, and binding sites for T Ag to help regulate viral infection (41). Due to these functions all having important roles in establishing infection, the early proximal region is highly conserved among polyomaviruses and is not prone to mutation (387). However, this is in considerable contrast to the late proximal region. The late region is hypervariable, undergoing mutations and rearrangements that can account for increased viral gene expression, increase tissue tropism, and disease pathogenesis (41, 69, 112). The JCPyV NCCR is divided into DNA sequence blocks denoted as lowercase letters “a”, “b”, “c”, “d”, “e” and “f” which can undergo rearrangements (106–108). The non-pathogenic strain, also called the archetype or CY, is found predominately in the kidneys of healthy individuals, and has all six DNA sequence blocks in alphabetical order (74, 109). The viral sequences associated with PML, also known as the prototype JCPyV NCCR sequence, is the Mad-1 variant, composed of only three blocks, “a,” “c,”, and “e” (41, 74). There are numerous Mad-isolates, with Mad-8, having similar blocks to Mad-1 but also having a portion of block “b” as well as insertions of single base pairs, Mad-8 is more typical of NCCR variants found in PML patients, versus Mad-1 (74, 388, 389).

Pathogenic isolates share a 98 base pair direct tandem repeat, referred to as an enhancer element in the NCCR. These enhancer elements are composed of blocks, “a,” “c,” and “e” and therefore, contain duplicate TATA boxes, located in the “a” block, and have additional transcription factor binding sites (TFBS) (69, 110, 111). Due to the prevalence of these tandem repeats in the NCCR sequences of viral isolates from PML patients, as well as the archetype rarely associated with PML tissue (41, 74, 111),

it is suggestive that these enhancer elements and the addition of TFBS are critical for viral pathogenesis. Furthermore, the loss of the 23-base pair “b” block and the 66-base pair “d” block can also result in increased viral gene expression. These deletions of both regions in the NCCR allow for additional TFBS, such as YB-1/Purα and NF-1, to facilitate enhanced viral gene expression (112, 113). TFBS, such as Spi-B transcription factor (Spi-B), nuclear factor of activated T cells 4 (NFAT4) and subtypes of the nuclear factor 1 (NF-1) family are also important in early gene transcription and may also play a role in cellular tropism as well (100, 101, 390, 391). Specifically, JCPyV can infect B cells, and as these cells mature, transcription factors such as NFI-X and Spi-B have been shown to be upregulated (100, 104). These changes can enhance viral transcription and most notably in individuals who are receiving natalizumab treatment, induce B cell differentiation, possibly inducing the development of PML (105).

Associations between the genetic mutations in the NCCR and PML have been found. There has also been evidence to highlight transcription factors (TFs) that are important for JCPyV infection, even though, there has not been a large analysis approach to observe the changes in the NCCR in the archetype and prototype strains as well as location of sequence isolates. Most importantly, there has not been an extensive bioinformatic approach to validate and uncover TFBS that are influenced by these rearrangements which ultimately enhance viral transcription and cause disease. This study, using already published sequences isolated from deidentified patient samples, characterizes the NCCRs of 181 nucleotide sequences, defining them by both their location of isolation and disease status. Most importantly, by using the largest open-access database of curated and non-redundant TFBS, known as JASPAR (392), this study validated and elucidated possible novel TFBS that influence JCPyV infection in each of the 6 blocks that arise from their rearrangements in the NCCR. This data will provide additional rationale and framework to understand how this hypervariable region of the JCPyV genome can persist in almost 80% of the population, however upon mutations in the NCCR can enhance viral infection, expand its tissue tropism, and ultimately, cause the fatal disease PML.

Materials and Methods

Curating the dataset of NCCR viral isolates and performing a phylogenetic analysis

The workflow to curate a dataset of NCCR sequences is illustrated in Figure 5.1. In all, 10 studies, published and unpublished, represent the 181 NCCR sequences of JCPyV used in this analysis (109, 393–401). Disease classification of the sequences were both from author annotation in GenBank and/or in the Materials and Methods section from published manuscripts. The sequences were aligned using Clustal Omega in the command line, using the specific packages and programs, the European Molecular Bioinformatic Open Software Suite (EMBOSS) and ClustalW. Specifically, Clustal 2.1 Multiple Sequence Alignments was used to perform a multiple alignment using the slow and accurate method (402). Briefly, all 181 sequences were pairwise aligned and a dendrogram was constructed, describing the approximate groupings of the sequences by similarity (402). Finally, the multiple alignment was carried out, using the dendrogram as a guide. To generate a phylogenetic tree, the alignment output was used to calculate the distances between all pairs of sequences. Then the neighbor joining method was used to create the distance matrix (402–404). The .ph file generated from this output was imported into R using the function “read.tree” from the package “ape” (Version 5.4-1). The “phylo4d” function from the package, “phylobase” (Version 0.8.10) was used to merge the phylogenetic tree with sequence information, such as where the sequence was isolated from and disease status. Lastly, to visualize the circular cladogram the function “ggtree” was used from the package, “ggtree” (Version 2.2.4).

Determining and visualizing the blocks of each NCCR viral isolate

To obtain each block (“a”- “f”) within the NCCR, already published sequences for each, were used to scan the NCCRs (107). First, the sequences were separated by isolate site and aligned using the same method described above. This step resulted in more accurate block sequences and faster quality control of each NCCR. The blocks were extracted using the command line and the toolkit, SeqKit, an

ultrafast FASTA/Q Go programming language (405). Specifically, the function "locate" was used in the seqkit executable file with varying max mismatch values when matching the known sequence for each block with the 181 sequences, based on the length of nucleotides for the individual blocks (Table 5.1). Additionally, only the "+" strand was used. Each block was manually inspected using the program Jalview (Version 2.11.0), an open-source program developed for the editing, analyzing, and visualizing of multiple sequence alignments.

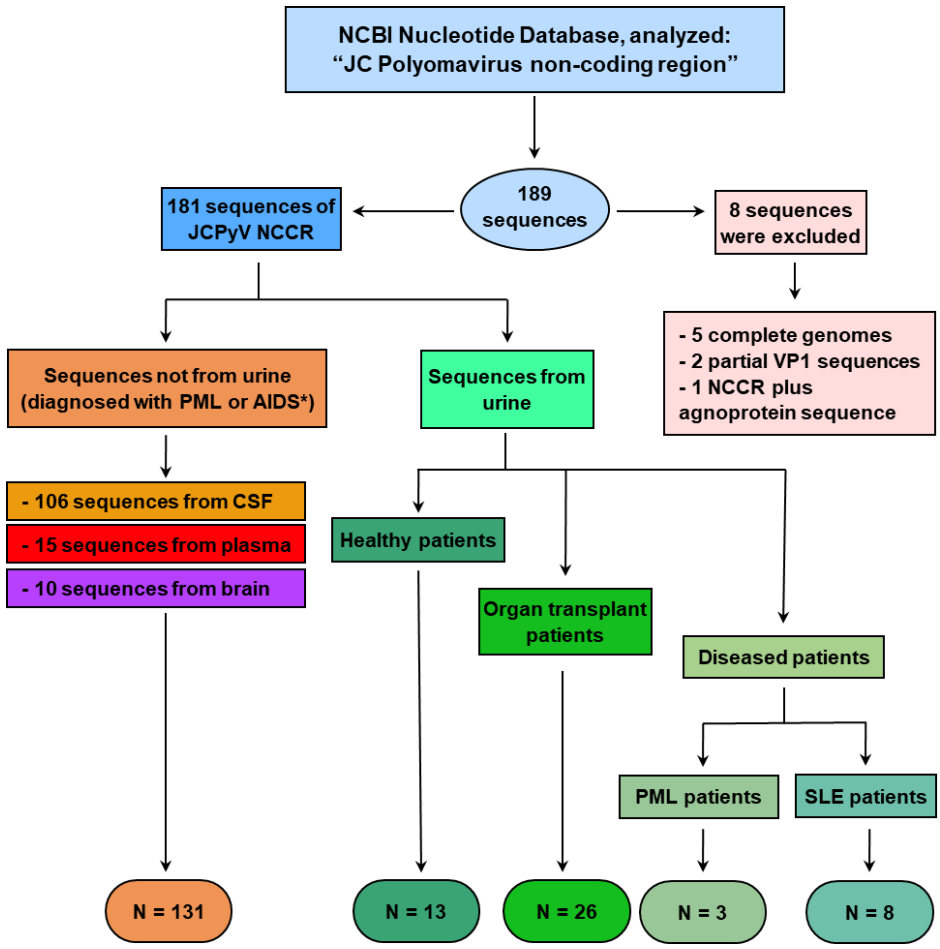

Figure 5.1. Flowchart of sequences of JCPyV NCCRs retrieved from the NCBI database. 181 sequences were analyzed in this study. Sequences were isolated from the CSF (N = 106), plasma (N = 15), brain (N = 10), or urine (N = 50). The sequences isolated from the CSF, plasma, and brain were patients diagnosed with PML or AIDS*. *, 1 sequence isolated from the brain and 1 sequence from the CSF were from patients who had AIDS but were not diagnosed PML. NCCR, noncoding control region; CSF, cerebral spinal fluid; PML, progressive multifocal leukoencephalopathy; SLE, systemic lupus erythematosus.

Table 5.1. Block sequences and criteria used to locate them in each sequence

Block letter	Nucleotide sequence	Maximum mismatch value
Block "a"	CCTGTATATATAAAAAAAAGGGAAGG	9
Block "b"	AGGGAGGAGCTGGCTAAAACTG	8
Block "c"	GATGGCTGCCAGCCAAGCATGAGCTCATACCTAGGGA GCCAACCAGCTGACAGCC	27
Block "d"	AGAGGGAGCCCTGGCTGCATGCCACTGGCAGTTATAGTGAAACCCCTCC CATAGTCCTTAATCACA	31
Block "e"	AGTAAACAAAGCACAAGG	1
Block "f"	GGAAGTGGAAAGCAGCCAAGGGAACATGTTTTGCGAGCCAGAGCTGTT TTGGCTTGTCACCAGCTGGCCAGT	31

Data were visualized using the package, ggplot2 (Version 3.3.3) in R and the function geom_pointrange was used to illustrate the position of each block for all the NCCRs faceted by location and disease status. Additionally, the function, geom_histogram was used to determine the density distribution of each block, by length, also faceted by location and disease status. Overall, there were a total of 1,416 blocks across all four locations, 85 blocks from the brain, 938 from the CSF, 99 from the plasma and 294 from the urine.

Determining the TFBS for each NCCR viral isolated using the JASPAR database

To curate the dataset of TFBS for the 1,416 blocks, the package "TFBStools" (Version 1.26.0) was used in RStudio, along with the package "Biostrings" (Version 2.56.0) to upload the sequences in the RStudio environment, with the function "readDNAStringSet." The matrix for each TFBS in humans (species ID: 9606) was uploaded into RStudio with the function "getMatrixSet" from the 2020 JASPAR database. TFBS for all 181 sequences were obtained with a minimum score of 70%, only examining the "+" strand, based on the same approach that was used to extract the individual blocks. A minimum score of 70% was determined through analyzing output data with varying scores that resulted in TFBS, like SPIB and SP1 that are known to influence JCPyV infection to be included in the dataset. In total, there were 2,083 TFBS with 600 unique TFBS, in sequences isolated from the brain, there were 2,423

TFBS with 625 unique TFBS, from the CSF; 1,839 TFBS with 594 unique TFBS, from the plasma and lastly, there were 1,778 TFBS, with 597 unique TFBS from sequences isolated in the urine. To compare the frequency of TFBS with varying number of sequences from each location, the normalized frequency was determined (equation 5.1).

$$\text{normalized frequency of TFBS} = \frac{\left(\text{\# of TFBS}/_{\text{Block}}\right)}{(\text{\#of sequences})} \qquad (5.1)$$

Statistical techniques and code availability

All statistical tests were performed in R. The Kruskal-Wallis test to was used to compare the median distribution of the normalized frequency of TFBS across all 6 groups (location and disease status). When the Kruskal-Wallis test was significant, the pairwise Wilcoxon rank sum test, along with the Bonferroni adjustment was used to determine the pair of groups that were statistically different.

R scripts are available upon request. Datasets for the nucleotide sequences, block sequences, and frequency of TFBS is available as supplemental material.

Results

The curation of the JCPyV NCCR from patient samples

181 sequences were acquired from GenBank from 10 published and unpublished studies in both diseased and healthy patients (Fig. 5.1). Disease status was determined from both the GenBank record and from the Materials and Methods described from published manuscripts. Searching for “JC Polyomavirus non-coding region” resulted in 189 sequences, of which 181 sequences were exclusively the JCPyV NCCR. As the archetype strain is rarely associated with PML (41, 74), these sequences were separated by urine and nonurine samples (Fig. 5.1). There were 131 nonurine sequences, 106 from the cerebral spinal fluid (CSF), 15 from the plasma, and 10 sequences from the brain. Most patients (N =

129) had PML, however two other sequences, one sequence isolated from the brain and one sequence from the CSF, were from patients who had AIDS but were not diagnosed with PML. Sequences isolated from urine were further divided by disease status as the archetype strain can be detected in the urine (398). Most samples were either healthy patients (N = 13) or organ transplant patients (N = 26), while three sequences were from PML patients, and 8 sequences were isolated from SLE patients (Fig. 5.1). Collectively, using sequences readily available in GenBank, we were able to curate a dataset composed of 181 unique sequences, isolated from urine, CSF, brain, and plasma, from both healthy and diseased patients.

Phylogenetic analysis reveals distinct differences from sequences isolated from the urine versus other sites while revealing similarities in the NCCR across the CSF, brain, and plasma among PML patients

The 181 sequences from the NCBI database were aligned using Clustal Omega (402) and a phylogenetic analysis was performed using the neighbor-joining clustering algorithm to illustrate the nucleotide similarities across various sites and disease status (Fig. 5.2). The analysis revealed that 37 of the 50 sequences isolated from the urine had higher sequence similarity with each other compared to other samples (Fig. 5.2). There was also no distinct clustering in sequences isolated from the CSF, brain, or plasma. Interestingly, there were sequences isolated from PML patients, in the brain, plasma, or CSF that had nucleotide similarities to NCCR sequences from healthy individuals in the urine, and specifically, three sequences from the CSF and plasma that clustered with the 37 sequences isolated from the urine (Fig. 5.2). Conversely, one sample from a PML patient in the urine (AF35477.1) shared the highest dissimilarity from other urine samples and clustered with nonurine samples from PML patients (Fig. 5.2). This can suggest that within the kidneys, the JCPyV genome, specifically the NCCR, does not vary greatly, however genetic variation can occur and can resemble the high dissimilarity that was observed across other locations from diseased patients. Overall, this analysis revealed the phylogenetic relationships of

NCCR sequences isolated from the various tissues and fluids among PML patients and healthy individuals and demonstrates the clustering of sequences isolated from the urine.

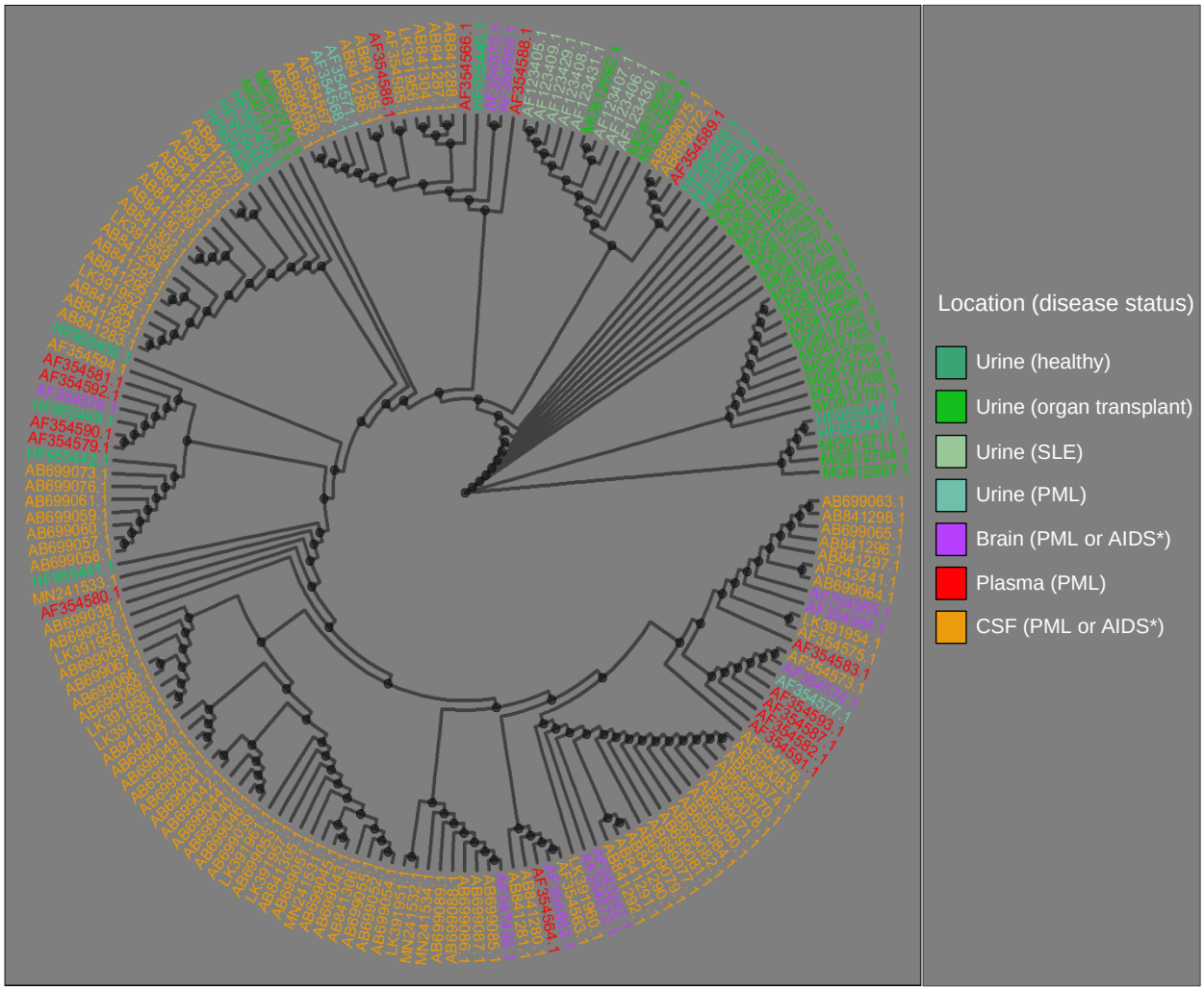

Figure 5.2. A phylogenetic analysis of the NCCR sequences of the JCPyV genome based on the location of sequence isolation and the disease status of the patients. JCPyV NCCR sequences were obtained from the NCBI Nucleotide Database and aligned using Clustal Omega available in the EMBOSS package. The 181 sequences are illustrated as a circular cladogram, where the color of the Accession numbers illustrates both the site of sequence isolation and disease status of individual patients. The cladogram was created using the package 'ggtree' in RStudio. *, 1 sequence isolated from the brain (AF047456.1) and 1 sequence from the CSF (AF043241.1) were from patients who had AIDS and but were not diagnosed with PML.

The heterogenicity of NCCR sequences across isolation sites and disease status

To visually understand the differences in rearrangement within the NCCR, the individual blocks ("a" – "f") were analyzed in all 181 sequences (Fig. 5.3). Previously published data was used to

determine the sequence for each block (107) and the FASTA/Q toolkit, SeqKit, (405) within the command line was used, to locate the blocks for each sequence. All sequences were manually inspected using Jalview (Version 2.11.0), and the package 'ggplot2' was used to illustrate the 181 sequences for each location. Samples extracted from urine, specifically from healthy individuals and organ transplant recipients, illustrated the highest degree of uniformity, and resembled the archetype strain ("a", "b", "c", "d", "e", and "f") (Fig. 5.3A). Interestingly, one of the three sequences isolated from the urine of a PML patient resembled that of other sequences isolated from nonurine locations and sequences isolated from SLE patients lacked the "a" block (Fig. 5.3A). The 10 NCCR sequences isolated from the brain (Fig. 5.3B) and the 15 sequences isolated from the plasma (Fig. 5.3C) showed more variation in block arrangement compared to sequences isolated from the urine. Moreover, upon visual analysis, more sequences from the plasma compared to the brain, resembled the archetype, having a "d" block present in the NCCR. The highest degree of variation, however, was observed in the 106 sequences isolated from the CSF (Fig. 5.3D). Almost all the 106 NCCR sequences illustrated the 98 base pair direct tandem repeat while also having segments of the "b" block, resembling the Mad-8 prototype (Fig. 5.3D). Overall, this plot demonstrates the excessive degree of rearrangement in the NCCR of the JCPyV genome from PML patients isolated from the brain, plasma, and CSF, compared to sequences isolated from the urine of healthy individuals.

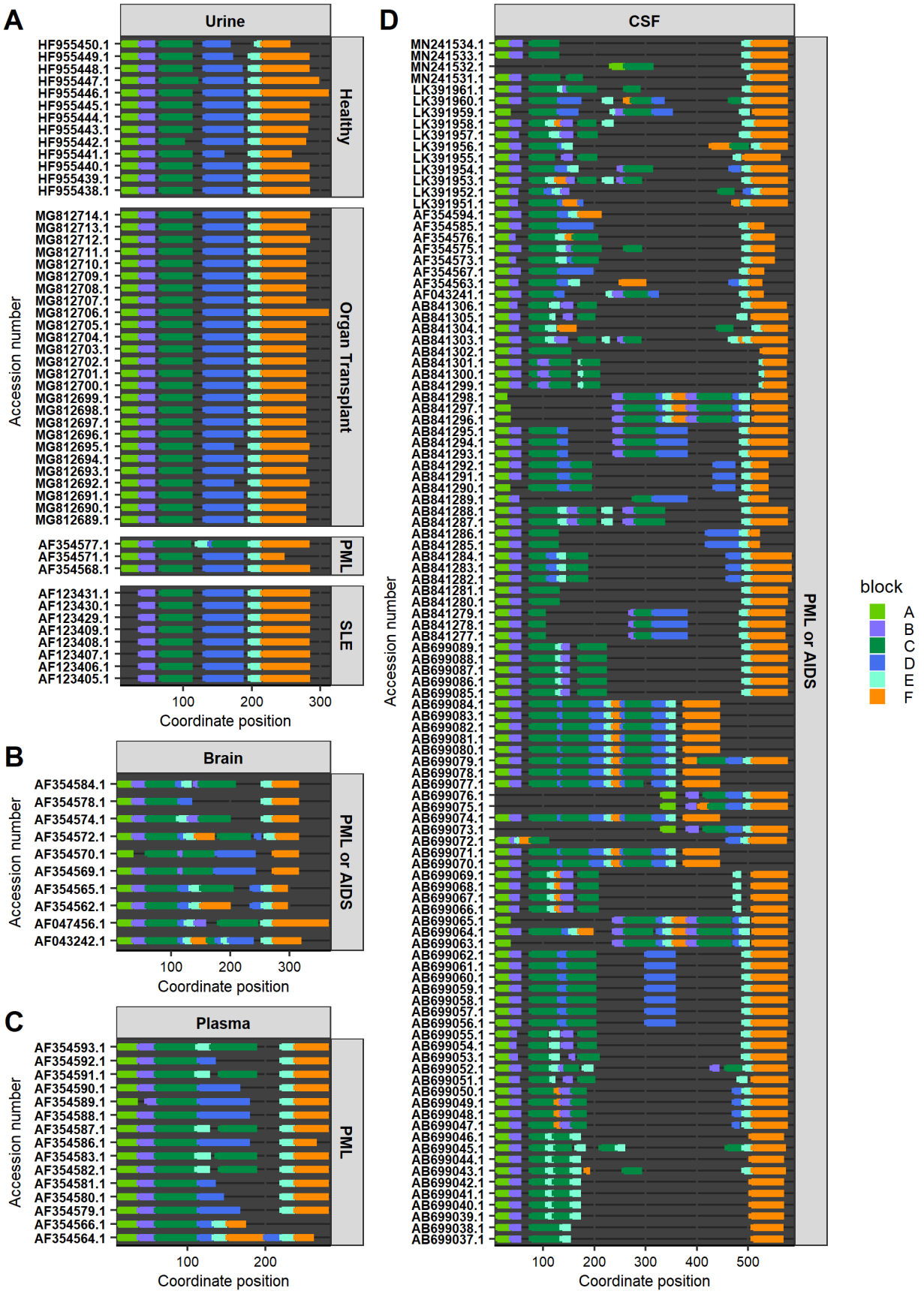
A
Urine
HF955450.1
HF955449.1
HF955448.1
HF955447.1
HF955446.1
HF955445.1
HF955444.1
HF955443.1
HF955442.1
HF955441.1
HF955440.1
HF955439.1
HF955438.1
Healthy
MG812714.1
MG812713.1
MG812712.1
MG812711.1
MG812710.1
MG812709.1
MG812708.1
MG812707.1
MG812706.1
MG812705.1
MG812704.1
MG812703.1
MG812702.1
MG812701.1
MG812700.1
MG812699.1
MG812698.1
MG812697.1
MG812696.1
MG812695.1
MG812694.1
MG812693.1
MG812692.1
MG812691.1
MG812690.1
MG812689.1
Organ Transplant
AF354577.1
AF354571.1
AF354568.1
PML
AF123431.1
AF123430.1
AF123429.1
AF123409.1
AF123408.1
AF123407.1
AF123406.1
AF123405.1
SLE
Accession number
100
200
300
Coordinate position
B
Brain
AF354584.1
AF354578.1
AF354574.1
AF354572.1
AF354570.1
AF354569.1
AF354565.1
AF354562.1
AF047456.1
AF043242.1
PML or AIDS
Accession number
100
200
300
Coordinate position
C
Plasma
AF354593.1
AF354592.1
AF354591.1
AF354590.1
AF354589.1
AF354588.1
AF354587.1
AF354586.1
AF354583.1
AF354582.1
AF354581.1
AF354580.1
AF354579.1
AF354566.1
AF354564.1
PML
Accession number
100
200
Coordinate position
D
CSF
MN241534.1
MN241533.1
MN241532.1
MN241531.1
LK391961.1
LK391960.1
LK391959.1
LK391958.1
LK391957.1
LK391956.1
LK391955.1
LK391954.1
LK391953.1
LK391952.1
LK391951.1
AF354594.1
AF354585.1
AF354576.1
AF354575.1
AF354573.1
AF354567.1
AF354563.1
AF043241.1
AB841306.1
AB841305.1
AB841304.1
AB841303.1
AB841302.1
AB841301.1
AB841300.1
AB841299.1
AB841298.1
AB841297.1
AB841296.1
AB841295.1
AB841294.1
AB841293.1
AB841292.1
AB841291.1
AB841290.1
AB841289.1
AB841288.1
AB841287.1
AB841286.1
AB841285.1
AB841284.1
AB841283.1
AB841282.1
AB841281.1
AB841280.1
AB841279.1
AB841278.1
AB841277.1
AB699089.1
AB699088.1
AB699087.1
AB699086.1
AB699085.1
AB699084.1
AB699083.1
AB699082.1
AB699081.1
AB699080.1
AB699079.1
AB699078.1
AB699077.1
AB699076.1
AB699075.1
AB699074.1
AB699073.1
AB699072.1
AB699071.1
AB699070.1
AB699069.1
AB699068.1
AB699067.1
AB699066.1
AB699065.1
AB699064.1
AB699063.1
AB699062.1
AB699061.1
AB699060.1
AB699059.1
AB699058.1
AB699057.1
AB699056.1
AB699055.1
AB699054.1
AB699053.1
AB699052.1
AB699051.1
AB699050.1
AB699049.1
AB699048.1
AB699047.1
AB699046.1
AB699045.1
AB699044.1
AB699043.1
AB699042.1
AB699041.1
AB699040.1
AB699039.1
AB699038.1
AB699037.1
PML or AIDS
Accession number
100
200
300
400
500
Coordinate position
block
A
B
C
D
E
F

Figure 5.3. Sequences isolated from the CSF illustrate the greatest degree of rearrangement in the NCCR of the JCPyV genome. The NCCR sequences are arranged in 6 blocks (A-F) and these blocks were extracted using SeqKit, an ultrafast FASTA/Q toolkit in Go programming language. Following Clustal Omega alignment, the command 'locate' in SeqKit was used to determine the arrangement of the 6 blocks. All sequences were manually inspected to validate accuracy and confirm no overlapping/duplicate regions. The package, 'ggplot2' in RStudio was used, specifically the function geom_pointrange, to illustrate the coordinate position of the blocks for each accession number, faceted by the location of where the sequences were isolated from.

Density distribution of the individual blocks reveals a high frequency of deletions in block "c", "d", and "f" in NCCR sequences from PML patients isolated from the CSF

To further analyze the large variation in NCCR sequences illustrated in Figure 5.3, a quantitative analysis was used to determine frequency distribution of the individual blocks in each sequence based on the length of each block (Fig. 5.4). Histograms were generated as density plots for all 181 NCCR sequences based on site of isolation and disease status. Due to the degree of similarity observed in sequences isolated from healthy individuals and donor transplant recipients from the urine (Fig. 5.2 and Fig. 5.3), these groups were combined. Overall, sequences isolated from the urine regardless of disease status demonstrated few variations in block length (< 2%) (Fig. 5.4). Furthermore, it was previously illustrated that sequences from the plasma resembled the archetype more than sequences isolated from the brain (Fig. 3). The density distribution of block "d" from the plasma versus the brain demonstrates a higher density (~7.5%) versus ~2% that coordinate to the same sequence length of block "d" from sequences isolated from the urine of healthy individuals (Fig. 5.4). This was also observed in the "b" block, where most of the distribution of that sequence isolated from the plasma resembled that of sequences isolated from the urine compared to the distribution of block "b" in sequences isolated from the brain and CSF of PML patients (Fig. 5.4). Lastly, the density plot revealed a high degree of deletions, specifically in NCCR sequences from the CSF. Block "c", "d" and "f" displayed the largest range in sequence length, demonstrating that numerous blocks within these sequences were deleted (Fig. 5.4). Altogether, the density plot quantified the observations in Figure 3 and demonstrate the high degree of

variation in both the number of blocks and block length that compose the NCCR, especially from sequences isolated from the CSF in PML patients.

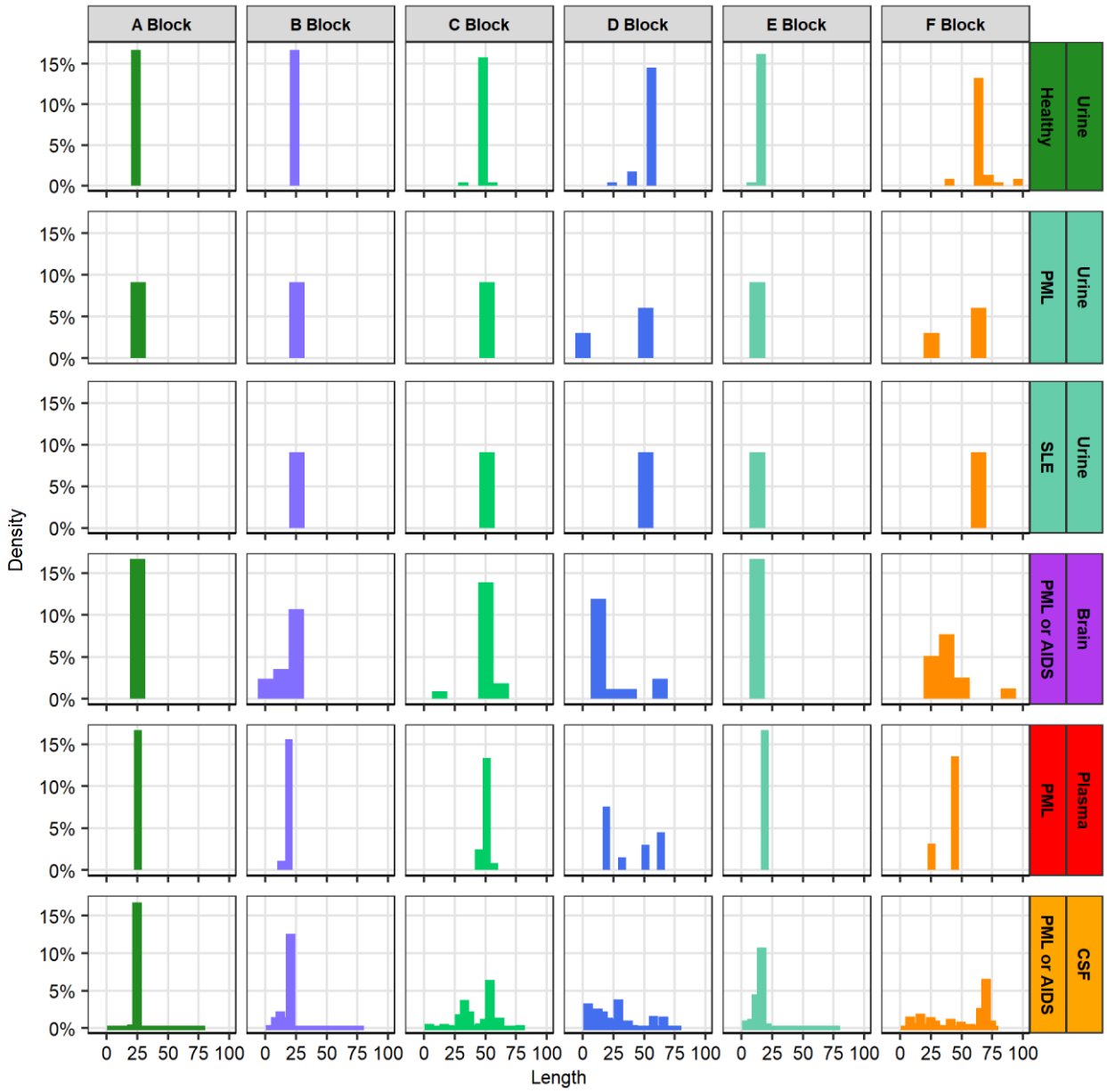

Figure 5.4. Deletions and duplications of the C block, D block, and F block accumulate more in patients with PML or AIDS in the NCCR of viral isolates from the brain, plasma, and CSF. Histograms represent Density plots for each block (A-F) in all 6 groups based on the length of the blocks (x axis) using 'ggplot2' as follows: 1. Urine/Healthy + Urine/Organ Transplant, 2. Urine/PML, 3. Urine/SLE, 4. Brain/PML or AIDS, 5. Plasma/PML, 6. CSF/PML or AIDS. Bin size for each group was determined using Rice's role. Each row sums to 100% except for groups 2 and 3, both adding to 100%.

TFBS that facilitate activation of JCPyV infection are more frequent in nonurine sequences from PML patients, and TFBS that repress JCPyV infection are higher in sequences isolated from the urine

To understand how NCCR variation among these 181 sequences may influence JCPyV infection, the frequency of known TFBS involved in JCPyV replication from literature review were determined in each block of every sequence (Fig. 5.5). The RStudio package, 'TFBStools' (Version 1.26.0) was used along with the 2020 JASPAR database to find the TFBS motifs of each NCCR sequence per block. Sequences isolated from the CSF had the highest number of known TFBS that influence JCPyV infection (Fig. 5.5). Block "c" and block "d" had the highest variation in TFBS between locations, specifically, CCAAT Enhancer Binding Protein β (CEBPβ) and Nuclear Factor I X (NFIX), known repressors and activators of JCPyV infection, respectively (Fig. 5.5). There were more TFBS for NFIX in the "c" block of sequences isolated from PML patients versus patients with SLE or healthy individuals, and there were more TFBS for CEBPβ in the "d" block from sequences isolated from SLE patients and healthy individuals (Fig. 5.5). Interestingly, NFIX sites in block "d", part of the NCCR that is not an enhancer element (96) was higher in sequences isolated from the urine. Lastly, the TFBS, Spi-B (SPIB) was present in sequences isolated from the plasma, specifically in block "d," adding evidence to the importance of this TF during JCPyV infection of B cells. Overall, this data supports previously-published data recognizing the importance of TFBS in the archetype versus prototypical strains (i.e., PML-type strains) and how genetic rearrangements can alter the frequency of TFBS, especially in the brain, plasma, and CSF of PML patients.

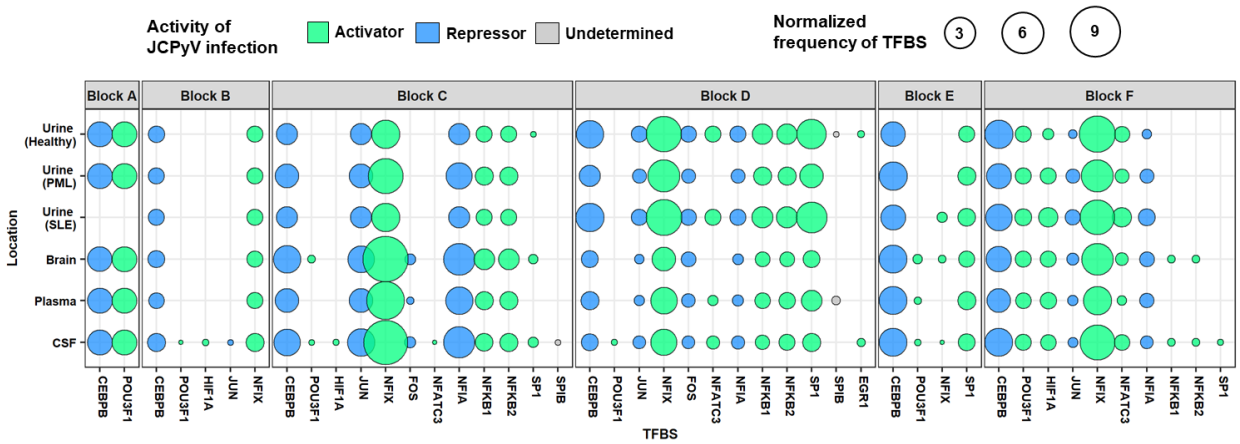

Figure 5.5. Transcription factors binding sites that activate JCPyV infection are more prevalent in patients that have PML or AIDS in the NCCR of viral isolates from the brain, plasma, and especially, the CSF. The RStudio package, 'TFBStools' was used to determine the TFBS for each block in all 181 sequences, using the 2020 JASPAR database. Known TFBS that have are associated with JCPyV transcription and replication were illustrated as a balloon plot using 'ggplot2'. TFBS are faceted by the 6 blocks (A-F). The size of the circle represents the normalized frequency of the TFBS (i.e., the number of times the TFBS is present) [(# of TFBS/Block)/(# of sequences)] in each of the 6 groups/locations and the color represents the activity that correlates with JCPyV infection.

Significant differences are observed in the number of TFBS in NCCR viral isolates from the brain, plasma, and CSF, specifically in block "c," block "d," and block "f" of the NCCR

To determine how rearrangements in the NCCR alter TFBS, especially based on site of viral isolation and disease status, the total number of TFBS were determined in each location faceted by each block and overall enhancer elements (Fig. 5.6). A pairwise Wilcoxon rank sum test, along with the Bonferroni adjustment was used to compare the number of TFBS between groups; however, only the significance comparing the TFBS from the urine of healthy individuals compared to the other locations is illustrated (Table 5.2). As previously illustrated in Figure 5.5, the most significant variation in the number of TFBS by location was observed in block "c," block "d," and block "f" (Fig. 5.6). The number of TFBS were higher in diseased patients, specifically comparing the number of TFBS from the urine of healthy individuals to the brain and urine of PML patients (Fig. 5.6). Additionally, the number of TFBS was significantly lower in nonurine sequences compared to sequences isolated from the urine (Fig. 5.6 and Table 5.2). This is most likely attributed to the fewer number and deleted portions of the "d" block in

nonurine locations (Fig. 5.3 and Fig. 5.4). Taken together, this data suggests that the number of TFBS is influenced by the genetic rearrangements in diseased patients, specifically, attributed to the duplications and deletions of specific blocks in the NCCR.

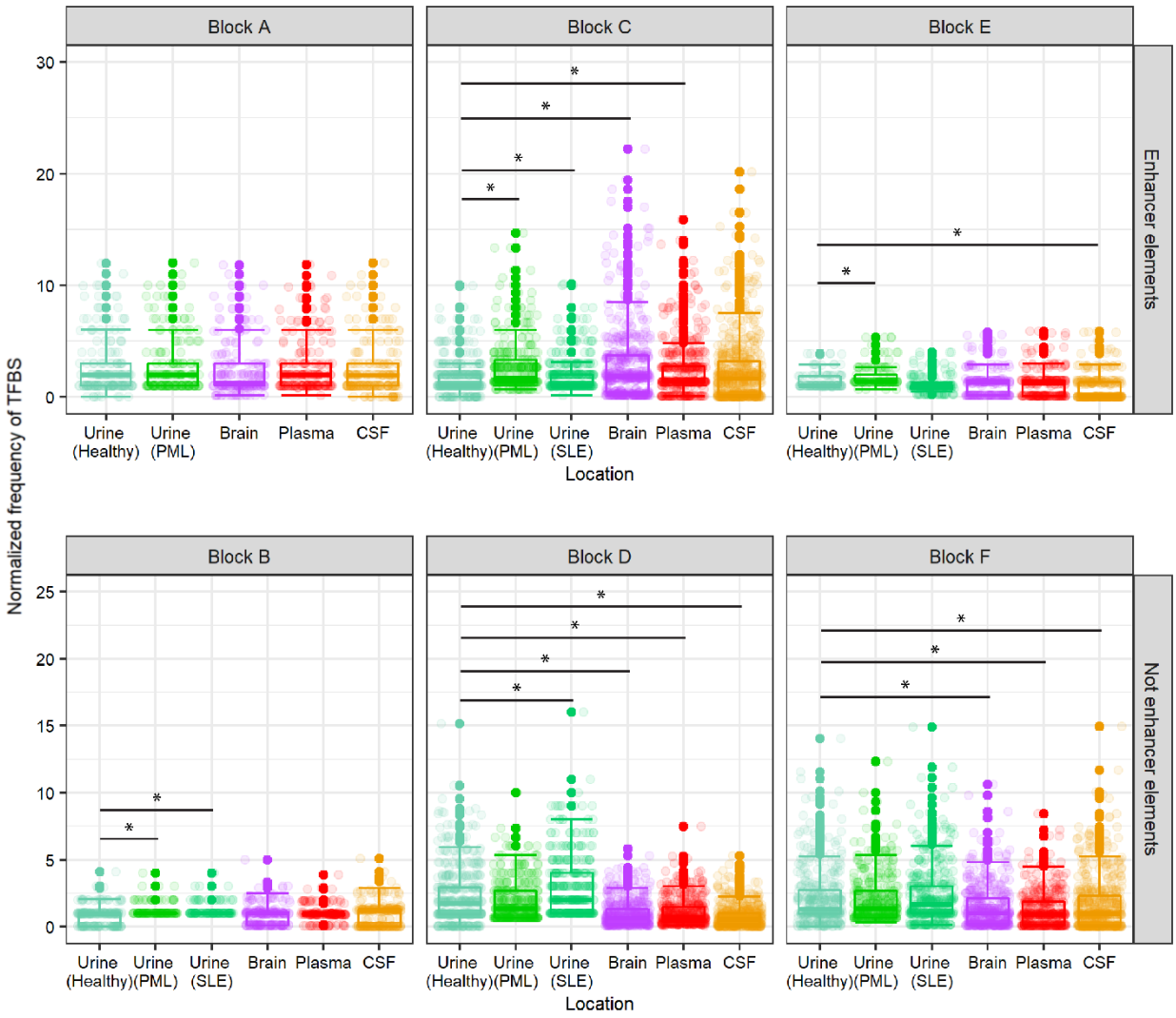

Figure 5.6. Block C, D, and F of the JCPyV NCCR has the largest variation in the frequency of TFBS in sequences isolated from the brain, plasma, and CSF, compared to sequences isolated from the urine of healthy individuals. The overall distribution of the normalized frequency of TFBS [(# of TFBS/Block)/(# of sequences)] were plotted for each of the 6 groups, faceted by the 6 blocks (A-F) using the RStudio package, 'ggplot2.' In addition, the 6 blocks were also faceted by enhancer element for JCPyV infection (top) and not or non-enhancer element for JCPyV infection (bottom). A pairwise Wilcoxon rank sum test, along with the Bonferroni adjustment was used to compare the occurrence of TFBS of each group. Statistics are only illustrated comparing the frequency of TFBS from sequences isolated from the urine of healthy individuals versus the other five locations (x axis) *, $P < 0.01$. (Full list of *P values* illustrated in Table 5.2).

Table 5.2. Bonferroni adjusted *P values* from pairwise comparisons using Wilcoxon Rank Sum Test with continuity correction of the normalized frequency of TFBS versus each location.

Block A					
Location	Urine (Healthy)	Urine (PML)	Brain	Plasma	
Urine (PML)	1.00	-	-	-	
Brain	1.00	1.00	-	-	
Plasma	1.00	1.00	1.00	-	
CSF	0.68	0.12	1.00	0.19	
Block B					
Location	Urine (Healthy)	Urine (PML)	Urine (SLE)	Brain	Plasma
Urine (PML)	2.8e-12	-	-	-	-
Urine (SLE)	2.8e-12	1.00	-	-	-
Brain	0.02	9.0e-06	9.0e-06	-	-
Plasma	1.00	< 2e-16	< 2e-16	-	-
CSF	1.00	0.40	0.40	1.00	1.00
Block C					
Location	Urine (Healthy)	Urine (PML)	Urine (SLE)	Brain	Plasma
Urine (PML)	< 2e-16	-	-	-	-
Urine (SLE)	2.9e-05	1.4e-10	-	-	-
Brain	2.9e-05	1.00	1.00	-	-
Plasma	6.5e-09	0.09	0.02	0.07	-
CSF	1.00	6.2e-07	0.82	2.5e-04	0.21
Block D					
Location	Urine (Healthy)	Urine (PML)	Urine (SLE)	Brain	Plasma
Urine (PML)	1.00	-	-	-	-
Urine (SLE)	9.2e-14	2.0e-11	-	-	-
Brain	< 2e-16	< 2e-16	< 2e-16	-	-
Plasma	< 2e-16	< 2e-16	< 2e-16	0.25	-
CSF	< 2e-16	< 2e-16	< 2e-16	6.4e-05	3.5e-10
Block E					
Location	Urine (Healthy)	Urine (PML)	Urine (SLE)	Brain	Plasma
Urine (PML)	1.8e-11	-	-	-	-
Urine (SLE)	1.00	< 2e-16	-	-	-
Brain	1.00	1.3e-06	1.00	-	-
Plasma	0.63	4.2e-04	1.00	1.00	-
CSF	2.2e-10	< 2e-16	2.0e-09	< 2e-16	< 2e-16
Block F					
Location	Urine (Healthy)	Urine (PML)	Urine (SLE)	Brain	Plasma
Urine (PML)	1.00	-	-	-	-
Urine (SLE)	1.00	1.00	-	-	-
Brain	6.1e-08	5.7e-13	3.7e-12	-	-
Plasma	4.5e-13	6.9e-14	< 2e-16	0.50	-
CSF	4.2e-09	5.0e-10	2.2e-13	1.00	1.00

No Block A sequences from SLE patients were isolated; -, Wilcoxon Sum Rank Test with same location.

The number of TFBS that are related to forkhead and homeobox proteins are increased in the "c" block and decreased in the "d" block of patients with PML

To understand the specific TFBS that are altered in the NCCR sequences of nonurine locations and PML patients, the difference in TFBS from those groups were taken from the TFBS of urine sequences isolated from healthy individuals (control). TFBS that were greater or less than four sites compared to the control group are illustrated as a heatmap based on the outlier distribution of Figure 5.6 (Fig. 5.7). All groups are represented except TFBS from SLE patients as there were none isolated with TFBS that were greater or less than 4. In all, 76 TFBS occurred more frequently in PML patients and 9 TFBS were in all 4 isolation sites; all of these occurred in the "c" block (Fig. 5.7). Numerous TFBS are in the group of homeobox genes including: HOXA4, MEIS1, and HOXB3, as well as forkhead genes, such as FOXL1 and FOXP3 (Fig. 5.7). Another TFBS that was increased in PML patients was Nuclear Respiratory Factor 1 (NRF1). This protein-coding gene has DNA-binding transcription activator activity (406, 407). Most importantly, this analysis also revealed a TFBS for Oligodendrocyte transcription factor 3 (OLIG3). This TFBS, which occurred more frequently in the "c" block, may contribute to cellular tropism as it was only observed in sequences isolated from the CSF and brain (Fig. 5.7).

The TFBS that occurred less frequently in PML patients occurred in block "d" and block "f." In all, there were 67 TFBS that occurred less often in block "d" and 24 TFBS in block "f" (Fig. 5.7). In block "d," 3 of the 67 TFBS were common among all locations: SOX18, MEIS1, and NKX2-8. No TFBS in block "f" were similar across isolation sites, however RFX7 occurred less frequently in sequences isolated from the brain, plasma, and urine of PML patients (Fig. 5.7). Specifically, the TFBS MEIS1 demonstrated the largest difference in the number of sites changed between blocks "c" and "d" in PML patients compared to NCCR sequences of healthy individuals. This may suggest that MEIS1 is important in the development of PML as it was found more frequently in the enhancer element of the JCPyV NCCR. Additionally, an already known TFBS that influences JCPyV infection, NFIX was demonstrated in this analysis to occur

more frequently in the “c” block and less frequently in the “d” block of sequences isolated from the brain, CSF, and plasma (Fig. 5.7). Collectively, this analysis reveals novel TFBS that may influence the development of PML, expand the cellular tropism of the virus, and validates TFBS that are known to influence JCPyV infection.

Discussion

The NCCR is a hypervariable region within the JCPyV genome that can enhance JCPyV infection, and rearrangement of the NCCR is associated with the fatal disease PML (74). However, our understanding of how the NCCR is implicated in disease is limited, due in part, from low sample sizes (408), and few studies demonstrating the changes in TFBS from sequences isolated from the urine to nonurine locations, and asymptomatic to symptomatic individuals. This study addresses these gaps in knowledge by compiling 181 NCCR sequences from the Nucleotide database in NCBI and examines how TFBS are altered across various locations based on disease status of the individuals. Our results demonstrate the variability in the NCCR of PML patients and illustrate the differences in the archetype versus PML-type strains of JCPyV. Furthermore, this analysis validates and elucidates novel TFBS that are perhaps involved in JCPyV infection and PML.

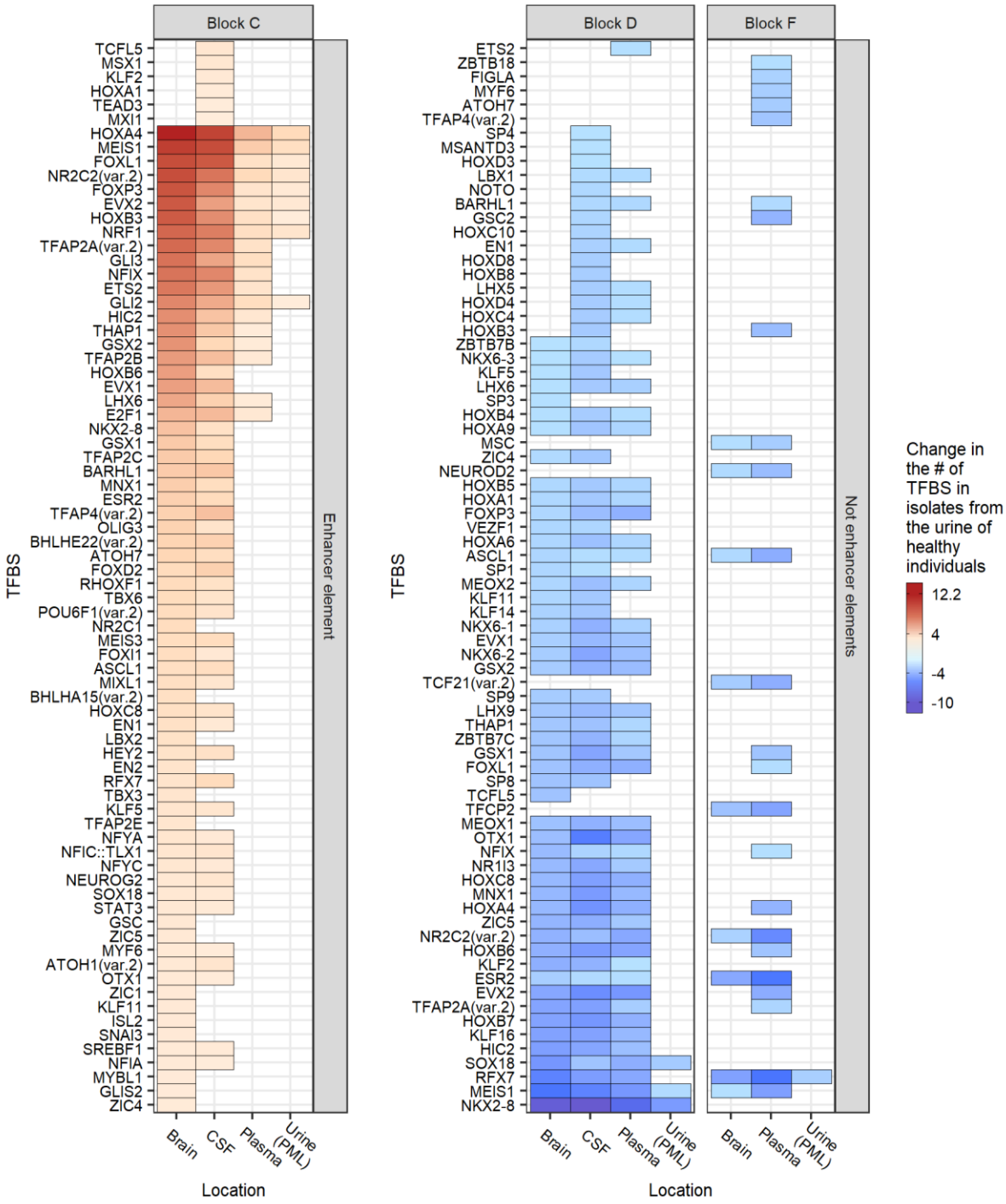

Figure 5.7. The number of TFBS compared to sequences isolated from the urine of healthy individuals are greatly added to enhancer elements and removed from other elements in patients with PML. The difference in the number of TFBS in each group was compared to sequences isolated from the urine of healthy individuals (control group). Based on the outliers from the distribution of TFBS in each group, a difference of 4 binding sites for each transcription factor was used and results are illustrated as a heat map. The order of TFBS are sorted in descending order based on the TFBS of sequences isolated from the brain (i.e. the greatest number of TFBS added compared to sequences from the control group). Sequences isolated from the urine of SLE patients and Block A, Block B, and Block E are not illustrated because there was no TFBS that had a difference of 4 binding sites added or removed compared to the control group. No TFBS were greater or less than 4 in SLE patients.

Phylogenetic analysis revealed that many sequences isolated from the urine clustered together, however a few sequences had nucleotide similarity to sequences isolated outside the urine from PML patients (Fig. 5.2). This was especially true for a sequence isolated from the urine of a PML patient, suggesting that PML-type strains could also be found in the kidney and not restricted to the CNS. These same conclusions were also deduced from Pfister et. al, who analyzed this sequence initially (398). This was contradictory to earlier findings in that significant rearrangement did not occur in the kidney (409, 410), however more evidence suggested that mutations, specifically the duplication of the 98 base pair tandem repeat can occur in the kidneys of PML patients with immunodeficiency disorders (408) (Fig. 5.3). This data suggests, that even though reactivation of JCPyV is poorly understood, immunosuppressed individuals may not have adequate immune surveillance, prompting enhanced JCPyV replication driven by the increased probability of promoter rearrangements within the NCCR (74). However, Figure 5.2 and Figure 5.3 also illustrate nucleotide similarity and block rearrangement in sequences isolated from the plasma of PML patients comparable to that of sequences isolated from the urine. Lymphocytes can act as reservoirs for JCPyV, and it has been hypothesized that rearrangement of the NCCR can occur here, as B cells have the machinery to facilitate genome rearrangement (41). Sequences isolated from the plasma illustrated archetype-like structure of the NCCR (Fig. 5.3) and had overall block distribution corresponding to sequences isolated from the urine, among all the other locations isolated from PML patients (Fig. 5.4). Taken together, this data demonstrates the likelihood of multiple mechanisms of JCPyV reactivation when comparing sequence identity and block structure of the NCCR in sequences isolated from the urine of healthy individuals versus PML patients.

There have been numerous TFs reported to influence JCPyV infection (41) however the impact on the TFBS from rearrangements in the NCCR, in the context of isolation location and disease status, has not been well studied. NFIX is a well characterized TF that activates JCPyV transcription (391, 411). This analysis validates the importance of this TFBS, occurring more frequently in PML patients,

specifically, in sequences isolated from the brain and CSF in block “c” of the NCCR (Fig. 5.5). Additionally, this supports the hypothesis that rearrangements in the NCCR increase tissue tropism as NFIX is highly expressed in the CNS, and the addition of these TFBS most likely aids in the replication of viral transcription (391). Interestingly though, the NFIX TFBS occurred more frequently in sequences isolated from the urine and plasma of PML patients compared to healthy individuals, which speaks to the importance of NFIX enhancing JCPyV transcription, regardless of location, which may lead to PML.

NCCR mutations are complex and most likely the result of homologous recombination that leads to large deletions and tandem duplications in the NCCR (74). The influence of these rearrangements is also observed in TFBS that are known to influence JCPyV infection (Fig. 5.5). In many sequences isolated from PML, there are deletions of block “d” (Fig. 5.3 and Fig. 5.4), which is important in the success of viral transcription as there are TFBS for CEBPβ, a repressor of viral transcription (Fig. 5.5). Deletion of portions or even the full block leads to less TFBS for CEBPβ which enhances viral transcription (412). Interestingly however, there were TFBS for NFIX located on the “d” block that occurred more frequently compared to sequences isolated from the brain, plasma, and CSF (Fig. 5.5). This highlights the complexity of not only NCCR rearrangement but also the regulation of TFs in the replication of JCPyV. Romagnoli et al. demonstrated the important inhibitory role of CEBPβ during JCPyV infection of human glioblastoma and transformed human glial cells but also revealed the activation of JCPyV transcription by NF-κB. They suggested that there was a unique interplay between both TFs that control the balance of JCPyV latency and reactivation during immunosuppression (412). Furthermore, research has also demonstrated that TFs that repress viral transcription, specifically AP-1 TFs, block NF-1 binding sites, because of the proximity of these TFBS (103). This study isolated human CNS progenitor cells and differentiated them into an astrocytic cell line to determine that AP-1 TFs, like c-Jun bind to AP-1 binding sites thus blocking TFs that activate transcription as they can no longer bind to NF-1 sites (103). This analysis revealed that even though there was an increase in NFIX sites in block “d” there was also an

increase in TFBS that inhibit JCPyV transcription, like CEPBβ and JUN, which result in lower transcriptional levels that are observed in healthy individuals. These studies examining the importance of TFs in JCPyV infection, mainly used *in vitro* techniques and were across various cell types, and thus it should be noted that cell-type differences can be observed. Overall, examining the known TFBS that influence JCPyV transcription of 181 sequences from healthy and diseased patients reinforced the intricate balance between viral transcription, expanding cellular tropism, and possibly leading to disease caused by enhanced JCPyV replication.

JASPAR is one of the largest databases of known TFBS, and this study examined known TFBS that influence JCPyV infection. In addition to this validation, we further examined other TFBS that have not been previously characterized in viral transcription and cellular tropism, identifying novel TFBS that may correlate with the disease PML (Fig. 5.6 and Fig. 5.7). Differences in the number of TFBS were most notable in blocks “c”, “d”, and “f” (Fig. 5.6 and Table 5.2). This was most likely due to the extent of rearrangements, deletions, and duplications that these blocks are subject to within the NCCR (Fig. 5.3 and Fig. 5.4). TFBS that occurred more frequently in PML patients, including sequences isolated from the urine, were TFBS associated with HOX gene families (Fig. 5.7). Even though HOX genes are important in their role in embryonic development, they have also been implicated in angiogenesis and tumor metastasis (413). Recently, these genes have also been shown to be involved in hepatitis C virus (HCV) and human cytomegalovirus (HCMV) infection (414, 415). During HCMV infection, numerous HOX genes, including MEIS1 is differentially expressed (414). A TFBS for MEIS1 was identified in the NCCR of JCPyV across all four isolation sites, was more prevalent in the “c” block and was the least prevalent in the “d” block (Fig. 5.7). During HCMV infection, the authors postulated that as TFs, HOX genes regulate downstream gene expression involved in angiogenesis and repair, promoting cell proliferation, inhibiting cell apoptosis, and possibly being involved in vascular disease pathogenesis (414). Additionally, these genes are associated with cell cycle-related genes (416). JCPyV promotes cellular proliferation and

inhibits cellular apoptosis through T Ag (114, 122) and can influence cyclin expression during the infectious cycle (130). Perhaps, as viral replication is enhanced by NCCR rearrangements, it may promote further induction of HOX-related genes, which further promote viral transcription; however, molecular studies would need to be performed to validate this hypothesis.

Other TFBS that varied between sequences were binding sites that were associated with FOX genes (Fig. 5.7). The FOX TF family are critical in regulating numerous biological processes, including metabolism, differentiation, proliferation, and apoptosis (417). Numerous FOX proteins have been demonstrated to be involved in viral infection as well (418). For example, FOXP3 is upregulated upon human papillomavirus (HPV) infection and may accelerate the cancerous transformation of cervical epithelial cells (418–420). JCPyV can activate cellular pathways that can influence the expression of the FOX TF family, which in turn, may benefit viral transcription, as there are more TFBS in block "c" of the NCCR, isolated from PML patients (Fig. 5.7). Overall, this analysis discovered novel TFBS, specifically related to HOX and FOX TF families that are possibly important in JCPyV replication and disease outcomes. Future studies should validate these findings using molecular and infectivity assays to determine if these TFBS require the binding of TFs to activate JCPyV transcription.

Conclusions

The NCCR of the JCPyV genome is a hypervariable region that is susceptible to complex mutations and rearrangements that are associated with the fatal disease PML. By curating a dataset of 181 sequences of the JCPyV NCCR, as well as characterizing the block orientation of each sequence, we have illustrated the complexity of this region based on viral isolated site and disease status of the individual (Fig. 5.8). Additionally, we have validated TFBS that are important in activating or repressing JCPyV transcription by location, disease status, and by each block of the NCCR (Fig 5.5). Given the effectiveness of this approach, we have discovered possible novel TFBS that correlate with JCPyV

infection based on location and disease status (Fig. 5.7). Future studies should revisit the outcome of these TFBS in JCPyV transcription and replication. To conclude, this research validates and establishes the importance of the NCCR of the JCPyV genome, an understudied area, and in turn, further uncovers the mechanisms of reactivation and PML outcome, which are also poorly understood.

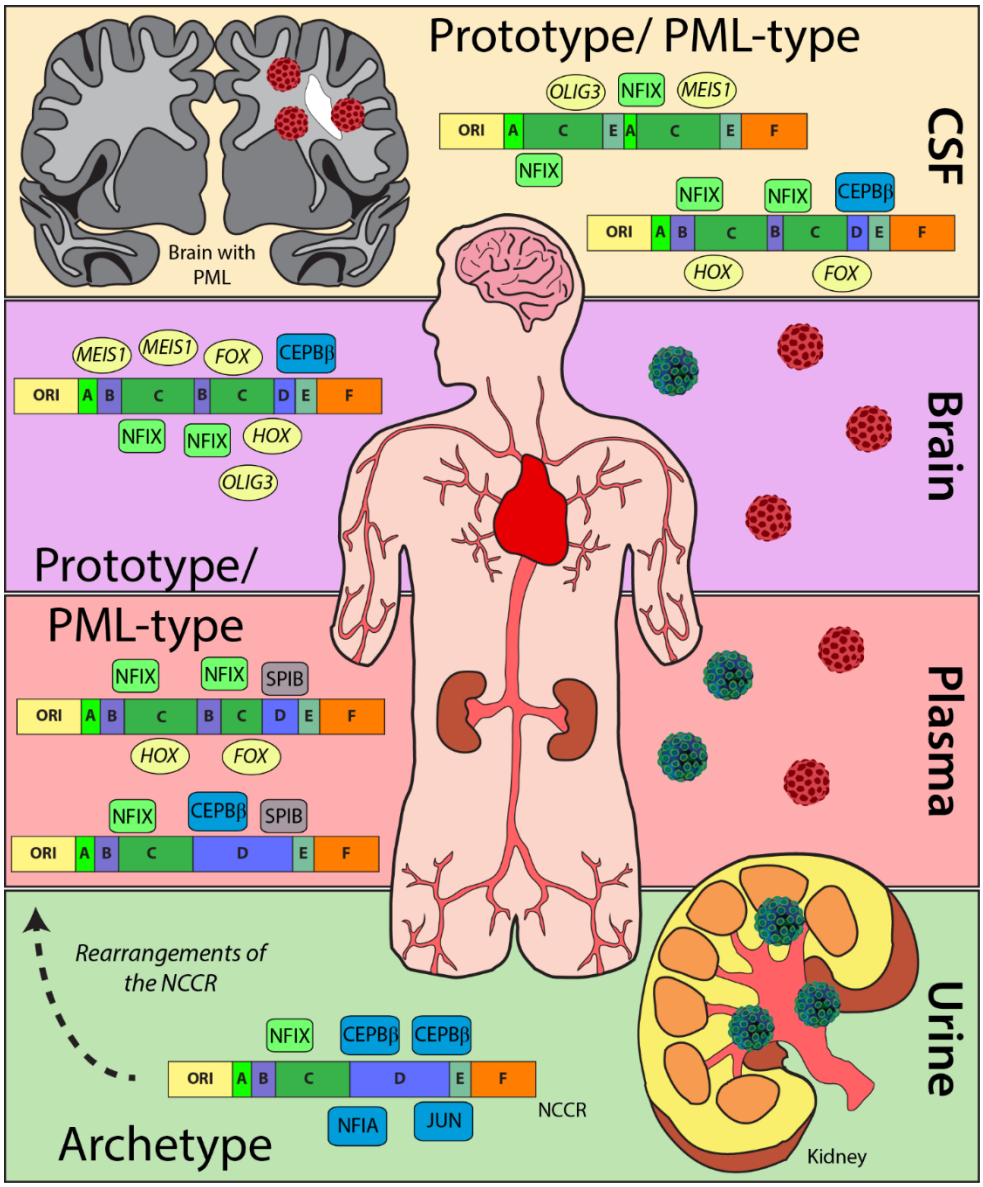

Figure 5.8. Rearrangements of the NCCR and changes in TFBS. The archetype strain is predominantly located in the urine of healthy patients (blue/green virus) with numerous TFBS (blue) that inhibit replication. Rearrangements in diseased patients (red virus) causes an increase in TFBS (green) that enhance viral replication of the prototype/ PML-type strain. TFBS, like SPIB (gray) or possibly OLIG3 (yellow) enhance cellular tropism from the rearrangements in the NCCR. Additionally, TFBS, including MEIS1, FOX family transcription factors (*FOX*), and HOX family transcription factors (*HOX*) can also be observed from NCCR rearrangements in disease patients compared to TFBS in the NCCR from healthy individuals.

CHAPTER 6

CONCLUSIONS AND FUTURE DIRECTIONS

This research focused on uncovering the underlying mechanisms of JCPyV infection in primary human astrocytes, cells that are critical players in PML development in the CNS. JCPyV astrocytic infection represented a key gap in knowledge of JCPyV pathogenesis given that astrocytes are a main target of JCPyV in the CNS and are thought to be a reservoir for infection (68). The work presented in this dissertation characterized JCPyV infection in primary human astrocytes (NHAs) in comparison to a more well-studied but immortalized glial cell line, SVGAs. This research demonstrated key differences in the infectious cycle in primary vs. immortalized cell types (Chapter 2) and further defined cell-type dependent differences in gene expression and signaling pathway activation (Chapter 3 and 4). This work advances our knowledge in the field as little is known about JCPyV astrocytic infection and thoroughly demonstrates some limitations of utilizing immortalized cells models. In addition, using a bioinformatic approach, the NCCR, a hyper-variable region of the JCPyV genome was characterized across 181 sequences from patient isolates to further understand how rearrangements influence TFBS and may contribute to viral disease (Chapter 5). Taken together, this research highlights the complexities of viral and host-cell factors that contribute to JCPyV infection, which advances our knowledge of virus-host interactions and establishes new tools to understand these intricate processes.

This dissertation combined bioinformatic techniques along with cell-based assays, including infectivity assays, qPCR, and image analysis, to determine the infectious cycle of JCPyV in NHAs versus SVGAs but also characterize the rearrangements in the NCCR of the viral genome in patient samples. In patients that had PML, the degree of rearrangement was far more extreme, specifically viral isolates that were isolated from the CSF. Additionally, these rearrangements, increased the number of TFBS that were known to enhance JCPyV infection, including NFIX (391, 411). In contrast, among healthy

individuals, the TFBS that were known to inhibit JCPyV infection, like CEBPβ, were more prevalent in viral isolates from healthy individuals (412). To define how the virus influences the host cells, the expression of the early and late viral proteins over time in SVGAs and NHAs were quantified, serving as proxies for interpreting the JCPyV infectious cycle. Additionally, creating a cell line from NHAs that are immortalized with SV40 T Ag (i.e., NHA-Ts) allowed for fine-tuning our interpretation of JCPyV infection in astrocytes compared to SVGAs and how the expression of SV40 T Ag alters JCPyV infection. From these findings, we performed a large RNA-seq analysis of mock- and JCPyV-infected NHAs and SVGAs at time points established to be important in the production of T Ag and VP1 in both cell types. These findings validated previous research that had established the MAPK/ERK pathway during JCPyV infection in SVGAs but highlighted additional regulatory roles observed in NHAs, not observed in immortalized cells. Moreover, RNA-seq analysis discovered novel pathways during JCPyV infection of NHAs including activation of host inflammatory responses and utilization of the PI3K/AKT/mTor signaling pathway to transform the cell into a conducive environment for viral DNA replication, which was not observed in cells transformed with SV40 T Ag. Even though this methodological approach illuminated various mechanisms of JCPyV infection during primary astrocytes, other questions were introduced for future research, specifically understanding how astrocytes respond to virus infection through immune activation.

Through a gene enrichment analysis, it was discovered that the interleukin 10 (IL-10) pathway was activated during JCPyV infection in NHAs. IL-10 is an anti-inflammatory cytokine that is expressed in many cell types in the brain, including microglia, astrocytes, and oligodendrocytes, especially during times of stress (421, 422). Additionally, IL-10 expression is involved in many neurodegenerative diseases, including MS (421, 423–425). Numerous inflammatory cytokines, such as TNFα, IFN-γ, and IL-6, play a crucial role in MS pathology, additionally, individuals who take natalizumab for MS treatment are at heightened risk for PML development (80, 81, 423). Research has demonstrated that MS symptoms

were related to reduced expression of IL-10 (425) and increased expression of this anti-inflammatory cytokine led to less severe symptoms (426). Promoting IL-10 expression in astrocytes may serve as additional therapeutic options for PML, especially natalizumab-associated PML, however additional research is required to understand the role of astrocytes in the immune response.

Alternatively, the inflammatory response in astrocytes during JCPyV infection can also have adverse effects. Reactive astrocytes quickly change the molecular and biological function in the CNS from inter- and intra-cellular signals and recent studies have begun to address their complex role in pathogenesis and neurodegenerative diseases (427). Specifically, reactive astrocytes may contribute to the death of nearby cells, including through the release of matrix metalloproteinase (MMPs) (428, 429). Astrocytes are thought to be the reservoir for JCPyV, and during PML oligodendrocytes are destroyed, leading to demyelination. Research has demonstrated that oligodendrocyte injury may induce astrocyte reactivity, intensifying excitotoxic damage in the CNS, and promoting oligodendrocyte death (430, 431). Specifically, P2X purinoreceptor-7 (P2X7) ATP receptors are expressed more in oligodendrocytes of people with MS (432) and in astrocytes in secondary progressive MS (433). Stimulation of these receptors results in glutamate release, resulting in an excitotoxic environment (432). Due to this intricate crosstalk between glial cells in the CNS and the dynamic complexity of the inflammatory response in neurodegenerative diseases, future research should address how JCPyV induces the inflammatory response and how this response impacts surrounding cells by either using a co-culture model or chimeric animal model to study JCPyV infection *in vivo*.

Comparative approaches performed during this dissertation research, can be used to elucidate viral persistence versus viral-induced disease. For example, future research can compare JCPyV infection in a primary kidney cell line and an immortalized kidney cell line, such as HEK293 cells, using RNA-seq to determine the host transcriptomic profile in these two cell types. These findings can be further

compared to the research presented in this dissertation to help elucidate what genes are differentially expressed that induce viral persistence in kidney cells versus genes that activate viral replication and enhance infection in glial cell types.

In 2016, there was a study that performed an RNA-seq analysis of JCPyV and BKPyV infections in a primary kidney cell line, which concluded that there was differentially gene expression of interferon stimulating genes at day six postinfection in the in JCPyV- to BKPyV-infected samples (191). However, there are important considerations to be made from the conclusions of this paper (191). First, the authors used a lab-adapted JCPyV strain (referred to as Mad-1/SVEΔ), which is used often to study JCPyV infection *in vitro*, however this viral strain is not commonly found in the kidneys (398). Rather the archetype strain (non-disease strain) is predominantly found in the kidneys of healthy individuals and is rarely associated with PML tissue (69, 110, 111). Given the narrow cell tropism of the virus and the different strains isolated from various cell types and disease status, it is important to use the archetype strain to characterize JCPyV infection in the kidneys. There are challenges to utilizing archetype strain, as it replicates poorly in cell culture, but there have been several recent studies that demonstrate efficient propagation of archetype strain (119, 434). It has been demonstrated in this dissertation that through analyzing the NCCR sequences of viral isolates in diseased patients that the NCCR of the JCPyV genome significantly changes from the archetype to PML-like strain, which influences the transcription factor binding sites (i.e., TFBS), which ultimately impacts the efficiency of viral replication. However, it must be considered that there could be significant alterations in host gene expression between virus strains. The interpretation of differential gene expression of interferon stimulating genes in JCPyV- to BKPyV-infected samples suggests that the relationship of genes associated with IFN signaling are differentially expressed across the polyomaviruses, however the significance may not hold true among mock- and JCPyV-infected cells, as gene expression was not defined in mock cells.

Overall, the mechanisms of JCPyV infection, specifically, the events surrounding reactivation and disease are poorly understood. Through examining the host transcriptomic profile during JCPyV infection across primary cell types, *ex* vivo, we will better understand PML pathogenesis and reactivation without the difficulty of interpreting and deducing conclusions from a chimeric animal model. Additionally, innovative techniques such as single-cell RNA sequencing as it pertains to viral infection is becoming a valuable tool to study the heterogeneity cellular response to virus infection (435). A study using single-cell transcriptomics has already been performed to analyze BKPyV infection (436). The authors demonstrated that in a population of BKPyV-infected cells, the levels of Large T Ag production and viral capsid protein expression were significantly variable, and cells expressing the highest levels of viral protein had a distinct gene expression pattern from cells expressing lower levels of viral protein (436). These analyses would be important to conduct in primary astrocytes during JCPyV infection because a population of astrocytes may react differently based on proximity of an infected cell. Reactive astrocytes are known to activate pro-inflammatory signals in the center or the immediate location of a damage region, but outside this region, astrocytes exert anti-inflammatory roles, and in extreme instances, may even form scars to act as barriers to contain the inflammation and protect healthy cells around it (144, 148, 152). Single cell analyses may be able to elucidate how astrocytes react to JCPyV infection in the overall population, examining both infected cells and cells in the proximity of infection.

Even though the research presented in this manuscript addressed important questions, there are a few limitations to note. NHA-Ts were used as a control cell line to understand how SV40 T Ag influenced the biological findings between SVGAs and NHAs; unfortunately, they were not used during the RNA-seq analysis as the analysis preceded these findings. Additionally, an unadjusted *p value* < 0.05 was used as a statistical threshold for exploring differentially expressed genes across time points and cell types instead of using an adjusted *p value.* This could increase the false positive rate of genes that were

differentially expressed (437). To minimize this, differentially expressed genes were further validated using complementary cell-based assays. It has been recommended that future RNA-seq studies should have at least six replicates per condition for all experiments, and as high as 12 replicates per condition for experiments were identifying the majority of differentially expressed genes is important (437), yet the number of samples were limited due to resource constraints and the number of necessary time points and samples required for the analysis. Lastly, future experiments should address examination of other cell types in the CNS. Oligodendrocytes, choroid plexus epithelial cells (384), human brain microvascular endothelial cells (327), and even neurons (438, 439) are infected by JCPyV. Additionally, future studies should validate conclusions from this dissertation in different cell types, including chemical inhibitors that target the PI3K/AKT/mTor signaling pathway, to further justify using these drugs as potential therapeutic treatments.

Overall, the CNS is a very dynamic location, containing numerous glial cell types, yet astrocytes are the most abundant glial cell type in the brain (141–143). Continued analyses examining how astrocytes respond to JCPyV infection and how a population responds are important to advance our understanding of PML pathogenesis. Moreover, using the same methodological approach outlined in this dissertation, could be adapted to understand JCPyV persistence in the kidneys, comparing these results to JCPyV infection in glial cell types. This analysis would further elucidate mechanism of viral reactivation, potentially providing new information that could be used to prevent or treat PML and illuminating mechanisms of reactivation among other opportunistic viruses.

CHAPTER 7

REFERENCES

1. Koonin EV. 2014. The wonder world of microbial viruses. Expert Rev Anti-infe 8:1097–1099.

2. Kristensen DM, Mushegian AR, Dolja VV, Koonin EV. 2010. New dimensions of the virus world discovered through metagenomics. Trends Microbiol 18:11–19.

3. Suttle CA. 2005. Viruses in the sea. Nature 437:356–361.

4. Collins KL, Kelly TJ. 1991. Effects of T antigen and replication protein A on the initiation of DNA synthesis by DNA polymerase alpha-primase. Mol Cell Biol 11:2108–2115.

5. Danna KJ, Nathans D. 1972. Bidirectional Replication of Simian Virus 40 DNA. Proc National Acad Sci 69:3097–3100.

6. NATHANS D, DANNA KJ. 1972. Specific Origin in SV40 DNA Replication. Nat New Biology 236:200–202.

7. Liang G, Bushman FD. 2021. The human virome: assembly, composition and host interactions. Nat Rev Microbiol 1–14.

8. 2020. WHO Coronavirus Disease (COVID-19) Dashboard. Bangladesh Physiotherapy J 10.

9. Jester B, Uyeki TM, Jernigan DB, Tumpey TM. 2019. Historical and clinical aspects of the 1918 H1N1 pandemic in the United States. Virology 527:32–37.

10. Chuong EB. 2018. The placenta goes viral: Retroviruses control gene expression in pregnancy. Plos Biol 16:e3000028.

11. Dupressoir A, Lavialle C, Heidmann T. 2012. From ancestral infectious retroviruses to bona fide cellular genes: Role of the captured syncytins in placentation. Placenta 33:663–671.

12. Arnaud F, Caporale M, Varela M, Biek R, Chessa B, Alberti A, Golder M, Mura M, Zhang Y, Yu L, Pereira F, DeMartini JC, Leymaster K, Spencer TE, Palmarini M. 2007. A Paradigm for Virus–Host Coevolution: Sequential Counter-Adaptations between Endogenous and Exogenous Retroviruses. Plos Pathog 3:e170.

13. Chuong EB. 2013. Retroviruses facilitate the rapid evolution of the mammalian placenta. Bioessays 35:853–861.

14. Liang G, Zhao C, Zhang H, Mattei L, Sherrill-Mix S, Bittinger K, Kessler LR, Wu GD, Baldassano RN, DeRusso P, Ford E, Elovitz MA, Kelly MS, Patel MZ, Mazhani T, Gerber JS, Kelly A, Zemel BS, Bushman FD. 2020. The stepwise assembly of the neonatal virome is modulated by breastfeeding. Nature 581:470–474.

15. Andersen JH, Osbakk SA, Vorland LH, Traavik T, Gutteberg TJ. 2001. Lactoferrin and cyclic lactoferricin inhibit the entry of human cytomegalovirus into human fibroblasts. Antivir Res 51:141–149.

16. Beljaars L, Strate BWA van der, Bakker HI, Reker-Smit C, Loenen-Weemaes A van, Wiegmans FC, Harmsen MC, Molema G, Meijer DKF. 2004. Inhibition of cytomegalovirus infection by lactoferrin in vitro and in vivo. Antivir Res 63:197–208.

17. Waarts B-L, Aneke OJC, Smit JM, Kimata K, Bittman R, Meijer DKF, Wilschut J. 2005. Antiviral activity of human lactoferrin: inhibition of alphavirus interaction with heparan sulfate. Virology 333:284–292.

18. Puddu P, Borghi P, Gessani S, Valenti P, Belardelli F, Seganti L. 1998. Antiviral effect of bovine lactoferrin saturated with metal ions on early steps of human immunodeficiency virus type 1 infection. Int J Biochem Cell Biology 30:1055–1063.

19. Lang J, Yang N, Deng J, Liu K, Yang P, Zhang G, Jiang C. 2011. Inhibition of SARS Pseudovirus Cell Entry by Lactoferrin Binding to Heparan Sulfate Proteoglycans. Plos One 6:e23710.

20. 1988. New Guinea Tapeworms and Jewish Grandmothers. By R. S. Desowitz. 224 pages. ISBN 0 393 30426 4. W. W. Norton, New York, 1987. £4.95. Parasitology 96:644–644.

21. Chen M, Zhang Y, Huang F, Wang H, Liu D, Li J, Rodewald L, Wu J, Deng Y, Xu W. 2015. Endemic and Imported Measles Virus–Associated Outbreaks among Adults, Beijing, China, 2013. Emerg Infect Dis 21:477–479.

22. Black FL. 1966. Measles endemicity in insular populations: Critical community size and its evolutionary implication. J Theor Biol 11:207–211.

23. Portnoy A, Jit M, Ferrari M, Hanson M, Brenzel L, Verguet S. 2019. Estimates of case-fatality ratios of measles in low-income and middle-income countries: a systematic review and modelling analysis. Lancet Global Heal 7:e472–e481.

24. Dabbagh A, Patel MK, Dumolard L, Gacic-Dobo M, Mulders MN, Okwo-Bele J-M, Kretsinger K, Papania MJ, Rota PA, Goodson JL. 2017. Progress Toward Regional Measles Elimination — Worldwide, 2000–2016. Mmwr Morbidity Mortal Wkly Rep 66:1148–1153.

25. Patel M, Lee AD, Clemmons NS, Redd SB, Poser S, Blog D, Zucker JR, Leung J, Link-Gelles R, Pham H, Arciuolo RJ, Rausch-Phung E, Bankamp B, Rota PA, Weinbaum CM, Gastañaduy PA. 2019. National Update on Measles Cases and Outbreaks — United States, January 1–October 1, 2019. Morbidity Mortal Wkly Rep 68:893–896.

26. Nicolay N, Mirinaviciute G, Mollet T, Celentano LP, Bacci S. 2020. Epidemiology of measles during the COVID-19 pandemic, a description of the surveillance data, 29 EU/EEA countries and the United Kingdom, January to May 2020. Eurosurveillance 25:2001390.

27. James C, Harfouche M, Welton NJ, Turner KM, Abu-Raddad LJ, Gottlieb SL, Looker KJ. 2020. Herpes simplex virus: global infection prevalence and incidence estimates, 2016. B World Health Organ 98:315–329.

28. Egli A, Infanti L, Dumoulin A, Buser A, Samaridis J, Stebler C, Gosert R, Hirsch HH. 2009. Prevalence of polyomavirus BK and JC infection and replication in 400 healthy blood donors. J Infect Dis 199:837–46.

29. Knowles WA, Pipkin P, Andrews N, Vyse A, Minor P, Brown DW, Miller E. 2003. Population-based study of antibody to the human polyomaviruses BKV and JCV and the simian polyomavirus SV40. Journal of medical virology 71:115–23.

30. Kean JM, Rao S, Wang M, Garcea RL. 2009. Seroepidemiology of human polyomaviruses. PLoS Pathog 5:e1000363.

31. Zheng H-Y, Kitamura T, Takasaka T, Chen Q, Yogo Y. 2004. Unambiguous identification of JC polyomavirus strains transmitted from parents to children. Arch Virol 149:261–273.

32. Bofill-Mas S, Girones R. 2003. Role of the environment in the transmission of JC virus. J Neurovirol 9:54–58.

33. Hirsch HH, Babel N, Comoli P, Friman V, Ginevri F, Jardine A, Lautenschlager I, Legendre C, Midtvedt K, Muñoz P, Randhawa P, Rinaldo CH, Wieszek A, Hosts ESG of I in C. 2014. European perspective on human polyomavirus infection, replication and disease in solid organ transplantation. Clin Microbiol Infec 20:74–88.

34. Moens U, Krumbholz A, Ehlers B, Zell R, Johne R, Calvignac-Spencer S, Lauber C. 2017. Biology, evolution, and medical importance of polyomaviruses: An update. Infect Genetics Evol 54:18–38.

35. Buck CB, Doorslaer KV, Peretti A, Geoghegan EM, Tisza MJ, An P, Katz JP, Pipas JM, McBride AA, Camus AC, McDermott AJ, Dill JA, Delwart E, Ng TFF, Farkas K, Austin C, Kraberger S, Davison W, Pastrana DV, Varsani A. 2016. The Ancient Evolutionary History of Polyomaviruses. Plos Pathog 12:e1005574.

36. Kaján GL, Doszpoly A, Tarján ZL, Vidovszky MZ, Papp T. 2020. Virus–Host Coevolution with a Focus on Animal and Human DNA Viruses. J Mol Evol 88:41–56.

37. Stoner GL, Jobes DV, Cobo MF, Agostini HT, Chima SC, Ryschkewitsch CF. 2000. JC virus as a marker of human migrationto the Americas. Microbes Infect 2:1905–1911.

38. Agostini HT, Yanagihara R, Davis V, Ryschkewitsch CF, Stoner GL. 1997. Asian genotypes of JC virus in Native Americans and in a Pacific Island population: Markers of viral evolution and human migration. Proc National Acad Sci 94:14542–14546.

39. Ikegaya H, Zheng H, Saukko PJ, Varesmaa-Korhonen L, Hovi T, Vesikari T, Suganami H, Takasaka T, Sugimoto C, Ohasi Y, Kitamura T, Yogo Y. 2005. Genetic diversity of JC virus in the Saami and the Finns: Implications for their population history. Am J Phys Anthropol 128:185–193.

40. Ryschkewitsch CF, Friedlaender JS, Mgone CS, Jobes DV, Agostini HT, Chima SC, Alpers MP, Koki G, Yanagihara R, Stoner GL. 2000. Human polyomavirus JC variants in Papua New Guinea and Guam reflect ancient population settlement and viral evolution. Microbes Infect 2:987–996.

41. Ferenczy MW, Marshall LJ, Nelson CD, Atwood WJ, Nath A, Khalili K, Major EO. 2012. Molecular biology, epidemiology, and pathogenesis of progressive multifocal leukoencephalopathy, the JC virus-induced demyelinating disease of the human brain. Clinical microbiology reviews 25:471–506.

42. Cui X, Wang JC, Deckhut A, Joseph BC, Eberwein P, Cubitt CL, Ryschkewitsch CF, Agostini HT, Stoner GL. 2004. Chinese Strains (Type 7) of JC Virus Are Afro-Asiatic in Origin But Are Phylogenetically Distinct from the Mongolian and Indian Strains (Type 2D) and the Korean and Japanese Strains (Type 2A). J Mol Evol 58:568–583.

43. Nerurkar VR, Yanagihara R, Ryschkewitsch CF, Cui X, Jobes DV, Stoner GL, Agostini HT, Mgone CS, Scheirich I, Cubitt CL, Friedlaender JS, Hrdy DB. 2002. JC Virus Genotypes in the Western Pacific Suggest Asian Mainland Relationships and Virus Association with Early Population Movements. Hum Biol 74:473–488.

44. Monaco MC, Atwood WJ, Gravell M, Tornatore CS, Major EO. 1996. JC virus infection of hematopoietic progenitor cells, primary B lymphocytes, and tonsillar stromal cells: implications for viral latency. J Virol 70:7004–7012.

45. Dubois V, Dutronc H, Lafon ME, Poinsot V, Pellegrin JL, Ragnaud JM, Ferrer AM, Fleury HJ. 1997. Latency and reactivation of JC virus in peripheral blood of human immunodeficiency virus type 1-infected patients. J Clin Microbiol 35:2288–92.

46. Chapagain ML, Nerurkar VR. 2010. Human polyomavirus JC (JCV) infection of human B lymphocytes: a possible mechanism for JCV transmigration across the blood-brain barrier. The Journal of infectious diseases 202:184-91–91.

47. White MK, Khalili K. 2011. Pathogenesis of Progressive Multifocal Leukoencephalopathy—Revisited. Journal of Infectious Diseases 203:578-586–586.

48. Monaco MCG, Jensen PN, Hou J, Durham LC, Major EO. 1998. Detection of JC Virus DNA in Human Tonsil Tissue: Evidence for Site of Initial Viral Infection. J Virol 72:9918–9923.

49. Ahmed W, Liu Z-F. 2018. Long Non-Coding RNAs: Novel Players in Regulation of Immune Response Upon Herpesvirus Infection. Front Immunol 9:761.

50. McGeoch DJ, Gatherer D. 2005. Integrating Reptilian Herpesviruses into the Family Herpesviridae. J Virol 79:725–731.

51. Valle LD, White MK, Khalili K. 2008. Potential Mechanisms of the Human Polyomavirus JC in Neural Oncogenesis. J Neuropathology Exp Neurology 67:729–740.

52. White MK, Khalili K. 2004. Polyomaviruses and human cancer: molecular mechanisms underlying patterns of tumorigenesis. Virology 324:1–16.

53. Yogo Y, Zhong S, Shibuya A, Kitamura T, Homma Y. 2008. Transcriptional control region rearrangements associated with the evolution of JC polyomavirus. Virology 380:118–123.

54. White FA, Ishaq M, Stoner GL, Frisque RJ. 1992. JC virus DNA is present in many human brain samples from patients without progressive multifocal leukoencephalopathy. J Virol 66:5726–5734.

55. Elsner C, Dörries K. 1992. Evidence of human polyomavirus BK and JC infection in normal brain tissue. Virology 191:72–80.

56. Perez-Liz G, Valle LD, Gentilella A, Croul S, Khalili K. 2008. Detection of JC virus DNA fragments but not proteins in normal brain tissue. Ann Neurol 64:379–387.

57. Mori M, Kurata H, Tajima M, Shimada H. 1991. JC virus detection by in situ hybridization in brain tissue from elderly patients. Ann Neurol 29:428–432.

58. Ferrante P, Caldarelli-Stefano R, Omodeo-Zorini E, Vago L, Boldorini R, Costanzi G. 1995. PCR detection of JC virus DNA in brain tissue from patients with and without progressive multifocal leukoencephalopathy. J Med Virol 47:219–225.

59. Gorelik L, Reid C, Testa M, Brickelmaier M, Bossolasco S, Pazzi A, Bestetti A, Carmillo P, Wilson E, McAuliffe M, Tonkin C, Carulli JP, Lugovskoy A, Lazzarin A, Sunyaev S, Simon K, Cinque P. 2011. Progressive multifocal leukoencephalopathy (PML) development is associated with mutations in JC virus capsid protein VP1 that change its receptor specificity. J Infect Dis 204:103–14.

60. Hirsch HH, Kardas P, Kranz D, Leboeuf C. 2013. The human JC polyomavirus (JCPyV): virological background and clinical implications. APMIS 121:685-727–727.

61. Padgett BL, Walker DL, ZuRhein GM, Eckroade RJ, Dessel BH. 1971. Cultivation of papova-like virus from human brain with progressive multifocal leucoencephalopathy. Lancet (London, England) 1:1257–60.

62. Silverman L, Rubinstein LJ. 1965. Electron microscopic observations on a case of progressive multifocal leukoencephalopathy. Acta Neuropathologica 5:215–224.

63. Zurhein G, Chou SM. 1965. Particles Resembling Papova Viruses in Human Cerebral Demyelinating Disease. Science 148:1477–9.

64. Cubitt CL, Cui X, Agostini HT, Nerurkar VR, Scheirich I, Yanagihara R, Ryschkewitsch CF, Stoner GL. 2001. Predicted amino acid sequences for 100 JCV strains. J Neurovirol 7:339–344.

65. Agostini HT, Ryschkewitsch CF, Baumhefner RW, Tourtellotte WW, Singer EJ, Komoly S, Stoner GL. 2000. Influence of JC virus coding region genotype on risk of multiple sclerosis and progressive multifocal leukoencephalopathy. J Neurovirol 6 Suppl 2:S101-8.

66. Dubois V, Moret H, Lafon M-E, Brodard V, Icart J, Ruffault A, Guist'hau O, Buffet-Janvresse C, Abbed K, Dussaix E, Ingrand D. 2001. JC Virus Genotypes in France: Molecular Epidemiology and Potential Significance for Progressive Multifocal Leukoencephalopathy. J Infect Dis 183:213–217.

67. Bag AK, Curé JK, Chapman PR, Roberson GH, Shah R. 2010. JC Virus Infection of the Brain. American Journal of Neuroradiology 31:1564–1576.

68. Kondo Y, Windrem MS, Zou L, Chandler-Militello D, Schanz SJ, Auvergne RM, Betstadt SJ, Harrington AR, Johnson M, Kazarov A, Gorelik L, Goldman SA. 2014. Human glial chimeric mice reveal astrocytic dependence of JC virus infection. The Journal of clinical investigation 124:5323–36.

69. Sabath BF, Major EO. 2002. Traffic of JC virus from sites of initial infection to the brain: the path to progressive multifocal leukoencephalopathy. The Journal of infectious diseases 186 Suppl 2:S180-6.

70. Khanna N, Wolbers M, Mueller NJ, Garzoni C, Pasquier RAD, Fux CA, Vernazza P, Bernasconi E, Viscidi R, Battegay M, Hirsch HH, Study SHC. 2009. JC Virus-Specific Immune Responses in Human Immunodeficiency Virus Type 1 Patients with Progressive Multifocal Leukoencephalopathy ▿ . J Virol 83:4404–4411.

71. Pavlovic D, Patera AC, Nyberg F, Gerber M, Liu M, Leukeoncephalopathy CPM. 2015. Progressive multifocal leukoencephalopathy: current treatment options and future perspectives. Ther Adv Neurol Diso 8:255–73.

72. Albrecht H, Hoffmann C, Degen O, Stoehr A, Plettenberg A, Mertenskötter T, Eggers C, Stellbrink H-J. 1998. Highly active antiretroviral therapy significantly improves the prognosis of patients with HIV-associated progressive multifocal leukoencephalopathy. Aids 12:1149–1154.

73. Engsig FN, Hansen A-BE, Omland LH, Kronborg G, Gerstoft J, Laursen AL, Pedersen C, Mogensen CB, Nielsen L, Obel N. 2009. Incidence, Clinical Presentation, and Outcome of Progressive Multifocal Leukoencephalopathy in HIV-Infected Patients during the Highly Active Antiretroviral Therapy Era: A Nationwide Cohort Study. J Infect Dis 199:77–83.

74. Cortese I, Reich DS, Nath A. 2021. Progressive multifocal leukoencephalopathy and the spectrum of JC virus-related disease. Nat Rev Neurol 17:37–51.

75. Carson KR, Evens AM, Richey EA, Habermann TM, Focosi D, Seymour JF, Laubach J, Bawn SD, Gordon LI, Winter JN, Furman RR, Vose JM, Zelenetz AD, Mamtani R, Raisch DW, Dorshimer GW, Rosen ST, Muro K, Gottardi-Littell NR, Talley RL, Sartor O, Green D, Major EO, Bennett CL. 2009. Progressive multifocal leukoencephalopathy after rituximab therapy in HIV-negative patients: a report of 57 cases from the Research on Adverse Drug Events and Reports project. Blood 113:4834–40.

76. Bloomgren G, Richman S, Hotermans C, Subramanyam M, Goelz S, Natarajan A, Lee S, Plavina T, Scanlon JV, Sandrock A, Bozic C. 2012. Risk of natalizumab-associated progressive multifocal leukoencephalopathy. New Engl J Medicine 366:1870–80.

77. Ho P-R, Koendgen H, Campbell N, Haddock B, Richman S, Chang I. 2017. Risk of natalizumab-associated progressive multifocal leukoencephalopathy in patients with multiple sclerosis: a retrospective analysis of data from four clinical studies. Lancet Neurology 16:925–933.

78. Phan-Ba R, Belachew S, Outteryck O, Moonen G, Sindic C, Vokaer M, Vermersch P. 2012. The earlier, the smaller, the better for natalizumab-associated PML. Neurology 79:1067–1069.

79. Tan IL, Koralnik IJ, Rumbaugh JA, Burger PC, King-Rennie A, McArthur JC. 2011. Progressive multifocal leukoencephalopathy in a patient without immunodeficiency. Neurology 77:297–299.

80. Vermersch P, Kappos L, Gold R, Foley JF, Olsson T, Cadavid D, Bozic C, Richman S. 2011. Clinical outcomes of natalizumab-associated progressive multifocal leukoencephalopathy(Podcast). Neurology 76:1697–1704.

81. Prosperini L, Rossi N de, Scarpazza C, Moiola L, Cosottini M, Gerevini S, Capra R, group IP study. 2016. Natalizumab-Related Progressive Multifocal Leukoencephalopathy in Multiple Sclerosis: Findings from an Italian Independent Registry. Plos One 11:e0168376.

82. Balduzzi A, Lucchini G, Hirsch HH, Basso S, Cioni M, Rovelli A, Zincone A, Grimaldi M, Corti P, Bonanomi S, Biondi A, Locatelli F, Biagi E, Comoli P. 2011. Polyomavirus JC-targeted T-cell therapy for progressive multiple leukoencephalopathy in a hematopoietic cell transplantation recipient. Bone Marrow Transpl 46:987–992.

83. Muftuoglu M, Olson A, Marin D, Ahmed S, Mulanovich V, Tummala S, Chi TL, Ferrajoli A, Kaur I, Li L, Champlin R, Shpall EJ, Rezvani K. 2018. Allogeneic BK Virus–Specific T Cells for Progressive Multifocal Leukoencephalopathy. New Engl J Med 379:1443–1451.

84. SHELBURNE SA, HAMILL RJ, RODRIGUEZ-BARRADAS MC, GREENBERG SB, ATMAR RL, MUSHER DM, GATHE JC, VISNEGARWALA F, TRAUTNER BW. 2002. Immune Reconstitution Inflammatory Syndrome. Medicine 81:213–227.

85. Summers NA, Kelley CF, Armstrong W, Marconi VC, Nguyen ML. 2019. Not a Disease of the Past: A Case Series of Progressive Multifocal Leukoencephalopathy in the Established Antiretroviral Era. Aids Res Hum Retrov 35:544–552.

86. Assetta B, Atwood WJ. 2017. The biology of JC polyomavirus. Biological chemistry 398:839-855–855.

87. Liddington RC, Yan Y, Moulai J, Sahli R, Benjamin TL, Harrison SC. 1991. Structure of simian virus 40 at 3.8-A resolution. Nature 354:278–84.

88. Neu U, Maginnis MS, Palma AS, Ströh LJ, Nelson CDS, Feizi T, Atwood WJ, Stehle T. 2010. Structure-Function Analysis of the Human JC Polyomavirus Establishes the LSTc Pentasaccharide as a Functional Receptor Motif. Cell Host Microbe 8:309–319.

89. Maginnis MS, Ströh LJ, Gee GV, O'Hara BA, Derdowski A, Stehle T, Atwood WJ. 2013. Progressive Multifocal Leukoencephalopathy-Associated Mutations in the JC Polyomavirus Capsid Disrupt Lactoseries Tetrasaccharide c Binding. Mbio 4:e00247-13.

90. Ströh LJ, Maginnis MS, Blaum BS, Nelson CDS, Neu U, Gee GV, O'Hara BA, Motamedi N, DiMaio D, Atwood WJ, Stehle T. 2015. The Greater Affinity of JC Polyomavirus Capsid for α2,6-Linked Lactoseries Tetrasaccharide c than for Other Sialylated Glycans Is a Major Determinant of Infectivity. J Virol 89:6364–6375.

91. Assetta B, Maginnis MS, Ahufinger IG, Haley SA, Gee GV, Nelson CDS, O'Hara BA, Ramdial SAA, Atwood WJ. 2013. 5-HT2 Receptors Facilitate JC Polyomavirus Entry. J Virol 87:13490–13498.

92. Mayberry CL, Soucy AN, Lajoie CR, DuShane JK, Maginnis MS. 2019. JC Polyomavirus Entry by Clathrin-Mediated Endocytosis Is Driven by β-Arrestin. Journal of virology 93.

93. Nelson CD, Derdowski A, Maginnis MS, O'Hara BA, Atwood WJ. 2012. The VP1 subunit of JC polyomavirus recapitulates early events in viral trafficking and is a novel tool to study polyomavirus entry. Virology 428:30–40.

94. Querbes W, Benmerah A, Tosoni D, Fiore PPD, Atwood WJ. 2003. A JC Virus-Induced Signal Is Required for Infection of Glial Cells by a Clathrin- and eps15-Dependent Pathway. Journal of Virology 78:250–256.

95. Querbes W, O'Hara BA, Williams G, Atwood WJ. 2006. Invasion of Host Cells by JC Virus Identifies a Novel Role for Caveolae in Endosomal Sorting of Noncaveolar Ligands†. J Virol 80:9402–9413.

96. Frisque RJ, Bream GL, Cannella MT. 1984. Human polyomavirus JC virus genome. J Virol 51:458–69.

97. Reid CE, Li H, Sur G, Carmillo P, Bushnell S, Tizard R, McAuliffe M, Tonkin C, Simon K, Goelz S, Cinque P, Gorelik L, Carulli JP. 2011. Sequencing and analysis of JC virus DNA from natalizumab-treated PML patients. The Journal of infectious diseases 204:237–44.

98. Ranganathan PN, Khalili K. 1993. The transcriptional enhancer element, kappa B, regulates promoter activity of the human neurotropic virus, JCV, in cells derived from the CNS. Nucleic acids research 21:1959-64–64.

99. Safak M, Gallia GL, Khalili K. 1999. A 23-bp sequence element from human neurotropic JC virus is responsive to NF-kappa B subunits. Virology 262:178–89.

100. Marshall LJ, Dunham L, Major EO. 2010. Transcription factor Spi-B binds unique sequences present in the tandem repeat promoter/enhancer of JC virus and supports viral activity. J Gen Virol 91:3042–52.

101. Manley K, O'hara BA, Gee GV, Simkevich CP, Sedivy JM, Atwood WJ. 2006. NFAT4 is required for JC virus infection of glial cells. Journal of virology 80:12079–85.

102. Monaco MG, Sabath BF, Durham LC, Major EO. 2001. JC virus multiplication in human hematopoietic progenitor cells requires the NF-1 class D transcription factor. Journal of virology 75:9687–9695.

103. Ravichandran V, Sabath BF, Jensen PN, Houff SA, Major EO. 2006. Interactions between c-Jun, Nuclear Factor 1, and JC Virus Promoter Sequences: Implications for Viral Tropism. Journal of Virology 80:10506–10513.

104. Marshall LJ, Ferenczy MW, Daley EL, Jensen PN, Ryschkewitsch CF, Major EO. 2014. Lymphocyte Gene Expression and JC Virus Noncoding Control Region Sequences Are Linked with the Risk of Progressive Multifocal Leukoencephalopathy. Journal of Virology 88:5177–5183.

105. Frohman EM, Monaco MC, Remington G, Ryschkewitsch C, Jensen PN, Johnson K, Perkins M, Liebner J, Greenberg B, Monson N, Frohman TC, Douek D, Major EO. 2014. JC Virus in CD34+ and CD19+ Cells in Patients With Multiple Sclerosis Treated With Natalizumab. Jama Neurol 71:596–602.

106. Yogo Y, Kitamura T, Sugimoto C, Ueki T, Aso Y, Hara K, Taguchi F. 1990. Isolation of a possible archetypal JC virus DNA sequence from nonimmunocompromised individuals. Journal of virology 64:3139–43.

107. Ault GS, Stoner GL. 1993. Human polyomavirus JC promoter/enhancer rearrangement patterns from progressive multifocal leukoencephalopathy brain are unique derivatives of a single archetypal structure. J Gen Virol 74:1499–1507.

108. Jensen PN, Major EO. 2001. A classification scheme for human polyomavirus JCV variants based on the nucleotide sequence of the noncoding regulatory region. Journal of neurovirology 7:280–7.

109. Loy TV, Thys K, Ryschkewitsch C, Lagatie O, Monaco MC, Major EO, Tritsmans L, Stuyver LJ. 2015. JC Virus Quasispecies Analysis Reveals a Complex Viral Population Underlying Progressive Multifocal Leukoencephalopathy and Supports Viral Dissemination via the Hematogenous Route. J Virol 89:1340–1347.

110. Frisque RJ. 1983. Nucleotide sequence of the region encompassing the JC virus origin of DNA replication. Journal of virology 46:170–6.

111. DANIEL AM, SWENSON JJ, MAYREDDY RPR, KHALILI K, FRISQUE RJ. 1996. Sequences within the Early and Late Promoters of Archetype JC Virus Restrict Viral DNA Replication and Infectivity. Virology 216:90–101.

112. Marshall LJ, Major EO. 2010. Molecular regulation of JC virus tropism: insights into potential therapeutic targets for progressive multifocal leukoencephalopathy. Journal of neuroimmune pharmacology : the official journal of the Society on NeuroImmune Pharmacology 5:404–17.

113. Gronostajski RM. 2000. Roles of the NFI/CTF gene family in transcription and development. Gene 249:31–45.

114. Dyson N, Bernards R, Friend SH, Gooding LR, Hassell JA, Major EO, Pipas JM, Vandyke T, Harlow E. 1990. Large T antigens of many polyomaviruses are able to form complexes with the retinoblastoma protein. J Virol 64:1353–6.

115. Vogelstein B, Lane D, Levine AJ. 2000. Surfing the p53 network. Nature 408:307–10.

116. Dickmanns A, Zeitvogel A, Simmersbach F, Weber R, Arthur AK, Dehde S, Wildeman AG, Fanning E. 1994. The kinetics of simian virus 40-induced progression of quiescent cells into S phase depend on four independent functions of large T antigen. J Virol 68:5496–508.

117. Safak M, Khalili K. 2003. An overview: Human polyomavirus JC virus and its associated disorders. J Neurovirol 9:3–9.

118. Hirsch HH, Randhawa P, Practice AIDC of. 2013. BK Polyomavirus in Solid Organ Transplantation. Am J Transplant 13:179–188.

119. Broekema NM, Imperiale MJ. 2012. Efficient propagation of archetype BK and JC polyomaviruses. Virology 422:235–41.

120. Lynch KJ, Frisque RJ. 1991. Factors contributing to the restricted DNA replicating activity of JC virus. Virology 180:306–317.

121. Sock E, Wegner M, Fortunato EA, Grummt F. 1993. Large T-Antigen and Sequences within the Regulatory Region of JC Virus Both Contribute to the Features of JC Virus DNA Replication. Virology 197:537-548–548.

122. Valle LD, Gordon J, Assimakopoulou M, Enam S, Geddes JF, Varakis JN, Katsetos CD, Croul S, Khalili K. 2001. Detection of JC virus DNA sequences and expression of the viral regulatory protein T-antigen in tumors of the central nervous system. Cancer Res 61:4287–93.

123. Ahuja D, Sáenz-Robles MT, Pipas JM. 2005. SV40 large T antigen targets multiple cellular pathways to elicit cellular transformation. Oncogene 24:7729–7745.

124. Major EO, Miller AE, Mourrain P, Traub RG, Widt E de, Sever J. 1985. Establishment of a line of human fetal glial cells that supports JC virus multiplication. Proceedings of the National Academy of Sciences of the United States of America 82:1257–61.

125. Peterson SR, Gadbois DM, Bradbury EM, Kraemer PM. 1995. Immortalization of human fibroblasts by SV40 large T antigen results in the reduction of cyclin D1 expression and subunit association with proliferating cell nuclear antigen and Waf1. Cancer Res 55:4651–7.

126. Chang TH, Schlegel R. 1996. SV40 T antigen increases the expression and activities of p34cdc2, cyclin A, and cyclin B prior to immortalization of human diploid fibroblasts. J Cell Biochem 60:161–172.

127. Ariza A, Mate JL, Isamat M, Calatrava A, Fernandez-Vasalo A, Navas-Palacios JJ. 1998. Overexpression of Ki-67 and Cyclins A and B1 in JC Virus-infected Cells of Progressive Multifocal Leukoencephalopathy. Journal of Neuropathology & Experimental Neurology 57:226-230–230.

128. Sanchez V, McElroy AK, Spector DH. 2003. Mechanisms governing maintenance of Cdk1/cyclin B1 kinase activity in cells infected with human cytomegalovirus. J Virol 77:13214–24.

129. Marshall A, Rushbrook S, Davies SE, Morris LS, Scott IS, Vowler SL, Coleman N, Alexander G. 2005. Relation between hepatocyte G1 arrest, impaired hepatic regeneration, and fibrosis in chronic hepatitis C virus infection. Gastroenterology 128:33-42–42.

130. Wilczek MP, DuShane JK, Armstrong FJ, Maginnis MS. 2019. JC polyomavirus infection reveals delayed progression of the infectious cycle in normal human astrocytes. J Virol https://doi.org/10.1128/jvi.01331-19.

131. Radhakrishnan S, Otte J, Enam S, Valle LD, Khalili K, Gordon J. 2003. JC virus-induced changes in cellular gene expression in primary human astrocytes. Journal of virology 77:10638–44.

132. Lukas J, Herzinger 1 T h o m a s, Hansen 2 Klaus, Moroni 1 Maria Cristina, y 3 Dalia R e s n i t z k, Helin 4 Kristian, Reed 3 Steven I., 1'5 2 and Jiri Bartek. 1997. Cyclin E-induced S phase without activation of the pRb/E2F pathway. Genes & Dev https://doi.org/10.1101/gad.11.11.1479.

133. Siu KT, Rosner MR, Minella AC. 2014. An integrated view of cyclin E function and regulation. Cell Cycle 11:57–64.

134. Chellappan SP, Hiebert S, Mudryj M, Horowitz JM, Nevins JR. 1991. The E2F transcription factor is a cellular target for the RB protein. Cell 65:1053–1061.

135. Chen XS, Stehle T, Harrison SC. 1998. Interaction of polyomavirus internal protein VP2 with the major capsid protein VP1 and implications for participation of VP2 in viral entry. The EMBO journal 17:3233–40.

136. Safak M, Barrucco R, Darbinyan A, Okada Y, Nagashima K, Khalili K. 2001. Interaction of JC virus agno protein with T antigen modulates transcription and replication of the viral genome in glial cells. Journal of virology 75:1476–86.

137. Suzuki T, Orba Y, Okada Y, Sunden Y, Kimura T, Tanaka S, Nagashima K, Hall WW, Sawa H. 2010. The human polyoma JC virus agnoprotein acts as a viroporin. PLoS pathogens 6:e1000801.

138. Sofroniew MV. 2020. Astrocyte Reactivity: Subtypes, States, and Functions in CNS Innate Immunity. Trends Immunol 41:758–770.

139. Tavčar P, Potokar M, Kolenc M, Korva M, Avšič-Županc T, Zorec R, Jorgačevski J. 2021. Neurotropic Viruses, Astrocytes, and COVID-19. Front Cell Neurosci 15:662578.

140. Niazkar HR, Zibaee B, Nasimi A, Bahri N. 2020. The neurological manifestations of COVID-19: a review article. Neurol Sci 41:1667–1671.

141. Tabata H. 2015. Diverse subtypes of astrocytes and their development during corticogenesis. Front Neurosci-switz 9:114.

142. Kiray H, Lindsay SL, Hosseinzadeh S, Barnett SC. 2016. The multifaceted role of astrocytes in regulating myelination. Exp Neurol 283:541–9.

143. Barnett SC, Linington C. 2013. Myelination: do astrocytes play a role? Neurosci 19:442–50.

144. Sofroniew MV, Vinters HV. 2010. Astrocytes: biology and pathology. Acta Neuropathol 119:7–35.

145. Barres BA. 2008. The Mystery and Magic of Glia: A Perspective on Their Roles in Health and Disease. Neuron 60:430–440.

146. Keyser JD, Mostert JP, Koch MW. 2008. Dysfunctional astrocytes as key players in the pathogenesis of central nervous system disorders. J Neurol Sci 267:3–16.

147. Seifert G, Schilling K, Steinhäuser C. 2006. Astrocyte dysfunction in neurological disorders: a molecular perspective. Nat Rev Neurosci 7:194–206.

148. Sofroniew MV. 2005. Reactive Astrocytes in Neural Repair and Protection. Neurosci 11:400–407.

149. Takano T, Oberheim N, Cotrina ML, Nedergaard M. 2009. Astrocytes and Ischemic Injury. Stroke 40:S8–S12.

150. Khakh BS, Sofroniew MV. 2015. Diversity of astrocyte functions and phenotypes in neural circuits. Nat Neurosci 18:942–52.

151. Cahoy JD, Emery B, Kaushal A, Foo LC, Zamanian JL, Christopherson KS, Xing Y, Lubischer JL, Krieg PA, Krupenko SA, Thompson WJ, Barres BA. 2008. A transcriptome database for astrocytes, neurons, and oligodendrocytes: a new resource for understanding brain development and function. J Neurosci 28:264–78.

152. Sofroniew MV. 2009. Molecular dissection of reactive astrogliosis and glial scar formation. Trends Neurosci 32:638–647.

153. Farina C, Aloisi F, Meinl E. 2007. Astrocytes are active players in cerebral innate immunity. Trends Immunol 28:138–145.

154. Min K-J, Yang M, Kim S-U, Jou I, Joe E. 2006. Astrocytes Induce Hemeoxygenase-1 Expression in Microglia: A Feasible Mechanism for Preventing Excessive Brain Inflammation. J Neurosci 26:1880–1887.

155. Wang Z, Trillo-Pazos G, Kim S-Y, Canki M, Morgello S, Sharer LR, Gelbard HA, Su Z, Kang D, Brooks AI, Fisher PB, Volsky DJ. 2004. Effects of human immunodeficiency virus type 1 on astrocyte gene expression and function: Potential role in neuropathogenesis. J Neurovirol 10:25–32.

156. Donati D, Martinelli E, Cassiani-Ingoni R, Ahlqvist J, Hou J, Major EO, Jacobson S. 2005. Variant-Specific Tropism of Human Herpesvirus 6 in Human Astrocytes. J Virol 79:9439–9448.

157. Akaoka H, Szymocha R, Beurton-Marduel P, Bernard A, Belin M-F, Giraudon P. 2001. Functional changes in astrocytes by human T-lymphotropic virus type-1 T-lymphocytes. Virus Res 78:57–66.

158. Szymocha R, Akaoka H, Dutuit M, Malcus C, Didier-Bazes M, Belin M-F, Giraudon P. 2000. Human T-Cell Lymphotropic Virus Type 1-Infected T Lymphocytes Impair Catabolism and Uptake of Glutamate by Astrocytes via Tax-1 and Tumor Necrosis Factor Alpha. J Virol 74:6433–6441.

159. Soung A, Klein RS. 2018. Viral Encephalitis and Neurologic Diseases: Focus on Astrocytes. Trends Mol Med 24:950–962.

160. Hult B, Chana G, Masliah E, Everall I. 2009. Neurobiology of HIV. Int Rev Psychiatr 20:3–13.

161. Vazeux R, Cumont M, Girard PM, Nassif X, Trotot P, Marche C, Matthiessen L, Vedrenne C, Mikol J, Henin D, Katlama C, Bolgert F, Montagnier L. 1990. Severe encephalitis resulting from coinfections with HIV and JC virus. Neurology 40:944–944.

162. Jr RE. 1961. Progressive multifocal leukoencephalopathy https://doi.org/10.1056/NEJM196110262651701.

163. Barcia C, Sanderson NSR, Barrett RJ, Wawrowsky K, Kroeger KM, Puntel M, Liu C, Castro MG, Lowenstein PR. 2008. T Cells' Immunological Synapses Induce Polarization of Brain Astrocytes In Vivo and In Vitro: A Novel Astrocyte Response Mechanism to Cellular Injury. Plos One 3:e2977.

164. Barcia C, Thomas CE, Curtin JF, King GD, Wawrowsky K, Candolfi M, Xiong W-D, Liu C, Kroeger K, Boyer O, Kupiec-Weglinski J, Klatzmann D, Castro MG, Lowenstein PR. 2006. In vivo mature immunological synapses forming SMACs mediate clearance of virally infected astrocytes from the brain. J Exp Medicine 203:2095–2107.

165. Seth P, Diaz F, Tao-Cheng J-HH, Major EO. 2004. JC virus induces nonapoptotic cell death of human central nervous system progenitor cell-derived astrocytes. Journal of virology 78:4884–91.

166. Ferenczy MW, Johnson KR, Marshall LJ, Monaco M, Major EO. 2013. Differentiation of Human Fetal Multipotential Neural Progenitor Cells to Astrocytes Reveals Susceptibility Factors for JC Virus. Journal of Virology 87:6221–6231.

167. Erickson KD, Garcea RL. 2019. Viral replication centers and the DNA damage response in JC virus-infected cells. Virology 528:198-206–206.

168. Lynch KJ, Frisque RJ. 1990. Identification of critical elements within the JC virus DNA replication origin. J Virol 64:5812–22.

169. Rhein GMZ, Varakis JN. 1979. Perinatal induction of medulloblastomas in Syrian golden hamsters by a human polyoma virus (JC). National Cancer Inst Monogr 205–8.

170. Walker DL, Padgett BL, ZuRhein GM, Albert AE, Marsh RF. 1973. Human papovavirus (JC): induction of brain tumors in hamsters. Science 181:674–6.

171. London WT, Houff SA, Madden DL, Fuccillo DA, Gravell M, Wallen WC, Palmer AE, Sever JL, Padgett BL, Walker DL, ZuRhein GM, Ohashi T. 1978. Brain tumors in owl monkeys inoculated with a human polyomavirus (JC virus). Science 201:1246–9.

172. Houff SA, London WT, Rhein GMZ, Padgett BL, Walker DL, Sever JL. 1983. New world primates as a model of viral-induced astrocytomas. Prog Clin Biol Res 105:223–6.

173. London WT, Houff SA, McKeever PE, Wallen WC, Sever JL, Padgett BL, Walker DL. 1983. Viral-induced astrocytomas in squirrel monkeys. Prog Clin Biol Res 105:227–37.

174. Major E, Vacante D, Traub R, London W, Sever J. 1987. Owl monkey astrocytoma cells in culture spontaneously produce infectious JC virus which demonstrates altered biological properties. Journal of virology 61:1435–1441.

175. Tan CS, A. JrB T, Seung E, Vrbanac V, Viscidi R, Gordon J, Tager AM, Koralnik IJ. 2013. Detection of JC virus-specific immune responses in a novel humanized mouse model. PLoS One 8:e64313.

176. Radford AD, Chapman D, Dixon L, Chantrey J, Darby AC, Hall N. 2012. Application of next-generation sequencing technologies in virology. J Gen Virol 93:1853–1868.

177. Tang P, Chiu C. 2010. Metagenomics for the discovery of novel human viruses. Future Microbiol 5:177–189.

178. Feng H, Shuda M, Chang Y, Moore PS. 2008. Clonal Integration of a Polyomavirus in Human Merkel Cell Carcinoma. Science 319:1096–1100.

179. Siebrasse EA, Reyes A, Lim ES, Zhao G, Mkakosya RS, Manary MJ, Gordon JI, Wang D. 2012. Identification of MW Polyomavirus, a Novel Polyomavirus in Human Stool. J Virol 86:10321–10326.

180. Yu G, Greninger AL, Isa P, Phan TG, Martínez MA, Sanchez M de la L, Contreras JF, Santos-Preciado JI, Parsonnet J, Miller S, DeRisi JL, Delwart E, Arias CF, Chiu CY. 2012. Discovery of a Novel Polyomavirus in Acute Diarrheal Samples from Children. Plos One 7:e49449.

181. Buck CB, Phan GQ, Raiji MT, Murphy PM, McDermott DH, McBride AA. 2012. Complete Genome Sequence of a Tenth Human Polyomavirus. J Virol 86:10887–10887.

182. Sauvage V, Foulongne V, Cheval J, Gouilh MA, Pariente K, Dereure O, Manuguerra JC, Richardson J, Lecuit M, Burguière A, Caro V, Eloit M. 2011. Human Polyomavirus Related to African Green Monkey Lymphotropic Polyomavirus. Emerg Infect Dis 17:1364–1370.

183. Holt RA, Jones SJM. 2008. The new paradigm of flow cell sequencing. Genome Res 18:839–846.

184. Marioni JC, Mason CE, Mane SM, Stephens M, Gilad Y. 2008. RNA-seq: An assessment of technical reproducibility and comparison with gene expression arrays. Genome Res 18:1509–1517.

185. Wilhelm BT, Landry J-R. 2009. RNA-Seq—quantitative measurement of expression through massively parallel RNA-sequencing. Methods 48:249–257.

186. Anders S, Pyl PT, Huber W. 2015. HTSeq—a Python framework to work with high-throughput sequencing data. Bioinformatics 31:166–169.

187. Robinson MD, McCarthy DJ, Smyth GK. 2010. edgeR: a Bioconductor package for differential expression analysis of digital gene expression data. Bioinformatics 26:139–140.

188. Anders S, Huber W. 2010. Differential expression analysis for sequence count data. Genome Biology 11:R106.

189. Lin Z, Xu G, Deng N, Taylor C, Zhu D, Flemington EK. 2010. Quantitative and Qualitative RNA-Seq-Based Evaluation of Epstein-Barr Virus Transcription in Type I Latency Burkitt's Lymphoma Cells ▿ †. J Virol 84:13053–13058.

190. Gatherer D, Seirafian S, Cunningham C, Holton M, Dargan DJ, Baluchova K, Hector RD, Galbraith J, Herzyk P, Wilkinson GWG, Davison AJ. 2011. High-resolution human cytomegalovirus transcriptome. Proc National Acad Sci 108:19755–19760.

191. Assetta B, Cecco MD, O'Hara B, Atwood WJ. 2016. JC Polyomavirus Infection of Primary Human Renal Epithelial Cells Is Controlled by a Type I IFN-Induced Response. mBio 7:e00903-16.

192. Shaul YD, Seger R. 2007. The MEK/ERK cascade: From signaling specificity to diverse functions. Biochimica Et Biophysica Acta Bba - Mol Cell Res 1773:1213–1226.

193. DuShane JK, Wilczek MP, Mayberry CL, Maginnis MS. 2018. ERK Is a Critical Regulator of JC Polyomavirus Infection. Journal of virology 92.

194. Peterson JN, Lin B, Shin J, Phelan PJ, Tsichlis P, Schwob JE, Bullock PA. 2017. THE REPLICATION OF JCV DNA IN THE G144 OLIGODENDROCYTE CELL LINE IS DEPENDENT UPON AKT. Journal of Virology JVI.00735-17.

195. Orellana JA, Kwun HJ, Artusi S, Chang Y, Moore PS. 2020. Sirolimus and other mTOR inhibitors directly activate latent pathogenic human polyomavirus replication. J Infect Dis https://doi.org/10.1093/infdis/jiaa071.

196. Clark P, Gee GV, Albright BS, Assetta B, Han Y, Atwood WJ, DiMaio D. 2020. Phosphoinositide 3'-Kinase γ Facilitates Polyomavirus Infection. Viruses 12:1190.

197. Yang S, Liu G. 2017. Targeting the Ras/Raf/MEK/ERK pathway in hepatocellular carcinoma. Oncol Lett 13:1041–1047.

198. Pearson G, Robinson F, Gibson TB, Xu B, Karandikar M, Berman K, Cobb MH. 2001. Mitogen-Activated Protein (MAP) Kinase Pathways: Regulation and Physiological Functions. Endocr Rev 22:153–183.

199. Agell N, Bachs O, Rocamora N, Villalonga P. 2002. Modulation of the Ras/Raf/MEK/ERK pathway by Ca2+, and Calmodulin. Cell Signal 14:649–654.

200. Roskoski R. 2012. ERK1/2 MAP kinases: Structure, function, and regulation. Pharmacol Res 66:105–143.

201. WATTS . W. 1998. Activation of the Mitogen-activated Protein Kinase Pathway via the 5-HT2A Receptora. Ann Ny Acad Sci 861:162–168.

202. Lewis TS, Shapiro PS, Ahn NG. 1998. Signal Transduction through MAP Kinase Cascades. Adv Cancer Res 74:49–139.

203. Hladik F, McElrath JM. 2008. Setting the stage: host invasion by HIV. Nature Reviews Immunology 8:447–457.

204. Ravichandran V, Jensen PN, Major EO. 2007. MEK1/2 Inhibitors Block Basal and Transforming Growth Factor β1-Stimulated JC Virus Multiplication ▿ . J Virol 81:6412–6418.

205. DuShane JK, Mayberry CL, Wilczek MP, Nichols SL, Maginnis MS. 2019. JCPyV-Induced MAPK Signaling Activates Transcription Factors during Infection. Int J Mol Sci 20:4779.

206. Pleschka S. 2008. RNA viruses and the mitogenic Raf/MEK/ERK signal transduction cascade. Biol Chem 389:1273–1282.

207. Panteva M, Korkaya H, Jameel S. 2003. Hepatitis viruses and the MAPK pathway: is this a survival strategy? Virus Res 92:131–140.

208. Bonjardim CA. 2017. Viral exploitation of the MEK/ERK pathway – A tale of vaccinia virus and other viruses. Virology 507:267–275.

209. Pérez-Sen R, Queipo MJ, Gil-Redondo JC, Ortega F, Gómez-Villafuertes R, Miras-Portugal MT, Delicado EG. 2019. Dual-Specificity Phosphatase Regulation in Neurons and Glial Cells. Int J Mol Sci 20:1999.

210. Dickinson RJ, Keyse SM. 2006. Diverse physiological functions for dual-specificity MAP kinase phosphatases. J Cell Sci 119:4607–4615.

211. Junttila MR, Li S, Westermarck J. 2008. Phosphatase-mediated crosstalk between MAPK signaling pathways in the regulation of cell survival. Faseb J 22:954–965.

212. Patterson KI, Brummer T, O'brien PM, Daly RJ. 2009. Dual-specificity phosphatases: critical regulators with diverse cellular targets. Biochem J 418:475–489.

213. Huang C-Y, Tan T-H. 2012. DUSPs, to MAP kinases and beyond. Cell Biosci 2:24.

214. Ma RYM, Tong THK, Cheung AMS, Tsang ACC, Leung WY, Yao K-M. 2005. Raf/MEK/MAPK signaling stimulates the nuclear translocation and transactivating activity of FOXM1c. J Cell Sci 118:795–806.

215. Brondello J-M, Pouysségur J, McKenzie FR. 1999. Reduced MAP Kinase Phosphatase-1 Degradation After p42/p44MAPK-Dependent Phosphorylation. Science 286:2514–2517.

216. Lin Y-W, Yang J-L. 2006. Cooperation of ERK and SCFSkp2 for MKP-1 Destruction Provides a Positive Feedback Regulation of Proliferating Signaling*. J Biol Chem 281:915–926.

217. DuShane JK, Maginnis MS. 2019. Human DNA Virus Exploitation of the MAPK-ERK Cascade. Int J Mol Sci 20:3427.

218. Chi H, Barry SP, Roth RJ, Wu JJ, Jones EA, Bennett AM, Flavell RA. 2006. Dynamic regulation of pro- and anti-inflammatory cytokines by MAPK phosphatase 1 (MKP-1) in innate immune responses. P Natl Acad Sci Usa 103:2274–2279.

219. Choi JE, Kwon JH, Kim J-H, Hur W, Sung PS, Choi SW, Yoon SK. 2015. Suppression of Dual Specificity Phosphatase I Expression Inhibits Hepatitis C Virus Replication. Plos One 10:e0119172.

220. Choi SS, Lee HJ, Lim I, Satoh J, Kim SU. 2014. Human Astrocytes: Secretome Profiles of Cytokines and Chemokines. Plos One 9:e92325.

221. Chang F, Lee JT, Navolanic PM, Steelman LS, Shelton JG, Blalock WL, Franklin RA, McCubrey JA. 2003. Involvement of PI3K/Akt pathway in cell cycle progression, apoptosis, and neoplastic transformation: a target for cancer chemotherapy. Leukemia 17:590–603.

222. n.d. PI-3-kinase and MAPK regulate mesangial cell proliferation and migration in response to PDGF.

223. Diehl JA, Cheng M, Roussel MF, Sherr CJ. 1998. Glycogen synthase kinase-3β regulates cyclin D1 proteolysis and subcellular localization. Gene Dev 12:3499–3511.

224. Gille H, Downward J. 1999. Multiple Ras Effector Pathways Contribute to G1Cell Cycle Progression*. J Biol Chem 274:22033–22040.

225. Medema RH, Kops GJPL, Bos JL, Burgering BMT. 2000. AFX-like Forkhead transcription factors mediate cell-cycle regulation by Ras and PKB through p27kip1. Nature 404:782–787.

226. Muise-Helmericks RC, Grimes HL, Bellacosa A, Malstrom SE, Tsichlis PN, Rosen N. 1998. Cyclin D Expression Is Controlled Post-transcriptionally via a Phosphatidylinositol 3-Kinase/Akt-dependent Pathway*. J Biol Chem 273:29864–29872.

227. Choudhury GG. 2001. Akt Serine Threonine Kinase Regulates Platelet-derived Growth Factor-induced DNA Synthesis in Glomerular Mesangial Cells REGULATION OF c-fos AND p27 kip1 GENE EXPRESSION*. J Biol Chem 276:35636–35643.

228. Bilanges B, Posor Y, Vanhaesebroeck B. 2019. PI3K isoforms in cell signalling and vesicle trafficking. Nat Rev Mol Cell Bio 20:515–534.

229. Jafari M, Ghadami E, Dadkhah T, Akhavan-Niaki H. 2019. PI3k/AKT signaling pathway: Erythropoiesis and beyond. J Cell Physiol 234:2373–2385.

230. Xu F, Na L, Li Y, Chen L. 2020. Roles of the PI3K/AKT/mTOR signalling pathways in neurodegenerative diseases and tumours. Cell Biosci 10:54.

231. Tuncel G, Kalkan R. 2018. Receptor tyrosine kinase-Ras-PI 3 kinase-Akt signaling network in glioblastoma multiforme. Med Oncol 35:122.

232. Ma Z, Xin Z, Hu W, Jiang S, Yang Z, Yan X, Li X, Yang Y, Chen F. 2018. Forkhead box O proteins: crucial regulators of cancer EMT. Semin Cancer Biol 50:21–31.

233. Maiese K. 2018. Forkhead Transcription Factors: Formulating a FOXO Target for Cognitive Loss. Curr Neurovasc Res 14:415–420.

234. Wei X, Luo L, Chen J. 2019. Roles of mTOR Signaling in Tissue Regeneration. Cells 8:1075.

235. Kim J, Guan K-L. 2019. mTOR as a central hub of nutrient signalling and cell growth. Nat Cell Biol 21:63–71.

236. Murugan AK. 2019. mTOR: Role in cancer, metastasis and drug resistance. Semin Cancer Biol 59:92–111.

237. Yuan H-X, Russell RC, Guan K-L. 2013. Regulation of PIK3C3/VPS34 complexes by MTOR in nutrient stress-induced autophagy. Autophagy 9:1983–1995.

238. Jhanwar-Uniya M, Wainwright JV, Mohan AL, Tobias ME, Murali R, Gandhi CD, Schmidt MH. 2019. Diverse signaling mechanisms of mTOR complexes: mTORC1 and mTORC2 in forming a formidable relationship. Adv Biological Regul 72:51–62.

239. Liacini A, Seamone ME, Muruve DA, Tibbles LA. 2010. Anti-BK Virus Mechanisms of Sirolimus and Leflunomide Alone and in Combination: Toward a New Therapy for BK Virus Infection. Transplantation 90:1450–1457.

240. Hirsch HH, Yakhontova K, Lu M, Manzetti J. 2016. BK Polyomavirus Replication in Renal Tubular Epithelial Cells Is Inhibited by Sirolimus, but Activated by Tacrolimus Through a Pathway Involving FKBP-12. American Journal of Transplantation 16:821–832.

241. Mayberry CL, Wilczek MP, Fong TM, Nichols SL, Maginnis MS. 2021. GRK2 Mediates β-Arrestin Interactions with 5-HT 2 Receptors for JC Polyomavirus Endocytosis. J Virol 95.

242. Stacey G, MacDonald C. 2001. Immortalisation of Primary Cells. Cell Biol Toxicol 17:231.

243. Yu Y, Alwine JC. 2002. Human Cytomegalovirus Major Immediate-Early Proteins and Simian Virus 40 Large T Antigen Can Inhibit Apoptosis through Activation of the Phosphatidylinositide 3′-OH Kinase Pathway and the Cellular Kinase Akt. J Virol 76:3731–3738.

244. Yu Y, Alwine JC. 2008. Interaction between Simian Virus 40 Large T Antigen and Insulin Receptor Substrate 1 Is Disrupted by the K1 Mutation, Resulting in the Loss of Large T Antigen-Mediated Phosphorylation of Akt ▿ . J Virol 82:4521–4526.

245. Campistol JM, Eris J, Oberbauer R, Friend P, Hutchison B, Morales JM, Claesson K, Stallone G, Russ G, Rostaing L, Kreis H, Burke JT, Brault Y, Scarola JA, Neylan JF, Group for the RMRS. 2006. Sirolimus Therapy after Early Cyclosporine Withdrawal Reduces the Risk for Cancer in Adult Renal Transplantation. J Am Soc Nephrol 17:581–589.

246. Zoncu R, Efeyan A, Sabatini DM. 2011. mTOR: from growth signal integration to cancer, diabetes and ageing. Nat Rev Mol Cell Bio 12:21–35.

247. Hayashi H, Tsuchiya Y, Nakayama K, Satoh T, Nishida E. 2008. Down-regulation of the PI3-kinase/Akt pathway by ERK MAP kinase in growth factor signaling. Genes Cells 13:941–947.

248. Rhim J heon, Luo X, Gao D, Xu X, Zhou T, Li F, Wang P, Wong STC, Xia X. 2016. Cell type-dependent Erk-Akt pathway crosstalk regulates the proliferation of fetal neural progenitor cells. Sci Rep-uk 6:26547.

249. Turke AB, Song Y, Costa C, Cook R, Arteaga CL, Asara JM, Engelman JA. 2012. MEK Inhibition Leads to PI3K/AKT Activation by Relieving a Negative Feedback on ERBB Receptors. Cancer Res 72:3228–3237.

250. Mendoza MC, Er EE, Blenis J. 2011. The Ras-ERK and PI3K-mTOR pathways: cross-talk and compensation. Trends Biochem Sci 36:320–328.

251. McCubrey JA, Lee JT, Steelman LS, Blalock WL, Moye PW, Chang F, Pearce M, Shelton JG, White MK, Franklin RA, Pohnert SC. 2001. Interactions between the PI3K and Raf signaling pathways can result in the transformation of hematopoietic cells. Cancer Detect Prev 25:375–93.

252. Rodriguez-Viciana P, Warne PH, Dhand R, Vanhaesebroeck B, Gout I, Fry MJ, Waterfield MD, Downward J. 1994. Phosphatidylinositol-3-OH kinase direct target of Ras. Nature 370:527–532.

253. Hu Q, Klippel A, Muslin A, Fantl W, Williams L. 1995. Ras-dependent induction of cellular responses by constitutively active phosphatidylinositol-3 kinase. Science 268:100–102.

254. Wennström S, Downward J. 1999. Role of Phosphoinositide 3-Kinase in Activation of Ras and Mitogen-Activated Protein Kinase by Epidermal Growth Factor. Mol Cell Biol 19:4279–4288.

255. Moelling K, Schad K, Bosse M, Zimmermann S, Schweneker M. 2002. Regulation of Raf-Akt Cross-talk. J Biol Chem 277:31099–31106.

256. Zimmermann S, Moelling K. 1999. Phosphorylation and Regulation of Raf by Akt (Protein Kinase B). Science 286:1741–1744.

257. Rommel C, Clarke BA, Zimmermann S, Nuñez L, Rossman R, Reid K, Moelling K, Yancopoulos GD, Glass DJ. 1999. Differentiation Stage-Specific Inhibition of the Raf-MEK-ERK Pathway by Akt. Science 286:1738–1741.

258. Guan K-L, Figueroa C, Brtva TR, Zhu T, Taylor J, Barber TD, Vojtek AB. 2000. Negative Regulation of the Serine/Threonine Kinase B-Raf by Akt*. J Biol Chem 275:27354–27359.

259. Aksamitiene E, Achanta S, Kolch W, Kholodenko BN, Hoek JB, Kiyatkin A. 2011. Prolactin-stimulated activation of ERK1/2 mitogen-activated protein kinases is controlled by PI3-kinase/Rac/PAK signaling pathway in breast cancer cells. Cell Signal 23:1794–1805.

260. Jun T, Gjoerup O, Roberts TM. 1999. Tangled Webs: Evidence of Cross-Talk Between c-Raf-1 and Akt. Sci Stke 1999:pe1–pe1.

261. Procaccia S, Ordan M, Cohen I, Bendetz-Nezer S, Seger R. 2017. Direct binding of MEK1 and MEK2 to AKT induces Foxo1 phosphorylation, cellular migration and metastasis. Sci Rep-uk 7:43078.

262. Padgett BL, Walker DL, ZuRhein GM, Eckroade RJ, Dessel BH. 1971. Cultivation of papova-like virus from human brain with progressive multifocal leucoencephalopathy. Lancet 1:1257–60.

263. Monaco MC, Atwood WJ, Gravell M, Tornatore CS, Major EO. 1996. JC virus infection of hematopoietic progenitor cells, primary B lymphocytes, and tonsillar stromal cells: implications for viral latency. J Virol 70:7004–12.

264. Dubois V, Dutronc H, Lafon ME, Poinsot V, Pellegrin JL, Ragnaud JM, Ferrer AM, Fleury HJ. 1997. Latency and reactivation of JC virus in peripheral blood of human immunodeficiency virus type 1-infected patients. J Clin Microbiol 35:2288–92.

265. Ferrante P, Caldarelli-Stefano R, Omodeo-Zorini E, Vago L, Boldorini R, Costanzi G. 1995. PCR detection of JC virus DNA in brain tissue from patients with and without progressive multifocal leukoencephalopathy. J Med Virol 47:219–25.

266. Kleinschmidt-DeMasters BK, Tyler KL. 2005. Progressive multifocal leukoencephalopathy complicating treatment with natalizumab and interferon beta-1a for multiple sclerosis. New Engl J Medicine 353:369–74.

267. Major EO. 2010. Progressive multifocal leukoencephalopathy in patients on immunomodulatory therapies. Annu Rev Med 61:35–47.

268. Adang L, Berger J. 2015. Progressive Multifocal Leukoencephalopathy. F1000Res 4.

269. Major EO, Yousry TA, Clifford DB. 2018. Pathogenesis of progressive multifocal leukoencephalopathy and risks associated with treatments for multiple sclerosis: a decade of lessons learned. Lancet Neurol 17:467–480.

270. Marzocchetti A, Tompkins T, Clifford DB, Gandhi RT, Kesari S, Berger JR, Simpson DM, Prosperi M, Luca AD, Koralnik IJ. 2009. Determinants of survival in progressive multifocal leukoencephalopathy. Neurology 73:1551–8.

271. Koralnik IJ. 2015. Progressive Multifocal Leukoencephalopathy.

272. Silverman L, Rubinstein LJ. 1965. Electron microscopic observations on a case of progressive multifocal leukoencephalopathy. Acta Neuropathol 5:215–24.

273. Kondo Y, Windrem MS, Zou L, Chandler-Militello D, Schanz SJ, Auvergne RM, Betstadt SJ, Harrington AR, Johnson M, Kazarov A, Gorelik L, Goldman SA. 2014. Human glial chimeric mice reveal astrocytic dependence of JC virus infection. J Clin Invest 124:5323–36.

274. Radhakrishnan S, Otte J, Enam S, Valle LD, Khalili K, Gordon J. 2003. JC virus-induced changes in cellular gene expression in primary human astrocytes. J Virol 77:10638–44.

275. Vacante DA, Traub R, Major EO. 1989. Extension of JC virus host range to monkey cells by insertion of a simian virus 40 enhancer into the JC virus regulatory region. Virology 170:353–61.

276. Manley K, B AO, Gee GV, Simkevich CP, Sedivy JM, Atwood WJ. 2006. NFAT4 is required for JC virus infection of glial cells. J Virol 80:12079–85.

277. Monaco MC, Sabath BF, Durham LC, Major EO. 2001. JC virus multiplication in human hematopoietic progenitor cells requires the NF-1 class D transcription factor. J Virol 75:9687–95.

278. Ravichandran V, Sabath BF, Jensen PN, Houff SA, Major EO. 2006. Interactions between c-Jun, Nuclear Factor 1, and JC Virus Promoter Sequences: Implications for Viral Tropism. Journal of virology 80:10506-10513–10513.

279. Dyson N, Bernards R, Friend SH, Gooding LR, Hassell JA, Major EO, Pipas JM, Vandyke T, Harlow E. 1990. Large T antigens of many polyomaviruses are able to form complexes with the retinoblastoma protein. Journal of virology 64:1353-6–6.

280. Valle LD, Gordon J, Assimakopoulou M, Enam S, Geddes JF, Varakis JN, Katsetos CD, Croul S, Khalili K. 2001. Detection of JC virus DNA sequences and expression of the viral regulatory protein T-antigen in tumors of the central nervous system. Cancer Res 61:4287–93.

281. Dickmanns A, Zeitvogel A, Simmersbach F, Weber R, Arthur AK, Dehde S, Wildeman AG, Fanning E. 1994. The kinetics of simian virus 40-induced progression of quiescent cells into S phase depend on four independent functions of large T antigen. Journal of virology 68:5496-508–508.

282. Ferenczy MW, Marshall LJ, Nelson CD, Atwood WJ, Nath A, Khalili K, Major EO. 2012. Molecular biology, epidemiology, and pathogenesis of progressive multifocal leukoencephalopathy, the JC virus-induced demyelinating disease of the human brain. Clinical microbiology reviews 25:471-506–506.

283. Rhein GMZ, Varakis JN. 1979. Perinatal induction of medulloblastomas in Syrian golden hamsters by a human polyoma virus (JC). Natl Cancer Inst Monogr 205–8.

284. Houff SA, London WT, Rhein GMZ, Padgett BL, Walker DL, Sever JL. 1983. New world primates as a model of viral-induced astrocytomas. Prog Clin Biol Res 105:223–6.

285. London WT, Houff SA, McKeever PE, Wallen WC, Sever JL, Padgett BL, Walker DL. 1983. Viral-induced astrocytomas in squirrel monkeys. Prog Clin Biol Res 105:227–37.

286. Major EO, Vacante DA, Traub RG, London WT, Sever JL. 1987. Owl monkey astrocytoma cells in culture spontaneously produce infectious JC virus which demonstrates altered biological properties. J Virol 61:1435–41.

287. Lynch KJ, Frisque RJ. 1990. Identification of critical elements within the JC virus DNA replication origin. Journal of virology 64:5812-22–22.

288. Seth P, Diaz F, Tao-Cheng JH, Major EO. 2004. JC virus induces nonapoptotic cell death of human central nervous system progenitor cell-derived astrocytes. J Virol 78:4884–91.

289. Messam CA, Hou J, Gronostajski RM. 2003. Lineage pathway of human brain progenitor cells identified by JC virus susceptability https://doi.org/10.1002/ana.10523.

290. Ferenczy MW, Johnson KR, Marshall LJ, Monaco M, Major EO. 2013. Differentiation of Human Fetal Multipotential Neural Progenitor Cells to Astrocytes Reveals Susceptibility Factors for JC Virus. Journal of virology 87:6221-6231–6231.

291. Major EO, Miller AE, Mourrain P, Traub RG, Widt E de, Sever J. 1985. Establishment of a line of human fetal glial cells that supports JC virus multiplication. Proc Natl Acad Sci U S A 82:1257–61.

292. DuShane JK, Wilczek MP, Crocker MA, Maginnis MS. 2019. High-Throughput Characterization of Viral and Cellular Protein Expression Patterns During JC Polyomavirus Infection. Front Microbiol 10:783.

293. Kelley JB, Paschal BM. 2019. Fluorescence-based quantification of nucleocytoplasmic transport. Methods 157:106–114.

294. DuShane JK, Wilczek MP, Mayberry CL, Maginnis MS. 2018. ERK Is a Critical Regulator of JC Polyomavirus Infection. J Virol 92.

295. Tang Y, Horikoshi M, Li W. 2016. ggfortify: Unified Interface to Visualize Statistical Results of Popular R Packages. R J 8:474.

296. Wickham H. 2016. ggplot2, Elegant Graphics for Data Analysis 3-10–10.

297. GmbH MS. 2018. XLConnect: Excel Connector for R.

298. Walz W, Lang MK. 1998. Immunocytochemical evidence for a distinct GFAP-negative subpopulation of astrocytes in the adult rat hippocampus. Neurosci Lett 257:127–30.

299. Shaw G, Morse S, Ararat M, Graham FL. 2002. Preferential transformation of human neuronal cells by human adenoviruses and the origin of HEK 293 cells. FASEB J 16:869–71.

300. Zhou B, Zuo YX, Jiang RT. 2019. Astrocyte morphology: Diversity, plasticity, and role in neurological diseases. CNS Neurosci Ther 25:665–673.

301. Draberova E, Valle LD, Gordon J, Markova V, Smejkalova B, Bertrand L, Chadarevian JP de, Agamanolis DP, Legido A, Khalili K, Draber P, Katsetos CD. 2008. Class III beta-tubulin is constitutively coexpressed with glial fibrillary acidic protein and nestin in midgestational human fetal astrocytes: implications for phenotypic identity. J Neuropathol Exp Neurol 67:341–54.

302. Lynch KJ, Frisque RJ. 1991. Factors contributing to the restricted DNA replicating activity of JC virus. Virology 180:306–17.

303. Minella AC, Loeb KR, Knecht A, Welcker M, Varnum-Finney BJ, Bernstein ID, Roberts JM, Clurman BE. 2008. Cyclin E phosphorylation regulates cell proliferation in hematopoietic and epithelial lineages in vivo. Genes Dev 22:1677–89.

304. Pines J, Hunter T. 1991. Human cyclins A and B1 are differentially located in the cell and undergo cell cycle-dependent nuclear transport. J Cell Biol 115:1–17.

305. Hagting A, Jackman M, Simpson K, Pines J. 1999. Translocation of cyclin B1 to the nucleus at prophase requires a phosphorylation-dependent nuclear import signal. Curr Biol 9:680–9.

306. Ferenczy MW, Johnson KR, Steinberg SM, Marshall LJ, Monaco MC, Beschloss AM, Jensen PN, Major EO. 2013. Clonal immortalized human glial cell lines support varying levels of JC virus infection due to differences in cellular gene expression. Journal of neuroimmune pharmacology : the official journal of the Society on NeuroImmune Pharmacology 8:1303-19–19.

307. Davey P, Rauth AM, Mason L, Addy L. 1990. Spontaneous phenotypic and karyotypic progression in the SV40 transfected cell line SVG during prolonged passage in vitro. J Neurooncol 8:13–22.

308. Hara K, Sugimoto C, Kitamura T, Aoki N, Taguchi F, Yogo Y. 1998. Archetype JC virus efficiently replicates in COS-7 cells, simian cells constitutively expressing simian virus 40 T antigen. J Virol 72:5335–42.

309. Assetta B, Cecco MD, O'Hara B, Atwood WJ. 2016. JC Polyomavirus Infection of Primary Human Renal Epithelial Cells Is Controlled by a Type I IFN-Induced Response. mBio 7:e00903-16–16.

310. O'Hara BA, Gee GV, Atwood WJ, Haley SA. 2018. Susceptibility of Primary Human Choroid Plexus Epithelial Cells and Meningeal Cells to Infection by JC Virus. J Virol 92:e00105-18.

311. Schaumburg C, O'Hara BA, Lane TE, Atwood WJ. 2008. Human embryonic stem cell-derived oligodendrocyte progenitor cells express the serotonin receptor and are susceptible to JC virus infection. J Virol 82:8896–9.

312. Barth H, Solis M, Kack-Kack W, Soulier E, Velay A, Fafi-Kremer S. 2016. In Vitro and In Vivo Models for the Study of Human Polyomavirus Infection. Viruses 8.

313. Berger JR. 2011. The clinical features of PML. Cleve Clin J Med 78 Suppl 2:S8-12.

314. Dey D, Dahl J, Cho S, Benjamin TL. 2002. Induction and bypass of p53 during productive infection by polyomavirus. Journal of virology 76:9526-32–32.

315. Peterson SR, Gadbois DM, Bradbury EM, Kraemer PM. 1995. Immortalization of human fibroblasts by SV40 large T antigen results in the reduction of cyclin D1 expression and subunit association with proliferating cell nuclear antigen and Waf1. Cancer Res 55:4651–7.

316. Chang TH, Schlegel R. 1996. SV40 T antigen increases the expression and activities of p34cdc2, cyclin A, and cyclin B prior to immortalization of human diploid fibroblasts. J Cell Biochem 60:161–72.

317. Khanna N, Elzi L, Mueller NJ, Garzoni C, Cavassini M, Fux CA, Vernazza P, Bernasconi E, Battegay M, Hirsch HH, Study SHC. 2009. Incidence and Outcome of Progressive Multifocal Leukoencephalopathy over 20 Years of the Swiss HIV Cohort Study. Clin Infect Dis 48:1459–1466.

318. Major EO, Vacante DA, Traub RG, London WT, Sever JL. 1987. Owl monkey astrocytoma cells in culture spontaneously produce infectious JC virus which demonstrates altered biological properties. J Virol 61:1435–1441.

319. Mázló M, Tariska I. 1982. Are astrocytes infected in progressive multifocal leukoencephalopathy (PML)? Acta Neuropathol 56:45–51.

320. Farooq A, Zhou M-M. 2004. Structure and regulation of MAPK phosphatases. Cell Signal 16:769–779.

321. Wang H, Liu D, Sun Y, Meng C, Tan L, Song C, Qiu X, Liu W, Ding C, Ying L. 2021. Upregulation of DUSP6 impairs infectious bronchitis virus replication by negatively regulating ERK pathway and promoting apoptosis. Vet Res 52:7.

322. Cáceres A, Perdiguero B, Gómez CE, Cepeda MV, Caelles C, Sorzano CO, Esteban M. 2013. Involvement of the Cellular Phosphatase DUSP1 in Vaccinia Virus Infection. Plos Pathog 9:e1003719.

323. Robitaille AC, Caron E, Zucchini N, Mukawera E, Adam D, Mariani MK, Gélinas A, Fortin A, Brochiero E, Grandvaux N. 2017. DUSP1 regulates apoptosis and cell migration, but not the JIP1-protected cytokine response, during Respiratory Syncytial Virus and Sendai Virus infection. Sci Rep-uk 7:17388.

324. Mamoor S. n.d. Coronaviruses induce the expression of the dual specificity phosphatase DUSP1/MKP1. https://doi.org/10.31219/osf.io/q8fuy.

325. Nelson CDS, Carney DW, Derdowski A, Lipovsky A, Gee GV, O'Hara B, Williard P, DiMaio D, Sello JK, Atwood WJ. 2013. A Retrograde Trafficking Inhibitor of Ricin and Shiga-Like Toxins Inhibits Infection of Cells by Human and Monkey Polyomaviruses. Mbio 4:e00729-13.

326. Shen J, Xing W, Liu R, Zhang Y, Xie C, Gong F. 2019. MiR-32-5p influences high glucose-induced cardiac fibroblast proliferation and phenotypic alteration by inhibiting DUSP1. Bmc Mol Biol 20:21.

327. Chapagain ML, Verma S, Mercier F, Yanagihara R, Nerurkar VR. 2007. Polyomavirus JC infects human brain microvascular endothelial cells independent of serotonin receptor 2A. Virology 364:55–63.

328. Bolger AM, Lohse M, Usadel B. 2014. Trimmomatic: a flexible trimmer for Illumina sequence data. Bioinformatics 30:2114–2120.

329. Kim D, Langmead B, Salzberg SL. 2015. HISAT: a fast spliced aligner with low memory requirements. Nat Methods 12:357–360.

330. Szklarczyk D, Franceschini A, Wyder S, Forslund K, Heller D, Huerta-Cepas J, Simonovic M, Roth A, Santos A, Tsafou KP, Kuhn M, Bork P, Jensen LJ, von Mering C. 2015. STRING v10: protein–protein interaction networks, integrated over the tree of life. Nucleic Acids Res 43:D447–D452.

331. Mi H, Muruganujan A, Casagrande JT, Thomas PD. 2013. Large-scale gene function analysis with the PANTHER classification system. Nat Protoc 8:1551–1566.

332. Walter W, Sánchez-Cabo F, Ricote M. 2015. GOplot: an R package for visually combining expression data with functional analysis. Bioinformatics 31:2912–2914.

333. Wortzel I, Seger R. 2011. The ERK Cascade: Distinct Functions within Various Subcellular Organelles. Genes Cancer 2:195–209.

334. Dhanasekaran N, Reddy EP. 1998. Signaling by dual specificity kinases. Oncogene 17:1447–1455.

335. Molina G, Vogt A, Bakan A, Dai W, Oliveira PQ de, Znosko W, Smithgall TE, Bahar I, Lazo JS, Day BW, Tsang M. 2009. Zebrafish chemical screening reveals an inhibitor of Dusp6 that expands cardiac cell lineages. Nat Chem Biol 5:680–687.

336. Tsang M, Maegawa S, Kiang A, Habas R, Weinberg E, Dawid IB. 2004. A role for MKP3 in axial patterning of the zebrafish embryo. Development 131:2769–2779.

337. Echevarria D, Martinez S, Marques S, Lucas-Teixeira V, Belo JA. 2005. Mkp3 is a negative feedback modulator of Fgf8 signaling in the mammalian isthmic organizer. Dev Biol 277:114–128.

338. ZHANG W, LIU HT. 2002. MAPK signal pathways in the regulation of cell proliferation in mammalian cells. Cell Res 12:9–18.

339. Hillig RC, Sautier B, Schroeder J, Moosmayer D, Hilpmann A, Stegmann CM, Werbeck ND, Briem H, Boemer U, Weiske J, Badock V, Mastouri J, Petersen K, Siemeister G, Kahmann JD, Wegener D, Böhnke N, Eis K, Graham K, Wortmann L, Nussbaum F von, Bader B. 2019. Discovery of potent SOS1 inhibitors that block RAS activation via disruption of the RAS–SOS1 interaction. Proc National Acad Sci 116:201812963.

340. Poltorak M, Meinert I, Stone JC, Schraven B, Simeoni L. 2014. Sos1 regulates sustained TCR-mediated Erk activation. Eur J Immunol 44:1535–1540.

341. Salojin KV, Owusu IB, Millerchip KA, Potter M, Platt KA, Oravecz T. 2006. Essential Role of MAPK Phosphatase-1 in the Negative Control of Innate Immune Responses. J Immunol 176:1899–1907.

342. Hammer M, Mages J, Dietrich H, Servatius A, Howells N, Cato ACB, Lang R. 2006. Dual specificity phosphatase 1 (DUSP1) regulates a subset of LPS-induced genes and protects mice from lethal endotoxin shock. J Exp Medicine 203:15–20.

343. Cortes-Sempere M, Chattopadhyay S, Rovira A, Rodriguez-Fanjul V, Belda-Iniesta C, Tapia M, Cejas P, Machado-Pinilla R, Manguan-García C, Sánchez-Pérez I, Nistal M, Moratilla C, Castro-Carpeño J de, Gonzalez-Barón M, Albanell J, Perona R. 2009. MKP1 repression is required for the chemosensitizing effects of NF-κB and PI3K inhibitors to cisplatin in non-small cell lung cancer. Cancer Lett 286:206–216.

344. Schmierer B, Hill CS. 2007. TGFβ–SMAD signal transduction: molecular specificity and functional flexibility. Nat Rev Mol Cell Bio 8:970–982.

345. Rohini M, Arumugam B, Vairamani M, Selvamurugan N. 2019. Stimulation of ATF3 interaction with Smad4 via TGF-β1 for matrix metalloproteinase 13 gene activation in human breast cancer cells. Int J Biol Macromol 134:954–961.

346. Anand P, Hotan GC, Vogel A, Venna N, Mateen FJ. 2019. Progressive multifocal leukoencephalopathy: A 25-year retrospective cohort study. Neurology - Neuroimmunol Neuroinflammation 6:e618.

347. Cortese I, Muranski P, Enose-Akahata Y, Ha S-K, Smith B, Monaco M, Ryschkewitsch C, Major EO, Ohayon J, Schindler MK, Beck E, Reoma LB, Jacobson S, Reich DS, Nath A. 2019. Pembrolizumab Treatment for Progressive Multifocal Leukoencephalopathy. New Engl J Med 380:1597–1605.

348. Vanhaesebroeck B, Guillermet-Guibert J, Graupera M, Bilanges B. 2010. The emerging mechanisms of isoform-specific PI3K signalling. Nat Rev Mol Cell Bio 11:329–341.

349. Fruman DA, Rommel C. 2014. PI3K and cancer: lessons, challenges and opportunities. Nat Rev Drug Discov 13:140–156.

350. Yang J, Nie J, Ma X, Wei Y, Peng Y, Wei X. 2019. Targeting PI3K in cancer: mechanisms and advances in clinical trials. Mol Cancer 18:26.

351. Oki Y, Fanale M, Romaguera J, Fayad L, Fowler N, Copeland A, Samaniego F, Kwak LW, Neelapu S, Wang M, Feng L, Younes A. 2015. Phase II study of an AKT inhibitor MK2206 in patients with relapsed or refractory lymphoma. Brit J Haematol 171:463–470.

352. Blagosklonny MV. 2019. Rapamycin for longevity: opinion article. Aging Albany Ny 11:8048–8067.

353. Augustine JJ, Bodziak KA, Hricik DE. 2007. Use of Sirolimus in Solid Organ Transplantation. Drugs 67:369–391.

354. Kastrati A, Mehilli J, Beckerath N von, Dibra A, Hausleiter J, Pache J, Schühlen H, Schmitt C, Dirschinger J, Schömig A, Investigators for the I-DS. 2005. Sirolimus-Eluting Stent or Paclitaxel-Eluting Stent vs Balloon Angioplasty for Prevention of Recurrences in Patients With Coronary In-Stent Restenosis: A Randomized Controlled Trial. Jama 293:165–171.

355. Cloughesy TF, Yoshimoto K, Nghiemphu P, Brown K, Dang J, Zhu S, Hsueh T, Chen Y, Wang W, Youngkin D, Liau L, Martin N, Becker D, Bergsneider M, Lai A, Green R, Oglesby T, Koleto M, Trent J, Horvath S, Mischel PS, Mellinghoff IK, Sawyers CL. 2008. Antitumor Activity of Rapamycin in a Phase I Trial for Patients with Recurrent PTEN-Deficient Glioblastoma. Plos Med 5:e8.

356. Kaeberlein M, Galvan V. 2019. Rapamycin and Alzheimer's disease: Time for a clinical trial? Sci Transl Med 11:eaar4289.

357. Kanehisa M, Furumichi M, Sato Y, Ishiguro-Watanabe M, Tanabe M. 2020. KEGG: integrating viruses and cellular organisms. Nucleic Acids Res 49:gkaa970-.

358. Kanehisa M, Goto S. 2000. KEGG: Kyoto Encyclopedia of Genes and Genomes. Nucleic Acids Res 28:27–30.

359. Kanehisa M. 2019. Toward understanding the origin and evolution of cellular organisms. Protein Sci 28:1947–1951.

360. Howe KL, Achuthan P, Allen J, Allen J, Alvarez-Jarreta J, Amode MR, Armean IM, Azov AG, Bennett R, Bhai J, Billis K, Boddu S, Charkhchi M, Cummins C, Da Rin Fioretto L, Davidson C, Dodiya K, El Houdaigui B, Fatima R, Gall A, Garcia Giron C, Grego T, Guijarro-Clarke C, Haggerty L, Hemrom A, Hourlier T, Izuogu OG, Juettemann T, Kaikala V, Kay M, Lavidas I, Le T, Lemos D, Gonzalez Martinez J, Marugán JC, Maurel T, McMahon AC, Mohanan S, Moore B, Muffato M, Oheh DN, Paraschas D, Parker A, Parton A, Prosovetskaia I, Sakthivel MP, Salam AIA, Schmitt BM, Schuilenburg H, Sheppard D, Steed E, Szpak M, Szuba M, Taylor K, Thormann A, Threadgold G, Walts B, Winterbottom A, Chakiachvili M, Chaubal A, De Silva N, Flint B, Frankish A, Hunt SE, IIsley GR, Langridge N, Loveland JE, Martin FJ, Mudge JM, Morales J, Perry E, Ruffier M, Tate J, Thybert D, Trevanion SJ, Cunningham F, Yates AD, Zerbino DR, Flicek P. 2020. Ensembl 2021. Nucleic Acids Res 49:gkaa942-.

361. J L. 2020. eulerr: Area-Proportional Euler and Venn Diagrams with Ellipses. R package.

362. Dangoria NS, Breau WC, Anderson HA, Cishek DM, Norkin LC. 1996. Extracellular Simian Virus 40 Induces an ERK/MAP Kinase-independent Signalling Pathway that Activates Primary Response Genes and Promotes Virus Entry. J Gen Virol 77:2173–2182.

363. Rodriguez-Viciana P, Collins C, Fried M. 2006. Polyoma and SV40 proteins differentially regulate PP2A to activate distinct cellular signaling pathways involved in growth control. Proc National Acad Sci 103:19290–19295.

364. Link A, Shin SK, Nagasaka T, Balaguer F, Koi M, Jung B, Boland CR, Goel A. 2009. JC Virus Mediates Invasion and Migration in Colorectal Metastasis. Plos One 4:e8146.

365. Andrabi S, Gjoerup OV, Kean JA, Roberts TM, Schaffhausen B. 2007. Protein phosphatase 2A regulates life and death decisions via Akt in a context-dependent manner. Proc National Acad Sci 104:19011–19016.

366. Bollag B, Hofstetter CA, Reviriego-Mendoza MM, Frisque RJ. 2010. JC Virus Small t Antigen Binds Phosphatase PP2A and Rb Family Proteins and Is Required for Efficient Viral DNA Replication Activity. Plos One 5:e10606.

367. Pollard SM, Yoshikawa K, Clarke ID, Danovi D, Stricker S, Russell R, Bayani J, Head R, Lee M, Bernstein M, Squire JA, Smith A, Dirks P. 2009. Glioma Stem Cell Lines Expanded in Adherent Culture Have Tumor-Specific Phenotypes and Are Suitable for Chemical and Genetic Screens. Cell Stem Cell 4:568–580.

368. Louis N, Evelegh C, Graham FL. 1997. Cloning and Sequencing of the Cellular–Viral Junctions from the Human Adenovirus Type 5 Transformed 293 Cell Line. Virology 233:423–429.

369. Berk AJ. 2005. Recent lessons in gene expression, cell cycle control, and cell biology from adenovirus. Oncogene 24:7673–7685.

370. Moran E. 1993. DNA tumor virus transforming proteins and the cell cycle. Curr Opin Genet Dev 3:63–70.

371. Nevins. 1992. E2F: a link between the Rb tumor suppressor protein and viral oncoproteins. Science 258:424–429.

372. Frisch SM, Mymryk JS. 2002. Adenovirus-5 E1A: paradox and paradigm. Nat Rev Mol Cell Bio 3:441–452.

373. Levine AJ. 1990. The p53 protein and its interactions with the oncogene products of the small DNA tumor viruses. Virology 177:419–426.

374. Arroyo JD, Hahn WC. 2005. Involvement of PP2A in viral and cellular transformation. Oncogene 24:7746–7755.

375. Sariyer IK, Khalili K, Safak M. 2008. Dephosphorylation of JC virus agnoprotein by protein phosphatase 2A: inhibition by small t antigen. Virology 375:464–79.

376. Sarbassov DD, Ali SM, Kim D-H, Guertin DA, Latek RR, Erdjument-Bromage H, Tempst P, Sabatini DM. 2004. Rictor, a Novel Binding Partner of mTOR, Defines a Rapamycin-Insensitive and Raptor-Independent Pathway that Regulates the Cytoskeleton. Curr Biol 14:1296–1302.

377. Feldman ME, Apsel B, Uotila A, Loewith R, Knight ZA, Ruggero D, Shokat KM. 2009. Active-Site Inhibitors of mTOR Target Rapamycin-Resistant Outputs of mTORC1 and mTORC2. Plos Biol 7:e1000038.

378. Kwun HJ, Chang Y, Moore PS. 2017. Protein-mediated viral latency is a novel mechanism for Merkel cell polyomavirus persistence. Proc National Acad Sci 114:E4040–E4047.

379. Wu J, Su H, Yu Z, Xi S, Guo C, Hu Z, Qu Y, Cai H, Zhao Y, Zhao H, Chen F, Huang Y, To ST, Feng B, Sai K, Chen Z, Wang J. 2020. Skp2 modulates proliferation, senescence and tumorigenesis of glioma. Cancer Cell Int 20:71.

380. Zhang L, Wang C. 2006. F-box protein Skp2: a novel transcriptional target of E2F. Oncogene 25:2615–2627.

381. Wipf P, Halter RJ. 2005. Chemistry and biology of wortmannin. Org Biomol Chem 3:2053–2061.

382. Pittini Á, Casaravilla C, Allen JE, Díaz Á. 2016. Pharmacological inhibition of PI3K class III enhances the production of pro- and anti-inflammatory cytokines in dendritic cells stimulated by TLR agonists. Int Immunopharmacol 36:213–217.

383. Brunn GJ, Williams J, Sabers C, Wiederrecht G, Lawrence JC, Abraham RT. 1996. Direct inhibition of the signaling functions of the mammalian target of rapamycin by the phosphoinositide 3-kinase inhibitors, wortmannin and LY294002. Embo J 15:5256–5267.

384. O'Hara BA, Morris-Love J, Gee GV, Haley SA, Atwood WJ. 2020. JC Virus infected choroid plexus epithelial cells produce extracellular vesicles that infect glial cells independently of the virus attachment receptor. Plos Pathog 16:e1008371.

385. Khalili K, Sariyer IK, Safak M. 2008. Small tumor antigen of polyomaviruses: role in viral life cycle and cell transformation. Journal of cellular physiology 215:309–19.

386. Bollag B, Kilpatrick LH, Tyagarajan SK, Tevethia MJ, Frisque RJ. 2006. JC virus T'135, T'136 and T'165 proteins interact with cellular p107 and p130 in vivo and influence viral transformation potential. Journal of neurovirology 12:428–42.

387. White MK, Safak M, Khalili K. 2009. Regulation of gene expression in primate polyomaviruses. Journal of virology 83:10846–56.

388. Martin JD, Foster GC. 1984. Multiple JC Virus Genomes from One Patient. J Gen Virol 65:1405–1411.

389. Martin JD, King DM, Slauch JM, Frisque RJ. 1985. Differences in regulatory sequences of naturally occurring JC virus variants. Journal of virology 53:306–11.

390. Amemiya K, Traub R, Durham L, Major EO. 1992. Adjacent nuclear factor-1 and activator protein binding sites in the enhancer of the neurotropic JC virus. A common characteristic of many brain-specific genes. J Biol Chem 267:14204–14211.

391. Sumner C, Shinohara T, Durham L, Traub R, Major EO, Amemiya K. 1996. Expression of multiple classes of the Nuclear Factor-1 family in the developing human brain: Differential expression of two classes of NF-1 genes. J Neurovirol 2:87–100.

392. Fornes O, Castro-Mondragon JA, Khan A, van der Lee R, Zhang X, Richmond PA, Modi BP, Correard S, Gheorghe M, Baranašić D, Santana-Garcia W, Tan G, Chèneby J, Ballester B, Parcy F, Sandelin A, Lenhard B, Wasserman WW, Mathelier A. 2019. JASPAR 2020: update of the open-access database of transcription factor binding profiles. Nucleic Acids Res 48:D87–D92.

393. Nakamichi K, Kishida S, Tanaka K, Suganuma A, Sano Y, Sano H, Kanda T, Maeda N, Kira J, Itoh A, Kato N, Tomimoto H, Kurane I, Lim C-K, Mizusawa H, Saijo M. 2013. Sequential changes in the non-coding control region sequences of JC polyomaviruses from the cerebrospinal fluid of patients with progressive multifocal leukoencephalopathy. Arch Virol 158:639–650.

394. Nakamichi K, Tajima S, Lim C-K, Saijo M. 2014. High-resolution melting analysis for mutation scanning in the non-coding control region of JC polyomavirus from patients with progressive multifocal leukoencephalopathy. Arch Virol 159:1687–1696.

395. Ferrante P, Caldarelli-Stefano R, Omodeo-Zorini E, Cagni AE, Cocchi L, Suter F, Maserati R. 1997. Comprehensive investigation of the presence of JC virus in AIDS patients with and without progressive multifocal leukoencephalopathy. J Med Virol 52:235–242.

396. Caldarelli-Stefano R, Vago L, Omodeo-Zorini E, Mediati M, Losciale L, Nebuloni M, Costanzi G, Ferrante P. 1999. Detection and typing of JC virus in autopsy brains and extraneural organs of AIDS patients and non-immunocompromised individuals. J Neurovirol 5:125–133.

397. Sundsfjord A, Osei A, Rosenqvist H, Ghelue MV, Silsand Y, Haga H-J, Rekvig OP, Moens U. 1999. BK and JC Viruses in Patients with Systemic Lupus Erythematosus: Prevalent and Persistent BK Viruria, Sequence Stability of the Viral Regulatory Regions, and Nondetectable Viremia. J Infect Dis 180:1–9.

398. Pfister L-A, Letvin NL, Koralnik IJ. 2001. JC Virus Regulatory Region Tandem Repeats in Plasma and Central Nervous System Isolates Correlate with Poor Clinical Outcome in Patients with Progressive Multifocal Leukoencephalopathy. J Virol 75:5672–5676.

399. Loy TV, Thys K, Tritsmans L, Stuyver LJ. 2013. Quasispecies Analysis of JC Virus DNA Present in Urine of Healthy Subjects. Plos One 8:e70950.

400. Horthongkham, N., Athipanyasilp, N., Pattama, A., Sirijatupat, R., Sutthent, R., Kantakamalakul, W., Romputtan, Sornprasert P and, S. 2018. Genotypic and clinical characteristic of JC virus from organ transplant patients in tertiary hospital during 2012-2015. unpublished.

401. Prezioso, C., Zingaropoli, M.A., Iannetta, M., Pietropaolo, Ciardi V and, M.R. 2020. unpublished.

402. Larkin MA, Blackshields G, Brown NP, Chenna R, McGettigan PA, McWilliam H, Valentin F, Wallace IM, Wilm A, Lopez R, Thompson JD, Gibson TJ, Higgins DG. 2007. Clustal W and Clustal X version 2.0. Bioinformatics 23:2947–2948.

403. 1987. The neighbor-joining method: a new method for reconstructing phylogenetic trees. Mol Biol Evol https://doi.org/10.1093/oxfordjournals.molbev.a040454.

404. Mailund T, Brodal GS, Fagerberg R, Pedersen CN, Phillips D. 2006. Recrafting the neighbor-joining method. Bmc Bioinformatics 7:29.

405. Shen W, Le S, Li Y, Hu F. 2016. SeqKit: A Cross-Platform and Ultrafast Toolkit for FASTA/Q File Manipulation. Plos One 11:e0163962.

406. Scarpulla RC. 2008. Nuclear Control of Respiratory Chain Expression by Nuclear Respiratory Factors and PGC-1-Related Coactivator. Ann Ny Acad Sci 1147:321–334.

407. Dhar SS, Wong-Riley MTT. 2009. Coupling of Energy Metabolism and Synaptic Transmission at the Transcriptional Level: Role of Nuclear Respiratory Factor 1 in Regulating both Cytochrome c Oxidase and NMDA Glutamate Receptor Subunit Genes. J Neurosci 29:483–492.

408. Boldorini R, Omodeo-Zorini E, Nebuloni M, Benigni E, Vago L, Ferri A, Monga G. 2003. Lytic JC Virus Infection in the Kidneys of AIDS Subjects. Modern Pathol 16:35–42.

409. Inaga TT, Yogo Y, Kitamura T, Aso Y. 1992. Persistence of archetypal JC virus DNA in normal renal tissue derived from tumor-bearing patients. Virology 186:736–741.

410. Agostini HT, Ryschkewitsch CF, Stoner GL. 1998. Rearrangements of archetypal regulatory regions in JC virus genomes from urine. Research in virology 149:163–70.

411. Shinohara T, Nagashima K, Major EO. 1997. Propagation of the Human Polyomavirus, JCV, in Human Neuroblastoma Cell Lines. Virology 228:269–277.

412. Romagnoli L, Wollebo HS, Deshmane SL, Mukerjee R, Valle LD, Safak M, Khalili K, White MK. 2009. Modulation of JC virus transcription by C/EBPbeta. Virus research 146:97–106.

413. Li B, Huang Q, Wei G-H. 2019. The Role of HOX Transcription Factors in Cancer Predisposition and Progression. Cancers 11:528.

414. Li L, Liu M, Kang L, Li Y, Dai Z, Wang B, Liu S, Chen L, Tan Y, Wu G. 2016. HHEX: A Crosstalker between HCMV Infection and Proliferation of VSMCs. Front Cell Infect Mi 6:169.

415. Kasai H, Mochizuki K, Tanaka T, Yamashita A, Matsuura Y, Moriishi K. 2020. Induction of HOX Genes by Hepatitis C Virus Infection via Impairment of Histone H2A Monoubiquitination. J Virol 95.

416. LIU W-J, ZHANG T, GUO Q-L, LIU C-Y, BAI Y-Q. 2016. Effect of ATRA on the expression of HOXA5 gene in K562 cells and its relationship with cell cycle and apoptosis. Mol Med Rep 13:4221–4228.

417. Golson ML, Kaestner KH. 2016. Fox transcription factors: from development to disease. Development 143:4558–4570.

418. Ramezani A, Nikravesh H, Faghihloo E. 2019. The roles of FOX proteins in virus-associated cancers. J Cell Physiol 234:3347–3361.

419. Zeng C, Yao Y, Jie W, Zhang M, Hu X, Zhao Y, Wang S, Yin J, Song Y. 2013. Up-regulation of Foxp3 participates in progression of cervical cancer. Cancer Immunol Immunother 62:481–487.

420. Mitildzans A, Isajevs S, Rezeberga D. 2019. P33 Up-regulation of FOXP3 T regulatory lymphocytes in patients with high-grade squamous intraepithelial lesions correlated with HPV infection. Int J Gynecol Cancer 29:A70.

421. Mosser DM, Zhang X. 2008. Interleukin-10: new perspectives on an old cytokine. Immunol Rev 226:205–218.

422. Peferoen L, Kipp M, Valk P, Noort JM, Amor S. 2014. Oligodendrocyte-microglia cross-talk in the central nervous system. Immunology 141:302–313.

423. Porro C, Cianciulli A, Panaro MA. 2020. The Regulatory Role of IL-10 in Neurodegenerative Diseases. Biomol 10:1017.

424. Doncel AM, Rubio A, Arroyo R, Heras V de las, Martín C, Fernandez-Arquero M, Concha EG de la. 2002. Interleukin-10 polymorphisms in Spanish Multiple Sclerosis patients. J Neuroimmunol 131:168–172.

425. Myhr K-M, Vågnes KS, Marøy TH, Aarseth JH, Nyland HI, Vedeler CA. 2002. Interleukin-10 promoter polymorphisms in patients with multiple sclerosis. J Neurol Sci 202:93–97.

426. O'Neill EJ, Day MJ, Wraith DC. 2006. IL-10 is essential for disease protection following intranasal peptide administration in the C57BL/6 model of EAE. J Neuroimmunol 178:1–8.

427. Li K, Li J, Zheng J, Qin S. 2019. Reactive Astrocytes in Neurodegenerative Diseases. Aging Dis 10:664–675.

428. Cervo PR di V, Romanov RA, Spigolon G, Masini D, Martín-Montañez E, Toledo EM, Manno GL, Feyder M, Pifl C, Ng Y-H, Sánchez SP, Linnarsson S, Wernig M, Harkany T, Fisone G, Arenas E. 2017. Induction of functional dopamine neurons from human astrocytes in vitro and mouse astrocytes in a Parkinson's disease model. Nat Biotechnol 35:444–452.

429. 2015. Astrocyte mediated MMP-9 activation in the synapse dysfunction: An implication in Alzheimer disease. Ther Targets Neurological Dis https://doi.org/10.14800/ttnd.243.

430. Nutma E, Gent D van, Amor S, Peferoen LAN. 2020. Astrocyte and Oligodendrocyte Cross-Talk in the Central Nervous System. Cells 9:600.

431. Bezzi P, Domercq M, Brambilla L, Galli R, Schols D, Clercq ED, Vescovi A, Bagetta G, Kollias G, Meldolesi J, Volterra A. 2001. CXCR4-activated astrocyte glutamate release via TNFα: amplification by microglia triggers neurotoxicity. Nat Neurosci 4:702–710.

432. Jeremic A, Jeftinija K, Stevanovic J, Glavaski A, Jeftinija S. 2001. ATP stimulates calcium-dependent glutamate release from cultured astrocytes. J Neurochem 77:664–675.

433. Amadio S, Parisi C, Piras E, Fabbrizio P, Apolloni S, Montilli C, Luchetti S, Ruggieri S, Gasperini C, Laghi-Pasini F, Battistini L, Volonté C. 2017. Modulation of P2X7 Receptor during Inflammation in Multiple Sclerosis. Front Immunol 8:1529.

434. Prezioso C, Scribano D, Bellizzi A, Anzivino E, Rodio DM, Trancassini M, Palamara AT, Pietropaolo V. 2017. Efficient propagation of archetype JC polyomavirus in COS-7 cells: evaluation of rearrangements within the NCCR structural organization after transfection. Arch Virol 162:3745–3752.

435. Rato S, Golumbeanu M, Telenti A, Ciuffi A. 2017. Exploring viral infection using single-cell sequencing. Virus Res 239:55–68.

436. An P, Cantalupo PG, Zheng W, Sáenz-Robles MT, Duray AM, Weitz D, Pipas JM. 2021. Single-Cell Transcriptomics Reveals a Heterogeneous Cellular Response to BK Virus Infection. J Virol 95.

437. Schurch NJ, Schofield P, Gierliński M, Cole C, Sherstnev A, Singh V, Wrobel N, Gharbi K, Simpson GG, Owen-Hughes T, Blaxter M, Barton GJ. 2016. How many biological replicates are needed in an RNA-seq experiment and which differential expression tool should you use? Rna 22:839–851.

438. Wüthrich C, Batson S, Anderson MP, White LR, Koralnik IJ. 2016. JC Virus Infects Neurons and Glial Cells in the Hippocampus. J Neuropathology Exp Neurology 75:712–717.

439. Miskin DP, Koralnik IJ. 2015. Novel syndromes associated with JC virus infection of neurons and meningeal cells. Curr Opin Neurol 28:288–294.

CHAPTER 8

BIOGRAPHY OF THE AUTHOR

Michael Wilczek was born in New Hartford, New York on August 23rd, 1991. He was raised in Marcy, New York and graduated from Holland Patent High School in 2009. He attended the University at Albany, State University of New York and graduated in 2013 with a Bachelor's degree in Biology. After his degree he volunteered and interned at the New York State Health Department. He arrived in Maine and entered the Microbiology graduate program at The University of Maine in the fall of 2015. Michael is a candidate for the Doctor of Philosophy degree in Microbiology from the University of Maine in August 2021.